Water Cycles of Mercury and the Moon:

Sources, Evolution, and Current States of Polar Volatiles

By

Ariel N. Deutsch

B.S. Geology, The College of William & Mary, 2014

M.Sc. Planetary Geosciences, Brown University, 2017

A dissertation submitted in partial fulfillment of the requirements for the degree of

Doctor of Philosophy in the program of Earth, Environmental, and Planetary Sciences at

Brown University

Providence, Rhode Island

May 2020

This dissertation by Ariel N. Deutsch is accepted in its present form by the Department of Earth, Environmental, and Planetary Sciences as satisfying the dissertation requirement for the degree of Doctor of Philosophy

Date ________________ ______________________________________

James W. Head, Brown University, Advisor

Recommended to the Graduate Council

Date ________________ ______________________________________

Gregory A. Neumann, NASA Goddard Space Flight Center, Reader

Date ________________ ______________________________________

Carlé M. Pieters, Brown University, Reader

Date ________________ ______________________________________

James M. Russell, Brown University, Reader

Date ________________ ______________________________________

Dana M. Hurley, Johns Hopkins University Applied Physics Laboratory, Reader

Approved by the Graduate Council

Date ________________ ______________________________________

Andrew G. Campbell, Dean of the Graduate School

Ariel N. Deutsch
Ph.D. Candidate | NASA Graduate Fellow
Department of Earth, Environmental, and Planetary Sciences
Brown University, Box 1846, Providence, RI 02912
https://www.arieldeutsch.com

Education

Brown University, *Department of Earth, Environmental and Planetary Sciences* (2015–present)
Ph.D. Candidate, Planetary Geosciences, 4.0 GPA
M.Sc., Planetary Geosciences, 4.0 GPA
Thesis: *Water cycles of Mercury and the Moon: Sources, evolution, and state of polar volatiles*
Adviser: James W. Head III
NASA Technical Adviser: Gregory A. Neumann (NASA GSFC)
Committee Members: Carle M. Pieters, James M. Russell

The College of William & Mary, *Department of Geology* (2010–2014)
B.Sc., Geological Sciences, High Honors
Thesis: *Investigating water ice in persistently shadowed craters in Mercury's north polar region*
Adviser: Joel Levine (Applied Science)
Committee Members: Christopher Bailey, Heather Macdonald, Eugene Tracy (Physics)

Publications

1. **Deutsch, A.N.,** Head, J.W., Parman, S.W., Wilson, L., Neumann, G.A., Lowden, F., *In Review.* The flux of volcanic eruptions on Mercury: Potential contributions to transient atmospheres and buried polar deposits.
2. Moore, K., Courville, S.W., Ferguson, S., Shoenfeld, A., Llera, K., Agrawal, R., Buhler, P., Brack, D., Connour, K., Czaplinski, E., DeLuca, M., **Deutsch, A.N.,** Hammond, N., Kuettel, D., Marusiak, A., Nerozzi, S., Stuart, J., Tarnas, J., Thelen, A., Castillo, J., Smythe, W., Landau, D., Mitchell, K., Budney, C., *In Review.* Bridge to the stars: A mission concept to an interstellar object. *Planetary and Space Science.*
3. **Deutsch, A.N.,** Head, J.W., Neumann, G.A., *Accepted.* Assessing the roughness properties of circumpolar lunar craters: Implications for the timing of water ice delivery to the Moon. *Geophysical Research Letters.*
4. **Deutsch, A.N.,** Neumann, G.A., Head, J.W., Lucey, P.G., *Accepted*. Temperature-dependent changes in the normal albedo of the lunar surface at 1064 nm. *Journal of Geophysical Research: Planets*.
5. **Deutsch, A.N.,** Head, J.W., Neumann, G.A., 2019. Analyzing the ages of south polar craters on the Moon: Implications for the sources and evolution of surface water ice. *Icarus 336,* 113455. https://doi.org/10.1016/j.icarus.2019.113455.
6. **Deutsch, A.N.**, Head, J.W., Neumann, G.A., 2019. Age constraints of Mercury's polar deposits suggest recent delivery of ice. *Earth and Planetary Science Letters 520*, 26–33. https://doi.org/10.1016/j.epsl.2019.05.027.
7. **Deutsch, A.N.**, Neumann, G.A., Head, J.W., Wilson, L., 2019. GRAIL-identified gravity anomalies in Oceanus Procellarum: Insight into subsurface impact and magmatic structures on the Moon. *Icarus 331*, 192–208. https://doi.org/10.1016/j.epsl.2019.05.027.
8. Palumbo, A.M. and **Deutsch, A.N.**, Bramble, M.S., Tarnas, J.T., Boatwright, B.D., Lark, L.H., Nathan, E.M., Wilner, J.A., Chen, Y., Anzures, B.A., Denton, C.A., Tokle, L., Casey, G., Pimentel, A.G., Head, J.W., Ramsley, K.R., Shah, U., Kothandhapani, A., Gokul, H.P., Mehta, J., Vatsal, V, 2019. A manuscript titled Scientific exploration of Mare Imbrium with OrbitBeyond, Inc.: Characterizing the regional volcanic history of the Moon. *New Space 7,* 137–150. https://doi.org/10.1089/space.2019.0016.
9. Fastook, J.L., Head, J.W., **Deutsch, A.N.**, 2019. Glaciation on Mercury: Accumulation and flow of ice in permanently shadowed circum-polar crater interiors. *Icarus 317,* 81–93. https://doi.org/10.1016/j.icarus.2018.07.004.

10. **Deutsch, A.N.**, Head, J.W, Chabot, N.L., Neumann, G.A., 2018. Constraining the thickness of polar ice deposits on Mercury using the Mercury Laser Altimeter and small craters in permanently shadowed regions. *Icarus 305,* 139–148. https://doi.org/10.1016/j.icarus.2018.01.013.
11. **Deutsch, A.N.**, et al., 2018. Science exploration architecture for Phobos and Deimos: The role of Phobos and Deimos in the future exploration of Mars. *Advances in Space Research 62*, 2174–2186. https://doi.org/10.1016/j.asr.2017.12.017.
12. **Deutsch, A.N.**, Neumann, G.A., Head, J.W., 2017. New evidence for surface water ice in small-scale cold traps and in three large craters at the north polar region of Mercury from the Mercury Laser Altimeter. *Geophysical Research Letters 44,* 9233–9241, https://doi.org/10.1002/2017GL074723.
13. Hurley, D.M., Pendleton, Y. **Deutsch, A.N.**, 2017. Signs of water in a moon rock. *Eos 98,* https://doi.org/10.1029/2017EO077313.
14. **Deutsch, A.N.**, Chabot, N.L., Mazarico, E., Ernst, C.M., Head, J.W., Neumann, G.A., Solomon, S.C., 2016. Comparison of areas in shadow from imaging and altimetry in the north polar region of Mercury and implications for polar ice deposits. *Icarus 280,* 158–171, https://doi.org/10.1016/j.icarus.2016.06.015.
15. Chabot, N.L., Ernst, C.M., Paige, D.A., Nair, H., Denevi, B.W., Blewett, D.T., Murchie, S.L., **Deutsch, A.N.**, Head, J.W., Solomon, S.C., 2016. Imaging Mercury's polar deposits during MESSENGER's low-altitude campaign. *Geophysical Research Letters 43,* 9461–9468, https://doi.org/10.1002/2016GL070403.
16. Chabot, N.L., Ernst, C.M., Denevi, B.W., Nair, H., **Deutsch, A.N.**, Blewett, D.T., Murchie, S.L., Neumann, G.A., Mazarico, E., Paige, D.A., Harmon, J.L., Head, J.W., Solomon, S.C., 2014. Images of surface volatiles in Mercury's polar craters acquired by the MESSENGER spacecraft. *Geology 42,* 1051–1054, https://doi.org/10.1130/G35916.1.

Professional Experience

NASA Advanced STEM Training And Research (ASTAR) Graduate Fellow (2016–present)
Planetary Geology, Geophysics, and Geochemistry Laboratory, NASA Goddard Space Flight Center
PI: Prof. James W. Head, NASA Technical Adviser: Dr. Gregory A. Neumann

NASA/APL Intern (May 2015–July 2015)
MESSENGER Science Operations Center, Applied Physics Laboratory at Johns Hopkins University
Adviser: Dr. Nancy L. Chabot

NASA/APL Intern (June 2014–Aug 2014)
MESSENGER Science Operations Center, Applied Physics Laboratory at Johns Hopkins University
Adviser: Dr. Nancy L. Chabot

NASA/APL Intern (June 2013–Aug 2013)
MESSENGER Science Operations Center, Applied Physics Laboratory at Johns Hopkins University
Adviser: Dr. Nancy L. Chabot

Research Assistant (May 2012–Aug 2012)
Laboratory of Analytical Biology, Smithsonian Institution, National Museum of Natural History
Adviser: Director Lee A. Weigt

Research Intern (May 2011–Aug 2011)
Laboratory of Analytical Biology, Smithsonian Institution, National Museum of Natural History
Adviser: Director Lee A. Weigt

Mission Experience

Science from Lunar Permanently Shadowed Regions (Concept Study)
Science Lead for a submitted mission concept study proposal (not selected) to further our understanding of the volatiles in lunar permanent shadows. Mission science focused on ground-truthing, processes that modulate the distribution, activity, composition, and transport of volatiles, and thermophysical and geotechnical properties of shadowed regions. *Study PI: Dr. Dana M. Hurley.*

OrbitBeyond, Inc. (NASA CLPS Provider)
Student co-lead in collaboration between Brown University and OrbitBeyond, a US-based lunar transportation company. Helping to provide regional geologic context of landing sites and to define scientific targets and observational parameters to integrate science activities into upcoming missions.

Bridge to the Stars: A Mission to an Interstellar Object (Concept Study)
Command and Data Handling Chair and Science Team Member in the 2019 JPL Planetary Science Summer Seminar. Worked with 17 other selected students, post-docs, and early career professionals to design a flyby of a yet-to-be-detected interstellar object as it passes through our own Solar System under New Frontiers constraints. Benefited under mentorship from JPL's A-Team and Team X.

Etna to Enceladus (Concept Study)
Science PI in the Caltech Space Challenge 2019. Worked together with 15 other internationally selected students to design a landed sample assay + geophysical network to explore the habitability and biosignatures of Enceladus under the constraints of New Frontiers requirements. Benefited under mentorship from JPL's A-Team and industry leaders.

Lunar Reconnaissance Orbiter (LRO)
Graduate Research Fellow at GSFC in the Planetary Geology, Geophysics, and Geochemistry Laboratory (PGGGL). Utilizing LOLA, Diviner, and WAC data to analyze characteristics of surface and subsurface ice at the lunar poles. Utilizing LOLA and Diviner data to analyze temperature-dependent changes in the surface reflectance of the Moon. *Project Scientist: Dr. Noah E. Petro.*

Gravity Recovery and Interior Laboratory (GRAIL)
Graduate Research Fellow at GSFC in the PGGL. Utilizing gravitational and topographic data to constrain subsurface density structures that may contribute to positive Bouguer gravity anomalies on the lunar nearside. *Mission PI: Dr. Maria T. Zuber.*

MErcury Surface, Space ENvironment, GEochemistry, and Ranging (MESSENGER)
Summer research intern in the Science Operations Center from 2014–2016. Utilized MDIS and MLA data to study the distribution of permanently shadowed regions, the distribution and characteristics of water-ice deposits, and the morphology of impact craters on Mercury. Presented at MESSENGER Science Team Meetings. *Mission PI: Dr. Sean C. Soloman.*

AWARDS AND HONORS

Funding

NASA ASTAR Graduate Fellow, Goddard Space Flight Center (80NSSC19K1289)	2019–2020
Society of Exploration Geophysicists Award, Earl D. & Reba C. Griffin Memorial Scholarship	2018–2019
NASA ASTAR Graduate Fellow, Goddard Space Flight Center (NNX16AT19H)	2016–2019
Brown Fellow, Department of Earth, Environmental and Planetary Sciences	2015–2016
Roland G.D. Richardson Fellow, Brown University	2015–2016
Virginia Space Grant, Applied Physics Laboratory	2014

Awards and Honors

JPL Planetary Science Summer Seminar, Science Team + C&DH Chair	2019
Apollo 50 Panel with Apollo 17 Lunar Module Pilot Harrison H. "Jack" Schmitt, U.S.S. Hornet *Lunar Geology: Past, Present, and Future*	2019
CalTech Space Challenge 2019: Encelanders, Principal Investigator	2019
LPI Career Development Award	2019
Best Poster Award, International Symposium on Lunar and Planetary Science	2018
Sigma Xi Honorary Scientific Society Associate Member	2018–present
William & Mary Young Alumni Fellow	2016–present
High Honors (Highest distinction), Department of Geology, College of William & Mary	2014

Travel Grants

Lunar Surface Science Workshop, Early Career Scientist Travel Award	2020
Larry Taylor Travel Fund for the 2019 Annual Meeting of the Lunar Exploration Analysis Group	2019
Mercury: Current and Future Science of the Innermost Planet Young Scientist Travel Award	2018
Graduate School Council Travel Award, Brown University	2018, 2019
LunGradCon Travel Grant	2016, 2017, 2019
Brown University International Travel Grant	2016, 2018, 2020
Brown University Graduate Travel Grant	2015–2020

Invited Talks

Department of Earth, Atmospheric, and Planetary Sciences, MIT	1 Oct 2019
Water Cycles of Mercury and the Moon: Sources, Evolution, and Current State of Polar Volatiles	
Microsymposium 60: Forward to the Moon to Stay: Undertaking Transformative Lunar Science with Commercial Partners	16 Mar 2019
An Example of Working with Commercial Partners: The OrbitBeyond Lunar Mare Imbrium Lava Flow Design Reference Mission	
Mercury: Current and Future Science of the Innermost Planet, USRA	2 May 2018
Differences between Surface Ice Deposits at the Poles of Mercury and the Moon: Insights into Ages of the Ice	
Research Matters Nominee and Selected Speaker, Brown University	4 Nov 2017
Ice on Mercury, The Moon, and Beyond	
SSERVI/NESF Autonomy for Future SMD Missions Workshop, NASA Ames	21 July 2017
Exploration of Water Ice and Organics at the Poles of Mercury	
LunGradCon, NASA Ames Research Center	17 July 2017
The Geology and Geophysics of the Moon	
Microsymposium 57: Polar Volatiles on the Moon and Mercury: Nature, Evolution and Future Exploration	19 Mar 2016
Mercury's Polar Deposits as Revealed by MESSENGER Mission Image Data: Correlation of Radar Bright Deposits and Large PSRs	

PROFESSIONAL ACTIVITIES AND SERVICE

Contributions

Lead, White Paper on Science Opportunities from Mercury's Polar Deposits	2020
Contributing Writer, White Paper on the Lunar Polar Volatiles Workshop Lead: Dr. Kathleen E. Mandt	2018
Contributing Writer, White Paper on the Case for Landed Mercury Exploration and the Timely Need for a Mission Concept Study Lead: Dr. Paul K. Byrne	2018
Contributing Writer, New Views of the Moon 2, Lunar Volatiles Chapter Leads: Dr. Dana M. Hurley and Dr. Matthew A. Siegler	2017–present
Executive Note-taker, SSERVI Special Workshop: Lunar Volatiles	2016

Departmental Service, Brown University

Graduate Student Writing Group Co-Lead	2020–present
Graduate Women in Science and Engineering (GWiSE) Co-President	2017–2019
First-Year Graduate Student Mentor	2017–present
Diversity Working Group	2017–present
GeoClub Co-President	2016–2017

Student Mentoring

Spacecraft Design Engineering, Brown University	2016–present
Panelist for Brown-Stanford Team Review International Genetically Engineered Machine (iGEM) Competition	2016, 2017, 2018
Panelist, The Leadership Alliance, Brown University "What's Grad School Like?"	1 Aug 2019
Panelist, The CareerLAB, Brown University "Succeeding in Graduate School"	14 Nov 2018
"Making the Graduate School Decision"	9 Oct 2018

Professional Service

NASA Executive Secretary, Review Panel	2020

Reviewer, JGR Planets	2019, 2020
Reviewer, Nature	2019
Reviewer, Icarus	2018
NASA External Proposal Reviewer	2018
Proposal Reviewer, Mercury Task Group, International Astronomical Union	2018–2020
Dwornik Judge for Undergraduate Presentations, LPSC	2017–2019
Student Organizer, Microsymposium Conference, Woodlands TX	2016–2019

Professional Memberships

European Geophysical Union	2020–present
American Geophysical Union	2018–present
Society of Exploration Geophysicists	2018–present
Association for Women Geoscientists	2016–present

Fieldwork

"The Sedimentary Rock Cycle on Mars and Earth" 2016
Permian Basin, New Mexico and West Texas (Brown University)

"Biosignatures and the Search for Life on Mars" 2016
Nordic Summer School, Iceland (NASA/ESF)

"Changes in Ecuadorian Forestry Detected through GIS" 2013
Coastal Ecuador (The College of William & Mary)

"Tropical Reef Environments" 2012
Gerace Research Center, San Salvador (The College of William & Mary)

"Identification of Fish Species through DNA Barcoding" 2011
Smithsonian Tropical Research Institute, Panama (Smithsonian Institution)

Conference Contributions

1. **Deutsch, A.N.**, Head, J.W., Parman, S.W., Neumann, G.A., Lowden, F., 2020. The mass flux of volatiles from effusive eruptions on Mercury. EGU General Assembly, abstract 3742. <u>Oral</u>.
2. Cannon, K.M., Mueller, R.P., **Deutsch, A.N.**, Van Susante, P., Tarnas, J.D., Colaprete, A.C., Sowers, G., Dreyer, C.B., Li, S., Sercel, J., Dove, A.R., Britt, D.T., 2020. The Snow Badger mission concept: Trenching for ice with humans and robots. Lunar Surface Science Workshop, abstract 5108. <u>Oral</u>.
3. Head, J.W., Scott, D.R., Pieters, C.M., Zuber, M.T., Smith, D.E., Mazarico, E., Barker, M., Neumann, G.A., Cremons, D.R., **Deutsch, A.N.**, 2020. The Artemis Lunar Exploration Program: A planetary science exploration perspective. Lunar Surface Science Workshop, abstract 5075. <u>Oral</u>.
4. **Deutsch, A.N.**, Head, J.W., Neumann, G.A., 2020. The roughness properties of small ice-bearing craters at the south pole of the Moon: Implications for accessing fresh water ice in future surface operations. LPSC 51, abstract 2115. <u>Oral</u>.
5. **Deutsch, A.N.**, Head, J.W., Parman, S.W., Neumann, G.A., Lowden, F., 2020. The mass flux of volatiles from effusive eruptions on Mercury. LPSC 51, abstract 2259. Poster.
6. Cannon, K.M., **Deutsch, A.N.**, Head, J.W., 2020. Stratigraphy of ice and ejecta deposits at the lunar poles. LPSC 51, abstract 1488. <u>Oral</u>.
7. Hurley, D.M., Prem, P., Stickle, A., Hibbitts, C., **Deutsch, A.N.**, Colaprete, A., Elphic, R., Li, S., Lucey, P., Liu, Y., Hosseini, S., Retherford, K.D., Zacny, K., Atkinson, J., Benna, M., Farrell, W., Needham, D., Gertsch, L., Delitsky, M., Hayne, P., 2020. Science from the lunar permanently shadowed regions. LPSC 51, abstract 1559. Poster.
8. Venigalla, C., **Deutsch, A.N.**, Panicucci, P., Peytaví, G.G., Pouplin, J., Tenelanda-Osorio, L., Guarriello, A., Castillo-Specia, E., Cho, Y.H., Da-Poian, V., Gunasekara, O., Jones, L., Krasteva, M., Mathanlal, T., Villanueva, N., Zaref, S., 2020. Assessing the habitability of an active ocean world: The Etna mission concept to explore Enceladus' tiger stripes. LPSC 51, abstract 2077. Poster.

9. Courville, S.W., Moore, K., Connour, K., Ferguson, S., Agrawal, R., Brack, D., Buhler, P., Czaplinski, E., DeLuca, M., **Deutsch, A.N.**, Hammond, N., Kuettel, D., Llera, K., Marusiak, A., Nerozzi, S., Shoenfeld, A., Tarnas, J., Thelen, A., Stuart, J., Castillo, J., Landau, D., Smythe, W., Budney, C., Mitchell K., 2020. Bridge to the stars: A mission concept to an interstellar object. LPSC 51, abstract 1766. Poster.
10. **Deutsch, A.N.**, Neumann, G.A., Head, J.W., Lucey, P.G., 2019. Temperature-dependent changes of the lunar surface at 1064 nm: Implications for future remotely sensed observations of the Moon. AGU Fall Meeting, abstract P34B-07. Oral.
11. Hurley, D.M., Colaprete, A., **Deutsch, A.N.**, Prem, P., Stickle, A.M., Hibbitts, C., Elphic, R.C., Li, S., Hosseini, S., Retherford, K.D., Gertsch, L.S., Zacny, K., Needham, D.H., Delitsky, M., Hayne, P.O., Benna, M., Lucey, P.G., Atkinson, J., Liu Y., Farrell, W.M. and The PIPELiNE Team, 2019. Mission to the Lunar Permanently Shadowed Regions: Polar Ice Prospecting Explorer for Lunar No-light Environments (PIPELiNE). AGU Fall Meeting, abstract P33D-02. Oral.
12. Panicucci, P., **Deutsch, A.N.**, Venigalla, C., Peytaví, G.G., Pouplin, J., Tenelanda-Osorio, L., Guarriello, A., Castillo-Specia, E., Cho, Y.H., Da-Poian, V., Gunasekara, O., Jones, L., Krasteva, M., Mathanlal, T., Villanueva, N., Zaref, S., 2019. Assessing the habitability of an active ocean world: The Etna mission concept to Enceladus' tiger stripes. Planetary Exploration, Horizon 2061, abstract H2061. Oral.
13. Hurley, D.M., **Deutsch, A.N.**, Colaprete, A., and the PIPELiNE Team, 2019. Science objectives of a mission to the lunar permanently shadowed regions. EPSC-DPS Joint Meeting, abstract 238-1. Poster.
14. Neumann, G.A., Goosens, S. **Deutsch, A.N.**, Head, J.W., 2019. Lunar gravity: Impact processes inform the density structure of the mare crust. GeoMünster, abstract 542. Poster.
15. **Deutsch, A.N.**, Neumann, G.A., Head, J.W., Lucey, P.G., 2019. Investigating diurnal changes in the normal albedo of the lunar surface at 1064 nm: A new analysis with the Lunar Orbiter Laser Altimeter. NASA Exploration Science Forum, abstract NESF2019-035. Oral.
16. Hurley, D.M., Prem, P., Stickle, A., Hibbitts, C., **Deutsch, A.N.**, Colaprete, A., Elphic, R., Li, S., Lucey, P., Liu, Y., Hosseini, S., Retherford, K., Zacny, K., Atkinson, J., Benna, M., Farrell, W., Needham, D., Gertsch, L., Hayne, P., Delitsky, M., 2019. Science objectives of a mission to the lunar permanently shadowed regions. NASA Exploration Science Forum, abstract NESF2019-113. Poster.
17. **Deutsch, A.N.**, Neumann, G.A., Head, J.W., Lucey, P.G., 2019. Investigating diurnal changes in the normal albedo of the lunar surface at 1064 nm: A new analysis with the Lunar Orbiter Laser Altimeter. 10th LunGradCon. Oral.
18. Wilson, L., Head, J.W., **Deutsch, A.N.**, 2019. Duration and significance of volcanically induced transient atmospheres on the Moon. 7th European Lunar Symosium. Oral.
19. **Deutsch, A.N.**, Neumann, G.A., Head, J.W., Lucey, P.G., 2019. Investigating diurnal changes in the normal albedo of the lunar surface at 1064 nm: A new analysis with the Lunar Orbiter Laser Altimeter. LPSC 50, abstract 1151. Poster.
20. **Deutsch, A.N.**, Head, J.W., Neumann, G.A., 2019. Distribution of surface water ice on the Moon: An analysis of host crater ages provides insights into the ages and sources of ice at the lunar south pole. LPSC 50, abstract 1150. Poster.
21. Wilson, L., Head, J.W., **Deutsch, A.N.**, 2019. Volcanically-induced transient atmospheres on the Moon: Assessment of duration and significance. LPSC 50, abstract 1343. Poster.
22. Tokle, L., Palumbo, A., **Deutsch, A.N.**, Anzures, B., Boatwright, B., Bramble, M., Casey, G., Chen, Y., Denton, C., Lark, L., Nathan, E., Pimentel, A., Tarnas, J., Wilner, J., Head, J., Ramsley, K., Shah, U., Kothandhapani, A., Prasad Gokul, H., Mehta, J., Vatsal, V., 2019. Scientific exploration of Mare Imbrium with OrbitBeyond, Inc.: Characterizing the regional volcanic history of the Moon. LPSC 50, abstract 2484. Poster.
23. **Deutsch, A.N.**, Head, J.W., Neumann, G.A., 2018. Polar ice on Mercury: Insight into delivery timing and sources from crater and Poisson analyses. AGU Fall Meeting, abstract P22B-06. Oral.

24. Neumann, G.A., Goosens, S. **Deutsch, A.N.**, Head, J.W., 2018. Density of lunar mare crust from GRAIL gravity data over young, unflooded craters. AGU Fall Meeting, abstract P31I-1393. Poster.
25. **Deutsch, A.N.**, Neumann, G.A., Head, J.W., 2018. Analysis of subsurface impact and volcanic structures on the Moon with Gravity Recovery and Interior Laboratory (GRAIL). 9th Moscow Solar System Symposium, abstract 9MS3-MN-03. Oral.
26. Neumann, G.A., **Deutsch, A.N.**, Head, J.W., 2018. Ancient buried basins in Oceanus Procellarum from the first billion years. Bombardment: Shaping Planetary Surfaces and Their Environments, abstract 2030. Oral.
27. **Deutsch, A.N.**, Head, J.W., Neumann, G.A., 2018. Patchy distribution of ancient, lunar ice contrasts young, coherent ice deposits on Mercury. Lunar Polar Volatiles, abstract 5021. Oral.
28. Neumann, G.A., Mazarico, E., Sun, X., **Deutsch, A.N.**, Lucey, P.G., 2018. Precision laser sensing of lunar polar volatiles. Lunar Polar Volatiles, abstract 5036. Poster.
29. **Deutsch, A.N.**, Head, J.W., 2018. Recent deposition of ice on Mercury: New results on the ages of north polar ice deposits and implications for the Moon. International Symposium on Lunar and Planetary Science, abstract 096. Oral.
30. **Deutsch, A.N.**, Head, J.W., 2018. Impact-bombarded ice on the Moon: Assessing the link between the ages of lunar polar deposits and their spatial heterogeneity. International Symposium on Lunar and Planetary Science, abstract 097. Poster.
31. **Deutsch, A.N.**, Neumann, G.A., Head, J.W., Wilson, L., 2018. GRAIL-identified gravity anomalies in Procellarum: Insight into subsurface impact and volcanic/magmatic structures on the Moon. NASA Exploration Science Forum, abstract NESF2018-013. Oral.
32. **Deutsch, A.N.**, Head, J.W., Neumann, G.A., 2018. Differences between surface ice deposits at the poles of Mercury and the Moon: Insights into ages of the ice. Mercury: Current and Future Science of the Innermost Planet, abstract 6118. Invited oral.
33. **Deutsch, A.N.**, Head, J.W., 2018. Production function of outgassed volatiles on Mercury: Implications for polar volatiles on Mercury and the Moon. Mercury: Current and Future Science of the Innermost Planet, abstract 6121. Poster.
34. Neumann, G.A., Sun, X., Cao, A., **Deutsch, A.N.**, Head, J.W., 2018. Reflectance of Mercury's polar regions: Calibration and implications for Mercury's volatiles. Mercury: Current and Future Science of the Innermost Planet, abstract 6115. Poster.
35. **Deutsch, A.N.**, Neumann, G.A., Head, J.W., 2018. GRAIL-identified gravity anomalies in Procellarum: Insight into subsurface impact and volcanic structures on the Moon. LPSC 49, abstract 1521. Oral.
36. **Deutsch, A.N.**, Neumann, G.A., Head, J.W., 2018. New evidence for surface water ice in small-scale cold traps and in three large craters at the north pole region of Mercury from the Mercury Laser Altimeter. LPSC 49, abstract 1537. Poster.
37. **Deutsch, A.N.**, Neumann, G.A., Head, J.W., 2017. New evidence for surface ice in micro-cold traps and in three large craters at the north polar region on Mercury: Implications for lunar exploration. 8th Moscow Solar System Symposium, abstract 8MS3-PG-11. Oral.
38. **Deutsch, A.N.**, Head, J.W., Neumann, G.A., 2017. Polar volatiles on the Moon and Mercury: Insights from comparisons. NASA Exploration Science Forum, abstract NESF2017-022. Poster.
39. **Deutsch, A.N.**, Neumann, G.A., Head, J.W., 2017. New evidence for exposed water ice in micro-cold traps and large craters at the north polar region on Mercury. 8th LunGradCon. Oral.
40. **Deutsch, A.N.**, 2017. An overview of geology and geophysics of the Moon. 8th LunGradCon. Invited oral.
41. **Deutsch, A.N.**, Head, J.W., Neumann, G.A., Chabot, N.L., 2017. Constraining the depth of polar ice deposits and evolution of cold traps on Mercury with small craters in permanently shadowed regions. LPSC 48, abstract 1634. Oral.
42. **Deutsch, A.N.**, Head, J.W., 2017. Formation of chloride salts on ancient Mars: A framework for deposition on an icy planet from Antarctic analogs. LPSC 48, abstract 2214. Poster.
43. **Deutsch, A.N.**, Head, J.W., Fassett, C.I., Chabot, N.L., 2016. Ice deposits at Mercury's north polar region: host craters provide maximum age. 7th Planetary Crater Consortium Meeting, abstract 1612. Oral.

44. **Deutsch, A.N.**, Head, J.W., 2016. Polar volatiles on the Moon and Mercury: Nature, Evolution, and Future Exploration. NASA Exploration Science Forum, abstract NESF2016-040. Oral.
45. **Deutsch, A.N.**, Ramsley, K.R., Bramble, M.S., Cassanelli, J.P., Horan, A.M., Jawin, E.R., Jozwiak, L.M., Kaplan, H.H., Lynch, C.F., Pascuzzo, A.C., Potter, R.W.K., Qiao, L., Weiss, D.K., Head, J.W., 2016. Science exploration architecture for Phobos and Deimos: Are the moons of Mars in the critical pathway of human martian exploration? 3rd Int. Conf. on Exploration of Phobos and Deimos. Oral.
46. **Deutsch, A.N.**, Ramsley, K.R., Bramble, M.S., Cassanelli, J.P., Horan, A.M., Jawin, E.R., Jozwiak, L.M., Kaplan, H.H., Lynch, C.F., Pascuzzo, A.C., Potter, R.W.K., Qiao, L., Weiss, D.K., Head, J.W., 2016. Science exploration architecture for Phobos and Deimos: Are the moons of Mars in the critical pathway of human martian exploration? 7th LunGradCon. Oral.
47. **Deutsch, A.N.**, Chabot, N.L., Mazarico, E., Ernst, C.M., Head, J.W., Neumann, G.A., Solomon, S.C., 2016. Comparison of areas in shadow from imaging and altimetry in the north polar region of Mercury and implications for polar ice deposits. LPSC 47, abstract 1134. Oral.
48. **Deutsch, A.N.**, Head, J.W., Fassett, C.I., Chabot, N.L., 2016. Ice deposits at Mercury's north polar region: host craters provide maximum age. LPSC 47, abstract 2319. Poster.
49. Chabot, N.L., Ernst, C.M., Nair, H., **Deutsch, A.N.**, Head, J.W., Solomon, S.C., 2016. Imaging of Mercury's polar deposits during MESSENGER's low-altitude campaign. LPSC 47, abstract 1252. Poster.
50. Ramsley, K.R., Bramble, M.S., Cassanelli, J.P., **Deutsch, A.N.**, J.P., Horan, A.M., Jawin, E.R., Jozwiak, L.M., Kaplan, H.H., Lynch, C.F., Pascuzzo, A.C., Potter, R.W.K., Qiao, L., Weiss, D.K., Head, J.W., 2016. Science exploration architecture for Phobos and Deimos: are the moons of Mars in the critical pathway of human exploration of Mars? LPSC 47, abstract 2345. Poster.
51. **Deutsch, A.N.**, Chabot, N.L., Head, J.W., 2015. Mapping areas of shadow in Mercury's north polar region to constrain the extent of stable thermal environments for ice deposits. 7th Moscow Solar System Symposium, abstract 6MS3-MN-12. Oral.
52. Ernst, C.M., Chabot, N.L., Denevi, B.W., Nair, H., **Deutsch, A.N.**, Murchie, S.L., Robinson, M.S., Blewett, D.T., Head, J.W., Harmon, J.K., Neumann, G.A., Solomon, S.C., 2013. Riddles in the dark: imaging inside Mercury's permanently shadowed craters. AGU Fall Meeting, abstract P11A-04. Poster.

Acknowledgements

All my thanks to the incredible people who were so intimately integral in this journey, particularly Jim and Greg. I am forever grateful for your guidance, mentorship, and friendship. Jim, you have ignited my passion for planetary exploration in infinite dimensions. I am so grateful for the once-unimaginable opportunities you afforded me. I look forward to having my own "Think your way to the Moon and back" story someday and I thank you for making that dream possible. Greg, thank you for your unwavering support and patience over the last many years. I appreciate every GMT lesson, laser waveform diagram, bureaucratic rant, chocolate-covered espresso bean, and homegrown spinach leaf that we shared.

All my thanks to the planetary faculty – Jack, 9003 Ralphmilliken, Pete, Marc, Chris, BrandON, Alexandria, Alex, and Ingrid and her brightening laugh – and in particular my committee – Carlé and other Jim – for their open doors, insightful research discussions, interesting courses, and enduring support throughout my time at Brown.

All my thanks to Melissa and Anne for their logistical assistance throughout the years, for facilitating conference travels, for organizing departmental activities, and for fueling me with free pizza lunches when I needed them most.

All my thanks to my mentors at Goddard, especially Erwan, Tim, Noah, Dave, Mike, Sander, and Xiaoli, and to my mentors who came before my Ph.D. adventure began, especially Nancy, as well as Carolyn, Dave, Brett, Scott, and Dana at APL, and Rowan, Chuck, Brent, Greg, Heather, and Joel at W&M.

All my thanks to Lab Fam, beginning with Lauren and her cookies, Kat, Ross, David, BBJ Cassasmelly, Erica, Jay and his ArcGIS wizardry, and Sister Qiao, and continuing on with Ben Balducci Boatwright, Adeene, Yuan, Yuqi, Laura, Erica, and Jingyi. Of course, a special thanks to my Lab Twin Ashley, who has been around the world with me (in more ways than one). Thank you for every walk, every laugh, every eye roll, every burrito, every glass wall, every gānbēi, every KTV survival. Thank you for buying our LPSC-forever home in The Woodlands. Exxon is lucky to have you, and I look forward to building a rig on the Moon together.

All my thanks to the Mission Room, where I have made my home the last five years with Alyssa (the only person to dethrone me in the Vertical Jump Contest although it is possible I was three-times-qualified that night) and Jesse (whose contagious optimism and secret handshakes kept me grounded through the years), as well as Mike, Chris, Carol, Elizabeth, a plethora of rotating friends (Dijun, Jingzhu, Honglei, Xing, and Yazhou), and even once in a while Sierra.

All my thanks to every other DEEPS graduate student with whom I have interacted, especially KCannon (who plays Xbox in his office), Shuai, Rachel, Evan, and Collin Jackson, who I have never met but whose name I carry on proudly as the USACJMSOOTPGS (Tenure 2019-2020).

All my thanks to my (real) family - to my mom, who sends me clip-outs of *Washington Post* space-related articles for verification, to my dad, who has an endless cache of questions re: *NASA's Unexplained Files*, to Taylor, who inspires me as she every day makes the world a better place as a computer science educator in places that need it most, and to Burke, who teaches me about teamwork, leadership, empathy, and foosball bank shots, and who is willing to fly 65.3 degrees of latitude to listen to me talk about ice and rocks on other planets.

All my thanks to the best friends in the world, including Emma, Ellen, and my Tribe: Niall, Michael, Jack, Aaron, Rosh, Sked, and Billiam.

All my thanks to the GCB, some thanks to Chipotle on Thayer, and definitely no thanks at all to COVID-19. You are the absolute worst. But, as someone ~~once~~ a-thousand-times told me, "**ONWARD AND UPWARD!!**"

Table of Contents

List of Tables

List of Illustrations

Introduction

Ariel N. Deutsch

Department of Earth, Environmental and Planetary Sciences, Brown University, Providence, RI 02912, USA

Despite similar thermal environments, Mercury and the Moon show distinct differences in the abundance and purity of ice cold-trapped in regions of permanent shadow. Both bodies have permanently shadowed regions (PSRs), which are thermally stable environments for water ice on geologic timescales (Vasavada et al., 1999) due to the small axial tilt of each body. While both Earth-based (Harmon et al., 2011) and orbital (Lawrence et al., 2013; Neumann et al., 2013; Paige et al., 2013; Chabot et al., 2014; Deutsch et al., 2016, 2017, 2018a) observations indicate that there are extensive water-ice deposits within Mercury's PSRs, data suggest that water-ice detections on the Moon (Stacy et al., 1997; Lawrence et al., 2006; Campbell et al., 2006; Haruyama et al., 2008; Spudis et al., 2010; Colaprete et al., 2010; Thomson et al., 2012; Zuber et al., 2012; Hayne et al., 2015; Fisher et al., 2017; Li et al., 2018) are smaller in extent and less concentrated than those on Mercury.

For example, neutron suppression measured at the north polar region of Mercury suggests that polar deposits are composed of nearly pure H_2O ice (Lawrence et al., 2013). While some ice deposits closest to the pole are exposed at the surface (Neumann et al., 2013; Deutsch et al., 2017), the majority of ice deposits on Mercury are insulated by 10–30 cm (Lawrence et al., 2013) of low-reflectance materials that are interpreted to be composed of volatiles other than water (Zhang and Paige, 2009; Paige et al., 2013; Chabot et al., 2016; Delitsky et al., 2017). Radar observations of Mercury's poles suggest that the ice deposits are at least several meters thick (Harmon, 2007; Black et al., 2010; Eke et al., 2017; Deutsch et al., 2018a; Rubanenko et al., 2019; Susorney et al., 2019), and modeling of the radar data suggests that these deposits are composed of ~95% pure water ice (Butler et al., 1993). Images (Chabot et al., 2014, 2016) and reflectance measurements (Neumann et al., 2013; Deutsch et al., 2017) of Mercury's PSRs reveal spatially coherent ice deposits with distinct albedos and sharp reflectance boundaries that align with boundaries of permanent shadow (Deutsch et al., 2016; Chabot et a., 2018). Even under the most favorable accumulation conditions, ice flow velocities are estimated to be very low (4×10^{-8} m yr^{-1}) and, with the exception of a sublimation lag deposit, the ice deposits are not predicted to leave any evidence of glaciation on the terrain (Fastook, Head, and Deutsch, 2019).

In contrast, neutron spectrometer data of the lunar polar regions are suggestive of concentrations of only ~1.5 % water ice by mass in the upper ~1 m of the lunar regolith (Lawrence et al., 2006). Furthermore, the Lunar CRater Observation and Sensing Satellite detected only ~6 wt. % water ice in the ejecta plume resulting from an impact into the south polar, permanently shadowed Cabeus crater (Colaprete et al., 2010). Earth-based radar observations do not show evidence for concentrated water ice on the Moon (Stacy et al., 1997; Campbell et al., 2006) and spacecraft radar observations are suggestive of only patches of ice (Spudis et al., 2010; Thomson et al., 2012; Patterson et al., 2017). Finally, imaging (Haruyama et al., 2008) and reflectance (Zuber et al., 2012; Hayne et al., 2015; Fisher et al., 2017; Li et al., 2018; Qiao et al., 2019) campaigns of the lunar poles have not revealed thick, coherent ice deposits, but instead are suggestive of a patchy distribution of water frost in some locations. Thus, ice on Mercury appears to be purer and more extensive than any ice on the Moon.

The cause for the differences between ice on Mercury and the Moon is not well understood and has motivated the work presented in this dissertation. In the following chapters, we explore how differences in delivery time and sources may explain the stark differences between surface ice on these two airless bodies. Resolving the differences between polar ice on Mercury and the Moon has implications for understanding the source, evolution, and ultimate fate of volatiles throughout the inner Solar System.

We begin these investigations in Chapter 1 (Deutsch et al., 2019a) with an analysis of the ages of surface ice on Mercury using a combination of observations of polar deposits and numerical probability models. Specifically, we quantify crater densities on polar deposits for the first time using MErcury Surface, Space ENvironment, GEochemistry, and Ranging (MESSENGER) images and model the time-resolved probability of possible ages using Poisson statistics. Our results indicate that the polar deposits have geologically young surface ages, and we conservatively estimate that ice was delivered to the surface of Mercury within the last 330 Myr (Deutsch et al., 2019a). These results provide important context for the remainder of the thesis. If ice on Mercury is young (10's to 100's of Myr old), a recent delivery may help explain the high purity and abundance of the ice. Over time, ice is expected to be broken up and buried as it is exposed to the space weathering environment (Hurley et al., 2012). In contrast to ice on Mercury, surface ice on the Moon is much less abundant (Eke et al., 2009; Li et al., 2018) and appears to be a heterogeneous mixture of species (Colaprete et al., 2010); perhaps this is related to an older age of lunar ice.

In order to understand how the timing of volatile delivery compares on Mercury and the Moon, we analyze the ages of lunar ice-bearing craters in Chapter 2 (Deutsch et al., 2020). Crater density statistics of the diffuse, lunar ice detections (Li et al., 2018) are not feasible, but age dating of the environments that host these detections provide a relative age of the ice. We find that the majority of surface ice is contained in geologically old craters ≥ ~3.1 Gyr, where the majority of cold-trapping area exists on the Moon (Deutsch et al., 2020). We also identify a group of ancient craters that does not host surface ice, even though these craters are present-day cold traps. These specific ancient craters would not have been thermally stable for the cold-trapping of water ice before the onset of true polar wander (TPW), as suggested by Siegler et al. (2016), suggesting that the present-day distribution of surface ice at the lunar poles may be controlled not only by ice supply rates and destruction rates, but also by some additional factor that affects the long-term stability of volatiles in individual cold traps, such as TPW. We note that the age of ice in Nobile and Shackleton craters can place a lower limit on the timing of TPW because while these craters host surface ice today (Li et al., 2018), they are not predicted to have been thermally stable for the retention of surface ice before the onset of TPW (Siegler et al., 2016).

In Chapter 2 (Deutsch et al., 2020), we also discuss that surface ice is present within some smaller impact craters (with diameters between ~1 and 15 km) that are too small to allow for robust cratering statistics. Very small craters on the Moon are all expected to be relatively young, given that older, smaller craters are predicted to have been resurfaced by subsequent impacts (e.g., Basilevsky, 1976; Neukum et al., 2001).

Some of the smaller ice-bearing craters that we identify appear to have relatively sharp rim crest morphologies suggestive of younger ages. Ice in young craters is particularly interesting because it suggests that there is some recent and perhaps ongoing mechanism that is delivering or redistributing water to polar cold traps. Therefore, understanding if ice is present within young craters (and not only old craters) is of essential importance to understanding the sources of lunar ice, and we explore this theme in the next chapter.

In Chapter 3 (Deutsch et al., *accepted-a*), we take a new approach to understanding the ages of these small polar cold traps: analyzing the roughness properties of small ice-bearing craters. The roughness properties of impact craters are valuable indicators of crater degradation and can provide insight into crater ages. In this chapter, we quantify the roughness of lunar craters from different geologic eras, confirming that young, Copernican craters are distinctly rougher than older craters (e.g., Neumann et al., 2015; Wang et al., 2019). We find a population of ice-bearing craters that is likely to be post-Nectarian in age, although no ice-bearing craters are within the Copernican-only domain in roughness space. Interestingly, all of the 15 rough, permanently shadowed craters that are found within the Copernican-only domain lack water-ice detections (Li et al., 2018), suggesting that either ice has not been delivered to these young craters, or that it has since been destroyed. These results suggest that that perhaps Copernican craters are not capable of hosting surface ice, or that the lunar water ice detected by Li et al. (2018) is older than Copernican in age.

If ice on the Moon is indeed relatively ancient, as suggested by its diffuse and patchy spatial distribution (Haruyama et al., 2008; Hayne et al., 2015; Fisher et al., 2017;

Li et al., 2018), by the ages of ice-bearing craters (Deutsch et al., 2020), and by the lack of ice in Copernican craters (Deutsch et al., *accepted-a*), then the mechanism(s) that delivered the ice must have been active earlier on in lunar history. Various processes may be responsible for the delivery or formation of ancient volatiles on the Moon, including impact bombardment (Nesvorný et al., 2017; Pokorný et al., 2019), in-situ interactions between the solar wind and lunar regolith (Crider and Vondrak, 2000; Jones et al., 2018), and volcanic outgassing (Crotts and Hummels, 2009; Needham and Kring, 2017), which is understood to be a primary pathway for delivering interior volatiles to the surfaces of various terrestrial bodies, including Earth (Moore, 1970; Cavosie et al., 2005), the Moon (Saal et al., 2008; Milliken and Li, 2017), and Mars (Greeley, 1987). In fact, it has been suggested that volcanism released substantial volatiles on the Moon during the production of the maria lava plains and that these released volatiles may have contributed significantly to the lunar polar deposits (Needham and Kring, 2017). If abundant volatiles were released during volcanic outgassing and ever cold-trapped on the Moon, then perhaps it is possible that substantial volatiles were also released on Mercury during the production of its volcanic plains, albeit with different chemical species and abundances (Nittler et al., 2011; Zolotov et al., 2013).

In Chapter 4 (Deutsch et al., *in review*), we explore the possibility that ancient volcanic eruptions on Mercury contributed some fraction of volatiles to polar cold traps. These volatiles would be distinctly different in age and composition from the relatively young (Crider and Killen, 2005; Deutsch et al., 2019a), H_2O-ice (Butler et al., 1993; Lawrence et al., 2013) deposits observed at the surface today. In this chapter we estimate the flux and timing of volcanism on Mercury. We discuss the potential fate of the erupted volatiles by analyzing the frequency of eruptions and the durations of possible volcanically-derived, transient atmospheres. We find that eruptions on Mercury may have resulted in the transient production of enhanced atmospheric pressures with lifetimes between ~500 and 40,000 years, which may have been longer than the time between individual eruptions (estimated to be between 270 and 53,000) years. The wide span in estimates reflects the extensive parameter space that we explored for oxygen fugacity conditions (Zolotov, 2011; McCubbin et al. 2012a, 2017; Zolotov et al., 2013; Namuer et al., 2016), degassed volatile content (Zolotov et al., 2013; Armstrong et al., 2015; Anzures et al., 2017), and eruption volumes and rates (Wilson and Head, 2008). If volcanically-derived volatiles did ever become cold-trapped at Mercury's poles, we estimate they would exist as a diffuse, weathered layer that is buried at least ~16 m below the subsurface. In contrast to the thick, pure deposits observed at the surface of Mercury, diffuse and buried volcanically-derived ice would be more similar to subsurface lunar ice in spatial distribution.

Next, in Chapter 5 (Deutsch et al., *accepted-b*), we discuss the importance of future reflectance measurements of volatiles, and analyze how surface temperature influences measurements of surface reflectance on airless bodies. This is particularly important given that enhanced surface reflectance has been used to characterize the presence of surface ice both on Mercury (Neumann et al., 2013; Chabot et al., 2014; Deutsch et al., 2017) and the Moon (e.g., Zuber et al., 2012; Fisher et al., 2017; Qiao et al., 2019), as well as on other planetary objects including smaller airless bodies (e.g., Platz et al., 2016; Ermakov et al., 2017) and Mars (e.g., Smith et al., 1998; Bell et al., 1999). In this chapter, we quantify temperature-dependent spectral changes of the lunar surface as measured from orbit by the Lunar Orbiter Laser Altimeter (LOLA) at 1064 nm. We couple LOLA measurements of normal albedo with measurements of surface temperature from the Diviner Lunar Radiometer Experiment, analyzing the maria and highlands terranes between ±50° in 1°x1° spatial bins. We provide the first evidence of temperature-dependent spectral changes on the lunar surface from orbital observations, finding that the majority of the lunar surface between 50°N and 50°S demonstrates a small, yet measurable, negative change in normal albedo at 1064 nm with temperature ($-\Delta R/\Delta T$). The measurable effect is on the order of a few percent change in reflectance per ~80 K, indicating temperature changes do not have a large effect on measurements of albedo at the sensitivity of the LOLA instrument. Stronger $-\Delta R/\Delta T$ values tend to be associated with regions with elevated orthopyroxene levels, and the maria typically have higher levels of orthopyroxene and stronger $-\Delta R/\Delta T$ values than the highlands. Our results suggest that single-wavelength lasers may be powerful tools for understanding the distribution of particular minerals on the lunar surface. As new, higher-resolution orbital lasers are designed and operated, the surface temperature of the target body should be taken into account as measurements are acquired and calibrated.

In the sixth and final chapter, I present a synthesis of the preceding chapters in order to frame the implications and importance of this dissertation toward understanding the nature and evolution of water cycles on Mercury and the Moon. I outline major outstanding questions regarding volatile cycles on Mercury and the Moon and suggest paths for future investigation. For example, this particular work has motivated a more detailed analysis of the possibility of volcanically-induced transient atmospheres on the Moon in order to understand the possible contribution of outgassed water to lunar polar cold traps (Head, Wilson, Deutsch, et al., *in prep.*). There are numerous additional measurements that can be taken to help further constrain lava flow thicknesses, volumes, ages, and volatile contents to address this question, and detailed studies of lunar volcanic complexes, such as Marius Hills (Deutsch et al., *in prep.*), can help refine our understanding of local eruption histories and repose periods, especially by coupling geologic and geophysical models (e.g., Deutsch et al., 2019b).

Particularly motivated by the excitement of future exploration, in Chapter 6 I outline how new measurements can address some of these outstanding questions, building upon previous frameworks we have developed for science exploration architectures (Deutsch et al., 2018b; Palumbo and Deutsch et al., 2019). With BepiColombo en route to Mercury (Benkhoff et al., 2010), and numerous upcoming missions planned for the Moon – including the Volatiles Investigating Polar Exploration Rover (VIPER; Colaprete et al., 2020), the Korean Pathfinder Lunar Orbiter (Robinson et al., 2018), and several smaller missions with NASA's Commercial Lunar Payload Services (CLPS) – I discuss how future exploration can help better resolve the sources, evolution, and current state of polar volatiles on Mercury and the Moon.

References

Anzures, B.A., Parman, S.W., Boesenberg, J.S., & Milliken, R.E. (2019). Using volatile (S, C, H, F, Cl) contents on enstatite in reduced meteorites to estimate oxygen fugacity and equilibrium melt compositions. *Lunar and Planetary Science Conference, 51*, Abstract #2179. https://www.hou.usra.edu/meetings/lpsc2019/pdf/2179.pdf

Armstrong, L. S., Hirschmann, M. M., Stanley, B. D., Falksen, E. G., & Jacobsen, S. D. (2015). Speciation and solubility of reduced C–O–H–N volatiles in mafic melt: Implications for volcanism, atmospheric evolution, and deep volatile cycles in the terrestrial planets. *Geochimica et Cosmochimica Acta*, *171*, 283–302. https://doi.org/10.1016/j.gca.2015.07.007

Basilevsky, A. T. (1976). On the evolution rate of small craters. *Lunar Science Conference, Proceedings 1,* 1005–1020. http://adsabs.harvard.edu/full/1976LPSC....7.1005B

Bell, J. F., Wolff, M. J., Daley, T. C., Crisp, D., James, P. B., Lee, S. W., et al. (1999). Near-infrared imaging of Mars from HST: Surface reflectance, photometric properties, and implications for MOLA data. *Icarus*, *138*(1), 25–35. https://doi.org/10.1006/icar.1998.6057

Benkhoff, J., van Casteren, J., Hayakawa, H., Fujimoto, M., Laakso, H., Novara, M., et al. (2010). BepiColombo—Comprehensive exploration of Mercury: Mission overview and science goals. *Planetary and Space Science*, *58*(1), 2–20. https://doi.org/10.1016/j.pss.2009.09.020

Campbell, D. B., Campbell, B. A., Carter, L. M., Margot, J.-L., & Stacy, N. J. S. (2006). No evidence for thick deposits of ice at the lunar south pole. *Nature*, *443*(7113), 835–837. https://doi.org/10.1038/nature05167

Cavosie, A. J., Valley, J. W., Wilde, S. A., & E.I.M.F. (2005). Magmatic δ18O in 4400–3900 Ma detrital zircons: A record of the alteration and recycling of crust in the Early Archean. *Earth and Planetary Science Letters*, *235*(3), 663–681. https://doi.org/10.1016/j.epsl.2005.04.028

Chabot, N. L., Ernst, C. M., Denevi, B. W., Nair, H., Deutsch, A. N., Blewett, D. T., et al. (2014). Images of surface volatiles in Mercury's polar craters acquired by the MESSENGER spacecraft. *Geology*, *42*, 1051–1054. https://doi.org/10.1130/G35916.1

Chabot, N. L., Ernst, C. M., Paige, D. A., Nair, H., Denevi, B. W., Blewett, D. T., et al. (2016). Imaging Mercury's polar deposits during MESSENGER's low-altitude campaign. *Geophysical Research Letters*, *43*(18), 9461–9468. https://doi.org/10.1002/2016GL070403

Colaprete, A., Elphic, R. C., Shirley, M., Ennico-Smith, K., Heldmann, J., Lim, D. S. S., et al. (2020). The Volatiles Investigating Polar Exploration Rover (VIPER) Mission: Measurement goals and traverse planning. *Lunar and Planetary Science Conference 51*, Abstract #2241. https://www.hou.usra.edu/meetings/lpsc2020/pdf/2241.pdf

Colaprete, A., Schultz, P., Heldmann, J., Wooden, D., Shirley, M., Ennico, K., et al. (2010). Detection of water in the LCROSS ejecta plume. *Science*, *330*(6003), 463–468. https://doi.org/10.1126/science.1186986

Crider, D. H., & Vondrak, R. R. (2000). The solar wind as a possible source of lunar polar hydrogen deposits. *Journal of Geophysical Research: Planets*, *105*(E11), 26773–26782. https://doi.org/10.1029/2000JE001277

Crotts, A. P. S., & Hummels, C. (2009). Lunar outgassing, transient phenomena, and the return to the Moon. II. Predictions and tests for outgassing/regolith interactions. *The Astrophysical Journal*, *707*(2), 1506. https://doi.org/10.1088/0004-637X/707/2/1506

Delitsky, M. L., Paige, D. A., Siegler, M. A., Harju, E. R., Schriver, D., Johnson, R. E., & Travnicek, P. (2017). Ices on Mercury: Chemistry of volatiles in permanently cold areas of Mercury's north polar region. *Icarus*, *281*, 19–31. https://doi.org/10.1016/j.icarus.2016.08.006

Deutsch, A. N., Head, J. W., & Neumann, G. A. (2020). Analyzing the ages of south polar craters on the Moon: Implications for the sources and evolution of surface water ice. *Icarus*, *336*, 113455. https://doi.org/10.1016/j.icarus.2019.113455

Deutsch, A. N., Head, J. W., Neumann, G. A., Kreslavsky, M. A., & Barker, M. K. (Accepted-a). Assessing the roughness properties of circumpolar lunar craters: Implications for the timing of water ice delivery to the Moon. *Geophysical Resesearch Letters.*

Deutsch, A. N., Head, J. W., Parman, S. W., Neumann, G. A., & Lowden, F. (In review). The flux of volcanic eruptions on Mercury: Potential contributions to transient atmospheres and buried polar deposits.

Deutsch, A. N., Head, J. W., Ramsley, K. R., Pieters, C. M., Potter, R. W. K., Palumbo, A. M., et al. (2018b). Science exploration architecture for Phobos and Deimos: The role of Phobos and Deimos in the future exploration of Mars. *Advances in Space Research*, *62*(8), 2174–2186. https://doi.org/10.1016/j.asr.2017.12.017

Deutsch, A. N., Neumann, G. A., Head, J. W., & Lucey, P. G. (Accepted-b). Temperature-dependent changes in the normal albedo of the lunar surface at 1064 nm. *Journal of Geophysical Research: Planets*.

Deutsch, A. N., Neumann, G. A., Head, J. W., & Wilson, L. (2019b). GRAIL-identified gravity anomalies in Oceanus Procellarum: Insight into subsurface impact and magmatic structures on the Moon. *Icarus*, *331*, 192–208. https://doi.org/10.1016/j.icarus.2019.05.027

Deutsch, A. N., Chabot, N. L., Mazarico, E., Ernst, C. M., Head, J. W., Neumann, G. A., & Solomon, S. C. (2016). Comparison of areas in shadow from imaging and altimetry in the north polar region of Mercury and implications for polar ice deposits. *Icarus*, *280*, 158–171. https://doi.org/10.1016/j.icarus.2016.06.015

Deutsch, A. N., Head, J. W., & Neumann, G. A. (2019a). Age constraints of Mercury's polar deposits suggest recent delivery of ice. *Earth and Planetary Science Letters*, *520*, 26–33. https://doi.org/10.1016/j.epsl.2019.05.027

Deutsch, A. N., Head, J. W., Chabot, N. L., & Neumann, G. A. (2018a). Constraining the thickness of polar ice deposits on Mercury using the Mercury Laser Altimeter and small craters in permanently shadowed regions. *Icarus*, *305*, 139–148. https://doi.org/10.1016/j.icarus.2018.01.013

Deutsch, A. N., Neumann, G. A., & Head, J. W. (2017). New evidence for surface water ice in small-scale cold traps and in three large craters at the north polar region of Mercury from the Mercury Laser Altimeter. *Geophysical Research Letters*, *44*, 9233–9241. https://doi.org/10.1002/2017GL074723

Deutsch, A. N., Head, J. W., Wilson, J. W., et al. (*In prep.*) A detailed analysis of the volcanic history of Marius Hills on the Moon.

Eke, V. R., Lawrence, D. J., & Teodoro, L. F. A. (2017). How thick are Mercury's polar water ice deposits? *Icarus*, *284*, 407–415. https://doi.org/10.1016/j.icarus.2016.12.001

Eke, V. R., Teodoro, L. F. A., & Elphic, R. C. (2009). The spatial distribution of polar hydrogen deposits on the Moon. *Icarus*, *200*(1), 12–18. https://doi.org/10.1016/j.icarus.2008.10.013

Ermakov, A. I., Mazarico, E., Schröder, S. E., Carsenty, U., Schorghofer, N., Preusker, F., et al. (2017). Ceres's obliquity history and its implications for the permanently shadowed regions. *Geophysical Research Letters*, *44*(6), 2652–2661. https://doi.org/10.1002/2016GL072250

Fastook, J. L., Head, J. W., & Deutsch, A. N. (2019). Glaciation on Mercury: Accumulation and flow of ice in permanently shadowed circum-polar crater interiors. *Icarus*, *317*, 81–93. https://doi.org/10.1016/j.icarus.2018.07.004

Fisher, E. A., Lucey, P. G., Lemelin, M., Greenhagen, B. T., Siegler, M. A., Mazarico, E., et al. (2017). Evidence for surface water ice in the lunar polar regions using reflectance measurements from the Lunar Orbiter Laser Altimeter and temperature measurements from the Diviner Lunar Radiometer Experiment. *Icarus*, *292*, 74–85. https://doi.org/10.1016/j.icarus.2017.03.023

Greeley, R. (1987). Release of juvenile water on Mars: Estimated amounts and timing associated with volcanism. *Science*, *236*(4809), 1653–1654. https://doi.org/10.1126/science.236.4809.1653

Harmon, J. K., Slade, M. A., & Rice, M. S. (2011). Radar imagery of Mercury's putative polar ice: 1999–2005 Arecibo results. *Icarus*, *211*(1), 37–50. https://doi.org/10.1016/j.icarus.2010.08.007

Haruyama, J., Ohtake, M., Matsunaga, T., Morota, T., Honda, C., Yokota, Y., et al. (2008). Lack of exposed ice inside lunar south pole Shackleton crater. *Science*, *322*(5903), 938–939. https://doi.org/10.1126/science.1164020

Hayne, P. O., Hendrix, A., Sefton-Nash, E., Siegler, M. A., Lucey, P. G., Retherford, K. D., et al. (2015). Evidence for exposed water ice in the Moon's south polar regions from Lunar Reconnaissance Orbiter ultraviolet albedo and temperature measurements. *Icarus*, *255*, 58–69. https://doi.org/10.1016/j.icarus.2015.03.032

Head, J. W., Wilson, L., Deutsch, A. N., Rutherford, M, J., & Saal, A. E. (*In prep.*) Volcanically-induced transient atmospheres on the Moon: Assessment of duration, significance, and contributions to polar volatiles traps.

Hurley, D. M., Lawrence, D. J., Bussey, D. B. J., Vondrak, R. R., Elphic, R. C., & Gladstone, G. R. (2012). Two-dimensional distribution of volatiles in the lunar regolith from space weathering simulations. *Geophysical Research Letters*, *39*(9), L09203. https://doi.org/10.1029/2012GL051105

Lawrence, D. J., Feldman, W. C., Elphic, R. C., Hagerty, J. J., Maurice, S., McKinney, G. W., & Prettyman, T. H. (2006). Improved modeling of Lunar Prospector neutron spectrometer data: Implications for hydrogen deposits at the lunar poles. *Journal of Geophysical Research: Planets*, *111*(E8), E08001. https://doi.org/10.1029/2005JE002637

Lawrence, D. J., Feldman, W. C., Goldsten, J. O., Maurice, S., Peplowski, P. N., Anderson, B. J., et al. (2013). Evidence for water ice near Mercury's north pole from MESSENGER Neutron Spectrometer measurements. *Science*, *339*(6117), 292–296. https://doi.org/10.1126/science.1229953

Li, S., Lucey, P. G., Milliken, R. E., Hayne, P. O., Fisher, E., Williams, J.-P., et al. (2018). Direct evidence of surface exposed water ice in the lunar polar regions. *Proceedings of the National Academy of Sciences*, *115*(36), 8907–8912. https://doi.org/10.1073/pnas.1802345115

McCubbin, F. M., Riner, M. A., Kaaden, K. E. V., & Burkemper, L. K. (2012). Is Mercury a volatile-rich planet? *Geophysical Research Letters*, *39*(9). https://doi.org/10.1029/2012GL051711

McCubbin, F. M., Vander Kaaden, K. E., Peplowski, P. N., Bell, A. S., Nittler, L. R., Boyce, J. W., et al. (2017). A low O/Si ratio on the surface of Mercury: Evidence for silicon smelting? *Journal of Geophysical Research: Planets*, *122*(10), 2053–2076. https://doi.org/10.1002/2017JE005367

Milliken, R. E., & Li, S. (2017). Remote detection of widespread indigenous water in lunar pyroclastic deposits. *Nature Geoscience*, *10*(8), 561–565. https://doi.org/10.1038/ngeo2993

Moore, J. G. (1970). Water content of basalt erupted on the ocean floor. *Contributions to Mineralogy and Petrology*, *28*(4), 272–279. https://doi.org/10.1007/BF00388949

Namur, O., Charlier, B., Holtz, F., Cartier, C., & McCammon, C. (2016). Sulfur solubility in reduced mafic silicate melts: Implications for the speciation and distribution of sulfur on Mercury. *Earth and Planetary Science Letters*, *448*, 102–114. https://doi.org/10.1016/j.epsl.2016.05.024

Needham, D. H., & Kring, D. A. (2017). Lunar volcanism produced a transient atmosphere around the ancient Moon. *Earth and Planetary Science Letters*, *478*, 175–178. https://doi.org/10.1016/j.epsl.2017.09.002

Neukum, G., Ivanov, B. A., & Hartmann, W. K. (2001). Cratering records in the inner Solar System in relation to the lunar reference system. *Space Science Reviews*, *96*(1–4), 55–86. https://doi.org/10.1023/A:1011989004263

Neumann, G.A., Glaeser, P. A., Hiesinger, H., Zuber, M. T., & Smith, D. E. (2015). Copernican-age craters and LOLA decameter-scale roughness. *Lunar and Planetary Science Conference 46*, Abstract #2218. https://www.hou.usra.edu/meetings/lpsc2015/pdf/2218.pdf

Neumann, Gregory A., Cavanaugh, J. F., Sun, X., Mazarico, E. M., Smith, D. E., Zuber, M. T., et al. (2013). Bright and dark polar deposits on Mercury: Evidence for surface volatiles. *Science*, *339*(6117), 296–300. https://doi.org/10.1126/science.1229764

Nittler, L. R., Starr, R. D., Weider, S. Z., McCoy, T. J., Boynton, W. V., Ebel, D. S., et al. (2011). The major-element composition of Mercury's surface from MESSENGER X-ray spectrometry. *Science*, *333*(6051), 1847–1850. https://doi.org/10.1126/science.1211567

Paige, D. A., Siegler, M. A., Harmon, J. K., Neumann, G. A., Mazarico, E. M., Smith, D. E., et al. (2013). Thermal stability of volatiles in the north polar region of Mercury. *Science*, *339*(6117), 300–303. https://doi.org/10.1126/science.1231106

Palumbo, A. M., Deutsch, A. N., Bramble, M. S., Tarnas, J. D., Boatwright, B. D., Lark, L. H., et al. (2019). Scientific exploration of Mare Imbrium with OrbitBeyond, Inc.: Characterizing the regional volcanic history of the Moon. *New Space*, *7*(3), 137–150. https://doi.org/10.1089/space.2019.0016

Patterson, G. W., Stickle, A. M., Turner, F. S., Jensen, J. R., Bussey, D. B. J., Spudis, P., et al. (2017). Bistatic radar observations of the Moon using Mini-RF on LRO and the Arecibo Observatory. *Icarus*, *283*, 2–19. https://doi.org/10.1016/j.icarus.2016.05.017

Platz, T., Nathues, A., Schorghofer, N., Preusker, F., Mazarico, E., Schröder, S. E., et al. (2016). Surface water-ice deposits in the northern shadowed regions of Ceres. *Nature Astronomy*, *1*(1), 1–6. https://doi.org/10.1038/s41550-016-0007

Qiao, L., Ling, Z., Head, J. W., Ivanov, M. A., & Liu, B. (2019). Analyses of Lunar Orbiter Laser Altimeter 1,064-nm albedo in permanently shadowed regions of polar crater flat floors: Implications for surface water ice occurrence and future in situ exploration. *Earth and Space Science*, *6*(3), 467–488. https://doi.org/10.1029/2019EA000567

Robinson, M. S., & the ShadowCam Team (2018). ShadowCam: Seeing in the shadows. *Lunar Polar Volatiles*, Abstract #5028. https://www.hou.usra.edu/meetings/lunarvolatiles2018/pdf/5028.pdf

Rubanenko, L., Venkatraman, J., & Paige, D. A. (2019). Thick ice deposits in shallow simple craters on the Moon and Mercury. *Nature Geoscience*, *12*(8), 597. https://doi.org/10.1038/s41561-019-0405-8

Saal, A. E., Hauri, E. H., Cascio, M. L., Orman, J. A. V., Rutherford, M. C., & Cooper, R. F. (2008). Volatile content of lunar volcanic glasses and the presence of water in the Moon's interior. *Nature*, *454*(7201), 192–195. https://doi.org/10.1038/nature07047

Siegler, M. A., Miller, R. S., Keane, J. T., Laneuville, M., Paige, D. A., Matsuyama, I., et al. (2016). Lunar true polar wander inferred from polar hydrogen. *Nature*, *531*(7595), 480–484. https://doi.org/10.1038/nature17166

Smith, D. E., Zuber, M. T., Frey, H. V., Garvin, J. B., Head, J. W., Muhleman, D. O., et al. (1998). Topography of the northern hemisphere of Mars from the Mars Orbiter Laser Altimeter. *Science*, *279*(5357), 1686–1692. https://doi.org/10.1126/science.279.5357.1686

Spudis, P. D., Bussey, D. B. J., Baloga, S. M., Butler, B. J., Carl, D., Carter, L. M., et al. (2010). Initial results for the north pole of the Moon from Mini-SAR, Chandrayaan-1 mission. *Geophysical Research Letters*, *37*(6), L06204. https://doi.org/10.1029/2009GL042259

Stacy, N. J. S., Campbell, D. B., & Ford, P. G. (1997). Arecibo radar mapping of the lunar poles: A search for ice deposits. *Science*, *276*(5318), 1527–1530. https://doi.org/10.1126/science.276.5318.1527

Susorney, H. C. M., James, P. B., Johnson, C. L., Chabot, N. L., Ernst, C. M., Mazarico, E. M., et al. (2019). The thickness of radar-bright deposits in Mercury's northern hemisphere from individual Mercury Laser Altimeter tracks. *Icarus*, *323*, 40–45. https://doi.org/10.1016/j.icarus.2019.01.016

Thomson, B. J., Bussey, D. B. J., Neish, C. D., Cahill, J. T. S., Heggy, E., Kirk, R. L., et al. (2012). An upper limit for ice in Shackleton crater as revealed by LRO Mini-RF orbital radar. *Geophysical Research Letters*, *39*(14), L14201. https://doi.org/10.1029/2012GL052119

Vasavada, A. R., Paige, D. A., & Wood, S. E. (1999). Near-surface temperatures on Mercury and the Moon and the stability of polar ice deposits. *Icarus*, *141*(2), 179–193. https://doi.org/10.1006/icar.1999.6175

Wang, J. T., Kreslavsky, M. A., Liu, J. Z., Head, J. W., & Kolenkina, M. M. (2019) Quantitative characterization of impact crater materials on the Moon: Implications for degradation processes and stratigraphic age. *Lunar and Planetary Science Conference 50*, Abstract #1262. https://www.hou.usra.edu/meetings/lpsc2019/pdf/1262.pdf

Wilson, L., & Head, J. W. (2008). Volcanism on Mercury: A new model for the history of magma ascent and eruption. *Geophysical Research Letters*, *35*(23). https://doi.org/10.1029/2008GL035620

Zhang, J. A., & Paige, D. A. (2009). Cold-trapped organic compounds at the poles of the Moon and Mercury: Implications for origins. *Geophysical Research Letters*, *36*(16), L16203. https://doi.org/10.1029/2009GL038614

Zolotov, M. Yu. (2011). On the chemistry of mantle and magmatic volatiles on Mercury. *Icarus*, *212*(1), 24–41. https://doi.org/10.1016/j.icarus.2010.12.014

Zolotov, M. Yu., Sprague, A. L., Hauck, S. A., Nittler, L. R., Solomon, S. C., & Weider, S. Z. (2013). The redox state, FeO content, and origin of sulfur-rich magmas on Mercury. *Journal of Geophysical Research: Planets*, *118*(1), 138–146. https://doi.org/10.1029/2012JE004274

Zuber, M. T., Smith, D. E., Phillips, R. J., Solomon, S. C., Neumann, G. A., Hauck, S. A., et al. (2012). Topography of the northern hemisphere of Mercury from MESSENGER laser altimetry. *Science*, *336*(6078), 217–220. https://doi.org/10.1126/science.1218805

Chapter 1

Age constraints of Mercury's polar deposits suggest recent delivery of ice

Ariel N. Deutsch[a], James W. Head III[a], Gregory A. Neumann[b]

[a]Department of Earth, Environmental and Planetary Sciences, Brown University, Providence, RI 02912, USA

[b]NASA Goddard Space Flight Center, Greenbelt, MD 20771, USA

Published in *Earth and Planetary Science Letters*

Deutsch, A. N., Head, J. W., Neumann, G. A., 2019. Age constraints of Mercury's polar deposits suggest recent delivery of ice. *Earth Planet. Sci. Lett., 520,* 26–33, https://doi.org/10.1016/j.epsl.2019.05.027.

Abstract

Surface ice at the poles of Mercury appears as several-m-thick deposits that are composed of nearly pure water. We provide new age estimates of the surfaces of Mercury's polar deposits from combined analyses of Poisson statistics and direct observations of crater densities within permanently shadowed, radar-bright regions imaged by the MESSENGER spacecraft. These age estimates conservatively suggest that ice was delivered to Mercury within the last ~330 Myr. The geologically young ages suggest that the surfaces have been recently refreshed, and this may be accomplished by the delivery of ice in a young impactor or impactors. A single, recent impactor is more consistent with the relative purity of the ice, as suggested by the Earth-based radar observations. In contrast to ice on Mercury, observations of the lunar poles are suggestive of a highly patchy distribution of surface frost. The patchiness of lunar polar deposits is consistent with long exposure times to the space weathering environment. Given enough time, the polar deposits on Mercury may age into a more heterogeneous spatial distribution, similar to that on the Moon.

1. Introduction

The polar terrains of Mercury are characterized by permanently shadowed regions (PSRs) that are thermally stable environments for water ice on geologic timescales (Vasavada et al., 1999, Paige et al., 2013). Observations from both Earth-based radar and the MErcury Surface, Space ENvironment, GEochemisty, and Ranging (MESSENGER) spacecraft have demonstrated that water-ice deposits occupy such PSRs (Fig. 1) (Deutsch et al., 2016, Chabot et al., 2018). For example, radar observations of Mercury's poles are suggestive of ice deposits that are at least several meters thick (Harmon, 2007, Black et al., 2010), and modeling of the radar data suggests that these deposits are composed of ~95% pure water ice (Butler et al., 1993). Neutron data acquired by the MESSENGER spacecraft of the north polar region of Mercury is also consistent with a near pure water-ice composition (Lawrence et al., 2013). While some ice deposits closest to the pole are exposed at the surface (Neumann et al., 2013, Chabot et al., 2014; Deutsch et al., 2017), the majority of ice deposits on Mercury are insulated by 10–30 cm (Lawrence et al., 2013) of low-reflectance materials that are interpreted to be a sublimation lag composed of carbon-rich material (e.g., Zhang and Paige, 2010, Paige et al., 2013). Finally, images (Chabot et al., 2016, Chabot et al., 2014) and reflectance measurements (Neumann et al., 2013, Deutsch et al., 2017) of Mercury's PSRs reveal spatially coherent ice deposits with distinct albedos and sharp reflectance boundaries that align with boundaries of permanent shadow.

Understanding the ages of Mercury's polar deposits is important when considering the possible source(s) and evolution of the ice. An early pre-MESSENGER analysis used regolith gardening models to constrain the age of Mercury's polar ice (Crider and Killen, 2005). Because Earth-based radar observations suggest that the radar-bright ice deposits on Mercury's surface have <5% volume fraction of silicates (Butler et al., 1993), it is likely that the ice deposits were emplaced relatively recently in order to maintain this high degree of purity through time (Butler et al., 1993, Crider and Killen, 2005). The regolith gardening models suggest that the ice deposits are <50 Myr in age, given that 20 cm of regolith is expected to cover the deposits in this timeframe, which is not observed

(Crider and Killen, 2005). Similarly, Lawrence et al. (2013) used the average thickness of the upper layer of ice inferred from neutron spectrometry and models of surface modification to predict that ice was delivered to the poles in the last 18 to 70 Myr.

Data acquired by the MErcury Surface, Space ENvironment, GEochemistry, and Ranging (MESSENGER) spacecraft support the hypothesis that the ice on Mercury may be relatively young. For example, images of the north polar region show that the ice deposits are not buried by regolith (Chabot et al., 2016, Chabot et al., 2014). Furthermore, images (Chabot et al., 2016, Chabot et al., 2014) and reflectance measurements (Neumann et al., 2013) reveal sharp reflectance boundaries delineating coherent deposits, suggesting that volatiles were delivered relatively recently or are actively restored.

Here we estimate the surface ages of specific ice deposits on Mercury using crater-counting methods and Poisson statistical analyses and discuss possible sources for ice on Mercury. We conclude by discussing the differences between ice at the poles of Mercury and the Moon, and suggest that differences in ages of the ice may be an important factor contributing to the stark differences in surface characteristics between ice on these two airless bodies.

2. Methods

2.1. Surface age estimates for polar deposits on Mercury

During MESSENGER's low-altitude campaign, high-resolution images (pixel resolution ≤100 m) were acquired of 35 host craters at the north polar region of Mercury (Chabot et al., 2016). These broadband Wide-Angle Camera (WAC) images use sunlight scattered from nearby illuminated peaks to image within PSRs. The permanently shadowed floors where radar-bright ice deposits are located can be resolved in these images, and the images sometimes reveal central crater structures or small impact craters superposing the host crater. Identified superposing impact craters are all < a few km in diameter, but are typically much smaller, between 100 and 300 m. While the majority of small craters (< a few km in diameter) observed in the PSRs may have formed before the deposition of the ice (Chabot et al., 2016, Deutsch et al., 2018), some anomalous small impact craters are associated with high-reflectance rings, suggestive of excavated material (Fig. 2). If these anomalous craters associated with high-reflectance material are superposing the ice, then they can be used to estimate the ages of the ice surfaces.

Each of the analyzed craters is located below ~86°N and has a low-reflectance layer of materials within its PSR. Low-reflectance layers are found exclusively within Mercury's PSRs, specifically in regions where biannual average surface temperatures are >110 K (the temperature at which water ice is stable) but still <210 K, suggesting that the distribution of these low-reflectance materials is thermally controlled and that the composition of these materials is volatile (Paige et al., 2013). Materials with a lower volatility than water can form as sublimation lags and help insulate water-ice deposits beneath (Paige et al., 2013), and the reflectance properties of Mercury's low-reflectance materials are consistent with organic-rich compounds such as those present in comets and primitive meteorites (e.g., Zhang and Paige, 2010, Paige et al., 2013). After the initial emplacement of ice, it is possible that any disturbance to the ice (e.g., bombardment) would result in the formation of new lag deposits, restoring the ice to a stable configuration.

We analyze all high-resolution MDIS images of the 35 host craters at the north polar region of Mercury that were acquired during MESSENGER's low-altitude campaign (Chabot et al., 2016). The PSRs of each crater (Deutsch et al., 2016) are visually inspected for the presence of any impact craters that are associated with high-reflectance rings suggestive of excavated material. Larger-scale brightness variations in polar craters correlate with variations in modeled maximum surface temperature, suggesting that multiple volatile species are contained within the surficial lag deposits that insulate the majority of polar deposits on Mercury (Chabot et al., 2016). The brightness variations associated with the craters selected for this study are smaller in size than the brightness variations that are suggestive of different volatiles, and they are also not correlated with any predicted temperature variations (Chabot et al., 2016). However, the thermal models presented by Chabot et al. (2016) have a spatial scale of 1 km, and therefore cannot predict variations at the spatial scale of these high-reflectance rings associated with small craters (between 100 m and 300 m in diameter).

If small craters associated with high-reflectance rings are identified in ≥2 images, then we interpret these small craters as superposing the ice deposit and we interpret the high-reflectance rings as crater ejecta. Thus, even if high-reflectance rings associated with small craters appear to be present in an image, if the remaining images are unclear due to poor lighting conditions or non-ideal viewing geometries, then we do not use the host craters in our analysis. For the majority of host craters analyzed (29 of 35 craters), the available images do not adequately resolve the permanently shadowed floors such that the presence or absence of high-reflectance rings can be confidently identified in association with small craters. If small craters associated with high-reflectance rings are not identified in any images (and ≥2 images) that clearly resolve the host crater floor, then we interpret the host crater as having no small craters that superpose the ice deposit.

We identify 3 north polar craters that host small impact craters (∼100–300 m) associated with high-reflectance ejecta rings: Ensor, Laxness, and Bechet (Fig. 1; Table 1). The images used to identify high-reflectance material for these 3 craters were acquired at phase angles between 77.2° and 118.3°, incidence angles between 82.8° and 84.7°, and emission angles between 0.3° and 34.0°. For each of these 3 craters, count areas for crater statistics are measured for the regions of the crater floors that could be resolved in all of the images. All small impact craters >100 m that are associated with high-reflectance rings are identified.

Using CraterStatsII (Michael and Neukum, 2010), crater size-frequency distributions (CSFDs) are derived for the ice surfaces by fitting models of the crater-derived retention ages to the chronology and production curves for Mercury (Le Feuvre and Wieczorek, 2011). We estimate surface ages for each ice deposit from the CraterStatsII output age model.

We also describe the relative likelihoods of possible ages of the ice surfaces using Poisson statistics, which do not require data binning or curve fitting techniques (Michael et al., 2016). In contrast to fitting best-fit model isochrons to some crater population, which results in an approximate evaluation of the crater chronology model prediction, this approach yields an exact evaluation of a crater chronology model using Poisson statistics and Bayesian inference (Michael et al., 2016). It is exact given that it does not rely on approximation in evaluating the predictions of the crater chronology model (although uncertainties inherent to the model itself remain). Poisson statistics determine the time-resolved probability of a given observation within the chronology model, where uncertainties stem from the predictions of the chronology model (Michael et al., 2016). With this technique, order-of-magnitude ages can even be estimated for surfaces that show no craters. The likelihood function for the set of observed craters, $\mathbb{D}$, as divided into n bins for any given time, t, is expressed by Michael et al. (2016) in their Eq. (8):

$$\mathrm{pr}(\mathbb{D}, t) \propto \exp\left(-A[C(d,t)]_{d_{\max}}^{d_{\min}}\right. \; \{\mathrm{C}(\mathrm{d}=1,\mathrm{t})\}^{n_{\mathbb{D}}} \qquad \text{(Eq. 1)}$$

where A is the crater accumulation area, $C(d, t)$ is the cumulative form of the production function, and d is crater diameter. The spread of possible ages and their relative likelihoods is equally valid for surfaces that have no craters, only a few craters, or many craters (Michael et al., 2016). Errors are reported as 1-σ of the median to include 68% of the function describing the likelihood that the surface has a particular age (Michael et al., 2016).

2.2. Statistical and observational biases affecting crater counts of ice deposits on Mercury

A variety of statistical and observational biases can affect the estimated absolute model ages (AMAs) of the ice deposits. For example, low image resolution and non-ideal illumination conditions can render crater identification difficult (Williams et al., 2018). Different illumination geometries can influence the apparent reflectance within individual images. To mitigate this issue, all of the small craters (~100–300 m) included within our counts are associated with high-reflectance deposits in ≥2 individual images.

The surface areas of the polar ice deposits (<150 km^2) require counting smaller craters, and production functions are less certain at smaller crater sizes (Williams et al., 2018). Due to the small size of the identified counted craters (~100–300 m), it is possible that some of the small craters are the result of secondary impacts. However, when excluding obvious secondary chains and clusters, age dating using small-crater statistics has been shown to be within the statistical uncertainty (e.g., Hartmann, 2007).

It is also possible that the identified craters are subject to modification, given that small craters are more sensitive to variation (Williams et al., 2018). Previous workers investigating the importance of viscous flow at the martian north polar layered deposits found that present-day impact craters are too small and cold for viscous relaxation to play an important role in controlling crater dimensions, and that this effect may be ignored in analyses of crater size-frequency distributions (Sori et al., 2016). Here, we choose to neglect viscous relaxation as an important modification factor given that the craters on Mercury's polar deposits that we analyze are similarly small and located in crater interiors, away from steep slopes or warmer topographies. Furthermore, analysis of flow conditions within permanently shadowed craters on Mercury suggests that the extremely cold conditions and limited thickness of the ice prevent substantial flow (Fastook et al., 2019).

The crater counts are completed for individual ice deposits, which have limited count areas (Williams et al., 2018). CSFDs can vary across a putative uniform geologic unit when count areas become small (Warner et al., 2015); however, small count areas down to 4 km^2 have been shown to be consistent with model ages derived from larger (100 km^2) count areas, although with lower accuracy (Pasckert et al., 2015). The count areas analyzed here are between 79 and 109 km^2, and thus we consider errors due to limited count areas negligible.

Finally, chronology and production curves for Mercury are derived for impact craters in regolith (Le Feuvre and Wieczorek, 2011). Given that the AMAs estimated here are derived from impact craters assumed to be in ice, we estimate AMAs after scaling the superposed impact craters to estimate the sizes of these craters as if they were in regolith. Impact experiments suggest that craters in ice are found to have final diameters 2 to 3 times larger than craters in competent rocky materials (e.g., Croft et al., 1979; Koschny and Grün, 2001). Thus, we estimate ages of the ice surfaces from crater populations that are 1 (unscaled), 1/2, and 1/3 times the size of the measured crater diameters.

2.3. Stability of ejected high-reflectance material in Mercury's PSRs

We use crater scaling laws (Eq. (2)) (Croft, 1981) to estimate the depth of material excavated by impacts into Ensor, Laxness, and Bechet, the three craters that are identified as hosting small impact craters that are located within PSRs and are associated with high-reflectance ejecta rings (Fig. 2). The identified small craters used in our crater-counting analysis range in size from 100 to 300 m in diameter, and the average diameter for all superposed craters is 211 m. We estimate the depth from which material is excavated ($d_{excavation}$) from the measured final crater diameter (D_{final}):

$$d_{excavation} = \frac{1}{10}(\mathrm{D}_{final}) \qquad \text{(Eq. 2)}$$

We estimate that impactors resulting in craters with diameters between 100 m and 300 m would have excavated material from depths of 10 m and 30 m.

We also estimate the depth of material excavated by impacts after scaling the impacts in order to account for target properties. As discussed above, the crater scaling laws (Eq. (2)) are derived for impacts into silicate material. Here we scale the diameters of the identified craters by a factor of 1/3 in order to estimate the minimum final crater diameters for equivalent impacts into regolith. This endmember scaling scenario results in a range of crater diameters from 33 m to 100 m and an average scaled diameter of 70 m. From Eq. (2), we estimate that small impact craters between 100 m and 300 m in diameter (scaled to new diameters between 33 m and 100 m) superposing a pure ice deposit would have excavated between ~3 m and ~8 m below the ice surface, respectively, with an average excavation depth of ~6 m expected for all identified craters.

The thickness of water-ice deposits on Mercury is estimated to be several m (Harmon, 2007, Black et al., 2010, Talpe et al., 2012), although possibly extending deeper with maximum thicknesses estimated of tens of m (Eke et al., 2017, Deutsch et al., 2018, Susorney et al., 2019). Most recently, an analysis of the changes in topography across radar-bright and non-radar-bright deposits resulted in an upper limit thickness of 15 m for Mercury's water-ice deposits (Susorney et al., 2019). Assuming a water-ice thickness of several (~5) m (Harmon, 2007, Black et al., 2010), then all small impactors resulting in craters >180 m (scaled regolith diameter of 60 m) may have excavated both ice as well as underlying regolith. If the sizes of the impact craters superposing Mercury's polar deposits do not differ substantially in size from impact craters in Mercury's regolith (given that the ice deposits may be only several m thick), then it is possible that all impactors resulting in the craters identified here have excavated both ice and regolith.

Exposed surface water ice and typical mercurian regolith are factors of 4 and 2 brighter, respectively, than the average reflectance of low-reflectance lag deposits that insulate the majority of ice deposits on Mercury, including all of the 35 ice deposits analyzed here (Neumann et al., 2013). Therefore, both water ice and excavated regolith would appear as anomalously bright ejecta superposing the ice deposits. Pure water ice may sublimate away on top of the low-reflectance lag deposit, but the rate of sublimation is relatively slow in comparison to the ages of the ice that we estimate (Sec. 4); 1 m of water ice sublimates in 1 Gyr at 110 K (Vasavada et al., 1999). Importantly, any ejected regolith would of course not sublimate away. While the morphologies of craters impacting into pure ice differ from the morphologies of craters that impact through ice into underlying regolith (e.g., Bramson et al., 2015), the spatial resolution of the images analyzed here is too low in order to observe the morphologies of any of the small craters (100–300 m in diameter). From the estimates of excavation depths above, all impact craters that superpose the ice deposits and have a preserved final diameter >180 m should be associated with high-reflectance materials, assuming an average ice deposit thickness of 5 m and that the preserved final diameters are 1/3 the size of craters from similar impacts into regolith.

3. Results: surface age estimates for Mercury's ice deposits

Here, we suggest that brightness variations associated with small impact craters (100–300 m in diameter) that appear bright in multiple images of different viewing geometries are indicative of excavated material. Under this assumption, we estimate the surface ages of specific ice deposits on Mercury using impact craters that superpose individual ice deposits (Fig. 2). Although high-resolution images of 35 north polar ice deposits have been acquired, only three individual ice deposits, hosted by Ensor, Laxness, and Bechet craters (Table 1, Supplementary Materials), show clear evidence for high-reflectance material associated with individual small craters (Fig. 2). The remaining ice deposits either show no small craters associated with high-reflectance ejecta rings using the aforementioned criteria (3 craters), or there are not multiple clear images for these craters that allow the PSRs to be resolved (29 craters).

Despréz, Fuller, and V2 craters host the three ice deposits in which no high-reflectance materials are identified in association with small craters (Fig. 3). These three north polar ice deposits were imaged multiple times (Table S1, Supplementary Materials) during MESSENGER's low-altitude imaging campaign. In none of the images do we identify high-reflectance material in association with impact craters (Fig. 3). Given that (1) ice is not expected to sublimate away quickly within these PSRs and (2) impact craters are expected to have excavated both ice and regolith (Sec. 2), the lack of high-reflectance ejecta materials suggests that the craters observed in these PSRs formed before the ice was emplaced (e.g., Deutsch et al., 2018). Furthermore, the lack of high-reflectance ejecta materials suggests that these polar ice deposits are very young, and that no impacts that can be observed at the spatial scale of these images have occurred since ice deposition. It is also possible that the top ice layer has been recently restored, thus erasing any visible brightness variations on the surface, and this scenario would also favor a very young age of the surface ice. Finally, it is possible that unfavorable viewing conditions have impeded our ability to identify bright ejecta, however we note that the images of these three craters (Despréz, Fuller, and V2) were acquired under viewing conditions similar to those of the three craters in which bright materials are identified (Ensor, Laxness, and Bechet). Specifically, the images of Despréz, Fuller, and V2 that were analyzed were acquired at phase angles between 74.4° and 129.2°, incidence angles between 80.5° and 87.0°, and emission angles between 1.6° and 42.2°, in comparison to the images of Ensor, Laxness, and Bechet, which were acquired at phase angles between 77.2° and 118.3°, incidence angles between 82.8° and 84.7°, and emission angles between 0.3° and 34.0°.

Absolute model ages (AMAs) (Le Feuvre and Wieczorek, 2011) derived from superposed impact craters on Ensor, Laxness, and Bechet (Table 1) suggest that the surficial layers of the ice deposits are geologically young (Fig. 4a), and were delivered in the most recent Kuiperian period. The specific AMAs estimated for the surface ice in Ensor, Laxness, and Bechet are 210 ± 60 Ma, 29 ± 10 Ma, and 47 ± 20 Ma before scaling the impact craters. There is overlap in the estimated surface ages between ice hosted by Laxness and Bechet when doubling the reported error to consider a 2-σ deviation. When the impact craters are scaled by 1/2 to represent craters impacting into pure ice, the estimated ages of all three craters overlap within a 2-σ deviation of the mean. Finally, when the impact craters are scaled by 1/3, then the estimated ages of ice surfaces within

Ensor and Bechet overlap within a 2-σ deviation of the mean, and the estimated ages of ice surfaces within Bechet and Laxness overlap as well. The reported errors for crater counting statistics are from counting statistics alone (Michael and Neukum, 2010), and as discussed in detail in Sec. 2.2, a variety of other statistics and observational biases may affect crater counting on Mercury's ice deposits. Thus, the errors reported here are considered to be a minimum.

Poisson analyses are used to describe the relative likelihoods of possible ages of the surface ice deposits (Michael et al., 2016). These analyses suggest that surface ice deposits hosted by Ensor, Laxness, and Bechet craters are 137 ± 15 Myr, 100 ± 18 Myr, and 81 ± 19 Myr, respectively, and that any ice deposits that lack superposing impact craters are likely to be <10 ± 1 Myr (Fig. 4b). Considering a 2-σ deviation of the mean, the ice surfaces in Ensor, Laxness, and Bechet overlap in age.

Relatively young ages for the ice deposits are consistent with stratigraphic relationships of host craters and contained polar ice. Global mapping of craters ≥40 km in diameter reveals that craters from the Mansurian period (280 Ma–1.7 Ga) are located within both the north and south polar regions (Prockter et al., 2016) and these craters host radar-bright materials indicative of water ice, placing an upper bound on the delivery of surface water ice (Deutsch et al., 2016, Chabot et al., 2018). Large Kuiperian craters (280 Ma–today) have not been mapped in the north polar region, and the only two Kuiperian craters mapped in the south polar region have not been well-imaged by Earth-based radio observations (Harmon et al., 2011, Chabot et al., 2018).

In conclusion, ages derived from both crater-counting statistics and Poisson statistics suggest that the surfaces of the individual ice deposits analyzed here are very geologically young. Even the most conservative crater-counting estimates (in which craters are not scaled for impacting into ice, and given a 2-σ uncertainty) suggest that the surface ice was delivered within the last ∼330 Myr.

4. Discussion

4.1. Implications of geologically young ice surfaces

Importantly, the age estimates presented here, derived both from crater-counting statistics as well as Poisson statistics, give constraints on the surface ages of the ice. If ice deposits accumulated from a single event, then the age of the surface is representative of the age of the whole deposit. Alternatively, if ice deposits have accumulated over time, then the surface age does not reflect the deposit age. It is not possible to determine which is the case from the current orbital data, however the high purity of the radar observations is suggestive of delivery in a single event. Analysis of the Earth-based radar data indicated that the ice deposits must be extremely pure, with less than ∼5% silicates by volume (Butler et al., 1993). This high degree of purity is consistent with the ice being delivered in a relatively short period of time (Butler et al., 1993), and is difficult to explain by a more continuous process in which ice accumulates over time. As discussed earlier, regolith gardening models suggested that all of the ice deposits are <50 Myr in age because 20 cm of regolith is predicted to cover the ice in this timeframe, which is not observed (Crider and Killen, 2005). An independent analysis of surface modification models also concluded that all of the ice deposits are relatively young (18–70 Myr old) using constraints on the average thickness of the upper layer of ice deduced from MESSENGER's neutron data (Lawrence et al., 2013). In line with these previous studies, we favor the hypothesis that all of the several-m thick ice deposits imaged by MESSENGER are young and may have been emplaced during a single event. However, it is certainly possible that there is additional older ice hidden beneath the visible ice deposits, gardened deep in the subsurface, and we discuss this in detail in Sec. 4.2. If all of the ice was emplaced in a single event, then the ages derived for the surface ice presented here are representative of the entire ice deposits. Alternatively, if the ice has accumulated over time in more than one event, then the ages we derived for the surface ice represent an age of the most recent emplacement episode.

A single event that led to the emplacement of surface ice in each of the analyzed craters is not favored if the error statistics reported here for crater counting are precise and thus the ages of all of the individual ice deposits do not overlap. In such a case, the surfaces of these individual ice deposits must have been emplaced by recent and discrete delivery mechanisms, such as individual, young impacts. However, given the fact that reported errors for crater counting are from counting statistics alone, and also given the overlap in estimated AMAs between two or three of the craters in all cases, we also find it worthwhile to consider the possibility that the ice analyzed here was emplaced at the same time. In such a case, we may consider an average AMA for polar ice on the basis of these three specific host craters; the average AMA is 95 Ma ± 33 Ma before scaling the impact craters and 4.2 Ma ± 1.2 Ma after scaling the impact craters by 1/3, where the reported uncertainties are 1-σ standard errors derived from counting statistics alone (Table 1).

Overall, a relatively recent delivery or deliveries may explain why ice deposits on Mercury have sharp reflectance boundaries, coherent surfaces (Neumann et al., 2013; Chabot et al., 2014, Chabot et al., 2016), and high radar backscatter (Butler et al., 1993; Harmon et al., 2011). If the ice deposits have accumulated over time via multiple events, the delivery rate must exceed the regolith overturn rate given the sharp reflectance boundaries observed for all ice deposits on Mercury (Neumann et al., 2013; Chabot et al., 2014, Chabot et al., 2016). Relatively young surface ages of the ice are inconsistent with volcanic outgassing delivering volatile species to Mercury's poles given that the bulk of volcanic activity on Mercury ceased >3.5 Ga (Byrne et al., 2016), and recent, localized pyroclastic eruptions (Jozwiak et al., 2018) are not expected to have produced 3.45×10^{17} g of water, which is the mass of ice calculated for Mercury (Susorney et al., 2019).

4.2. Comparison to lunar polar ice

Mercury and the Moon show distinct differences in the abundance and purity of ice cold-trapped at their poles, despite both bodies having PSRs that are thermally stable environments for water ice on geologic timescales (Vasavada et al., 1999) due to the small axial tilt of each body. While both Earth-based (Harmon et al., 2011) and orbital (Lawrence et al., 2013, Neumann et al., 2013, Paige et al., 2013; Chabot et al., 2014; Deutsch et al., 2016, Deutsch et al., 2017) observations indicate that there are extensive water-ice deposits within Mercury's PSRs (Fig. 1), data suggest that water-ice deposits on the Moon (Lawrence et al., 2006, Colaprete et al., 2010; Campbell et al., 2006, Spudis et al., 2010, Thomson et al., 2012, Haruyama et al., 2008, Zuber et al., 2012, Hayne et al., 2015, Fisher et al., 2017, Li et al., 2018) are smaller in extent and less concentrated than those on Mercury.

For example, neutron spectrometer data of the lunar polar regions are suggestive of concentrations of only ~1.5% water ice by mass in the upper ~1 m of the lunar regolith (Lawrence et al., 2006). Furthermore, Lunar CRater Observation and Sensing Satellite detected only ~6 wt.% water ice in the ejecta plume resulting from an impact into Cabeus crater (Colaprete et al., 2010). Earth-based radar observations do not show evidence for concentrated water ice on the Moon (e.g., Campbell et al., 2006) and spacecraft radar observations are suggestive of only patches of ice (e.g., Thomson et al., 2012). Finally, imaging (Haruyama et al., 2008) and reflectance (Zuber et al., 2012, Hayne et al., 2015, Fisher et al., 2017, Li et al., 2018) campaigns of the lunar poles have not revealed thick, coherent ice deposits, but instead are suggestive of a spatially heterogeneous, or patchy, distribution of water frost. Thus, ice on Mercury appears to be purer and more extensive than any ice on the Moon. The cause for the differences between ice on Mercury and the Moon is not understood. One possibility is that differences in delivery time may explain the stark differences between surface ice on these two airless bodies.

Impact gardening can produce spatial heterogeneities in ice distribution due to the loss and redistribution of volatiles through time (e.g., Hurley et al., 2012). Impacts introduce heterogeneity into the system because they remove volatiles via vaporization, and also preserve volatiles through the emplacement of ejecta, with a net effect of breaking up and burying the ice through time (e.g., Hurley et al., 2012). Because these processes take time, heterogeneity is inherently related to the age of the ice.

Hurley et al. (2012) present Monte Carlo simulations of the evolution of ice in PSRs on the Moon. They find that, statistically, individual locations on the Moon experience more burial events than excavation events and they estimate an average burial rate of 1 mm/Myr. Using this average burial rate, we extrapolate backwards in time from the present day (0 Myr) into the past (4500 Myr), starting with a present-day ice thickness of 1 mm. If an initial ice layer on the Moon was ever similar in thickness to the ice deposits observed at the poles of Mercury (and thus at least several meters thick (Harmon, 2007, Black et al., 2010)), then the ice observed at the surface of the Moon today must have been delivered very early on in lunar history. For example, in order for regolith gardening processes to rework a 4 m-thick layer of ice into a present-day 1-mm thickness on the surface, then the 4 m of ice should have been accumulated by ∼4 Ga. Interestingly, the average burial rate of 1 mm/Myr (Hurley et al., 2012) cannot account for an initial thickness of ice in the lunar PSRs that exceeds, on average, 4.5 m, which may be thinner than what is observed on Mercury today; lower estimates for the thickness of Mercury's polar ice deposits are at least several meters (Harmon, 2007, Black et al., 2010, Talpe et al., 2012, Susorney et al., 2019), while maximum estimates approach ∼50 m (Eke et al., 2017, Deutsch et al., 2018). Thus, the regolith gardening simulations presented by Hurley et al. (2012) suggest that the ice on the Moon is relatively ancient, that less ice has been delivered to the Moon than has been delivered to Mercury through time, or that additional loss processes are very efficient on the Moon.

5. Conclusion

Unlike surface water ice on the Moon, surface water ice on Mercury appears as coherent deposits whose distinct reflectance boundaries align directly with regions of permanent shadow (Chabot et al., 2014, Chabot et al., 2016, Chabot et al., 2018; Deutsch et al., 2016). If ice deposits on Mercury are relatively young, then they have not been exposed to extensive space weathering processes that would break up, destroy, or bury the ice. A relatively young age, as estimated here from both superposed impact craters on the ice surfaces and Poisson analyses, is consistent with (1) regolith gardening models that suggest the ice deposits were emplaced <50 Ma (Crider and Killen, 2005), (2) analyses of high-resolution images of the polar deposits that uniformly reveal sharp reflectance boundaries and spatial coherence within PSRs (Chabot et al., 2016, Chabot et al., 2014), and (3) the presence of ice in micro-cold traps (Rubanenko et al., 2018). If the ages and error statistics presented here are precise and not all individual ice surfaces overlap in age, then the surface ice must have been delivered by a multitude of young, discrete emplacement events. However, if the errors do overlap, it is possible that the surface ice was delivered by a single, young impact (e.g., Chabot et al., 2016, Rubanenko et al., 2018; Ernst et al., 2018). Recently, an analysis of Mercury's Hokusai (a 97-km Kuiperian crater) estimated that the Hokusai impact event could account for the entire ice inventory on the planet, strengthening the viability of a single-impact delivery scenario (Ernst et al., 2018).

To date, it is not clear why polar ice on the Moon is relatively less pure and extensive than polar ice on Mercury, which has a water-ice cold-trapping efficiency of only 50% of the Moon (Schörghofer et al., 2016). It is possible that these differences may be related to the age of the ice. Surface ice on the Moon is characterized by a substantial degree of spatial heterogeneity within and between PSRs (Hayne et al., 2015). If the ice observed at the lunar poles today was delivered early on during the Moon's history, it has undergone substantial impact bombardment, leading to a spatially heterogeneous surface distribution (e.g., Hurley et al., 2012). The ice deposits that show the greatest spatial heterogeneity on the surface may have substantial vertical heterogeneity as well, with additional ice buried in the subsurface (e.g., Hurley et al., 2012).

The same impact bombardment and space weathering processes operate on Mercury and the Moon, and Mercury's regolith may be overturned even more frequently than the lunar regolith (e.g., Domingue et al., 2014) due to higher impact rates and speeds (e,g., Borin et al., 2009). Thus, it is possible that relatively ancient, degraded ice deposits exist below the extensive, pure deposits observed on Mercury's surface today. The lunar polar deposits therefore provide an interesting opportunity to inform us about the ultimate fate of mercurian polar deposits, as well as ices on other airless bodies.

This work has provided new surface age estimates of Mercury's polar ice deposits, which provide critical insight into the possible delivery mechanism(s) for the ice. We find that individual ice surfaces on Mercury are all <330 Ma, and possibly as young as only a few Ma. These young ages are suggestive of recent comet impacts, or a single impact if larger errors on the estimated ages are considered. As BepiColombo prepares to enter its orbit around Mercury, this work will serve as an important test as the first high-resolution images of the south polar PSRs are acquired.

Acknowledgments

We thank Michael Sori and an anonymous reviewer for their helpful reviews and William McKinnon for his editorial handling of this manuscript. This work is supported by NASA (Grant number NNX16AT19H) issued through the Harriett G. Jenkins Graduate Fellowship to A.N.D., by the Solar System Exploration Research Virtual Institute (Grant number NNA14AB01A) to J.W.H., and by the NASA Discovery Program and Goddard Space Flight Center Internal Science Funding Model to G.A.N. We gratefully acknowledge Greg Michael for assistance in Poisson statistical analyses and Carle Pieters for helpful discussion about this work.

References

G.J. Black, D.B. Campbell, J.K. Harmon. Radar measurements of Mercury's north pole at 70 cm wavelength. Icarus, 209 (2010), pp. 224-229, 10.1016/j.icarus.2009.10.009.

P. Borin, G. Cremonese, F. Marzari, M. Bruno, S. Marchi. Statistical analysis of micrometeoroids flux on Mercury. Astron. Astrophys., 503 (2009), pp. 259-264, 10.1051/0004-6361/200912080.

A.M. Bramson, S. Byrne, N.E. Putzig, S. Sutton, J.J. Plaut, T.C. Brothers, J.W. Holt. Widespread excess ice in Arcadia Planitia, Mars. Geophys. Res. Lett., 42 (2015), pp. 6566-6574, 10.1002/2015GL064844.

B.J. Butler, D.O. Muhleman, M.A. Slade. Mercury: full-disk radar images and the detection and stability of ice at the North Pole. J. Geophys. Res., 98 (1993), pp. 15003-15023, 10.1029/93JE01581.

P.K. Byrne, L.R. Ostrach, C.I. Fassett, C.R. Chapman, B.W. Denevi, A.J. Evans, C. Klimczak, M.E. Banks, J.W. Head, S.C. Solomon. Widespread effusive volcanism on Mercury likely ended by about 3.5 Ga. Geophys. Res. Lett., 43 (2016), Article 2016GL069412, 10.1002/2016GL069412.

D.B. Campbell, B.A. Campbell, L.M. Carter, J.-L. Margot, N.J.S. Stacy. No evidence for thick deposits of ice at the lunar south pole. Nature, 443 (2006), pp. 835-837, 10.1038/nature05167.

N.L. Chabot, C.M. Ernst, B.W. Denevi, H. Nair, A.N. Deutsch, D.T. Blewett, S.L. Murchie, G.A. Neumann, E. Mazarico, D.A. Paige, J.K. Harmon, J.W. Head, S.C. Solomon. Images of surface volatiles in Mercury's polar craters acquired by the MESSENGER spacecraft. Geology, 42 (2014), pp. 1051-1054, 10.1130/G35916.1.

N.L. Chabot, C.M. Ernst, D.A. Paige, H. Nair, B.W. Denevi, D.T. Blewett, S.L. Murchie, A.N. Deutsch, J.W. Head, S.C. Solomon. Imaging Mercury's polar deposits during MESSENGER's low-altitude campaign. Geophys. Res. Lett., 43 (2016), pp. 9461-9468, 10.1002/2016GL070403.

N.L. Chabot, E.E. Shread, J.K. Harmon. Investigating Mercury's south polar deposits: Arecibo radar observations and high-resolution determination of illumination conditions. J. Geophys. Res., Planets, 123 (2018), pp. 666-681, 10.1002/2017JE005500.

A. Colaprete, P. Schultz, J. Heldmann, D. Wooden, M. Shirley, K. Ennico, B. Hermalyn, W. Marshall, A. Ricco, R.C. Elphic, D. Goldstein, D. Summy, G.D. Bart, E.

Asphaug, D. Korycansky, D. Landis, L. Sollitt. Detection of water in the LCROSS ejecta plume. Science, 330 (2010), pp. 463-468, 10.1126/science.1186986.

D. Crider, R.M. Killen. Burial rate of Mercury's polar volatile deposits. Geophys. Res. Lett., 32 (2005), Article L12201, 10.1029/2005GL022689.

S.K. Croft. Relationships between the apparent crater, transient crater and excavation cavity of a simple crater. B. Odette, J. Hörz, F. Hörz (Eds.), Workshop on Apollo, vol. 16, Lunar and Planet Inst., Houston, Tex. (1981), pp. 40-44.

S.K. Croft, S.W. Kieffer, T.J. Ahrens. Low-velocity impact craters in ice and ice-saturated sand with implications for Martian crater count ages. J. Geophys. Res., Solid Earth, 84 (1979), pp. 8023-8032, 10.1029/JB084iB14p08023.

A.N. Deutsch, N.L. Chabot, E. Mazarico, C.M. Ernst, J.W. Head, G.A. Neumann, S.C. Solomon. Comparison of areas in shadow from imaging and altimetry in the north polar region of Mercury and implications for polar ice deposits. Icarus, 280 (2016), pp. 158-171, 10.1016/j.icarus.2016.06.015.

A.N. Deutsch, J.W. Head, N.L. Chabot, G.A. Neumann. Constraining the thickness of polar ice deposits on Mercury using the Mercury Laser Altimeter and small craters in permanently shadowed regions. Icarus, 305 (2018), pp. 139-148, 10.1016/j.icarus.2018.01.013.

A.N. Deutsch, G.A. Neumann, J.W. Head. New evidence for surface water ice in small-scale cold traps and in three large craters at the north polar region of Mercury from the Mercury Laser Altimeter. Geophys. Res. Lett., 44 (2017), pp. 9233-9241, 10.1002/2017GL074723.

D.L. Domingue, C.R. Chapman, R.M. Killen, T.H. Zurbuchen, J.A. Gilbert, M. Sarantos, M. Benna, J.A. Slavin, D. Schriver, P.M. Trávníček, T.M. Orlando, A.L. Sprague, D.T. Blewett, J.J. Gillis-Davis, W.C. Feldman, D.J. Lawrence, G.C. Ho, D.S. Ebel, L.R. Nittler, F. Vilas, C.M. Pieters, S.C. Solomon, C.L. Johnson, R.M. Winslow, J. Helbert, P.N. Peplowski, S.Z. Weider, N. Mouawad, N.R. Izenberg, W.E. McClintock. Mercury's weather-beaten surface: understanding Mercury in the context of lunar and asteroidal space weathering studies. Space Sci. Rev., 181 (2014), pp. 121-214, 10.1007/s11214-014-0039-5.

V.R. Eke, D.J. Lawrence, L.F.A. Teodoro. How thick are Mercury's polar water ice deposits? Icarus, 284 (2017), pp. 407-415, 10.1016/j.icarus.2016.12.001.

C.M. Ernst, N.L. Chabot, O.S. Barnouin. Examining the potential contribution of the Hokusai impact to water ice on Mercury. J. Geophys. Res., Planets, 123 (2018), pp. 2628-2646, 10.1029/2018JE005552.

J.L. Fastook, J.W. Head, A.N. Deutsch. Glaciation on Mercury: accumulation and flow of ice in permanently shadowed circum-polar crater interiors. Icarus, 317 (2019), pp. 81-93, 10.1016/j.icarus.2018.07.004.

E.A. Fisher, P.G. Lucey, M. Lemelin, B.T. Greenhagen, M.A. Siegler, E. Mazarico, O. Aharonson, J.-P. Williams, P.O. Hayne, G.A. Neumann, D.A. Paige, D.E. Smith, M.T. Zuber. Evidence for surface water ice in the lunar polar regions using reflectance measurements from the Lunar Orbiter Laser Altimeter and temperature measurements from the Diviner Lunar Radiometer Experiment. Icarus, 292 (2017), pp. 74-85, 10.1016/j.icarus.2017.03.023.

J.K. Harmon. Radar imaging of Mercury. Space Sci. Rev., 132 (2007), pp. 307-349, 10.1007/s11214-007-9234-y.

J.K. Harmon, M.A. Slade, M.S. Rice. Radar imagery of Mercury's putative polar ice: 1999–2005 Arecibo results. Icarus, 211 (2011), pp. 37-50, 10.1016/j.icarus.2010.08.007.

W.K. Hartmann. Martian cratering 9: toward resolution of the controversy about small craters. Icarus, 189 (2007), pp. 274-278, 10.1016/j.icarus.2007.02.011.

J. Haruyama, M. Ohtake, T. Matsunaga, T. Morota, C. Honda, Y. Yokota, C.M. Pieters, S. Hara, K. Hioki, K. Saiki, H. Miyamoto, A. Iwasaki, M. Abe, Y. Ogawa, H. Takeda, M. Shirao, A. Yamaji, J.-L. Josset. Lack of exposed ice inside lunar south pole Shackleton crater. Science, 322 (2008), pp. 938-939, 10.1126/science.1164020.

P.O. Hayne, A. Hendrix, E. Sefton-Nash, M.A. Siegler, P.G. Lucey, K.D. Retherford, J.-P. Williams, B.T. Greenhagen, D.A. Paige. Evidence for exposed water ice in the Moon's south polar regions from Lunar Reconnaissance Orbiter ultraviolet albedo and temperature measurements. Icarus, 255 (2015), pp. 58-69, 10.1016/j.icarus.2015.03.032.

D.M. Hurley, D.J. Lawrence, D.B.J. Bussey, R.R. Vondrak, R.C. Elphic, G.R. Gladstone. Two-dimensional distribution of volatiles in the lunar regolith from space weathering simulations. Geophys. Res. Lett., 39 (2012), Article L09203, 10.1029/2012GL051105.

L.M. Jozwiak, J.W. Head, L. Wilson. Explosive volcanism on Mercury: analysis of vent and deposit morphology and modes of eruption. Icarus, 302 (2018), pp. 191-212, 10.1016/j.icarus.2017.11.011.

D. Koschny, E. Grün. Impacts into ice–silicate mixtures: crater morphologies, volumes, depth-to-diameter ratios, and yield. Icarus, 154 (2001), pp. 391-401, 10.1006/icar.2001.6707.

D.J. Lawrence, W.C. Feldman, R.C. Elphic, J.J. Hagerty, S. Maurice, G.W. McKinney, T.H. Prettyman. Improved modeling of Lunar Prospector neutron spectrometer data: implications for hydrogen deposits at the lunar poles. J. Geophys. Res., 111 (2006), Article E08001, 10.1029/2005JE002637.

D.J. Lawrence, W.C. Feldman, J.O. Goldsten, S. Maurice, P.N. Peplowski, B.J. Anderson, D. Bazell, R.L. McNutt, L.R. Nittler, T.H. Prettyman, D.J. Rodgers, S.C. Solomon, S.Z. Weider. Evidence for water ice near Mercury's north pole from MESSENGER neutron spectrometer measurements. Science, 339 (2013), pp. 292-296, 10.1126/science.1229953.

M. Le Feuvre, M.A. Wieczorek. Nonuniform cratering of the Moon and a revised crater chronology of the inner Solar System. Icarus, 214 (2011), pp. 1-20, 10.1016/j.icarus.2011.03.010.

S. Li, P.G. Lucey, R.E. Milliken, P.O. Hayne, E. Fisher, J.-P. Williams, D.M. Hurley, R.C. Elphic. Direct evidence of surface exposed water ice in the lunar polar regions. Proc. Natl. Acad. Sci. USA, 115 (2018), pp. 8907-8912, 10.1073/pnas.1802345115.

G.G. Michael, T. Kneissl, A. Neesemann. Planetary surface dating from crater size-frequency distribution measurements: Poisson timing analysis. Icarus, 277 (2016), pp. 279-285, 10.1016/j.icarus.2016.05.019.

G.G. Michael, G. Neukum. Planetary surface dating from crater size–frequency distribution measurements: partial resurfacing events and statistical age uncertainty. Earth Planet. Sci. Lett., 294 (2010), pp. 223-229, 10.1016/j.epsl.2009.12.041.

G.A. Neumann, J.F. Cavanaugh, X. Sun, E.M. Mazarico, D.E. Smith, M.T. Zuber, D. Mao, D.A. Paige, S.C. Solomon, C.M. Ernst, O.S. Barnouin. Bright and dark polar deposits on Mercury: evidence for surface volatiles. Science, 339 (2013), pp. 296-300, 10.1126/science.1229764.

D.A. Paige, M.A. Siegler, J.K. Harmon, G.A. Neumann, E.M. Mazarico, D.E. Smith, M.T. Zuber, E. Harju, M.L. Delitsky, S.C. Solomon. Thermal stability of volatiles in the north polar region of Mercury. Science, 339 (2013), pp. 300-303, 10.1126/science.1231106.

J.H. Pasckert, H. Hiesinger, C.H. van der Bogert. Small-scale lunar farside volcanism. Icarus, 257 (2015), pp. 336-354, 10.1016/j.icarus.2015.04.040.

L.M. Prockter, M.J. Kinczyk, P.K. Byrne, B.W. Denevi, J.W. Head, C.I. Fassett, J.L. Whitten, R.J. Thomas, D.L. Buczkowski, B.M. Hynek, L.R. Ostrach, D.T.

Blewett, C.M. Ernst, MESSENGER Mapping Group. The first global geologic map of Mercury. Lunar Planet. Sci., 47 (2016), Abstract 1245.

L. Rubanenko, E. Mazarico, G.A. Neumann, D.A. Paige. Ice in micro cold traps on Mercury: implications for age and origin. J. Geophys. Res., Planets, 123 (2018), pp. 2178-2191, 10.1029/2018JE005644.

N. Schörghofer, E. Mazarico, T. Platz, F. Preusker, S.E. Schröder, C.A. Raymond, C.T. Russell. The permanently shadowed regions of dwarf planet Ceres. Geophys. Res. Lett., 43 (2016), pp. 6783-6789, 10.1002/2016GL069368.

M.M. Sori, S. Byrne, C.W. Hamilton, M.E. Landis. Viscous flow rates of icy topography on the north polar layered deposits of Mars. Geophys. Res. Lett., 43 (2016), pp. 541-549, 10.1002/2015GL067298.

P.D. Spudis, D.B.J. Bussey, S.M. Baloga, B.J. Butler, D. Carl, L.M. Carter, M. Chakraborty, R.C. Elphic, J.J. Gillis-Davis, J.N. Goswami, E. Heggy, M. Hillyard, R. Jensen, R.L. Kirk, D. LaVallee, P. McKerracher, C.D. Neish, S. Nozette, S. Nylund, M. Palsetia, W. Patterson, M.S. Robinson, R.K. Raney, R.C. Schulze, H. Sequeira, J. Skura, T.W. Thompson, B.J. Thomson, E.A. Ustinov, H.L. Winters. Initial results for the north pole of the Moon from Mini-SAR, Chandrayaan-1 mission. Geophys. Res. Lett., 37 (2010), Article L06204, 10.1029/2009GL042259.

H.C.M. Susorney, P.B. James, C.L. Johnson, N.L. Chabot, C.M. Ernst, E.M. Mazarico, G.A. Neumann, M.J. Kinczyk. The thickness of radar-bright deposits in Mercury's northern hemisphere from individual Mercury Laser Altimeter tracks. Icarus, 323 (2019), pp. 40-45, 10.1016/j.icarus.2019.01.016.

M.J. Talpe, M.T. Zuber, D. Yang, G.A. Neumann, S.C. Solomon, E. Mazarico, F. Vilas. Characterization of the morphometry of impact craters hosting polar deposits in Mercury's north polar region. J. Geophys. Res., 117 (2012), Article E00L13, 10.1029/2012JE004155.

B.J. Thomson, D.B.J. Bussey, C.D. Neish, J.T.S. Cahill, E. Heggy, R.L. Kirk, G.W. Patterson, R.K. Raney, P.D. Spudis, T.W. Thompson, E.A. Ustinov. An upper limit for ice in Shackleton crater as revealed by LRO Mini-RF orbital radar. Geophys. Res. Lett., 39 (2012), Article L14201, 10.1029/2012GL052119.

A.R. Vasavada, D.A. Paige, S.E. Wood. Near-surface temperatures on Mercury and the Moon and the stability of polar ice deposits. Icarus, 141 (1999), pp. 179-193, 10.1006/icar.1999.6175.

N.H. Warner, S. Gupta, F. Calef, P. Grindrod, N. Boll, K. Goddard. Minimum effective area for high resolution crater counting of martian terrains. Icarus, 245 (2015), pp. 198-240, 10.1016/j.icarus.2014.09.024.

J.-P. Williams, C.H. van der Bogert, A.V. Pathare, G.G. Michael, M.R. Kirchoff, H. Hiesinger. Dating very young planetary surfaces from crater statistics: a review of issues and challenges. Meteorit. Planet. Sci., 53 (2018), pp. 554-582, 10.1111/maps.12924.

J.A. Zhang, D.A. Paige. Correction to “Cold-trapped organic compounds at the poles of the Moon and Mercury: implications for origins”. Geophys. Res. Lett., 37 (2010), Article L03203, 10.1029/2009GL041806.

M.T. Zuber, J.W. Head, D.E. Smith, G.A. Neumann, E. Mazarico, M.H. Torrence, O. Aharonson, A.R. Tye, C.I. Fassett, M.A. Rosenburg, H.J. Melosh. Constraints on the volatile distribution within Shackleton crater at the lunar south pole. Nature, 486 (2012), pp. 378-381, 10.1038/nature11216.

Table 1. Craters hosting water-ice deposits that do and do not have small craters identified as superposing the ice on the basis of high-reflectance ejecta rings.

Host craters identified as having superposing craters from high-reflectance ejecta rings			
Host crater	Ensor	Laxness	Bechet
Diameter (km)	25	26	18
Location	82.3°N, 342.5°E	83.3°N, 310.0°E	83.1°N, 266.3°E
Absolute model ages (Ma) of surfaces derived from crater-counting statistics†	210 ± 60* 23 ± 6** 8.4 ± 2***	29 ± 10* 5.1 ± 5** 1.5 ± 0.5***	47 ± 20* 7.9 ± 3** 2.7 ± 1***
Estimated likely ages (Ma) of surfaces calculated from Poisson statistics	137 ± 15	100 ± 18	81 ± 19
Count area (km^2)	109	79	86
Total craters superposing ice	17	8	6
Host craters identified as not having any superposing craters from high-reflectance ejecta rings			
Host crater	Despréz	Fuller	V2
Diameter (km)	47	27	18
Location	81.1°N, 258.8°E	82.6°N, 317.4°E	80.3°N, 293.2°E
Estimated likely ages (Ma) of surfaces calculated from Poisson statistics	<10 ± 1 Myr	<10 ± 1 Myr	<10 ± 1 Myr

†Reported errors are 1- σ from the mean.
*Crater diameters used in crater-counting statistics are the diameters measured from images.
**Crater diameters are scaled by ½ to represent possible sizes of craters impacting into pure ice (Croft et al., 1979; Koschny and Grün, 2001).
*** Crater diameters are scaled by 1/3 to represent the minimum possible sizes of craters impacting into pure ice (Croft et al., 1979; Koschny and Grün, 2001).

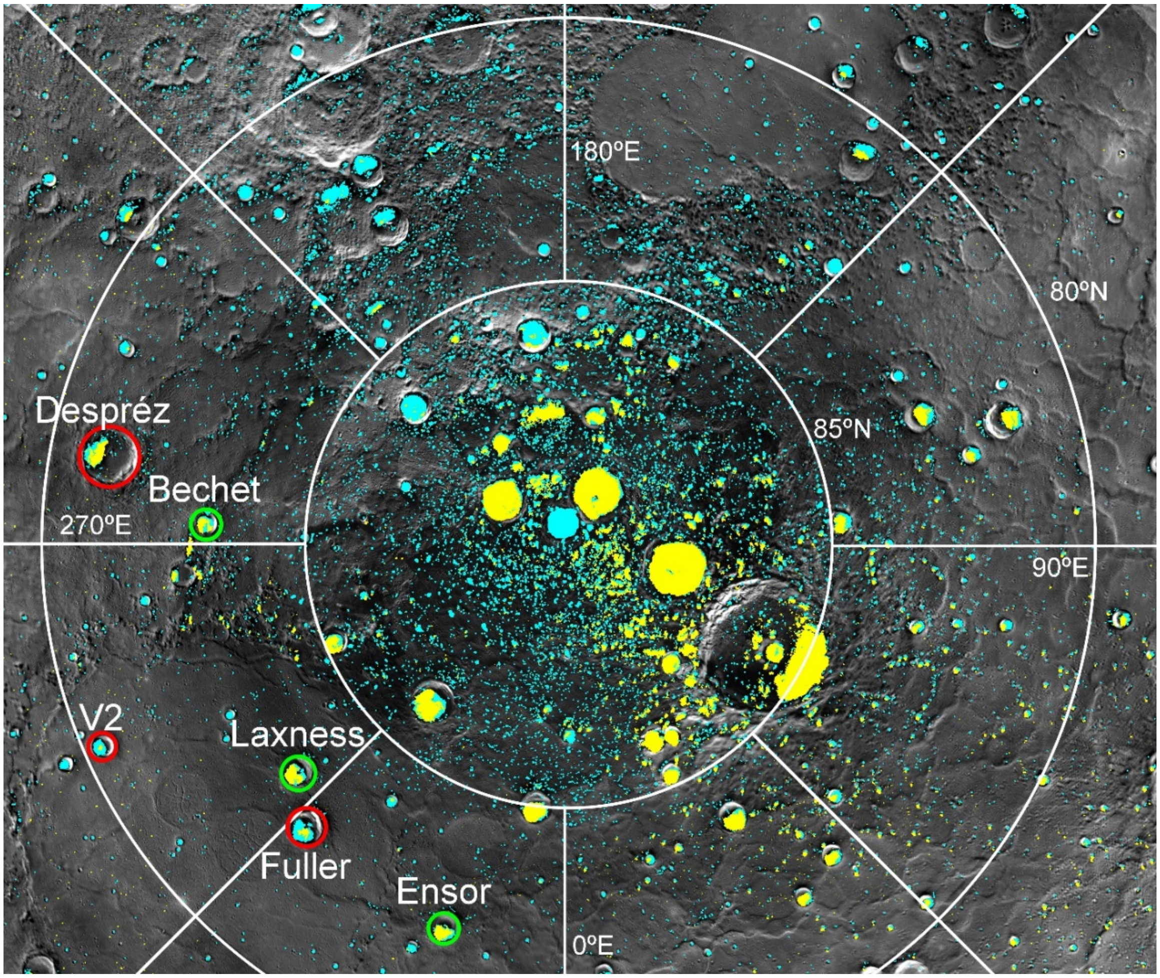

Figure 1. Water-ice deposits located at the north polar region on Mercury. Distribution of water ice at the north polar region of Mercury from 80°–90°N. Regions of permanent shadow (Deutsch et al., 2016) are shown in blue and radar-bright materials (Harmon et al., 2011) are shown in yellow. Host craters identified as having craters associated with high-reflectance rings in their PSRs are circled in green and host craters identified as lacking craters associated with high-reflectance rings are circled in red.

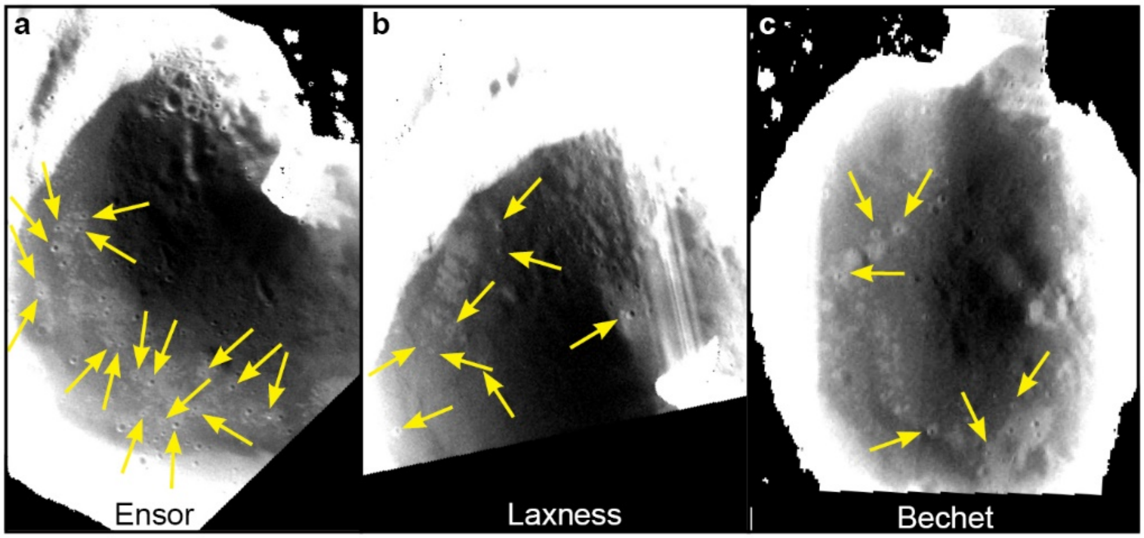

Figure 2. Brightness variations associated with impact craters suggest these impact craters superpose the ice deposits on Mercury. Low-altitude WAC broadband images reveal the interiors of (a) Ensor crater (25 km diameter; 82.3°N, 342.5°E), (b) Laxness crater (26 km diameter; 83.3°N, 310.0°E), and (c) Bechet crater (18 km diameter; 83.1°N, 266.3°E). Yellow arrows point to small craters (100–300 m in diameter) in the PSRs associated with high-reflectance material.

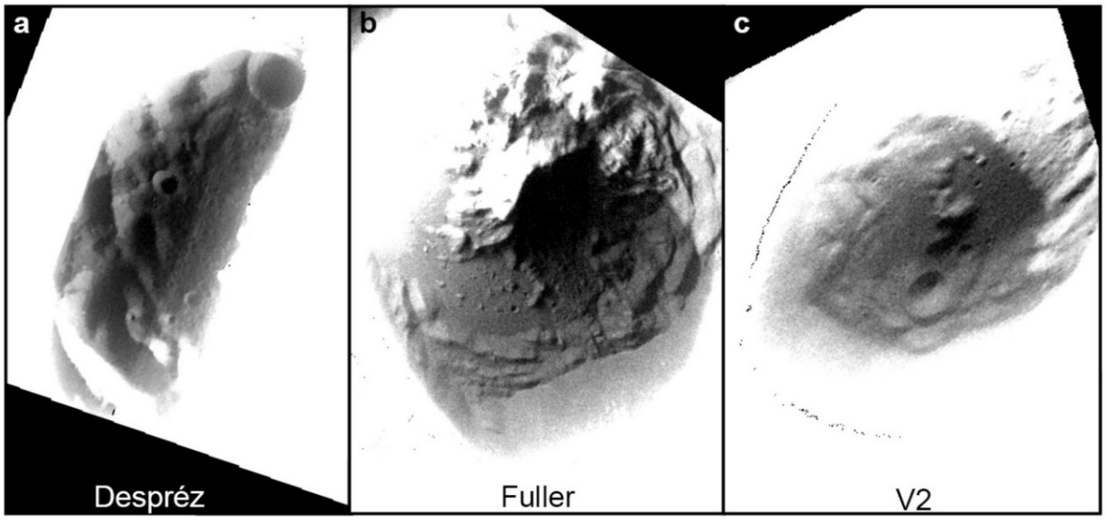

Figure 3. The lack of high-reflectance rings associated with impact craters suggests that no craters superpose these ice deposits. Low-altitude WAC broadband images reveal the interiors of (a) Despréz crater (47 km diameter; 81.1°N, 258.8°E), (b) Fuller crater (27 km diameter; 82.6°N, 317.4°E), and (c) V2 crater (18 km diameter; 80.3°N, 293.2°E). None of the craters in the PSRs is associated with high-reflectance material.

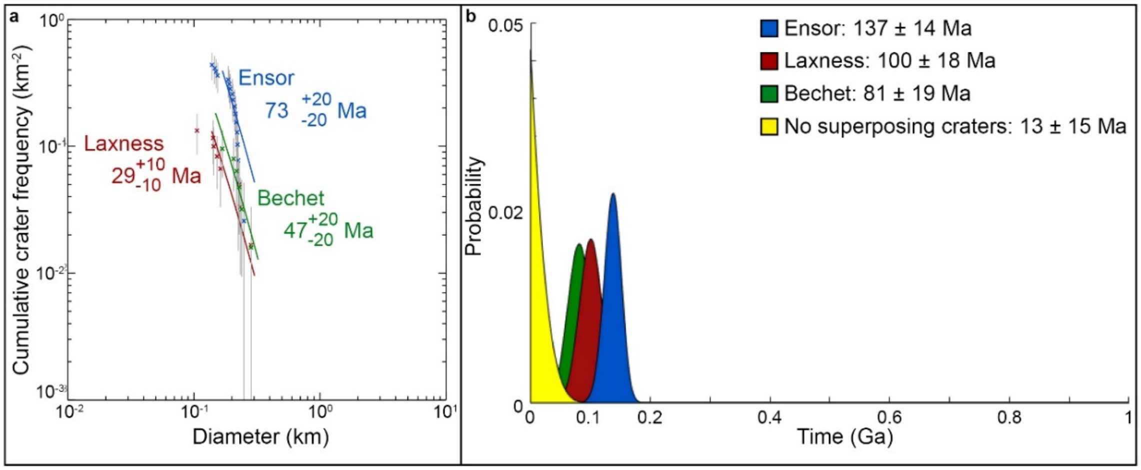

Figure 4. Estimated surface ages of water-ice deposits on Mercury are relatively young. a, Crater size-frequency distributions of ice deposits hosted by Ensor (blue), Laxness (red), and Bechet (green) craters. Crater counts include all craters >100 m that occur within permanently shadowed, radar-bright deposits and that are associated with high-reflectance rings suggestive of ejected material. b, Estimated ages of the ice surfaces hosted by Ensor (blue), Laxness (red), Bechet (green), and of an ice surface with no superposing craters (yellow). The probability distribution is calculated for 0.001 Gyr time intervals, and represents the likelihood (y-axis) that each surface has a particular age (x-axis).

Supporting material

Table S1. Images analyzed to identify the presence or absence of craters that superpose ice deposits.

Host craters identified as having superposing craters from high-reflectance ejecta rings			
Host crater	Ensor	Laxness	Bechet
Diameter (km)	25	26	18
Location	82.3°N, 342.5°E	83.3°N, 310.0°E	83.1°N, 266.3°E
Images analyzed (pixel resolution)	EW1051458815B (37.6 m) EW1067153761B (64.5 m) EW1046946306B (90.3 m)	EW1052529039B (46.1 m) EW1052586891B (48.0 m) EW1067392056B (55.2) EW1067451645B (57.4 m)	EW1068017656B (55.0 m) EW1068077244B (58.0 m) EW1053138269B (71.5 m) EW1052528979B (32.8 m) EW1068107038B (59.2 m) EW1068136833B (60.6 m)
Count area (km^2)	109	79	86
Total craters superposing ice	17	8	6
Diameters of superposed craters (km)	0.15 0.15 0.17 0.19 0.19 0.19 0.20 0.20 0.20 0.20 0.20 0.22 0.22 0.22 0.24 0.27 0.27	0.11 0.14 0.14 0.15 0.16 0.22 0.23 0.28	0.17 0.21 0.22 0.23 0.24 0.29
Host craters identified as not having any superposing craters from high-reflectance ejecta rings			
Host crater	Despréz	Fuller	V2
Diameter (km)	47	27	18
Location	81.1°N, 258.8°E	82.6°N, 317.4°E	80.3°N, 293.2°E

Images analyzed (pixel resolution)	EW1068404967B (70.7 m)	EW1067451658B (61.0 m)	EW1051776921B (24.3 m)
	EW1068434759B (71.0 m)	EW1047206595B (44.2 m)	EW1063405740B (45.7 m)
	EW1068732711B (40.4 m)	EW1051950532B (37.7 m)	EW1067123879B (41.9 m)
	EW1067540944B (38.4 m)	EW1062636818B (44.5 m)	EW1068017709B (37.7 m)

The following supporting material documents images analyzed to identify the presence or absence of craters that superpose ice deposits.

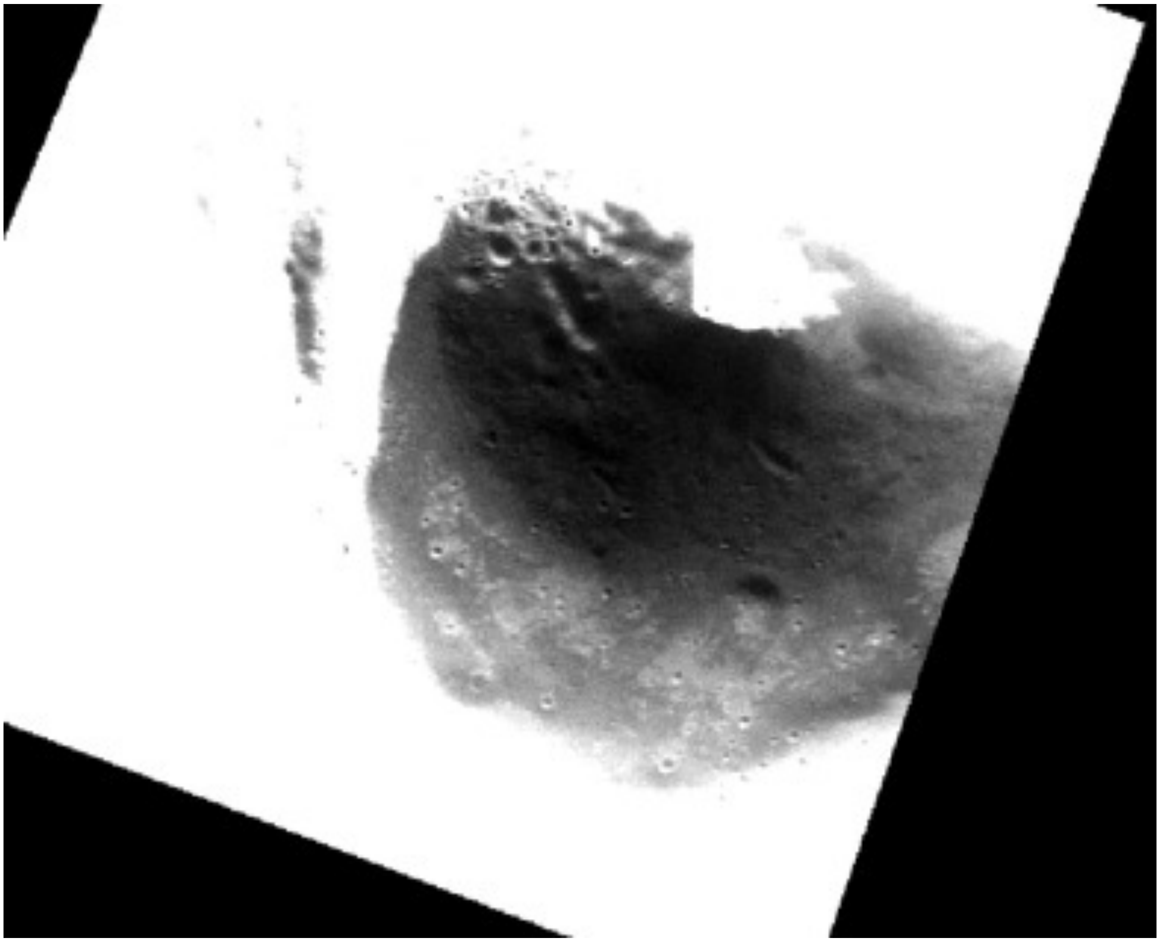

Figure S1. Stretched WAC image EW1051458815B (pixel resolution of 37.6 m) reveals the permanently shadowed interior of Ensor (82.3°N, 342.5°E).

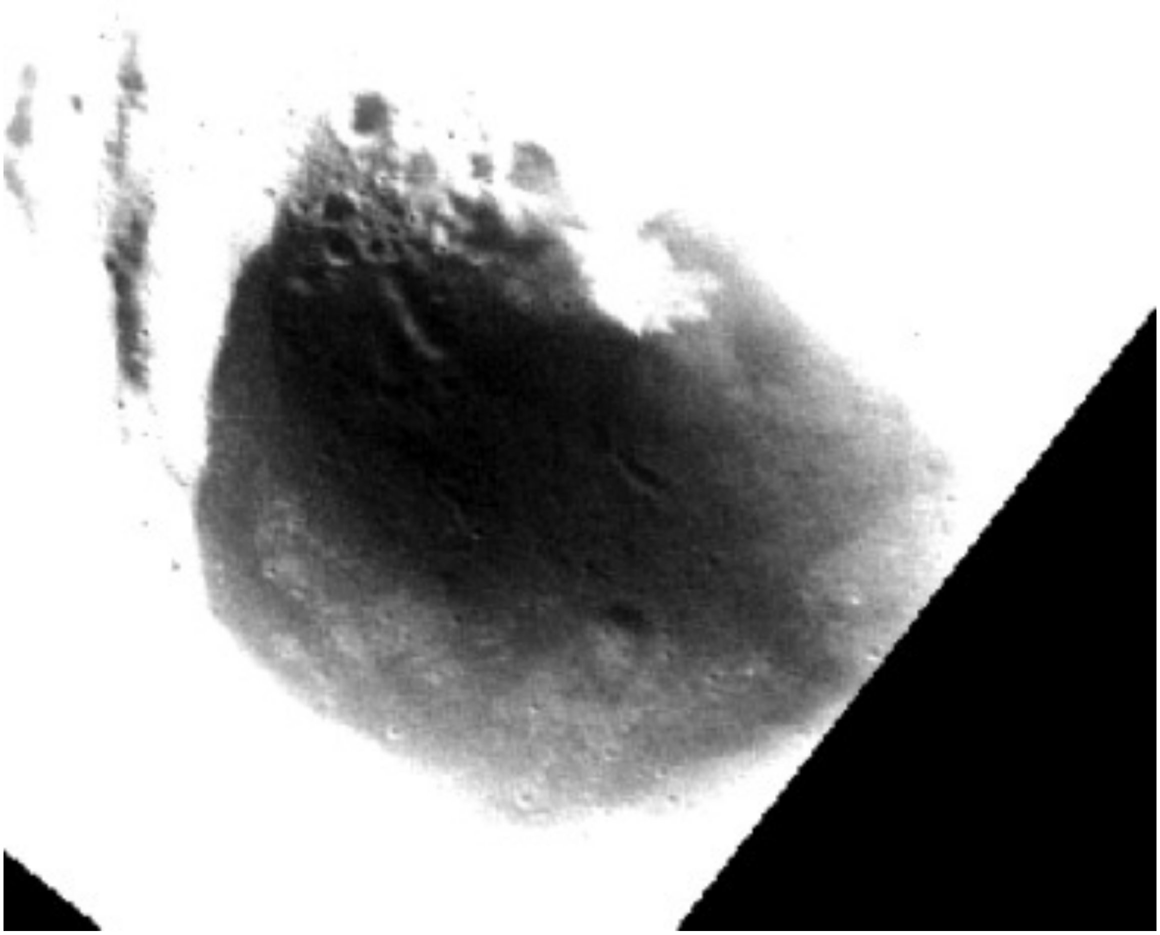

Figure S2. Stretched WAC image EW1067153761B (pixel resolution of 64.5 m) reveals the permanently shadowed interior of Ensor (82.3°N, 342.5°E).

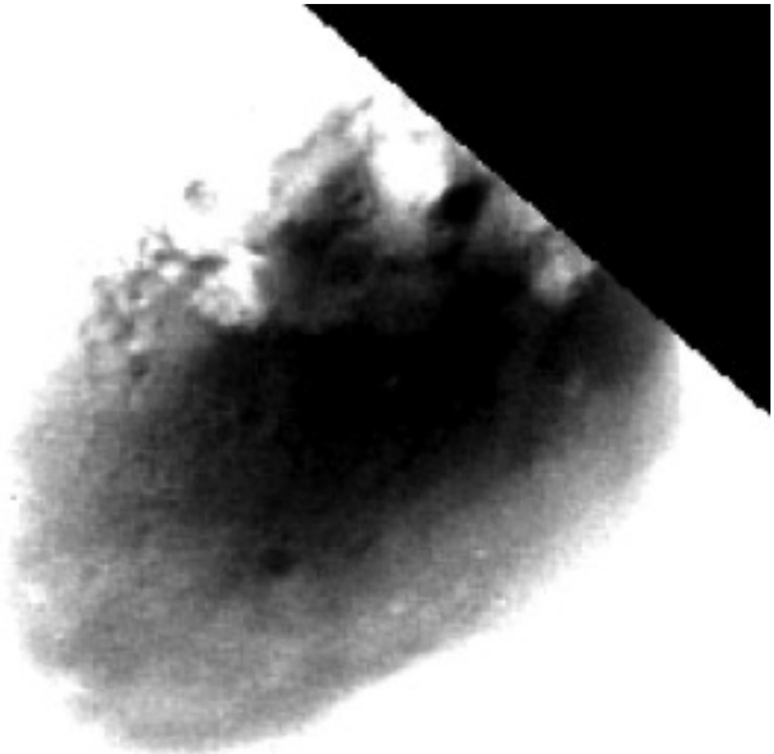

Figure S3. Stretched WAC image EW1046946306B (pixel resolution of 90.3 m) reveals the permanently shadowed interior of Ensor (82.3°N, 342.5°E).

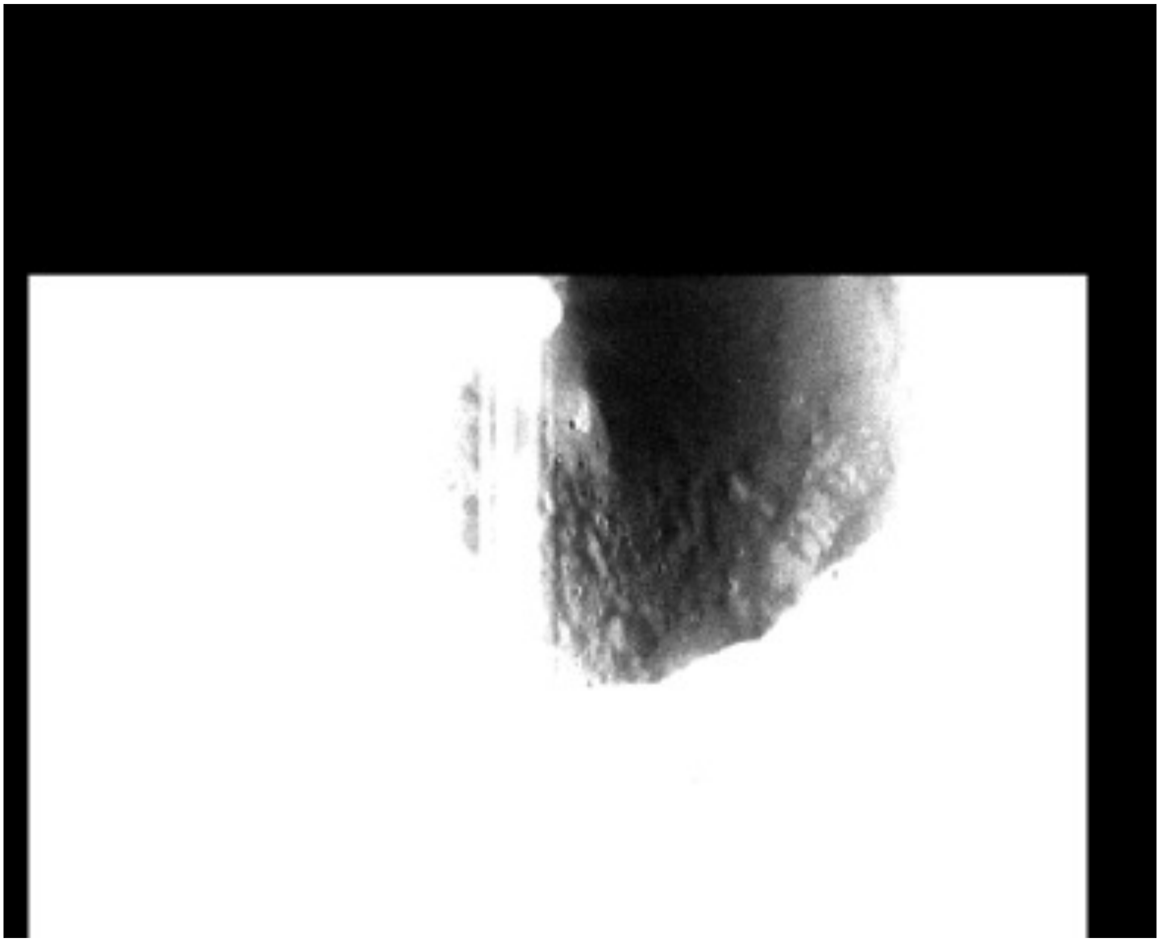

Figure S4. Stretched WAC image EW1052529039B (pixel resolution of 46.1 m) reveals the permanently shadowed interior of Laxness (83.3°N, 310.0°E).

Figure S5. Stretched WAC image EW1052586891B (pixel resolution of 48.0 m) reveals the permanently shadowed interior of Laxness (83.3°N, 310.0°E).

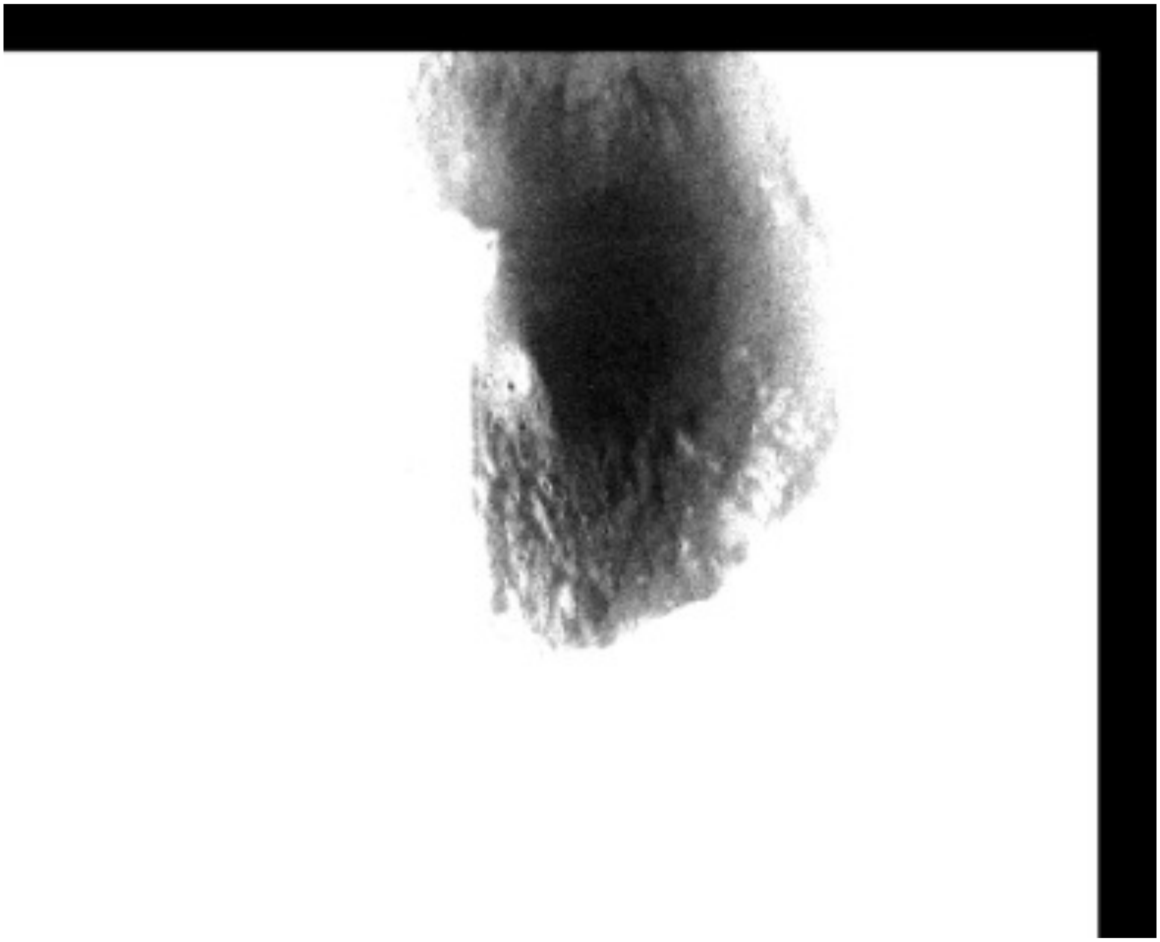

Figure S6. Stretched WAC image EW1067392056B (pixel resolution of 52.2 m) reveals the permanently shadowed interior of Laxness (83.3°N, 310.0°E).

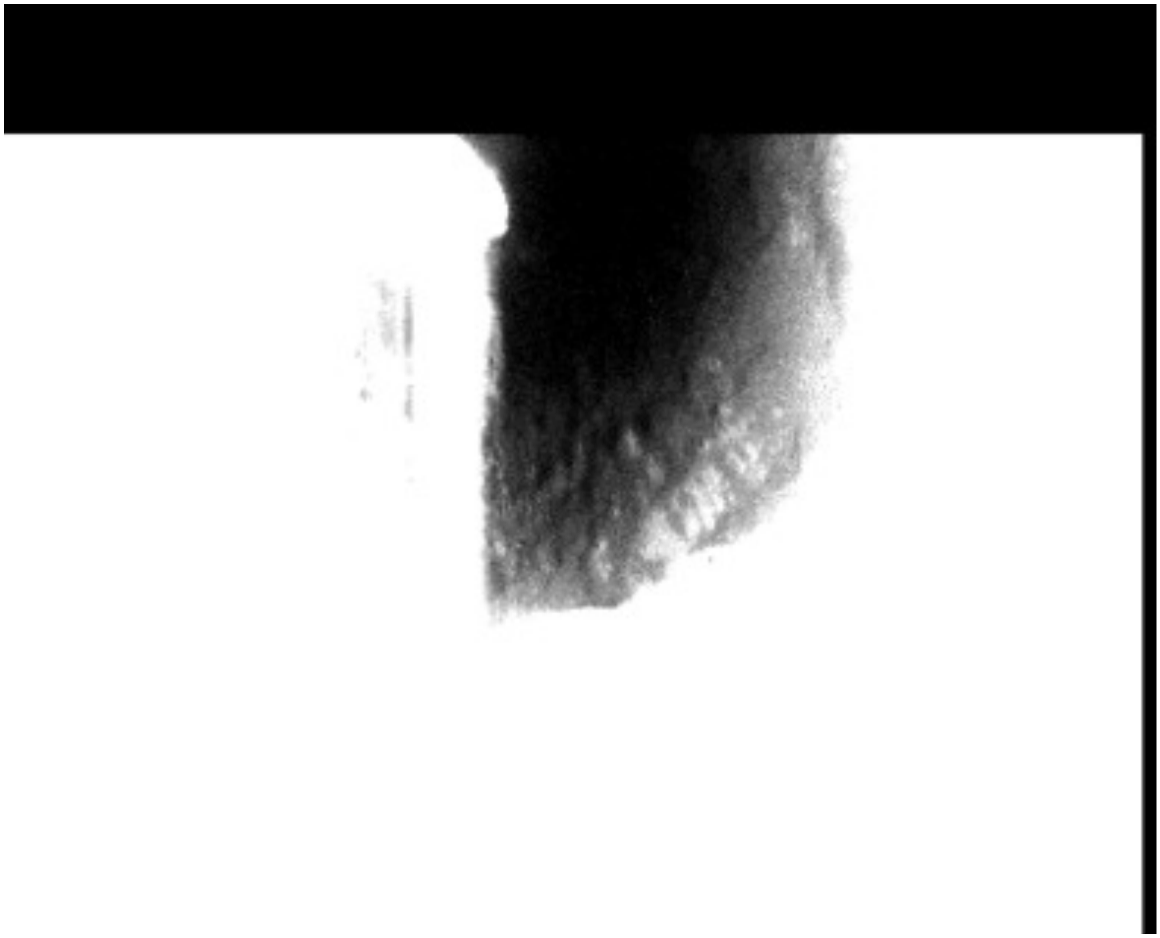

Figure S7. Stretched WAC image EW1067451645B (pixel resolution of 57.4 m) reveals the permanently shadowed interior of Laxness (83.3°N, 310.0°E).

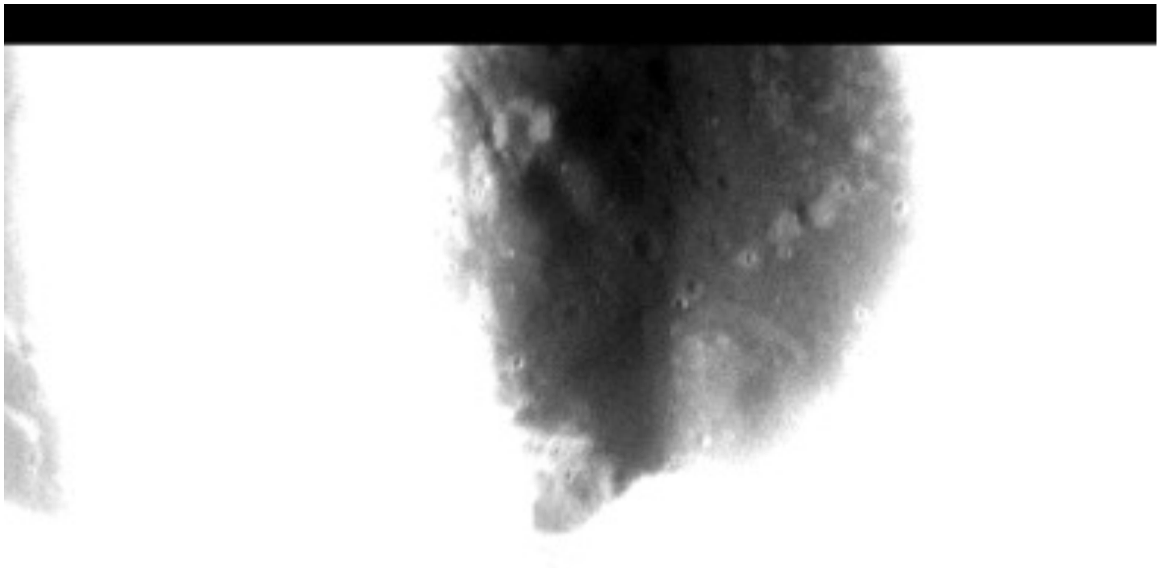

Figure S8. Stretched WAC image EW1068017656B (pixel resolution of 55.0 m) reveals the permanently shadowed interior of Bechet (83.1°N, 266.3°E).

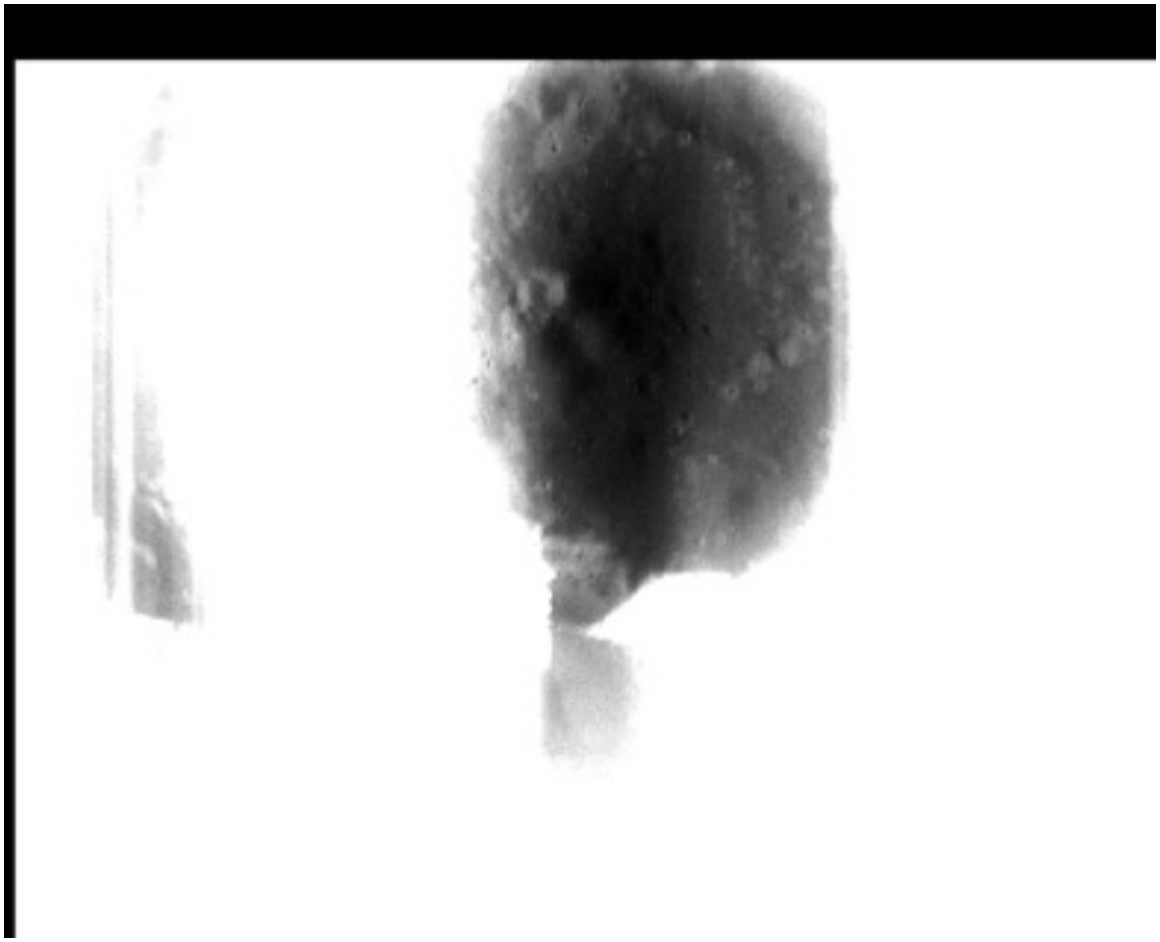

Figure S9. Stretched WAC image EW1068077244B (pixel resolution of 58.0 m) reveals the permanently shadowed interior of Bechet (83.1°N, 266.3°E).

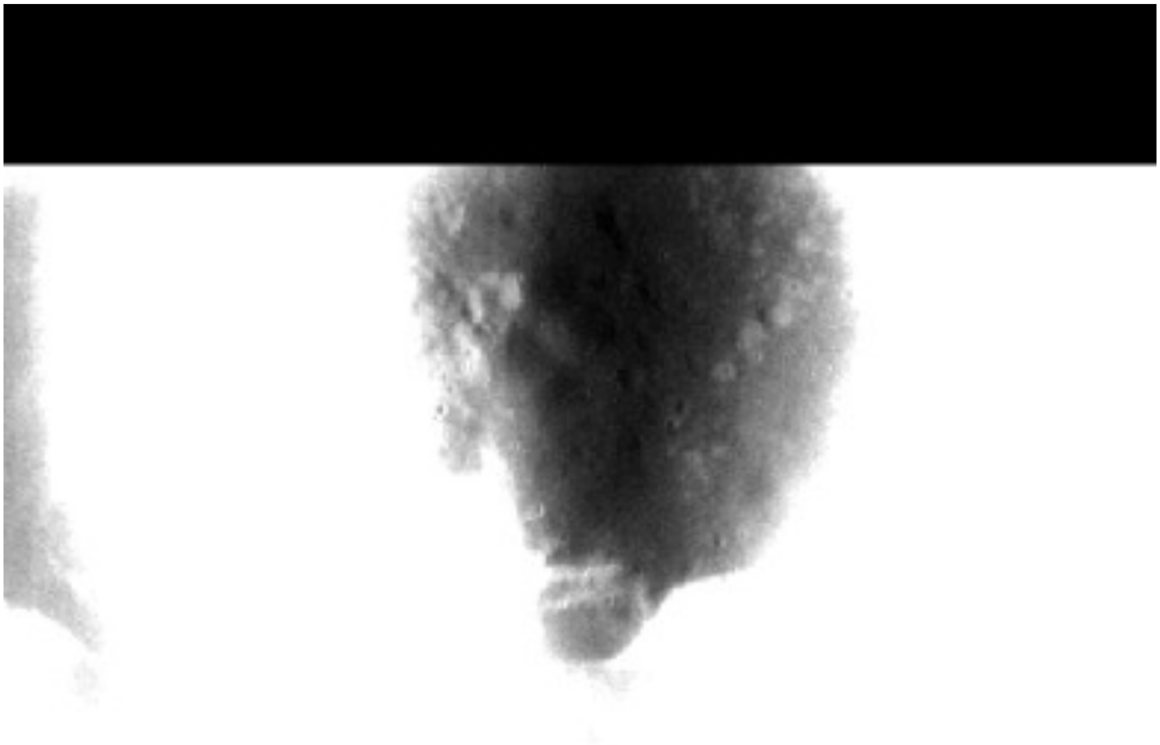

Figure S10. Stretched WAC image EW1053138269B (pixel resolution of 71.5 m) reveals the permanently shadowed interior of Bechet (83.1°N, 266.3°E).

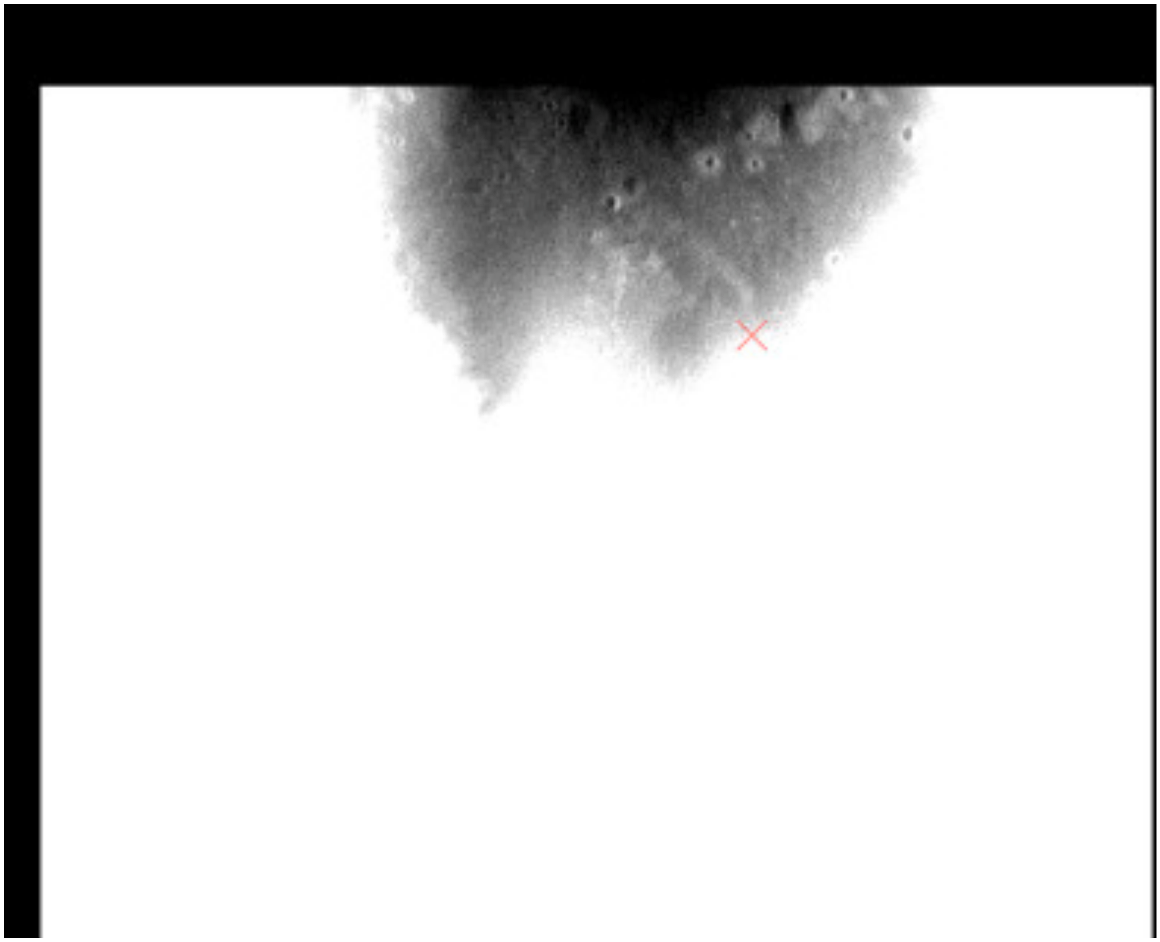

Figure S11. Stretched WAC image EW1052528979B (pixel resolution of 32.8 m) reveals the permanently shadowed interior of Bechet (83.1°N, 266.3°E).

Figure S12. Stretched WAC image EW1068107038B (pixel resolution of 59.2 m) reveals the permanently shadowed interior of Bechet (83.1°N, 266.3°E).

Figure S13. Stretched WAC image EW1068136833B (pixel resolution of 60.6 m) reveals the permanently shadowed interior of Bechet (83.1°N, 266.3°E).

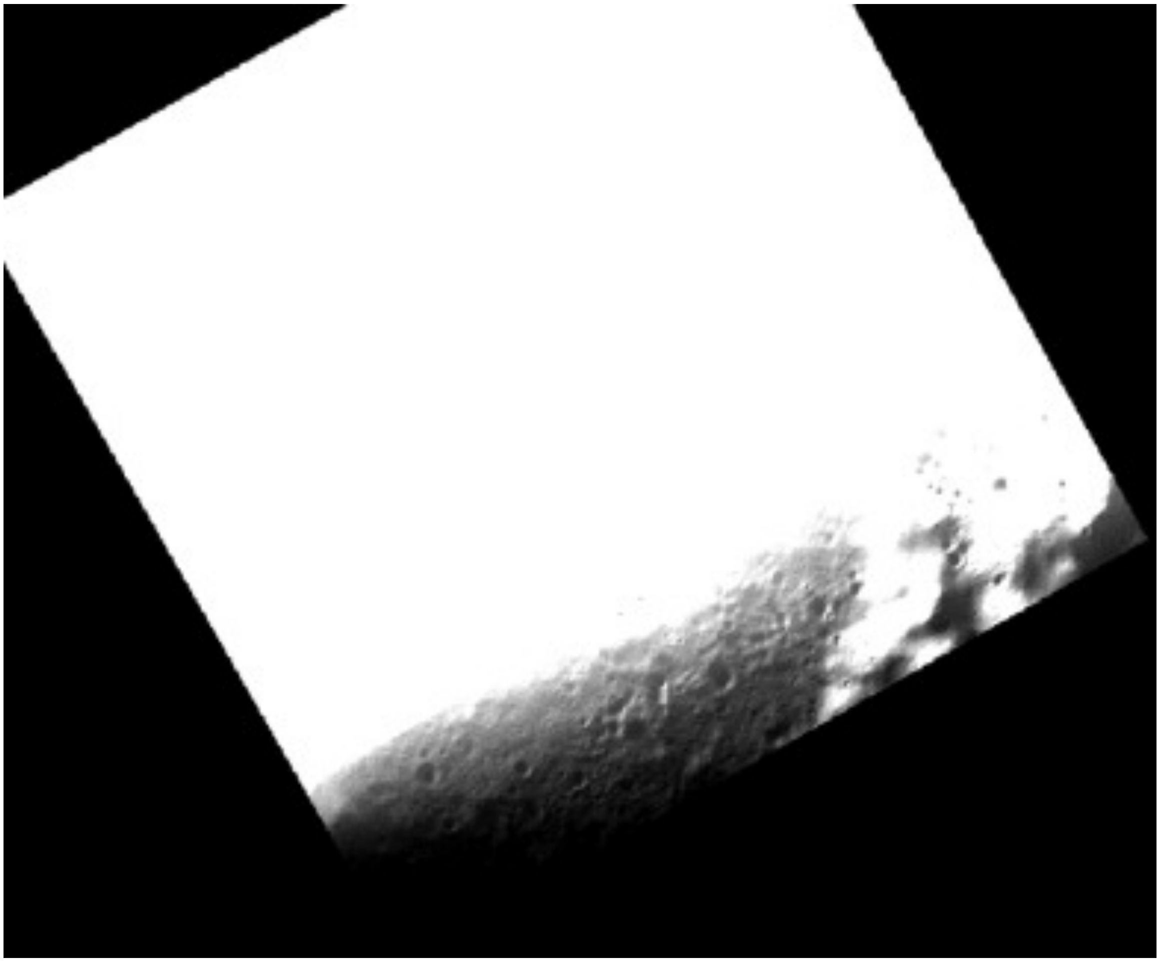

Figure S14. Stretched WAC image EW1067540944B (pixel resolution of 38.4 m) reveals the permanently shadowed interior of Despréz (81.1°N, 258.8°E).

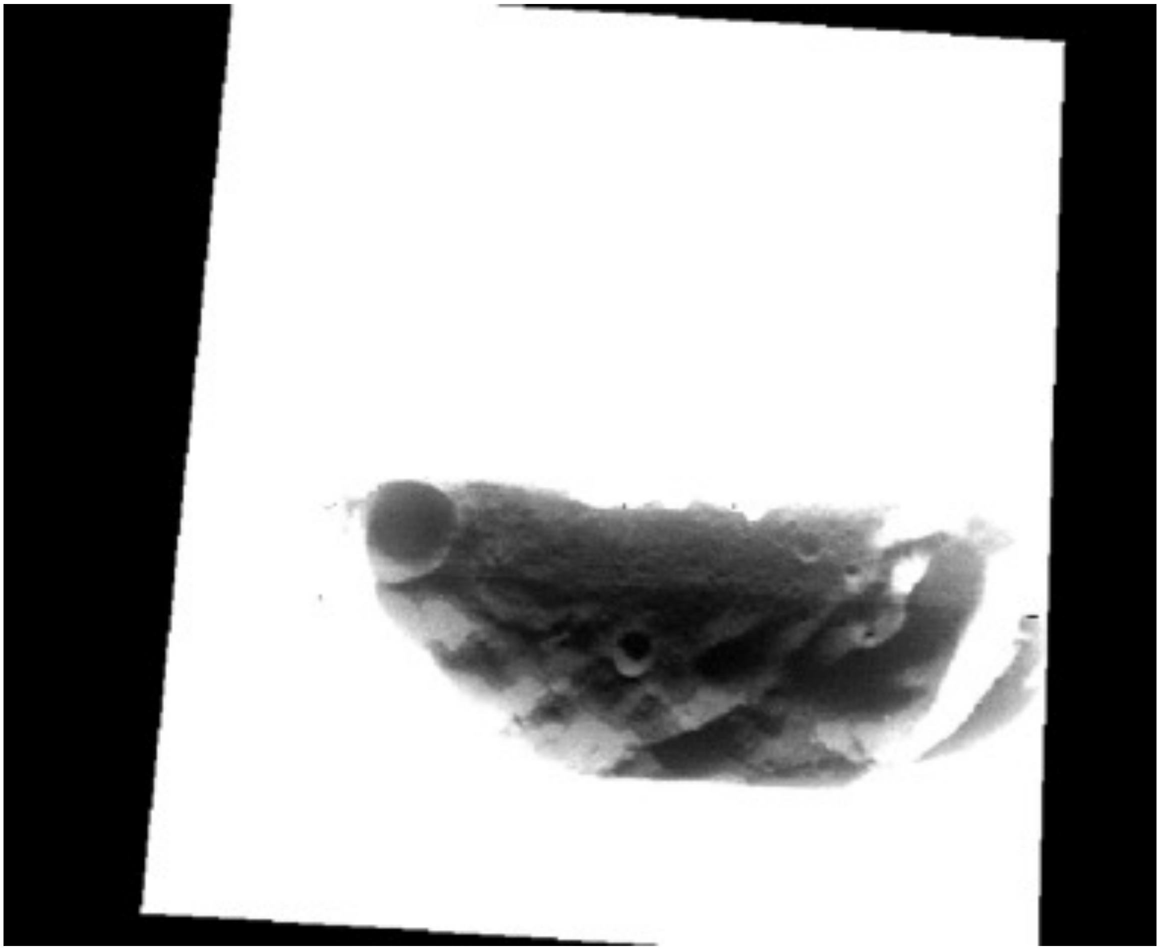

Figure S15. Stretched WAC image EW1068404967B (pixel resolution of 70.7 m) reveals the permanently shadowed interior of Despréz (81.1°N, 258.8°E).

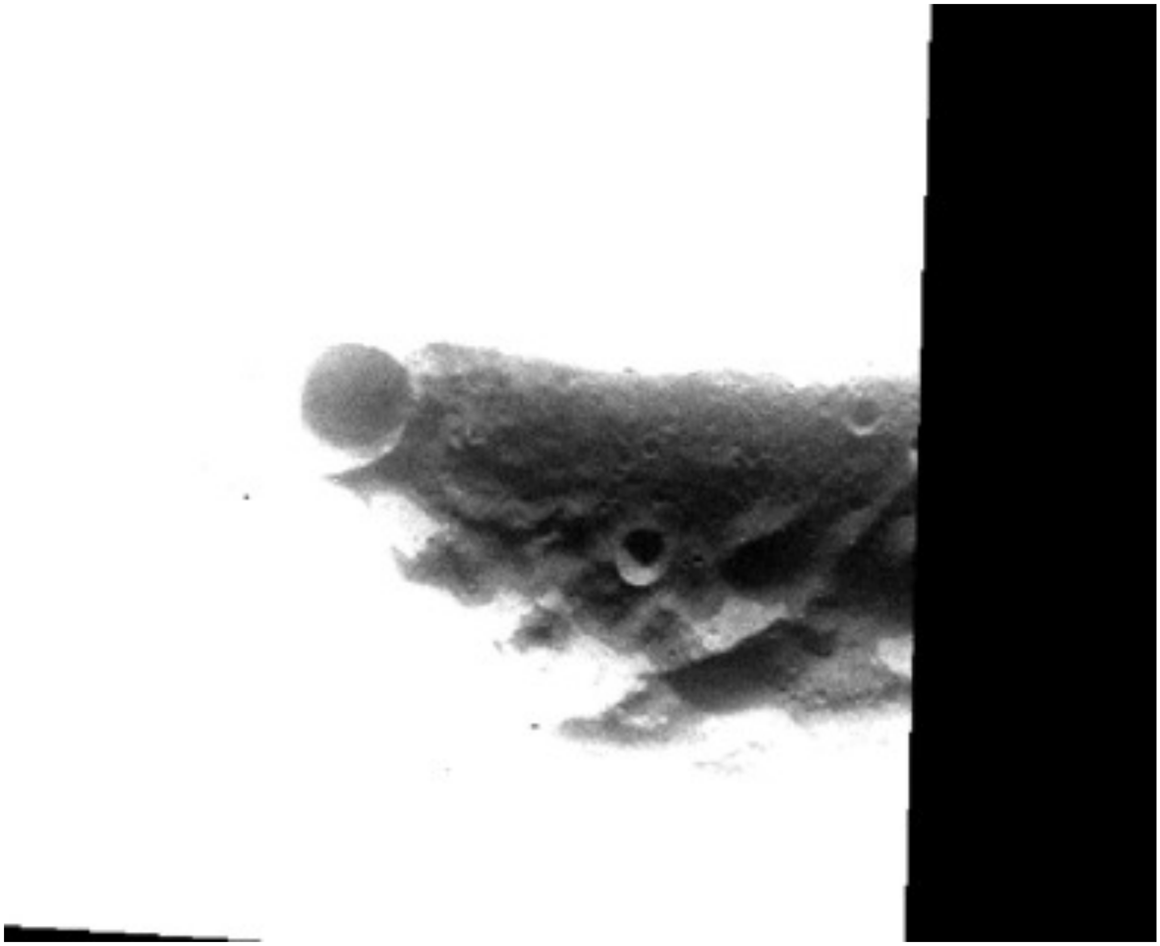

Figure S16. Stretched WAC image EW1068434759B (pixel resolution of 71.0 m) reveals the permanently shadowed interior of Despréz (81.1°N, 258.8°E).

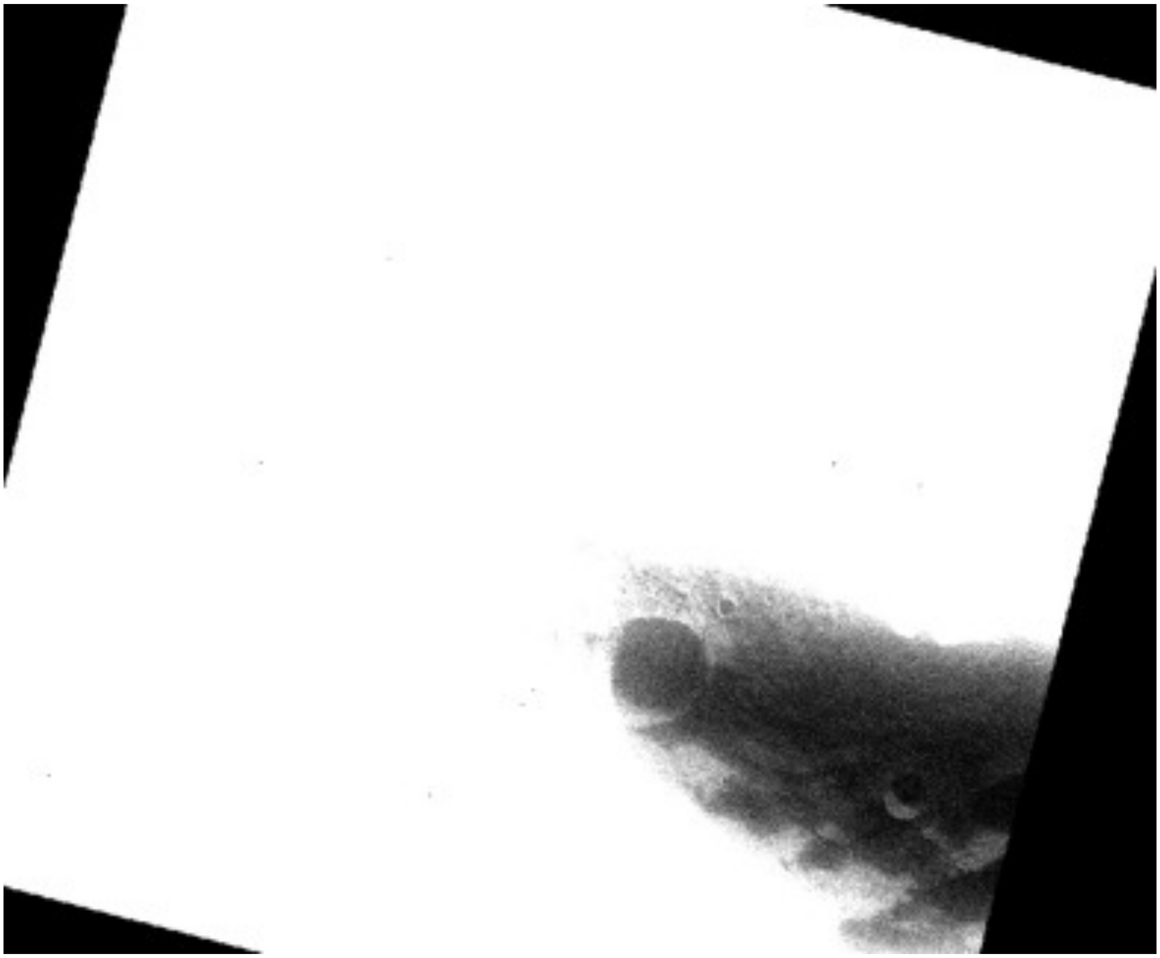

Figure S17. Stretched WAC image EW1068732711B (pixel resolution of 40.4 m) reveals the permanently shadowed interior of Despréz (81.1°N, 258.8°E).

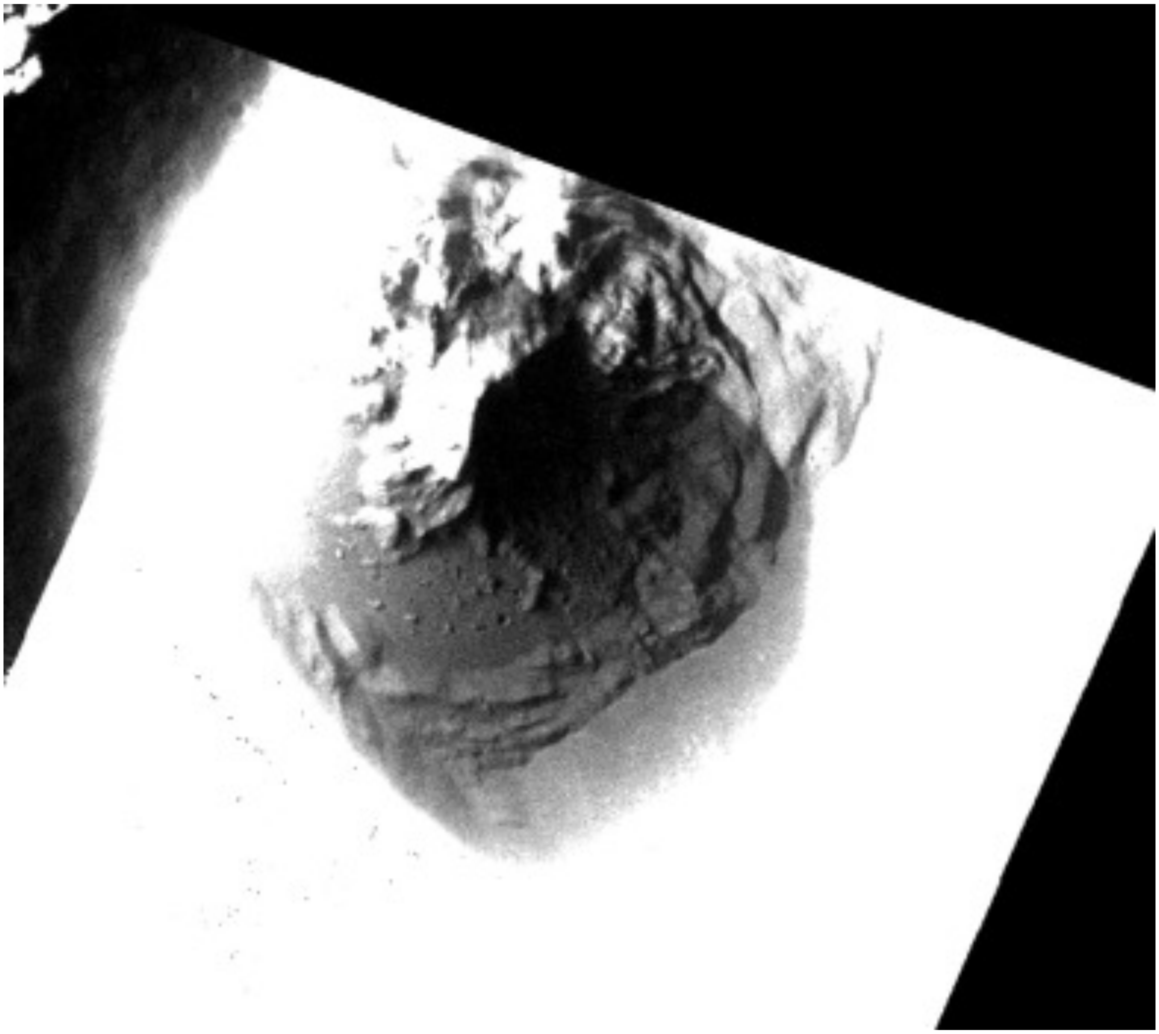

Figure S18. Stretched WAC image EW1047206595B (pixel resolution of 44.2 m) reveals the permanently shadowed interior of Fuller (82.6°N, 317.4°E).

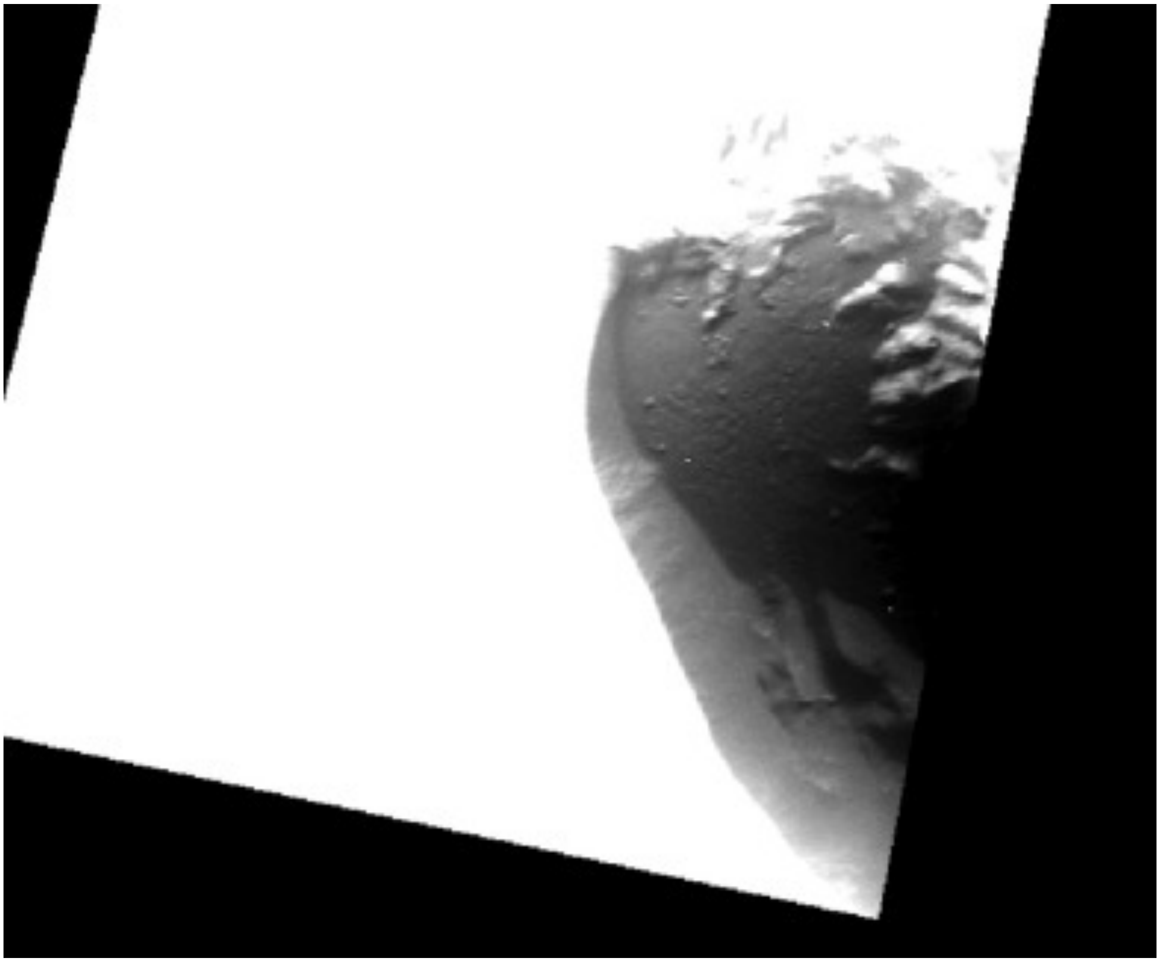

Figure S19. Stretched WAC image EW1051950532B (pixel resolution of 37.7 m) reveals the permanently shadowed interior of Fuller (82.6°N, 317.4°E).

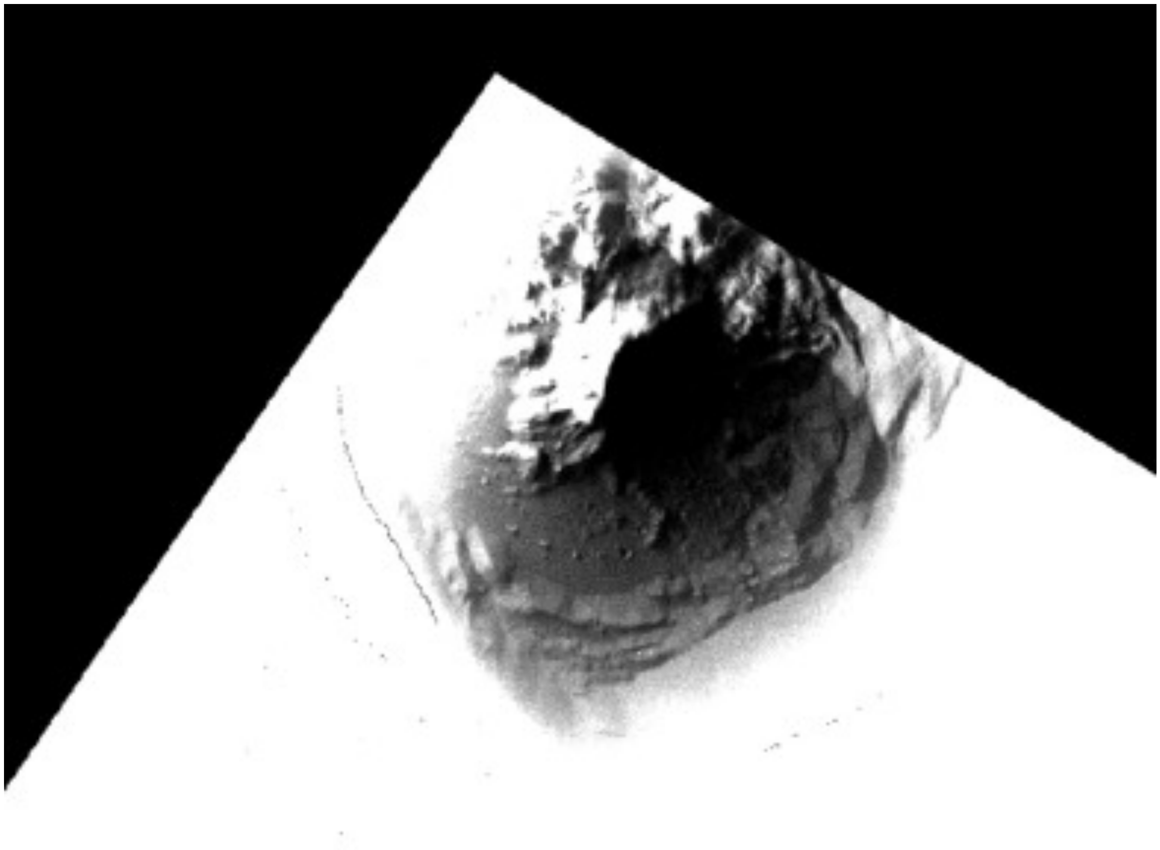

Figure S20. Stretched WAC image EW1062636818B (pixel resolution of 44.5 m) reveals the permanently shadowed interior of Fuller (82.6°N, 317.4°E).

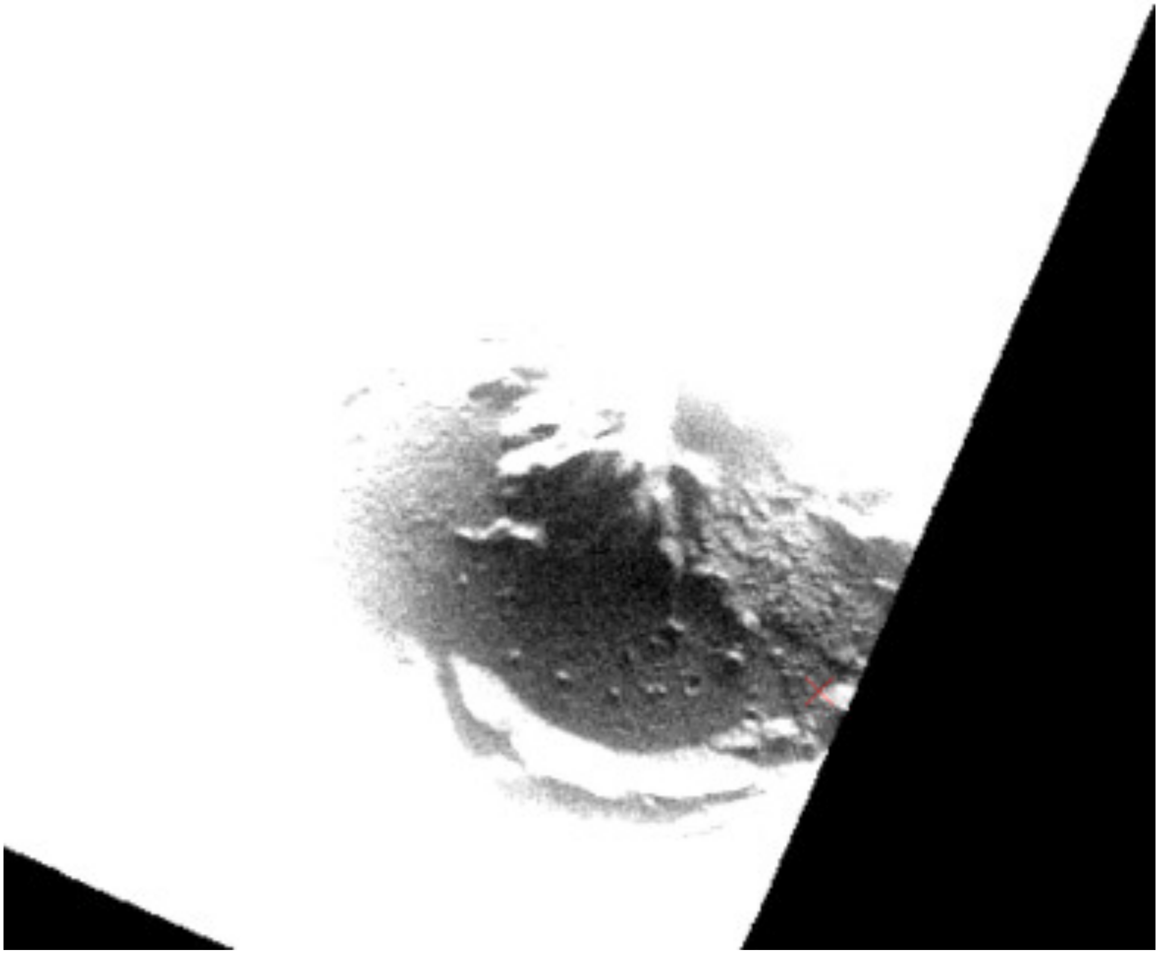

Figure S21. Stretched WAC image EW1067451658B (pixel resolution of 61.0 m) reveals the permanently shadowed interior of Fuller (82.6°N, 317.4°E).

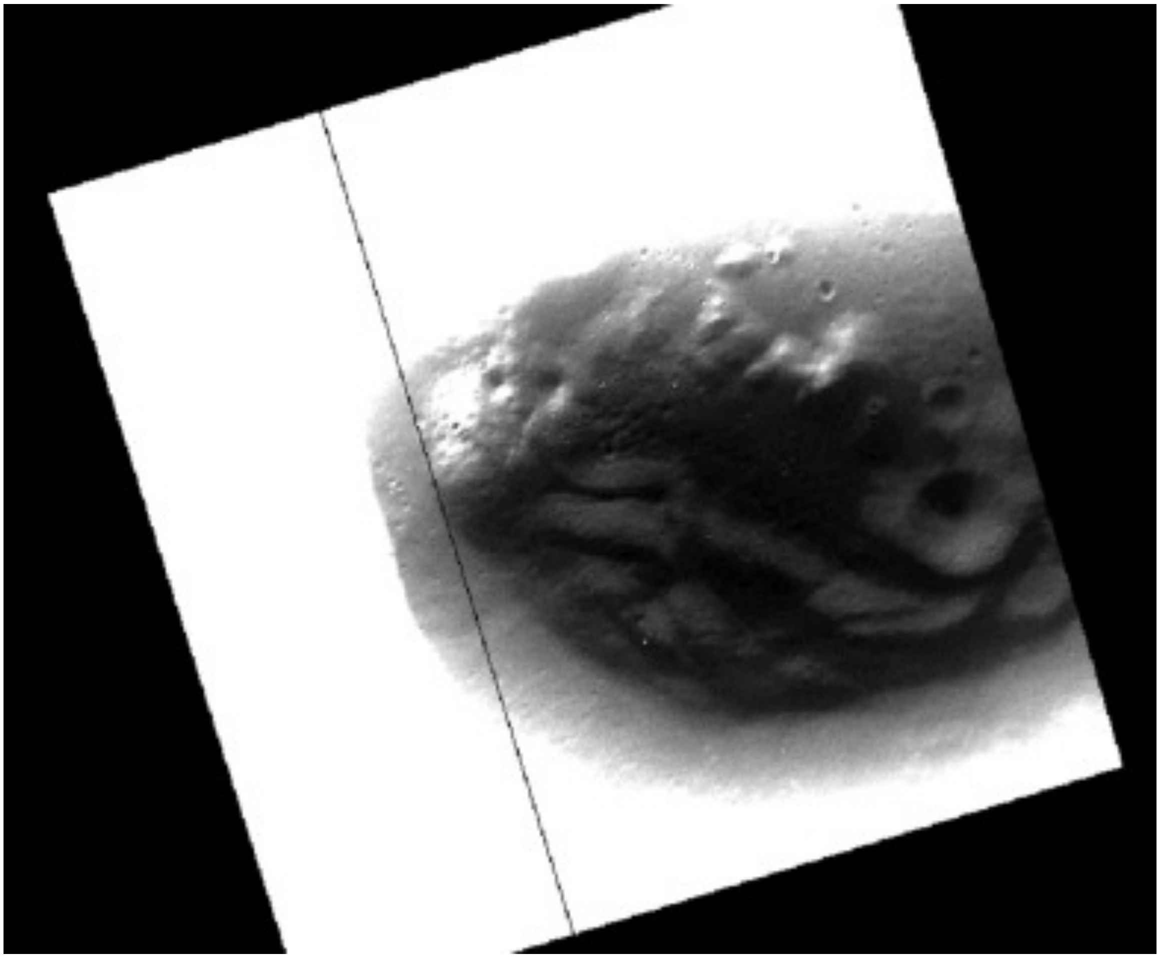

Figure S22. Stretched WAC image EW1051776921B (pixel resolution of 24.3 m) reveals the permanently shadowed interior of V2 (80.3°N, 293.2°E).

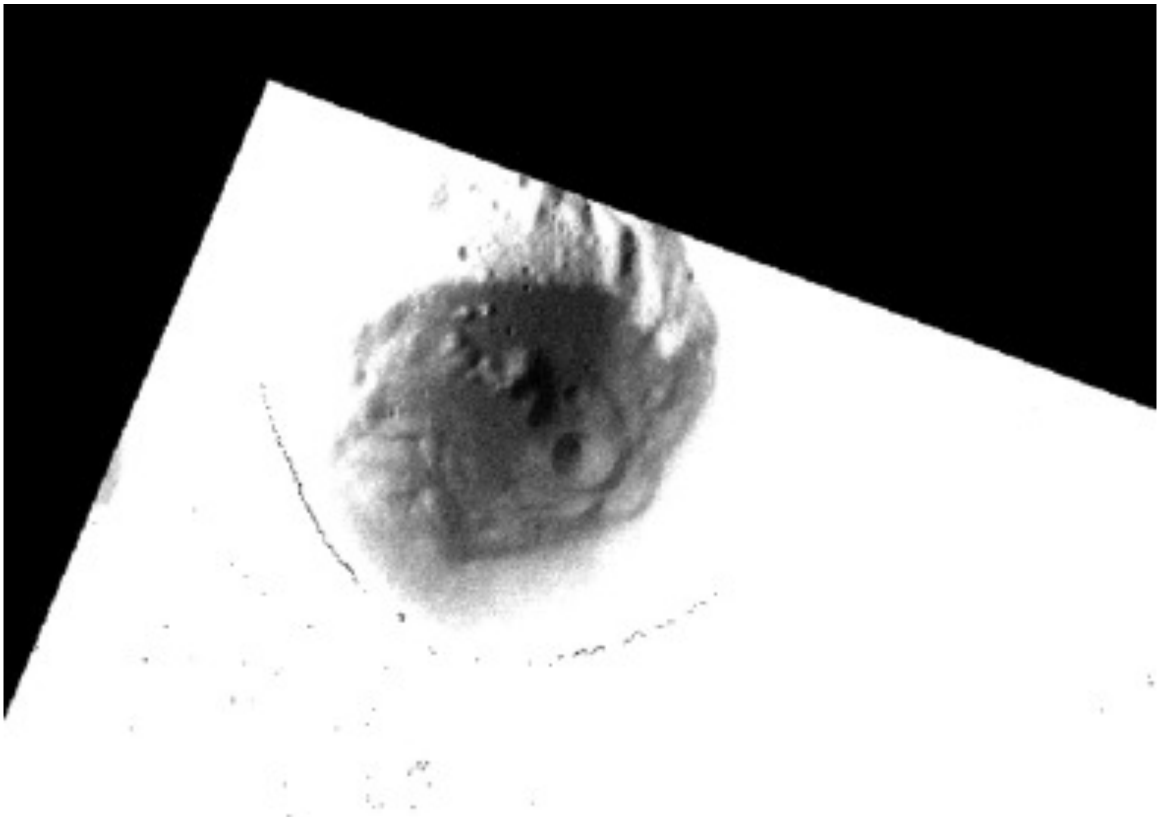

Figure S23. Stretched WAC image EW1063405740B (pixel resolution of 45.7 m) reveals the permanently shadowed interior of V2 (80.3°N, 293.2°E).

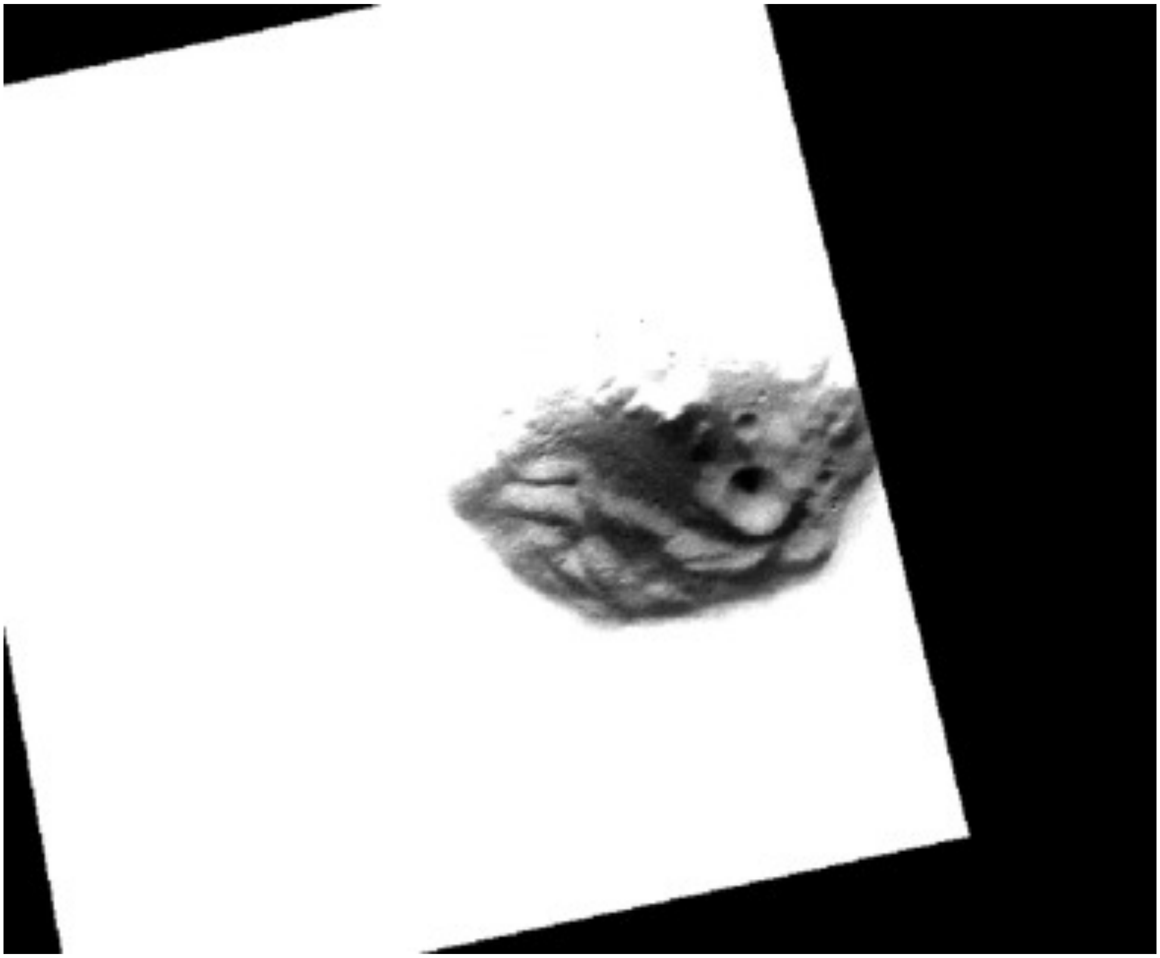

Figure S24. Stretched WAC image EW1067123879B (pixel resolution of 41.9 m) reveals the permanently shadowed interior of V2 (80.3°N, 293.2°E).

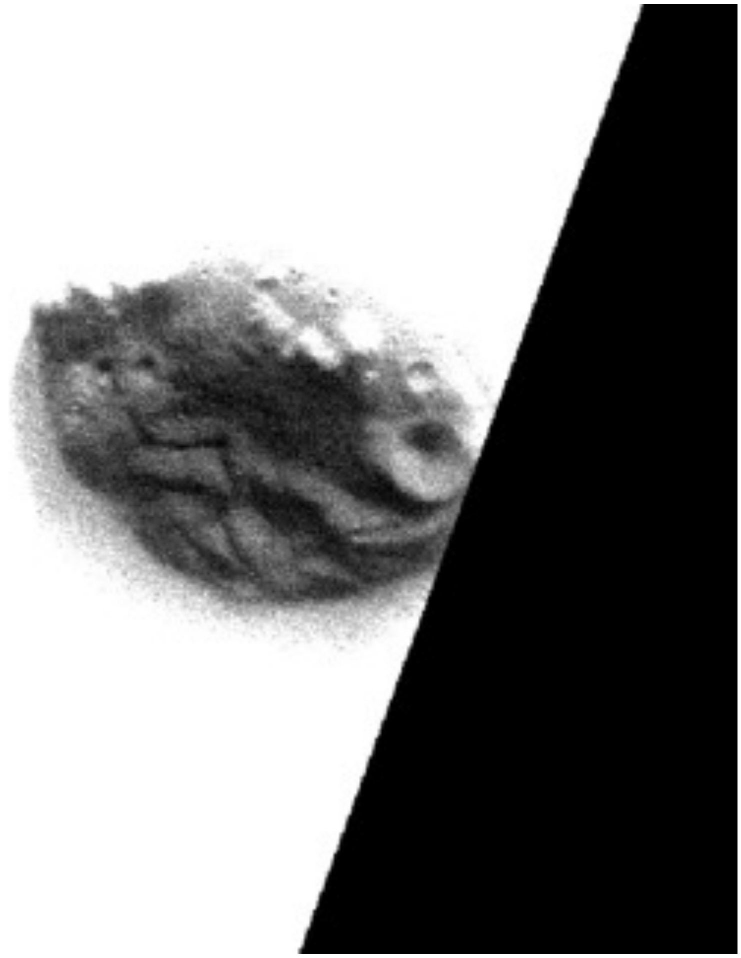

Figure S25. Stretched WAC image EW1068017709B (pixel resolution of 37.7 m) reveals the permanently shadowed interior of V2 (80.3°N, 293.2°E).

Chapter 2

Analyzing the ages of south polar craters on the Moon:

Implications for the sources and evolution of surface water ice

Ariel N. Deutsch[a], James W. Head III[a], Gregory A. Neumann[b]

[a]Department of Earth, Environmental and Planetary Sciences, Brown University, Providence, RI 02912, USA

[b]NASA Goddard Space Flight Center, Greenbelt, MD 20771, USA

Published in *Icarus*

Deutsch, A. N., Head, J. W., Neumann, G. A., 2020. Analyzing the ages of south polar craters on the Moon: Implications for the sources and evolution of surface water ice. *Icarus, 336,* 113455, https://doi.org/10.1016/j.icarus.2019.113455.

Abstract

Surface water ice in the permanently shadowed polar regions of the Moon has a patchy surficial distribution and is not found within all available cold-trapping areas. To date it is not well understood when the ice was delivered, which has important implications for the surficial characteristics of the ice as well as for possible delivery mechanisms. Here we present absolute model ages for 20 south polar craters that host surface water ice, providing maximum estimates of the ages of surface ice contained within these craters. We quantify the amount of available cold-trapping surface area that is occupied by water ice in order to examine the relationship between the patchiness of ice within each crater and the age of each host crater. The majority of surface ice is contained in old craters $\geq\sim 3.1$ Gyr, where the majority of cold-trapping area on the pole exists. The ice is these ancient craters is very patchy in surficial distribution, occupying <11.5% of cold-trapping surface area available in individual craters. This patchy distribution of ice in old craters is likely to be due to impact bombardment and regolith overturn within the polar regions. Interestingly, surface ice is also located within smaller craters (<15 km in diameter), whose sharp crater rim crest morphologies suggest that they may be relatively young. Ice in fresh-looking craters suggests that ice has been delivered to the lunar surface more recently, perhaps from micrometeorites or through solar wind interactions with the lunar regolith. Finally, we also analyze a group of ancient craters that does not host surface water ice, even though these craters are present-day cold traps. These specific ancient craters would not have been thermally stable for the cold-trapping of water ice before the onset of true polar wander suggested by Siegler et al. (2016). If true polar wander did

occur on the Moon, then the ages of ice-bearing craters presented here set an upper limit for the age of post-true polar wander hydrogen emplacement of 4.1 ± 0.1 Gyr.

1. Introduction

Due to the small axial tilt of the Moon, there are some regions within impact craters that do not receive any direct sunlight (Arnold, 1979; Mazarico et al., 2011). These shadowed regions are characterized by extremely low surface temperatures that are limited only by heat flow from crater interiors and scattered sunlight reflected from nearby topography (Vasavada et al., 1999; Salvail and Fanale, 1994; Ingersoll et al., 1992). Of both scientific and exploration interests, these low surface temperatures (<110 K) are predicted to be conducive to the cold-trapping of water ice over geologic timescales (Watson et al., 1961; Paige et al., 2010).

Over the last several decades, ground- and spacecraft-based observations have provided data to support the presence of water ice within these permanently shadowed regions (PSRs) at the poles of the Moon. For example, analysis of thermal and epithermal neutron counting rates suggest that the average hydrogen abundance at both poles is 100–150 ppm, and is likely to be buried beneath ~10 cm of dry lunar soil (Lawrence et al., 2006). If this hydrogen is in the form of water ice, then it is predicted that ~1.5% water ice by mass is present in the upper ~1 m of the lunar regolith (Lawrence et al., 2006). The Lunar CRater Observation and Sensing Satellite (LCROSS) detected ~6 wt.% water ice in the ejecta plume resulting from an impact into Cabeus crater (Colaprete et al., 2010). The relatively low abundances of water ice predicted from these data are consistent with both Earth-based radar observations, which do not show evidence for concentrated water ice on the Moon (Stacy et al., 1997; Campbell et al., 2006), and also spacecraft radar observations, which are suggestive of only patches of ice (Spudis et al., 2010; Thomson et al., 2012).

Interestingly, polar ice at the surface of the Moon appears to be spatially heterogeneous in distribution. Imaging (Haruyama et al., 2008) and reflectance (e.g., Zuber et al., 2012; Hayne et al., 2015; Fisher et al., 2017) campaigns of the lunar poles have not revealed thick, coherent ice deposits, but instead these data are suggestive of a patchy distribution of water frost in some locations. For example, mapping of UV albedo spectra and surface temperature measurements reveal a highly spatially heterogeneous distribution of water frost within PSRs (Hayne et al., 2015). The degree of spatial heterogeneity also appears to differ between individual cold traps. Enhanced surface albedo suggestive of water frost (Fisher et al., 2017; Qiao et al., 2019) also indicates a patchy distribution of surface water ice. Finally, analysis of reflectance spectra acquired by the Moon Mineralogy Mapper (M^3) instrument reveal diagnostic near-infrared absorption features of water ice, which indicate both a low abundance and a patchy distribution of exposed surface water ice (Li et al., 2018).

Impact gardening can produce spatial heterogeneities in ice distribution by causing loss and redistribution of volatiles (Crider and Vondrak, 2003; Hurley et al., 2012). Impacts remove volatiles via vaporization and also preserve volatiles through the emplacement of ejecta, with a net effect of breaking up and burying the ice (Crider and Vondrak, 2003; Hurley et al., 2012). Because these processes take time, the spatial heterogeneity of ice is highly likely to be related to the exposure age of the ice.

Here we estimate the ages of 20 lunar host craters at the south polar region of the Moon to determine how the ages of host craters are related to the spatial heterogeneity of lunar ice. The estimated crater ages provide upper limits for any surface ice (Li et al., 2018) contained within the craters. Given the results of our age analyses, we discuss possible sources for lunar water ice and compare ice on the Moon to ice on Mercury.

2. Methods

2.1. Age estimates for lunar cold traps

From crater-counting statistics, we estimate ages of 20 south polar lunar craters that are located between 80°S and 90°S (Table 1). Tye et al. (2015) previously reported estimates of Haworth, Shoemaker, Faustini, and Shackleton craters. By providing new age estimates for 20 additional polar craters, we present a catalogue of 24 large polar craters (Table 1) that can be used to analyze the surface ages of south polar craters on the Moon. The 20 craters analyzed here are selected on the basis of three criteria: location (between 80°S and 90°S), size (count areas ≥100 km^2), and slope (<10°).

In our analysis, superposing impact craters are counted on flat (<10° slope) regions of each crater's floor to minimize effects of mass wasting that may contaminate crater-counting statistics. To analyze the slopes of the south polar craters, we utilize data from Lunar Orbiter Laser Altimeter (LOLA) (Smith et al., 2010), which has a pixel resolution of 5–20 m at the pole (http://pds-geosciences.wustl.edu/missions/lro/lola.htm). The count areas are in permanent shadow, so we create artificially illuminated hillshade maps (pixel resolution of 20 m) at various azimuth angles from a gridded digital elevation model that was derived from LOLA data (http://pds-geosciences.wustl.edu/missions/lro/lola.htm). For each of the 20 craters analyzed, we catalogue superposing craters (Fig. 2). Obvious secondary craters (those that appear elongated in form, or in chains or clusters) are systematically excluded from the counts. Crater size-frequency distributions (CSFDs) are produced using identified craters with diameters >200 m, and are fit to models of the lunar production function (Neukum et al., 2001) in order to estimate absolute model ages (AMAs) of 20 south polar craters (Table 1; Fig. 3) using CraterStatsII (Michael and Neukum, 2010). The AMAs of Haworth, Shoemaker, Faustini, and Shackleton craters have been estimated previously by Tye et al. (2015) and are included in Table 1. The AMAs of the polar host craters provide a maximum age of any surface ice contained within each crater.

Because we require count areas to be ≥100 km^2 with slopes <10°, not all south polar impact craters (particularly smaller impact craters) can be analyzed using crater-counting statistics. However, many of these smaller impact craters have surface water ice detections (Li et al., 2018) (Fig. 5), and thus we are still interested in the ages of these small craters. While we cannot estimate AMAs for this population, we assess the morphology of individual craters to identify fresh-looking craters from the presence of crisp crater rims. To do this, we utilize images acquired by the narrow- and wide-angle images from the Lunar Reconnaissance Orbiter Camera (LROC) (Robinson et al., 2010) (https://www.lroc.asu.edu/).

An additional strategy for estimating the age of smaller craters stems from quantifying crater morphology and estimating the degree to which the crater has degraded through time (Fassett and Thomson, 2014). Specifically, topographic diffusion models can be used to estimate the ages of craters, given that craters have a well-understood initial morphology (Fassett and Thomson, 2014). This method cannot be applied in this study to polar ice-bearing craters because topographic analyses of lunar polar craters demonstrate that small impact craters 100 m–1 km (Kokhanov et al., 2015) and 3 km–15 km (Rubanenko et al., 2019) show shallowing with latitude suggestive of infill, which the authors interpret to be ice.

As discussed in Section 2.1, we only estimate AMAs of south polar craters that have flat-floored regions ≥100 km^2 in area so that robust crater statistics could be obtained. Although we found no surface water ice within any large crater that is <3.1 Gyr, it is possible that some smaller impact craters that are not included in the age analysis are relatively young and do host surface water ice. We identify 100 small impact craters in the study region (<∼15 km in diameter) that are present-day cold traps and appear to be relatively young on the basis of crisp rim crest morphologies (Fig. 5). These present-day cold traps are characterized by maximum surface temperatures ≤110 K (Paige et al., 2010).

2.2. Patchiness of lunar surface ice within individual craters

The patchiness of surface water ice within each of the 24 south polar craters analyzed here (Table 1) is quantified in Eq. (1) as the percent of the cold trap surface area occupied by surface water ice:

$$\%\, Ice\ Occupancy = \left(\frac{\#\ of\ pixels\ of\ surface\ ice\ detections}{\#\ of\ pixels\ of\ stable\ cold\ traps\ for\ surface\ ice}\right) * 100\% \quad \textbf{(Eq. 1).}$$

Cold traps are defined as surface areas with maximum surface temperatures ≤110 K, as measured by the Diviner Lunar Radiometer Experiment (Paige et al., 2010), representing temperatures at which surface water ice is stable. Direct detections of exposed surface water ice (Li et al., 2018) are used as surface ice detections. These surface water ice detections were made using NIR data acquired by the M^3instrument, specifically from diagnostic overtone and combination mode vibrations of water ice that occur near 1.3, 1.5, and 2.0 μm (Li et al., 2018). These unique ice absorptions are consistent with annual maximum surface temperatures ≤110 K, enhanced LOLA albedo (Fisher et al., 2017), and high UV ratios (Hayne et al., 2015) suggestive of surface water ice (Li et al., 2018).

3. Results

The majority of surface water ice at the lunar south pole (Li et al., 2018) is found in large, old (≥~3.1 Gyr) craters, which comprise the majority of the cold-trapping area available (Fig. 1). The surface ice deposits are distributed in a spatially heterogeneous manner, with a highly patchy appearance. No more than ∼11.5% of the surface areas of the polar craters in this study are occupied by water ice (Fig. 4; Table 1). On average, only ∼4.1% of cold trap surface areas are occupied. The precise surface areas of cold traps occupied by water ice may be even less, given that an M^3spectrum suggestive of only ∼30% water ice is classified as a positive ice detection, resulting in a single detection at the spatial scale of an M^3 pixel (∼280 m x 280 m). We do not find a statistically significant trend between the age of the host crater and the patchiness of surface ice. Instead, the ice occupancy (%) shows a wide variety between all of the host craters; individual large craters that do host surface water ice (ranging in AMAs from ∼3.1–4.2 Gyr) have between 0.1 and 11.5% of their cold-trapping surface areas occupied by surface ice (Fig. 4; Table 1).

We find that 76% (76/100) of these small craters lack surface water-ice detections. The remaining 24% (24/100) of smaller craters that appear fresh have at least one pixel with a positive water ice detection. While surface water ice is predominantly located in ancient craters (Fig. 1), surface water ice is present in relatively young craters as well, and it is possible that many additional surface ice deposits are cold-trapped below this resolution (e.g., Hayne et al., 2018; Rubanenko et al., 2018), both in ancient and young craters.

4. Discussion

4.1. Possible sources of water ice at the Moon's poles

The source(s) of volatiles trapped at the lunar poles is not currently well understood, but the AMAs of host craters estimated here can provide critical insight into this question. The majority of detected surface water ice (Li et al., 2018) is confined to large, ancient (≥~3.1 Gyr) cold traps and appears to be re-worked (Figs. 1,4; Table 1), given its very patchy spatial distribution within individual cold traps. The high degree of patchiness that we find for south polar host craters (Fig. 4; Table 1) is consistent with impact gardening models, suggesting that ancient ice deposits have a patchy distribution of surface ice due to their exposure to high rates of impact bombardment early on, and a longer exposure to the space-weathering environment through time (Crider and Vondrak, 2003; Hurley et al., 2012). The early lunar history (especially the Pre-Nectarian and Nectarian eras) is characterized both by relatively high impact rates of comets and asteroids (Nesvorný et al., 2017), which are suggestive of high ice delivery rates, as well as by relatively high impact rates of micrometeorite bombardment

(Cintala, 1992; Marchi et al., 2005), suggestive of high regolith gardening rates (Costello et al. 2018a,b). Thus, the patchy distribution of surface water ice observable in the older craters (Table 1) may be the artifact of ancient ice that has been broken up through time (Crider and Vondrak, 2003; Hurley et al., 2012, Costello et al., 2018a,b).

Because we also identify a population of small (<~15 km) ice-bearing craters that appear to be relatively young on the basis of their small size and sharp rim morphologies (Fig. 5), there must be some mechanism that has delivered or redistributed surface water ice to these south polar craters more recently. One possibility is that the surface ice was delivered to these small craters after their formation, and thus the ice is relatively fresh. The presence of ice in fresh craters suggests that ice delivery rates are greater than the rates of ongoing destructive and burial processes at these specific cold traps. One candidate for the recent delivery of surface ice is solar wind interactions with the lunar regolith (e.g., Crider and Vondrak, 2000). However, this process may be expected to deliver ice rather homogeneously across available cold traps (Crider and Vondrak, 2000), yet the majority of small craters lack surface water ice (Fig. 5). A second candidate for the recent delivery of surface ice is micrometeorite delivery (e.g., Mandt et al., 2016; Szalay et al., 2018; Pokorný et al., 2019), which may result in a stochastic distribution. A third is volcanic outgassing, which is discussed in detail in Section 4.2. Another possibility is that the surface ice was delivered to the south polar region prior to the formation of these small craters, and was redistributed to these small craters after their formation. The majority of small craters that do host surface water ice (circled in blue in Fig. 5) are located in regions that have higher concentrations of surface water ice (yellow pixels in Fig. 5). Older surface ice may have been redistributed to younger craters by the transportation of impact ejecta or condensation of impact vapors (e.g., Crider and Vondrak, 2003; Hurley et al., 2012; 2017; Farrell et al., 2015; Mandt et al., 2016; Szalay et al., 2018). However, if this is the case, an explanation is required in order to explain why all of the small, young craters proximal to higher concentrations of surface water ice do not host surface water ice (Fig. 5). Overall, understanding why some small, young craters host surface water and why others do not is an important open question.

Recently, analysis of the icy regolith surface layer in lunar PSRs detected by the Lyman Alpha Mapping Project (LAMP) UV instrument suggested that the icy regolith, which is sensed to a depth of <1 μm, must be <2000 years old (Farrell et al., 2019). The authors suggest that older surface ice would be eroded by plasma sputtering, meteoric impact vaporization, and meteoric impact ejection (Farrell et al., 2019). If this is the case, then the surface ice within the large, older craters (Fig. 1) and within the small, younger craters (Fig. 5) may be explained by the same, ongoing delivery mechanism.

It is an outstanding question why not all available cold traps on the surface today are occupied by ice. For the larger cold traps that are estimated to be relatively ancient (Table 1; Fig. 4), this may be related to some re-orientation of the lunar spin-axis, given that these cold traps appear to be spatially grouped (Section 4.2). Furthermore, they are not predicted to have been stable for the cold-trapping of surface water ice when the Moon was on its paleo-axis predicted by Siegler et al. (2016) (Section 4.2). However, for the smaller cold traps that are interpreted to be relatively young on the basis of crater morphology, paleo-thermal conditions do not appear to be a driving factor. For example, the smaller, younger craters that lack ice show a wide spatial distribution across the polar region (Fig. 5). Furthermore, if these craters are relatively young, then they are likely to have formed after the re-orientation of the Moon. Thus, the presence of surface ice in some but not all young cold traps suggests that ice delivery and destruction processes are not in equilibrium across the lunar south pole.

4.2. Constraints on the timing of potential TPW

There are also some large ancient craters that are present-day cold traps, but do not host surface water ice (Figs. 1 and 4). Analysis of the M^3 data that are used here to identify the presence of surface ice suggests that there are no biases in data acquisition related to these craters (Li et al., 2018). Previously, it has been suggested that the present-day distribution of lunar ice may be affected not only by the current distribution of cold-trapping area, but also by the ancient distribution of cold-trapping area (Siegler et al., 2016). Siegler et al. (2011; 2015) argue that long-term orbital changes have resulted in substantial variations in the polar thermal environment on the Moon, and that a high-obliquity period would have resulted in the loss of ice to space or the migration of ice into the subsurface. True polar wander (TPW) refers to the physical reorientation of the spin axis relative to the Moon's present-day poles, and has been suggested to have reoriented the Moon by ~5.5° since its formation (Siegler et al., 2016). The chronology of potential TPW is uncertain and Siegler et al. (2016) found it to be highly dependent on the evolution of mantle temperatures, the compensation state of the lithosphere, and the emplacement and relaxation of mare basalts. The representative models presented by Siegler et al. (2016) predicted a passage through the paleopole prior to 3.5 Gyr, although this is currently not well constrained.

Under the predicted paleo-conditions, the thermal surface environments of some present-day cold traps would not have been stable for the survival of surface water ice (Siegler et al., 2016). Siegler et al. (2016) found that the polar hydrogen concentrations sensed by the Lunar Prospector Neutron Spectrometer are best matched by a combination of hydrogen deposits being delivered pre-TPW (57%) and post-TPW (43%). This hypothesis is consistent with the presence of ice both in large, older craters (Fig. 1) and also in small, younger craters (Fig. 5).

We find that our age-dating analysis strengthens the interpretation that the retention of volatiles within cold traps may have been affected by the stability of these cold traps on long timescales, possibly related to TPW (Siegler et al., 2016; Li et al., 2018). This is because the large craters that are present-day cold traps are not predicted to have been thermally stable for the cold-trapping of water ice when the Moon was on its paleo-axis. Therefore, even if ice was delivered to these craters early on, the ice would not have remained on the surface due to average surface temperatures exceeding 110 K. Thus, the distribution of surface ice at the lunar poles today may be controlled not only by ice supply rates and impact destruction rates, but also some additional factor that affects the long-term stability of volatiles in individual cold traps, such as TPW. The lack of surface ice in these specific craters suggests that either the major flux of polar volatiles occurred pre-TPW, or that there has been a very asymmetrical delivery and/or destruction of volatiles since the onset of polar wander.

Importantly, our age estimates of south polar craters provide constraints on the timing of potential TPW on the Moon. For example, surface ice is not predicted to have been stable before the onset of TPW in Nobile (85.3°S, 53.3°S; 79.3-km diameter) or Shackleton (89.7°S, 129.8°S; 20.9-km diameter) (Siegler et al., 2016), yet surface ice is present within these craters (Fig. 1). For ice to be present at the surface of Nobile or Shackleton, the Moon must have already reoriented to its current spin-axis before ice was delivered to these craters. The AMAs of Nobile and Shackleton, respectively, are 4.1 ± 0.1 Ga (estimated here) and $3.15 + 0.05 - 0.08$ Ga (estimated by Tye et al., 2015). The ages of Nobile and Shackleton place an upper constraint on the age of the surface ice contained by each crater. The age of the hydrogen in Nobile and Shackleton craters can place a lower limit on the timing of TPW to help constrain TPW models (i.e., TPW must have occurred before hydrogen was emplaced within these craters) (Siegler et al., 2016). It has previously been suggested that volcanic outgassing has contributed water to the lunar poles (Crotts and Hummels, 2009). Recent analysis of the volume of effusive basalts on the Moon's surface suggests that peak mare emplacement ~3.5 Ga may have released $\sim 10^{19}$ g of volatiles around the Moon, resulting in a transient atmosphere that may have aided in the migration and delivery of volatiles to the poles (Needham and Kring, 2017). We find that 21/24 of all large craters hosting surface water ice analyzed here have AMAs ≥3.5 Gyr, and therefore it is possible that ice was delivered to them during this peak of volcanism 3.5 Ga. However, Unnamed Crater 3, Wiechert J, and Shackleton have AMAs younger than Gyr, and thus mare-vented volatiles can not easily explain the ice detected within these specific craters. The lack of ice in many present-day cold traps (Figs. 1, 4; Table 1) suggests that ice was not delivered at high rates with respect to ice destruction rates after the onset of TPW. Thus, if mare volcanism was the source of the surface ice detected by Li et al. (2018), and if TPW did occur on the Moon, then TPW must have occurred more recently than 3.5 Gyr. If TPW occurred before 3.5 Ga, then the lack of ice in ancient craters that are present-day cold traps suggests that peak mare volcanism either (1) did not deliver substantial water ice to the lunar poles, or (2) delivered water ice to the poles, which has since been destroyed.

4.3. Comparison of ice at the poles of the Moon and Mercury

The low percentages of cold trap surface areas that host surface water ice on the Moon are in stark contrast to the host craters on Mercury that are interpreted to be occupied by laterally contiguous ice deposits (Neumann et al., 2013; Chabot et al., 2014, 2016). While the surface areas of lunar cold traps are occupied by <12% surface water ice, cold traps on Mercury that host surface water ice are interpreted to be nearly 100% occupied (Deutsch et al., 2016; Chabot et al., 2018). To date, it is not well understood what causes this discrepancy in the amount of surface ice on the Moon and Mercury.

One possibility is that the surface ice on Mercury is much younger than the surface ice on the Moon. If ice deposits on Mercury are relatively young (Crider and Killen, 2005; Lawrence et al., 2013; Chabot et al., 2016; Rubanenko et al., 2018; Ernst et al., 2018; Deutsch et al., 2019), then they have not been exposed to extensive regolith gardening that would break up, destroy, or bury the ice. The same impact bombardment and space weathering processes operate on Mercury and the Moon, and differences in impact flux on these two bodies can affect the regolith overturn rate. If Mercury's regolith is overturned even more frequently than the lunar regolith due to higher impact rates and speeds (Domingue et al., 2014), then the laterally contiguous (Chabot et al., 2014; 2016) ice deposits composed of ~95% pure water ice (Butler et al., 1993) require for the ice to have been deposited within the last tens of Myrs (Crider and Killen, 2005; Lawrence et al., 2013; Deutsch et al., 2019). With such regolith gardening rates, it is possible that relatively ancient, degraded ice deposits exist below the extensive, pure deposits observed on Mercury's surface today. The lunar polar deposits therefore provide an important opportunity to inform us about the ultimate fate of mercurian polar deposits, as well as ices on other airless bodies.

Alternatively, it is possible that the regolith overturn rate at the Moon is higher than it is on Mercury. Costello et al. (2018a,b) find that the Moon has deeper gardening and a faster gardening rate when using the impact fluxes specifically for impactors of diameters between 1 cm and 100 m (Marchi et al., 2005) and modeling secondary impacts. Thus, while the regolith gardening rates on Mercury may allow for meters-thick ice deposits to remain intact for 2–3 Gyr, meters-thick ice deposits on the Moon are expected to have been gardened to the patchy distribution observed today over the same time scale (Costello et al., 2018a,b).

Interestingly, our analysis indicates that there is not a simple correlation between the patchiness of surface water ice and the AMAs of large lunar host craters (Fig. 4). If the surface ice in these large craters detected by Li et al. (2018) is relatively old, then there may be some saturation point at which gardening overturns materials without efficiently removing ice. However, the presence of surface ice in small, fresh-looking craters requires a model that can distribute (or re-distribute) ice on the lunar surface more recently.

5. Conclusions

The poles of the Moon are of high interest to both the scientific and exploration communities due to the presence of water ice. As we are beginning to understand the surficial distribution of this ice (e.g., Hayne et al., 2015; Fisher et al., 2017; Li et al., 2018), important questions regarding the ages and sources of the ice have emerged. Understanding when the ice was delivered to the lunar surface as well as the physical delivery mechanisms are of critical importance to unraveling the nature of these ice deposits, which has implications for the source and evolution of volatiles on other airless bodies and across the inner Solar System.

Here we have analyzed the ages of 20 large craters at the south polar region of the Moon that host surface water ice, as detected from overtone and combination vibrations in M^3 data (Li et al., 2018). Following stratigraphic principles, the estimated ages of the host craters provide a maximum age of the ice contained within them. We find that the majority of surface ice is hosted by ancient craters >3.1 Gyr. This ice appears to be very patchy in surface distribution, with no more than ~11.5% of cold-trapping areas being occupied by water ice. This patchy distribution of ice in old craters may be due to impact bombardment processes that work to break-up and bury the ice with time (Crider and Vondrak, 2003; Hurley et al., 2012).

There are also many ancient craters that are present-day cold traps that lack surface water ice (Fig. 1). If ice was delivered to the pole early on when the Moon was on its paleo-axis, then ice would not have been stable in these specific craters given the surface temperatures of these craters predicted for pre-TPW conditions. Our age analysis presented here can help constrain the chronology of TPW models given that the surface environments of Nobile (85.3°S, 53.3°S; 79.3-km diameter) and Shackleton (89.7°S, 129.8°S; 20.9-km diameter) are not predicted to have been stable for surface ice pre-TPW, yet surface ice is present (Fig. 1). The ice observed within Nobile crater places an upper constraint on the age of post-TPW hydrogen emplacement at 4.1 ± 0.1 Ga. If mare volcanism resulted in the surface ice observed at the poles today, then TPW must have occurred after 3.5 Ga (estimated age of peak mare emplacement); however, we also identify craters that host ice that are younger than this peak in volcanism, suggesting that mare-vented water cannot explain all of the surface ice observed at the lunar south pole.

Finally, while the majority of surface ice may be contained by ancient craters, where the majority of cold-trapping area on the pole exists, we also identify a population of small ($<\sim$15 km) craters that appear to be morphologically fresh and host surface water ice. Ice within fresh, relatively young craters suggests that ice has been delivered to the lunar surface more recently, perhaps from micrometeorites or through solar wind interactions with the lunar regolith.

The history of surface water ice on the Moon is complex and its lengthy story may not be over. Surface water ice on the Moon may be a combination of both old and younger volatiles, which are likely to have been delivered by more than one source given that the flux of volatiles from different delivery mechanisms has changed substantially over the course of lunar history. As exploration of the Moon continues, chemical measurements or samples of the water ice will be essential in more precisely describing the ages and origin of the ice.

Acknowledgments

We thank Matt Siegler and an anonymous reviewer for providing helpful reviews of this work, as well as Oded Aharonson for his editorial handling of our manuscript. This work is supported by NASA under Grant Number NNX16AT19H issued through the Harriett G. Jenkins Graduate Fellowship, by the NASA Solar System Exploration Research Virtual Institute (SSERVI), and by the NASA Discovery Program. We gratefully acknowledge Shuai Li for sharing his water ice detection data and Carle Pieters for helpful discussions about this work.

References

J.R. Arnold. Ice in the lunar polar regions. J. Geophys. Res., 84 (1979), pp. 5659-5668, https://doi.org/10.1029/JB084iB10p05659.

B.J. Butler, D.O. Muhleman, M.A. Slade. Mercury: full-disk radar images and the detection and stability of ice at the north pole. J. Geophys. Res., 98 (1993), pp. 15003-15023, https://doi.org/10.1029/93JE01581.

D.B. Campbell, B.A. Campbell, L.M. Carter, J.-.L. Margot, N.J.S. Stacy. No evidence for thick deposits of ice at the lunar south pole. Nature, 443 (2006), pp. 835-837, https://doi.org/10.1038/nature05167.

N.L. Chabot, C.M. Ernst, B.W. Denevi, H. Nair, A.N. Deutsch, D.T. Blewett, S.L. Murchie, G.A. Neumann, E. Mazarico, D.A. Paige, J.K. Harmon, J.W. Head, S.C. Solomon. Images of surface volatiles in Mercury's polar craters acquired by the MESSENGER spacecraft. Geology, 42 (2014), pp. 1051-1054, https://doi.org/10.1130/G35916.1.

N.L. Chabot, C.M. Ernst, D.A. Paige, H. Nair, B.W. Denevi, D.T. Blewett, S.L. Murchie, A.N. Deutsch, J.W. Head, S.C. Solomon. Imaging Mercury's polar deposits during MESSENGER's low-altitude campaign. Geophys. Res. Lett., 43 (2016), pp. 9461-9468, https://doi.org/10.1002/2016GL070403.

N.L. Chabot, E.E. Shread, J.K. Harmon. Investigating Mercury's south polar deposits: arecibo radar observations and high-resolution determination of illumination conditions. J. Geophys. Res. Planets, 123 (2018), pp. 666-681. https://doi.org/10.1002/2017JE005500.

M.J. Cintala. Impact-induced thermal effects in the lunar and mercurian regoliths. J. Geophys. Res., 97 (1992), pp. 947-973, https://doi.org/10.1029/91JE02207.

A. Colaprete, P. Schultz, J. Heldmann, D. Wooden, M. Shirley, K. Ennico, B. Hermalyn, W. Marshall, A. Ricco, R.C. Elphic, D. Goldstein, D. Summy, G.D. Bart, E. Asphaug, D. Korycansky, D. Landis, L. Sollitt. Detection of water in the LCROSS ejecta plume. Science, 330 (2010), pp. 463-468, https://doi.org/10.1126/science.1186986.

E.S. Costello, R.R. Ghent, P.G. Lucey. Impact gardening on the Moon and Mercury: the source, age, and depth to ice. Lunar Planet. Sci. Conf. (2018a), Abstract 1991.

E.S. Costello, R.R. Ghent, P.G. Lucey. Gardening ice at the poles of the Moon and Mercury. Lunar Polar Volatiles Meeting (2018b), Abstract 5031.

D. Crider, R.M. Killen. Burial rate of Mercury's polar volatile deposits. Geophys. Res. Lett., 32 (2005), p. L12201, https://doi.org/10.1029/2005GL022689.

D.H. Crider, R.R. Vondrak. The solar wind as a possible source of lunar polar hydrogen deposits. J. Geophys. Res., 105 (2000), pp. 26773-26782, https://doi.org/10.1029/2000JE001277.

D.H. Crider, R.R. Vondrak. Space weathering effects on lunar cold trap deposits. J. Geophys. Res., 108 (2003), p. 5079, https://doi.org/10.1029/2002JE002030.

A.P.S. Crotts, C. Hummels. Lunar outgassing, transient phenomena, and the return to the Moon. II. Predictions and tests for outgassing/regolith interactions. ApJ, 707 (2009), p. 1506, https://doi.org/10.1088/0004-637X/707/2/1506.

A.N. Deutsch, N.L. Chabot, E. Mazarico, C.M. Ernst, J.W. Head, G.A. Neumann, S.C. Solomon. Comparison of areas in shadow from imaging and altimetry in the north polar region of Mercury and implications for polar ice deposits. Icarus, 280 (2016), pp. 158-171, https://doi.org/10.1016/j.icarus.2016.06.015.

A.N. Deutsch, J.W. Head, G.A. Neumann. Age constraints of Mercury's polar deposits suggest recent delivery of ice. Earth Planet. Sci. Lett., 520 (2019), pp. 26-33, https://doi.org/10.1016/j.epsl.2019.05.027.

D.L. Domingue, C.R. Chapman, R.M. Killen, T.H. Zurbuchen, J.A. Gilbert, M. Sarantos, M. Benna, J.A. Slavin, D. Schriver, P.M. Trávníček, T.M. Orlando, A.L. Sprague, D.T. Blewett, J.J. Gillis-Davis, W.C. Feldman, D.J. Lawrence, G.C. Ho, D.S.

Ebel, L.R. Nittler, F. Vilas, C.M. Pieters, S.C. Solomon, C.L. Johnson, R.M. Winslow, J. Helbert, P.N. Peplowski, S.Z. Weider, N. Mouawad, N.R. Izenberg, W.E. McClintock. Mercury's weather-beaten surface: understanding Mercury in the context of lunar and asteroidal space weathering studies. Space Sci. Rev., 181 (2014), pp. 121-214, https://doi.org/10.1007/s11214-014-0039-5.

C.M. Ernst, N.L. Chabot, O.S. Barnouin. Examining the potential contribution of the Hokusai impact to water ice on Mercury. J. Geophys. Res. Planets, 123 (2018), pp. 2628-2646, https://doi.org/10.1029/2018JE005552.

C.I. Fassett, B.J. Thomson. Crater degradation on the lunar maria: topographic diffusion and the rate of erosion on the Moon. J. Geophys. Res. Planets, 119 (2014), pp. 2255-2271, 10.1002/2014JE004698.

W.M. Farrell, D.M. Hurley, M.J. Poston, P.O. Hayne, J.R. Szalay, J.L. McLain. The Young Age of the LAMP-observed Frost in Lunar Polar Cold Traps. Geophys. Res. Lett., 46 (2019), Article L083158, https://doi.org/10.1029/2019GL083158.

W.M. Farrell, D.M. Hurley, M.I. Zimmerman. Solar wind implantation into lunar regolith: hydrogen retention in a surface with defects. Icarus, 255 (2015), pp. 116-126, https://doi.org/10.1016/j.icarus.2014.09.014.

E.A. Fisher, P.G. Lucey, M. Lemelin, B.T. Greenhagen, M.A. Siegler, E. Mazarico, O. Aharonson, J.-.P. Williams, P.O. Hayne, G.A. Neumann, D.A. Paige, D.E. Smith, M.T. Zuber. Evidence for surface water ice in the lunar polar regions using reflectance measurements from the Lunar Orbiter Laser Altimeter and temperature measurements from the Diviner Lunar Radiometer Experiment. Icarus, 292 (2017), pp. 74-85, https://doi.org/10.1016/j.icarus.2017.03.023.

J. Haruyama, M. Ohtake, T. Matsunaga, T. Morota, C. Honda, Y. Yokota, C.M. Pieters, S. Hara, K. Hioki, K. Saiki, H. Miyamoto, A. Iwasaki, M. Abe, Y. Ogawa, H. Takeda, M. Shirao, A. Yamaji, J.-.L. Josset. Lack of exposed ice inside lunar south pole Shackleton crater. Science, 322 (2008), pp. 938-939, https://doi.org/10.1126/science.1164020.

Hayne, P., Aharonson, O., Schorghofer, N., Rubanenko, L., Paige, D.A., 2018. Cometary volatiles in micro cold traps on the Moon. DPS 50, Abstract 116.05.

P.O. Hayne, A. Hendrix, E. Sefton-Nash, M.A. Siegler, P.G. Lucey, K.D. Retherford, J.-P. Williams, B.T. Greenhagen, D.A. Paige. Evidence for exposed water ice in the Moon's south polar regions from Lunar Reconnaissance Orbiter ultraviolet albedo and temperature measurements. Icarus, 255 (2015), pp. 58-69, https://doi.org/10.1016/j.icarus.2015.03.032.

D.M. Hurley, D.J. Lawrence, D.B.J. Bussey, R.R. Vondrak, R.C. Elphic, G.R. Gladstone. Two-dimensional distribution of volatiles in the lunar regolith from space weathering simulations. Geophys. Res. Lett., 39 (2012), p. L09203, https://doi.org/10.1029/2012GL051105.

D.M. Hurley, J.C. Cook, K.D. Retherford, T. Greathouse, G.R. Gladstone, K. Mandt, C. Grava, D. Kaufmann, A. Hendrix, P.D. Feldman, W. Pryor, A. Stickle, R.M. Killen, S.A. Stern. Contributions of solar wind and micrometeoroids to molecular hydrogen in the lunar exosphere. Icarus, 283 (2017), pp. 31-37, https://doi.org/10.1016/j.icarus.2016.04.019.

A.P. Ingersoll, T. Svitek, B.C. Murray. Stability of polar frosts in spherical bowl-shaped craters on the Moon, Mercury, and Mars. Icarus, 100 (1992), pp. 40-47, https://doi.org/10.1016/0019-1035(92)90016-Z.

A.A. Kokhanov, M.A. Kreslavsky, I.P. Karachevtseva. Small impact craters in the polar regions of the Moon: peculiarities of morphometric characteristics. Solar Syst. Res., 49 (2015), pp. 295-302, https://doi.org/10.1134/S0038094615050068.

D.J. Lawrence, W.C. Feldman, R.C. Elphic, J.J. Hagerty, S. Maurice, G.W. McKinney, T.H. Prettyman. Improved modeling of Lunar Prospector neutron spectrometer data: implications for hydrogen deposits at the lunar poles. J. Geophys. Res., 111 (2006), p. E08001, https://doi.org/10.1029/2005JE002637.

D.J. Lawrence, W.C. Feldman, J.O. Goldsten, S. Maurice, P.N. Peplowski, B.J. Anderson, D. Bazell, R.L. McNutt, L.R. Nittler, T.H. Prettyman, D.J. Rodgers, S.C. Solomon, S.Z. Weider. Evidence for Water Ice near Mercury's North Pole from Messenger Neutron Spectrometer Measurements. Science, 339 (2013), pp. 292-296, https://doi.org/10.1126/science.1229953.

S. Li, P.G. Lucey, R.E. Milliken, P.O. Hayne, E. Fisher, J.-.P. Williams, D.M. Hurley, R.C. Elphic. Direct evidence of surface exposed water ice in the lunar polar regions. PNAS, 115 (2018), pp. 8907-8912, https://doi.org/10.1073/pnas.1802345115.

K.E. Mandt, T.K. Greathouse, K.D. Retherford, G. Randall Gladstone, A.P. Jordan, M. Lemelin, S.D. Koeber, E. Bowman-Cisneros, G. Wesley Patterson, M. Robinson, P.G. Lucey, A.R. Hendrix, D. Hurley, A.M. Stickle, W. Pryor. LRO-LAMP detection of geologically young craters within lunar permanently shaded regions. Icarus, 273 (2016), pp. 114-120, https://doi.org/10.1016/j.icarus.2015.07.031.

S. Marchi, A. Morbidelli, G. Cremonese. Flux of meteoroid impacts on Mercury. A&A, 431 (2005), pp. 1123-1127, https://doi.org/10.1051/0004-6361:20041800.

E. Mazarico, G.A. Neumann, D.E. Smith, M.T. Zuber, M.H. Torrence. Illumination conditions of the lunar polar regions using LOLA topography. Icarus, 211 (2011), pp. 1066-1081, https://doi.org/10.1016/j.icarus.2010.10.030.

G.G. Michael, G. Neukum. Planetary surface dating from crater size–frequency distribution measurements: partial resurfacing events and statistical age uncertainty. Earth Planet. Sci. Lett., 294 (2010), pp. 223-229, https://doi.org/10.1016/j.epsl.2009.12.041.

D.H. Needham, D.A. Kring. Lunar volcanism produced a transient atmosphere around the ancient Moon. Earth Planet. Sci. Lett., 478 (2017), pp. 175-178, https://doi.org/10.1016/j.epsl.2017.09.002.

D. Nesvorný, F. Roig, W.F. Bottke. Modeling the historical flux of planetary impactors. AJ, 153 (2017), p. 103, https://doi.org/10.3847/1538-3881/153/3/103.

G. Neukum, B.A. Ivanov, W.K. Hartmann. Cratering records in the inner solar system in relation to the lunar reference system. Space Sci. Rev., 96 (2001), pp. 55-86, https://doi.org/10.1023/A:1011989004263.

G.A. Neumann, J.F. Cavanaugh, X. Sun, E.M. Mazarico, D.E. Smith, M.T. Zuber, D. Mao, D.A. Paige, S.C. Solomon, C.M. Ernst, O.S. Barnouin. Bright and dark polar deposits on Mercury: evidence for surface volatiles. Science, 339 (2013), pp. 296-300, https://doi.org/10.1126/science.1229764.

D.A. Paige, M.A. Siegler, J.A. Zhang, P.O. Hayne, E.J. Foote, K.A. Bennett, A.R. Vasavada, B.T. Greenhagen, J.T. Schofield, D.J. McCleese, M.C. Foote, E. DeJong, B.G. Bills, W. Hartford, B.C. Murray, C.C. Allen, K. Snook, L.A. Soderblom, S. Calcutt, F.W. Taylor, N.E. Bowles, J.L. Bandfield, R. Elphic, R. Ghent, T.D. Glotch, M.B. Wyatt, P.G. Lucey. Diviner Lunar Radiometer observations of cold traps in the Moon's south polar region. Science, 330 (2010), pp. 479-482, https://doi.org/10.1126/science.1187726.

P. Pokorný, D. Janches, M. Sarantos, J.R. Szalay, M. Horányi, D. Nesvorný, M.J. Kuchner. Meteoroids at the Moon: orbital properties, surface vaporization, and impact ejecta production. J. Geophys. Res. Planets, 124 (2019), pp. 752-778, https://doi.org/10.1029/2018JE005912.

L. Qiao, Z. Ling, J.W. Head, M.A. Ivanov, B. Liu. Analyses of Lunar Orbiter Laser Altimeter 1,064-nm albedo in permanently shadowed regions of polar crater flat floors: implications for surface water ice occurrence and future in situ exploration. Earth Planet. Sci., 6 (2019), pp. 467-488, https://doi.org/10.1029/2019EA000567.

M.S. Robinson, S.M. Brylow, M. Tschimmel, D. Humm, S.J. Lawrence, P.C. Thomas, B.W. Denevi, E. Bowman-Cisneros, J. Zerr, M.A. Ravine, M.A. Caplinger, F.T. Ghaemi, J.A. Schaffner, M.C. Malin, P. Mahanti, A. Bartels, J. Anderson, T.N.

Tran, E.M. Eliason, A.S. McEwen, E. Turtle, B.L. Jolliff, H. Hiesinger. Lunar Reconnaissance Orbiter Camera (LROC) instrument overview. Space Sci. Rev., 150 (2010), pp. 81-124, https://doi.org/10.1007/s11214-010-9634-2.

L. Rubanenko, E. Mazarico, G.A. Neumann, D.A. Paige. Ice in micro cold traps on Mercury: implications for age and origin. J. Geophys. Res. Planets, 123 (2018), pp. 2178-2191, https://doi.org/10.1029/2018JE005644.

L. Rubanenko, J. Venkatraman, D.A. Paige. Thick ice deposits in shallow simple craters on the Moon and Mercury. Nat. Geosci., 12 (2019), pp. 597-601, https://doi.org/10.1038/s41561-019-0405-8.

J.R. Salvail, F.P. Fanale. Near-surface ice on Mercury and the Moon: a topographic thermal model.Icarus, 111 (1994), pp. 441-455, https://doi.org/10.1006/icar.1994.1155.

M.A. Siegler, R.S. Miller, J.T. Keane, M. Laneuville, D.A. Paige, I. Matsuyama, D.J. Lawrence, A. Crotts, M.J. Poston. Lunar true polar wander inferred from polar hydrogen. Nature, 531 (2016), pp. 480-484, https://doi.org/10.1038/nature17166.

M. Siegler, D. Paige, J.-P. Williams, B. Bills. Evolution of lunar polar ice stability. Icarus, Lunar Volatiles, 255 (2015), pp. 78-87, https://doi.org/10.1016/j.icarus.2014.09.037.

M.A. Siegler, B.G. Bills, D.A. Paige. Effects of orbital evolution on lunar ice stability. J. Geophys. Res., 116 (2011), p. E03010, https://doi.org/10.1029/2010JE003652.

D.E. Smith, M.T. Zuber, G.B. Jackson, J.F. Cavanaugh, G.A. Neumann, H.Riris, X. Sun, R.S. Zellar, C. Coltharp, J. Connelly, R.B. Katz, I. Kleyner, P. Liiva, A.

Matuszeski, E.M. Mazarico, J.F. McGarry, A.-.M. Novo-Gradac, M.N. Ott, C. Peters, L.A. Ramos-Izquierdo, L. Ramsey, D.D. Rowlands, S. Schmidt, V.S. Scott, G.B. Shaw, J.C. Smith, J.-.P. Swinski, M.H. Torrence, G. Unger, A.W. Yu, T.W. Zagwodzki. The Lunar Orbiter Laser Altimeter investigation on the Lunar Reconnaissance Orbiter mission. Space Sci. Rev., 150 (2010), pp. 209-241, https://doi.org/10.1007/s11214-009-9512-y.

P.D. Spudis, D.B.J. Bussey, S.M. Baloga, B.J. Butler, D. Carl, L.M. Carter, M. Chakraborty, R.C. Elphic, J.J. Gillis-Davis, J.N. Goswami, E. Heggy, M. Hillyard, R. Jensen, R.L. Kirk, D. LaVallee, P. McKerracher, C.D. Neish, S. Nozette, S. Nylund, M. Palsetia, W. Patterson, M.S. Robinson, R.K. Raney, R.C. Schulze, H. Sequeira, J. Skura, T.W. Thompson, B.J. Thomson, E.A. Ustinov, H.L. Winters. Initial results for the north pole of the Moon from Mini-SAR, Chandrayaan-1 mission. Geophys. Res. Lett., 37 (2010), p. L06204, https://doi.org/10.1029/2009GL042259.

N.J.S. Stacy, D.B. Campbell, P.G. Ford. Arecibo radar mapping of the lunar poles: a search for ice deposits. Science, 276 (1997), pp. 1527-1530, https://doi.org/10.1126/science.276.5318.1527.

J.R. Szalay, P. Pokorný, Z. Sternovsky, Z. Kupihar, A.R. Poppe, M. Horányi. Impact ejecta and gardening in the lunar polar regions. J. Geophys. Res. Planets, 124 (2018), pp. 143-154, https://doi.org/10.1029/2018JE005756.

B.J. Thomson, D.B.J. Bussey, C.D. Neish, J.T.S. Cahill, E. Heggy, R.L. Kirk, G.W. Patterson, R.K. Raney, P.D. Spudis, T.W. Thompson, E.A. Ustinov. An upper limit for ice in Shackleton crater as revealed by LRO Mini-RF orbital radar. Geophys. Res. Lett., 39 (2012), p. L14201, https://doi.org/10.1029/2012GL052119.

A.R. Tye, C.I. Fassett, J.W. Head, E. Mazarico, A.T. Basilevsky, G.A. Neumann, D.E. Smith, M.T. Zuber. The age of lunar south circumpolar craters Haworth, Shoemaker, Faustini, and Shackleton: implications for regional geology, surface processes, and volatile sequestration. Icarus, 255 (2015), pp. 70-77, https://doi.org/10.1016/j.icarus.2015.03.016.

A.R. Vasavada, D.A. Paige, S.E. Wood. Near-surface temperatures on Mercury and the Moon and the stability of polar ice deposits. Icarus, 141 (1999), pp. 179-193, https://doi.org/10.1006/icar.1999.6175.

K. Watson, B.C. Murray, H. Brown. The behavior of volatiles on the lunar surface. J. Geophys. Res., 66 (1961), pp. 3033-3045, https://doi.org/10.1029/JZ066i009p03033.

M.T. Zuber, J.W. Head, D.E. Smith, G.A. Neumann, E. Mazarico, M.H. Torrence, O. Aharonson, A.R. Tye, C.I. Fassett, M.A. Rosenburg, H.J. Melosh. Constraints on the volatile distribution within Shackleton crater at the lunar south pole. Nature, 486 (2012), pp. 378-381, https://doi.org/10.1038/nature11216.

Table 1. Lunar south polar craters analyzed within the study.

	Crater name (Label)	Latitude (°S)	Longitude (°E)	Diameter (km)	Absolute model age* (Ga)	Surface area occupied by surface water ice (%)
Craters that do host surface water ice	Haworth (Ha)	87.5	354.8	51.4	4.18 +0.02, −0.02 [**]	5.4
	Shoemaker (Sh)	88.1	45.9	51.8	4.15 +0.02, −0.02 [**]	7.0
	Faustini (Fa)	87.2	84.3	42.5	4.10 +0.03, −0.03 [**]	3.3
	Unnamed 1 (Un1)	83.7	69.2	57.7	3.9 +.1, −.1	11.5
	Cabeus B (CaB)	82.3	305.4	59.6	3.9 +.1, −.1	0.1
	de Gerlache (de)	88.5	271.7	32.7	3.9 +.1, −.1	2.3
	Nobile (No)	85.3	53.3	79.3	3.8 +0.1, −0.1	6.3
	Slater (Sl)	88.1	111.3	25.1	3.8 +0.1, −0.1	2.4
	Scott (Sc)	82.4	48.5	107.8	3.8 +0.1, −0.1	3.2
	Sverdrup (Sv)	88.3	206.6	32.8	3.8 +0.1, −0.1	6.1
	Unnamed 2 (Un2)	82.2	10.6	26.8	3.7 +.1, −.1	1.2
	Cabeus (Ca)	85.3	317.9	100.6	3.5 +.1, −.1	1.1
	Unnamed 3 (Un3)	83.9	338.3	22.3	3.4 +.1, −.5	1.1
	Wiechert J (WiJ)	85.2	182.4	34.9	3.2 +.3, −.1	2.7
	Shackleton (S)	89.7	129.8	20.9	3.15 +0.05, −0.08 [**]	7.3

	Idel'son L (IdL)	84.0	118.6	28.0	3.9 +.1, −.1	0.0
Craters that do not host surface water ice	Amundsen (Am)	84.4	83.1	103.4	3.9 +.1, −.1	0.0
	Hedervari (He)	81.8	85.6	74.1	3.9 +.1, −.1	0.0
	Wiechert P (WiP)	85.1	151.8	38.6	3.8 +.1, −.1	0.0
	Scott E (ScE)	81.2	35.7	29.2	3.8 +.1, −.1	0.0
	Wiechert (Wi)	84.0	164.7	40.8	3.7 +.1, −.2	0.0
	Idel'son (Id)	81.3	112.7	59.8	3.5 +.1, −.5	0.0
	Wiechert U (WiU)	83.4	149.0	30.0	3.4 +.1, −.7	0.0
	Amundsen C (AmC)	80.8	85.2	24.2	1.8 +.2, −.2	0.0

*The reported 1-sigma uncertainties are derived from counting statistics alone, and thus do not incorporate systematic errors associated with the chronology function. This is consistent with the statistical uncertainties reported by Tye et al. (2015).
**Estimated model ages as reported by Tye et al. (2015).

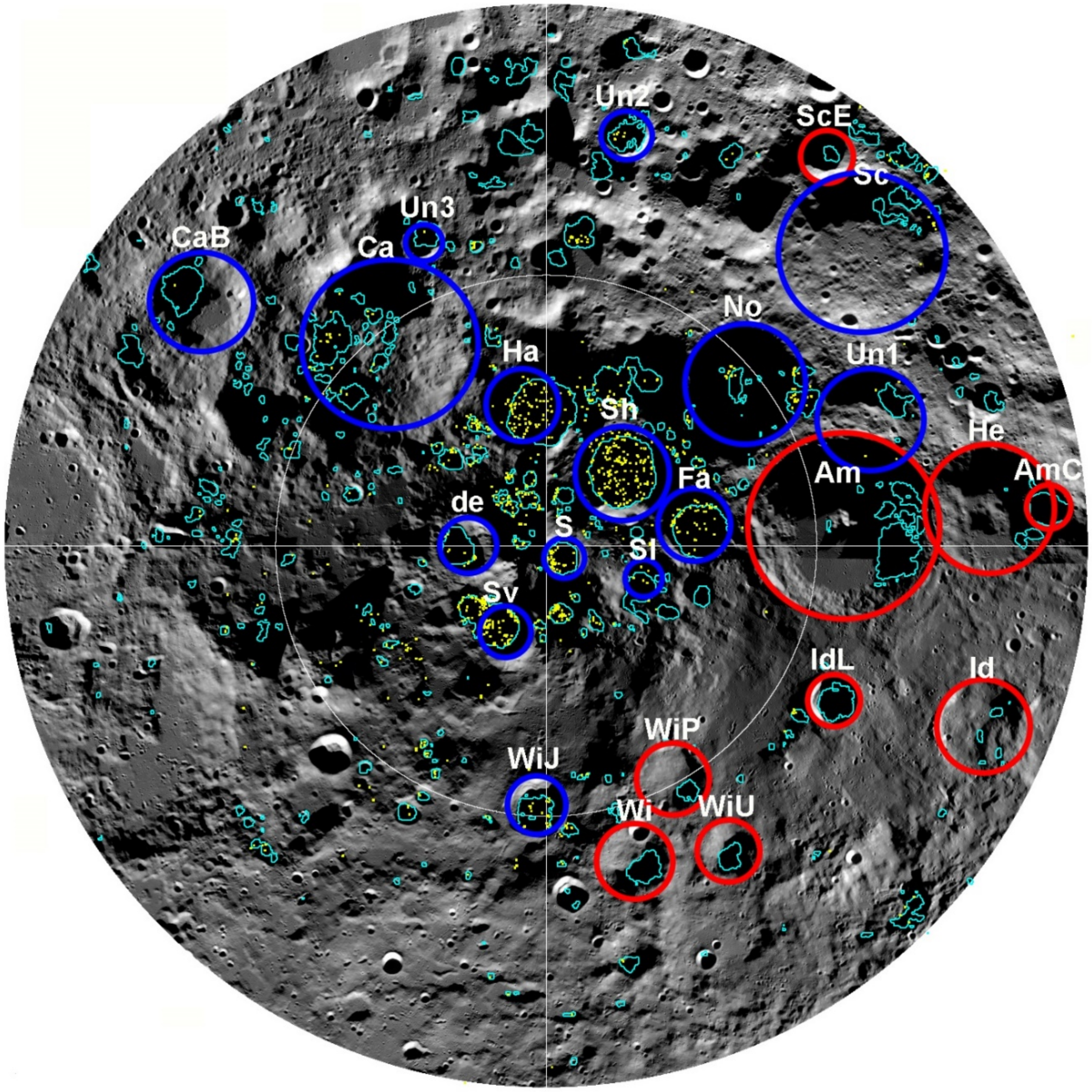

Figure 1. Distribution of south polar craters on the Moon for which AMAs are estimated in this study. Please refer to Table 1 to interpret the abbreviated name labels associated with each host crater. Water-ice detections from Li et al. (2018) are shown in yellow, where each colored dot represents a single M^3 pixel (~280 m × 280 m). Craters for which we estimate AMAs that host surface water ice are outlined in blue and those that do not host surface water ice are outlined in red. Present-day cold traps are defined by cyan contours outlining regions with maximum surface temperatures ≤110 K (Paige et al., 2010). Basemap is LROC WAC mosaic in polar stereographic projection between 80°S and 90°S.

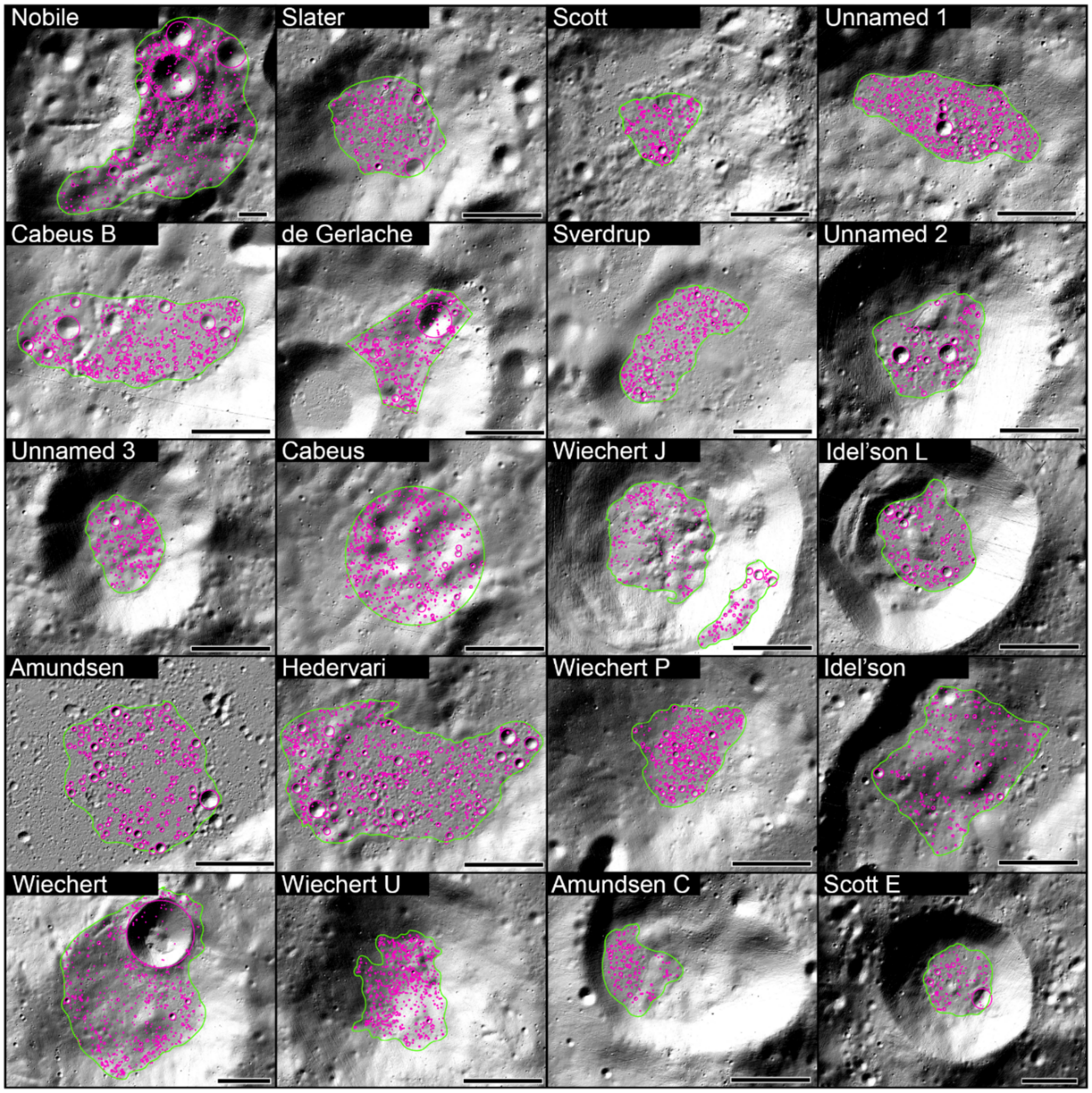

Figure 2. Absolute model ages (AMAs) are derived for 20 south polar craters located between 80°S and 90°S that have count areas ≥100 km^2 with slopes <10° (Table 1). The count areas for these 20 craters are outlined in green and the individual impact craters used to estimate AMAs are outlined in pink. Only impact craters >200 m in diameter are used in crater size-frequency distributions (Fig. 3).

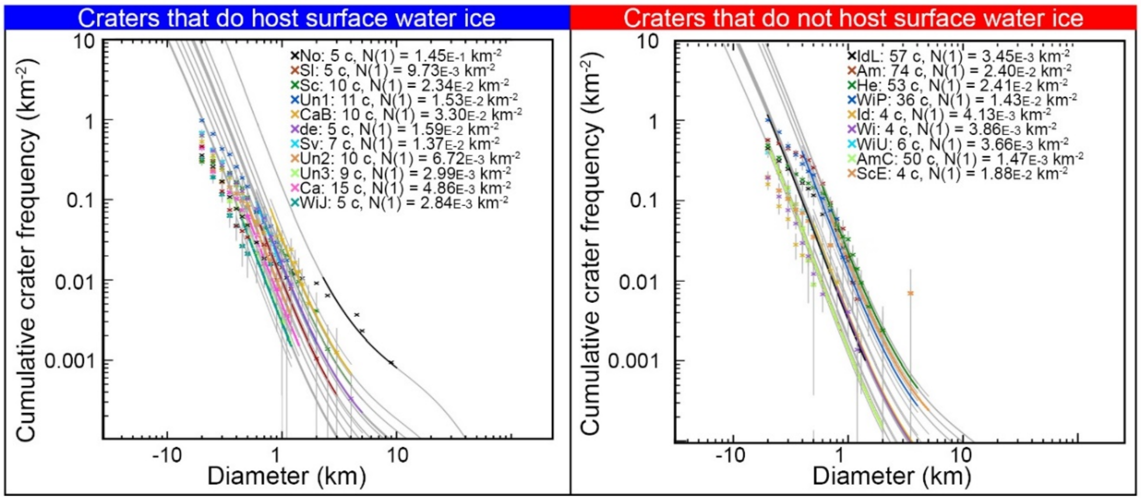

Figure 3. Crater size-frequency distributions (CSFDs) of count areas ≥100 km^2 with slopes <10° for 20 south polar craters analyzed in this study (Fig. 2; Table 1). CSFDs for craters that do host surface water ice are shown on the left and CSFDs for craters that do not host surface water ice are shown on the right. These dated craters are outlined in blue and red, respectively, in Fig. 1. Only impact craters >200 m in diameter are considered in CSFDs. We utilize the lunar chronology and production functions from Neukum et al. (2001).

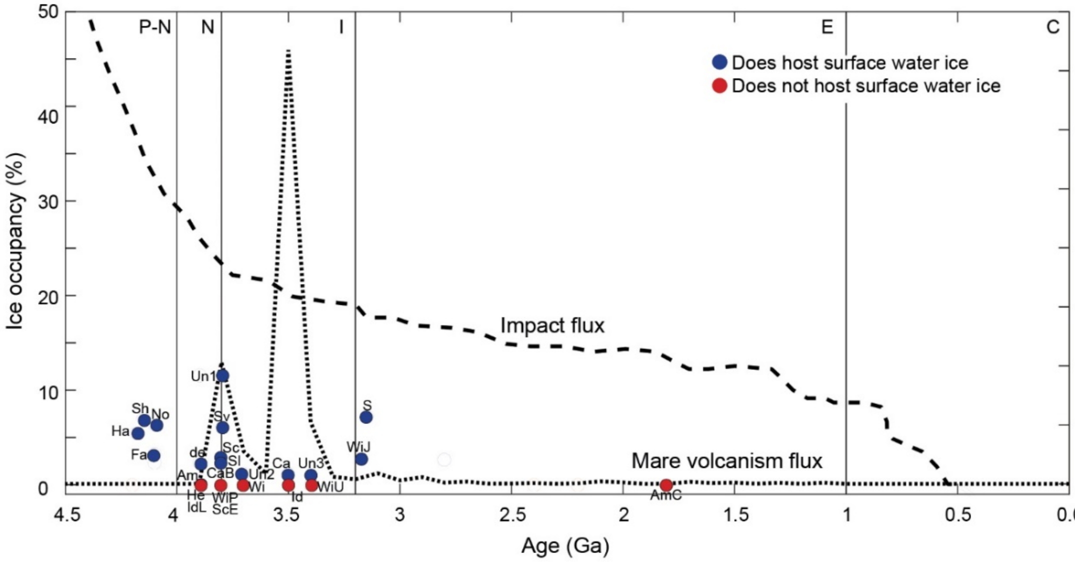

Figure 4. The percentage of specific cold traps occupied by water ice is plotted with respect to the estimated absolute model ages of the host craters. Please refer to Table 1 to interpret the abbreviated name labels associated with each host crater. The modeled impact flux for the Moon (Nesvorný et al., 2017) is plotted in the thick dashed line and the estimated effusive volcanic flux (Needham and Kring, 2017) is plotted in the thin black dashed line. Lunar geologic eras are separated by vertical lines.

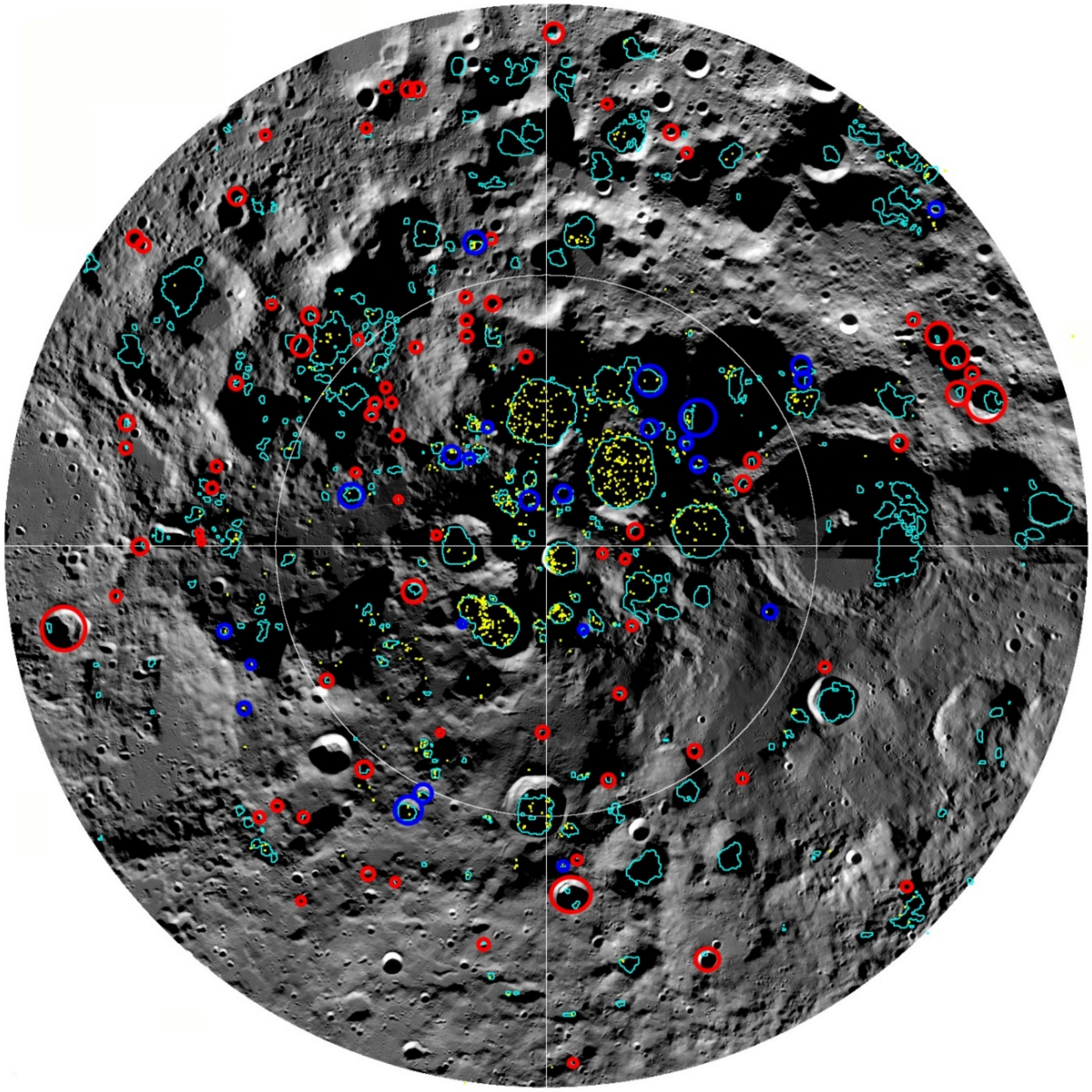

Figure 5. Distribution of south polar simple craters that have crisp-looking rim morphologies, are too small to date using robust crater counting, and are present-day cold traps. Cold traps are defined by cyan contours outlining regions with maximum surface temperatures ≤ 110 K (Paige et al., 2010). As in Fig. 1, water-ice detections from Li et al. (2018) are shown in yellow. Craters that host surface water ice are circled in blue and craters that do not host surface water ice are circled in red. Basemap is LROC WAC mosaic in polar stereographic projection between 80°S and 90°S.

Chapter 3

Assessing the roughness properties of circumpolar lunar craters: Implications for the timing of water-ice delivery to the Moon

Ariel N. Deutsch[a], James W. Head III[a], Gregory A. Neumann[b], Misha A. Kreslavsky[c], and Michael K. Barker[b]

[a]Department of Earth, Environmental and Planetary Sciences, Brown University, Providence, RI 02912, USA

[b]NASA Goddard Space Flight Center, Greenbelt, MD 20771, USA

[c]Department of Earth and Planetary Sciences, University of California - Santa Cruz, Santa Cruz, CA 95064, USA

Accepted for publication in *Geophysical Research Letters* (MS 2020GL087782R)

Deutsch, A. N., Head, J. W., Neumann, G. A., Kreslavsky, M. A., *Accepted.* Assessing the roughness properties of circumpolar lunar craters: Implications for young water ice on the Moon. *Geophysical Research Letters.*

Abstract

The roughness properties of impact craters are valuable indicators of crater degradation and can provide insight into crater ages. We evaluate the roughness of lunar craters from different geologic eras, confirming that young, Copernican craters are distinctly rougher than older craters. We evaluate the potential age of small (<~15 km) craters that are thought to host surface ice by quantifying the roughness inside these craters, as well as outside. Interior roughness may be subdued by slope processes or the presence of volatiles. The distribution of ice-bearing craters is skewed toward roughness values higher than those of pre-Imbrian craters, although no ice-bearing craters are within the Copernican-only domain in roughness space. All of the 15 rough, permanently shadowed craters that are found within the Copernican-only domain lack water-ice detections, suggesting that either ice has not been delivered to these young craters, or that it has since been destroyed.

Plain language Summary

When a planetary surface is struck by an impactor, the pre-existing surface is disturbed as rocks and boulders scatter from the high-energy collision. Over time, the surface texture becomes smoother as these rocks and boulders are broken up into smaller pieces and begin to diffuse away. Surface texture is thus a powerful tool for evaluating the degradation of impact craters, given that young, fresh craters tend to be rougher than old craters due to the presence of rocks and boulders on the recently disturbed surface. Here we quantify the surface texture of lunar craters of different geologic eras and establish a relationship between the roughness and age of craters. We evaluate the roughness of

small craters that host near-polar surface ice, and find a population of craters likely to be post-Nectarian in age. However, the youngest polar craters lack surface-ice detections.

1 Introduction

The lunar poles provide a fascinating thermal environment capable of cold-trapping water ice on geologic timescales (Vasavada et al., 1999; Schorghofer & Aharonson, 2014; Siegler et al., 2016; Williams et al., 2017). Water ice has been reported to be present on permanently shadowed surfaces, as detected from diagnostic near-infrared absorption features of water ice in reflectance spectra acquired by the Moon Mineralogy Mapper (M^3) instrument (Li et al., 2018). While there have been various observations indicating the presence of water ice at the lunar surface (Hayne et al., 2015; Fisher et al., 2017; Li et al., 2018), it is still not clear when this ice was delivered. The timing of volatile deposition provides important constraints on the origin of lunar ice because different delivery mechanisms have been active at different times throughout lunar history (e.g., Siegler et al., 2016; Lawrence, 2017). For example, impact bombardment and volcanic outgassing are capable of delivering water to the lunar surface, but both were more active early on in lunar history and have significantly declined toward the present (e.g., Hiesinger et al., 2011; Head & Wilson, 2017; Needham & Kring, 2017; Nesvorný et al., 2017; Pokorný et al., 2019). Interactions between the solar wind and the lunar regolith can also form water on the surface, and this process is still very active today (Crider & Vondrak, 2002; Jones et al., 2018).

To date, the origin of polar volatiles remains a major outstanding question in lunar science, but the age of the ice can provide important constraints. One approach to describing the age of the reported ice detections (Li et al., 2018; from here on referred to as "the ice") is to use relative dating to analyze the stratigraphic record of the ice and its host craters. We previously took this approach, using crater density statistics to estimate the ages of ice-bearing craters at the south pole of the Moon (Deutsch et al., 2020). The derived ages of the host craters provide an upper limit for the ages of the ice contained within the craters. While all of the craters that we dated have estimated model ages >2.8 Ga, some ice-bearing craters were too small to allow for robust cratering statistics and were excluded from the age-dating analysis (Deutsch et al., 2020). Interestingly, some of these small (<10 km) craters have morphologies suggestive of relatively young ages, on the basis of crisp crater rim crests. Ice in young craters is particularly interesting because it suggests that there is some recent and perhaps ongoing mechanism that is delivering or redistributing water to polar cold traps. Therefore, understanding if these small, ice-bearing craters are indeed young is essential in understanding the age and source of volatiles on the Moon.

Here we take a new approach to understand the ages of these small polar cold traps: analyzing the roughness properties of small ice-bearing (Li et al., 2018) craters. It is understood that impact crater properties evolve with time due to a variety of geologic and space-weathering processes; young, pristine craters can be characterized by sharper rim crest morphologies and greater depth-to-diameter ratios than old, degraded craters (Basilevsky, 1976; Pike, 1977; Offield & Pohn, 1980; Pohn & Offield, 1980; Fassett & Thomson, 2014; Agarwal et al., 2019). Younger craters are also associated with lower surface porosities (Mandt et al., 2016) and higher rock abundances, which tend to decrease with age (Ghent et al., 2014; Li et al., 2017; Mazrouei et al., 2019). Additionally, the topographic roughness of a crater and its ejecta evolves with time and can help provide insight into the age of the crater (Kreslavsky et al., 2013; Neumann et al., 2015).

Topographic roughness is a measurement of the local deviation from the mean topography, providing a measurement of surface texture, and is a powerful tool for evaluating surface evolution over geologic time (Kreslavsky & Head, 2000; Rosenburg et al., 2011; Kreslavsky et al., 2013; Neumann et al., 2015). Neumann et al. (2015) demonstrated that Copernican craters typically have high surface roughness at the small spatial scales (~dm–m) of multi-beam laser spots. More recently, Wang et al. (2019) analyzed various lunar impact craters that span in stratigraphic age from the Pre-Nectarian through the Copernican eras, and found that the youngest craters could be identified on the basis of greater roughness, as well as greater rock abundances and higher soil temperatures. They showed that these properties tend to decrease toward equilibrium with crater age (Wang et al., 2019).

Here, we seek to understand whether any craters that host surface ice on the Moon are geologically young, using roughness as a proxy for crater age. We first analyze the roughness properties of a variety of circumpolar craters from all geologic eras to establish the dependence of crater roughness on crater age. We then analyze the roughness properties of small (<~15 km) ice-bearing craters that may be geologically young (Deutsch et al., 2020) and compare them to the roughness properties of different-aged lunar craters. Understanding the timing of water delivery to the Moon is a critical step in understanding the nature of the lunar volatile cycle and how it is evolving with time.

2 Methods and results

We analyze the roughness of the lunar surface using the Lunar Orbiter Laser Altimeter (LOLA; Smith et al., 2010, 2017) Digital Roughness Maps (LDRM_40S_1000M; LDRM_40N_1000M; http://imbrium.mit.edu/DATA/LOLA_GDR/). In these data products, surface roughness was derived from the root mean square (RMS) variation in the surface elevation of the five adjacent spots returned from a single laser pulse acquired by LOLA (Neumann et al., 2015; Smith et al., 2017). For each group of returned spots, the local slope was removed and the roughness, R, was estimated from the residual heights:

$$R = \sqrt{\frac{1}{n-\nu}\sum_{i=1}^{n} {z_i}^2} \quad (1).$$

In Eq. 1, n is the number of LOLA spots (five), ν is the number of degrees of freedom (three) used to find the surface height and slope, and z is the height residual for a given spot. The RMS height represents an unbiased estimate of surface roughness of a random topographic field at the center of each LOLA spot (Neumann et al., 2015; Smith et al., 2017).

As explained in detail in the documentation of the LDRM (http://imbrium.mit.edu/DATA/LOLA_GDR /), the data account for changes in spacecraft altitude during data acquisition, residual uncorrelated noise of the instrument range measurements, and drift in system parameters over the course of the LRO mission that causes deviations from a flat measurement. The five-spot LOLA data were median-averaged at a pixel resolution of 1000 m for the lunar surface between ±40° to each pole. The separation between the five-spot footprints is ~15–25 m. The 1-km scale analyzed here could be refined in future studies of small regions.

2.1 The roughness of lunar craters as an indicator of age

We analyze the roughness of over 400 impact craters located between ±40°N and ±90°N (Table S1). These craters, identified using the LPI lunar crater database (Losiak et al., 2009), have previously been catalogued into lunar geologic eras. We find the mean roughness value for the interior of each crater and for rings extending 2 kilometers from the crater rim. We find that, at a distance of 2 km, the mean roughness outside of a crater is relatively similar to the mean roughness within a crater (Fig. 1). The roughness becomes increasingly less distinct with distance from the crater (Fig. 1).

The distinctness of roughness properties not only decreases with distance from the crater (Fig. 1), but also with crater age (Fig. 2). Figure 2a shows that Copernican craters have distinctly rougher interiors than older craters, consistent with previous work (Wang et al., 2019). This is also consistent with work that demonstrates that younger craters have higher circular polarization ratios (CPR) suggestive of higher surface roughness (Fa & Eke, 2018; Fassett et al., 2018). The interior roughness of different-aged craters is generally more distinct than the exterior roughness, as external units tend to reach equilibrium more quickly. However, the exterior units of Copernican-aged craters are also distinctly rougher (at a distance of 2 km from their rims) than the exterior units of older craters (Fig. 2b).

The major differences in roughness domains exist between Copernican craters and craters of older eras (Fig. 2). However, there are still statistically-significant differences ($\alpha = 0.001$) in surface roughness between the oldest lunar craters (Pre-Imbrian) and craters formed within the Imbrian and Eratosthenian periods (Fig. 3).

We note that while geologically young craters have distinct roughness properties (Fig. 2), as well as thermophysical (Ghent et al., 2014; Li et al., 2017; Mazrouei et al., 2019; Wang et al., 2019) and morphological properties (Pike, 1977; Fassett & Thomson, 2014; Agarwal et al., 2019), the roughness of a crater cannot independently establish its age. Instrument noise (Neumann et al., 2015; Smith et al., 2017), the natural variability and non-uniform degradation of individual craters (Head, 1975), and differences in target properties (Cintala et al., 1977) result in roughness variations between individual craters of similar stratigraphic age, and even statistical overlap between craters of different geologic eras (Wang et al., 2019). However, surface roughness remains an important tool in evaluating crater degradation and age (Kreslavsky & Head, 2000; Rosenburg et al., 2011; Kreslavsky et al., 2013; Neumann et al., 2015; Wang et al., 2019), specifically for the youngest, most pristine craters, which we are interested in here.

In addition to quantifying the roughness properties of lunar craters of different geologic eras, we also analyze the roughness properties with respect to crater size. We find that the roughness of craters does not vary with crater size in a statistically significant trend, either for the interiors or exteriors of craters (Fig. S1). Therefore, even though the craters included in the LPI database (Losiak et al., 2009) are all larger than the small ice-bearing craters that we are interested in here (typically <15 km), it is appropriate to directly compare the roughness properties of craters from both groups (Section 2.2).

2.2 The roughness of small ice-bearing craters on the Moon

Using reported ice detections from analyses of diagnostic vibrations of water ice (Li et al., 2018), we identify 82 small (<~15 km) ice-bearing craters that are located between ±80° and ±90° (Table S2). If all ice on the Moon was deposited early on in lunar history, we would expect ice to be present only in old, smooth craters. We compare the roughness of ice-bearing craters to the roughness of old craters of Nectarian and Pre-Nectarian age (Fig. 4). Although the histograms of both populations peak at similar roughness values ($R \approx 0.43$ m), the distribution of the ice-bearing craters is skewed toward higher interior roughness values. The Kolmogorov-Smirnov statistical test indicates that the difference between the interior roughness-frequency distribution is statistically significant with high confidence (p-value = 0.002). This indicates that the population of ice-bearing craters contains some rougher craters that are likely to be post-Nectarian.

Importantly, surface roughness within a crater may be lowered by either mass wasting (e.g., Zuber et al., 2012; Fassett & Thomson, 2014) or the presence of frozen volatiles (Kreslavsky & Head, 2000; Putzig et al., 2014). Additionally, at the spatial resolution of the LDRM, our roughness measurements are likely sampling more of the sloping crater walls for the relatively smaller ice-bearing craters than for the different-aged craters from the LPI crater database, and crater walls are relatively smoother than other impact crater units (Zuber et al., 2012). Furthermore, smaller impact craters may degrade and become smoother more quickly than larger craters of the same formation age (Bart & Melosh, 2010a, 2010b; Basilevsky et al., 2018; Mahanti et al., 2018). Due to these multiple variations between the small, ice-bearing craters and the larger craters analyzed, the roughness values that we find for the interiors of ice-bearing craters are likely to be lower than the roughness values of similarly-aged craters that lack ice. The ice-bearing craters that have higher interior roughness values than Nectarian or Pre-Nectarian craters (Fig. 4a) are therefore highly suggestive of post-Nectarian ages given that they are likely to have been subdued by the presence of surface ice (Kreslavsky & Head, 2000; Putzig et al., 2014; Moon et al., 2019). It is possible that some additional craters are also post-Nectarian, but that their roughness properties have been altered by surface ice such that they appear smoother and thus older.

Because the interior roughness properties of ice-bearing craters may be subdued (Kreslavsky & Head, 2000; Putzig et al., 2014; Moon et al., 2019), we also analyze the roughness outside of ice-bearing craters, for an exterior ring extending 2 kilometers from the rim (Fig. 4b). We find that although the surface roughness at a distance of 2 km from relatively large craters (~10–100 km in diameter) is a reasonable representation of crater roughness (Fig. 1) and appears to vary with crater age (Fig. 2), it is not a reliable measurement of degradation for relatively small impact craters (~1–15 km) at the resolution of the analyzed LDRM data. The roughness data have a pixel resolution of 1000 m (Neumann et al., 2015; Smith et al., 2017); therefore, the mean surface roughness values calculated for the exterior portions of the small impact craters rely on only a few individual roughness values. While expanding the analyzed area surrounding the crater would improve the number of values incorporated in calculating the mean, we find that the surface roughness becomes increasingly less distinct with distance from the crater and is not a good proxy for the crater's degradation state (Fig. 1).

2.2 Distinctly rough polar craters that lack ice

We find that none of the small craters analyzed here that are identified as ice-bearing (Li et al., 2018) have roughness properties that belong to a Copernican-only domain in the roughness space (Fig. 5). Interestingly though, we identify 15 polar craters between ±75° and ±90° that do not have positive detections of water ice (Li et al., 2018) but do have enhanced roughness values suggestive of Copernican ages (Table S3). All of these 15 craters have permanently shadowed surfaces, suggesting they may be thermally stable for the cold-trapping of water ice (Mazarico et al., 2012). The roughness values of these 15 craters are statistically distinct from Pre-Imbrian craters (Fig. 4b,c) and lie within the Copernican-only domain (Figs. 4b,c, 5).

3 The age of lunar surface ice

Overall, the statistical difference between the roughness-frequency distribution of pre-Imbrian and ice-bearing craters (Fig. 4a,b) suggests that some ice-bearing craters are post-Nectarian in age. The ages of the host craters provide an upper constraint on the age of the surface ice they contain, and it is possible that the small post-Nectarian craters identified here host ice that was delivered relatively recently. In fact, it has been suggested that perhaps all of the surface ice observed at the lunar poles is geologically young; analysis of the icy regolith detected by the Lyman Alpha Mapping Project (LAMP) UV instrument suggests ice was deposited very recently (Farrell et al., 2019).

Specifically, the ongoing rates of plasma sputtering and meteoric impact vaporization and ejection on the Moon suggest that the ice present at the surface or near-surface of regolith particles (as sensed by LAMP to a depth of <1 μm) must be <2000 years old (Farrell et al., 2019). Relatively young surface ice can be delivered to the Moon from micrometeorite bombardment (Ong et al., 2010; Pokorný et al., 2019; Szalay et al., 2019), or formed in-situ from the ongoing interactions between solar wind protons and oxygen in the lunar regolith (e.g., Crider & Vondrak, 2000; Dyar et al., 2010). Ice delivered during the Eratosthenian or Copernican eras is not predicted to be volcanic in origin, given that the bulk of lunar volcanism occurred prior to these eras (e.g., Needham & Kring, 2017).

Curiously, our analysis reveals that all of the polar impact craters with roughness properties that lie distinctly within a Copernican-only domain do not have positive water-ice detections by Li et al. (2018). All of these 15 impact craters have permanently shadowed surfaces (http://imbrium.mit.edu/BROWSE/EXTRAS/ILLUMINATION/), but it is possible that they are not thermally stable environments for the cold-trapping of surface ice (Ingersoll et al., 1992; Rubanenko et al., 2019). If these permanently shadowed surfaces are in fact stable to the cold-trapping of ice, then this finding suggests that (1) perhaps water ice has not been cold-trapped in the youngest polar craters on the Moon, which would imply that the most recent episodes of ice delivery occurred prior to the formation of these impact craters or (2) ice that was delivered to these particularly rough craters has since been destroyed. However, if these permanently shadowed surfaces are not stable to the cold-trapping of ice, then the youngest ice-bearing craters on the Moon appear to be Imbrian–Eratosthenian in age, on the basis of surface roughness (Fig. 4) and crater-density statistics (Deutsch et al., 2020).

4 Conclusion

It has been well demonstrated that the roughness properties of impact craters are valuable indicators of crater degradation states, and provide important insight into the ages of craters (Fig. 2) (Kreslavsky & Head, 2000; Rosenburg et al., 2011; Kreslavsky et al., 2013; Neumann et al., 2015; Wang et al., 2019). Here we find that the distribution of ice-bearing craters on the Moon is skewed toward roughness values that are higher than those of pre-Imbrian craters (Fig. 4a) (p-value = 0.002). It is possible that these ice-bearing craters are of relatively young ages, given that their surface textures are likely to be subdued by the presence of surface ice (Kreslavsky & Head, 2000; Putzig et al., 2014; Moon et al., 2019). We do not identify any ice-bearing craters that are within the Copernican-only domain in roughness space; in fact, all of the 15 rough polar craters (±75° to ±90°) that are found within this domain lack water-ice detections (Li et al., 2018). If surface ice is stable in these permanently shadowed craters, then either ice has not been delivered to these young craters since their formation, or it has since been destroyed. If these craters, however, are not thermally stable environments for surface ice, then the youngest ice-bearing craters on the Moon appear to be Imbrian–Eratosthenian in age, on the basis of surface roughness (Fig. 4) and crater-density statistics (Deutsch et al., 2020).

Determining the timing of water delivery to the Moon is a critical step in understanding the nature of the lunar volatile cycle and how it is evolving with time. The rough, ice-bearing craters identified here, as well as even smaller cold traps (Rubanenko & Aharonson, 2017; Hayne et al., 2018; Rubanenko et al., 2018), are excellent exploration candidates for studying the most recent history of volatile delivery to the Moon. Determining the abundance and precise chemical composition of volatiles within younger cold traps is essential in determining the recent fluxes and sources of volatiles to the lunar surface, providing insight into how the lunar volatile system is actively evolving.

Acknowledgements

We thank Caleb Fassett and one anonymous reviewer for their helpful reviews, as well as Andrew Dombard for his editorial handling of his manuscript. This work is supported by NASA via Grant Numbers 80NSSC19K1289 to A.N.D and NNX16AQ06G to M.A.K., by the LRO LOLA Team (80NSSC19K0605) to J.W.H., by the SSERVI (NNA14AB01A) to Brown University, and by the NASA Discovery Program to G.A.N. We thank Shuai Li for sharing his water-ice detections. Thanks to members of the LRO LOLA team for data acquisition and especially Erwan Mazarico, Dave Smith, and Maria Zuber for productive discussions.

Data availability

Topographic, roughness, and shadow data analyzed in this paper are all available at the LOLA PDS Data Node (http://imbrium.mit.edu/). Individual craters analyzed here can be found in the Supplementary Materials.

References

Agarwal, N., Haridas, A., Khanna, N., Srivastava, P., & Jain, V. (2019). Study of morphology and degradation of lunar craters using Chandrayaan–1 data. *Planetary and Space Science, 167,* 42–53. https://doi.org/10.1016/j.pss.2019.01.003

Bart, G. D., & Melosh, H. J. (2010a). Impact into lunar regolith inhibits high-velocity ejection of large blocks. *Journal of Geophysical Research: Planets, 115(E8)*, E08004. https://doi.org/10.1029/2009JE003441

Bart, G. D., & Melosh, H.J. (2010b). Distributions of boulders ejected from lunar craters. *Icarus, 209,* 337–357. https://doi.org/10.1016/j.icarus.2010.05.023

Basilevsky, A. T. (1976). On the evolution rate of small craters. *Lunar Science Conf., Proceedings, 1,* 1005–1020. http://adsabs.harvard.edu/full/1976LPSC....7.1005B.

Basilevsky, A. T., Kozlova, N. A., Zavyalov, I. Yu., Karachevtseva, I. P., & Kreslavsky, M. A. (2018). Morphometric studies of the Copernicus and Tycho secondary craters on the moon: Dependence of crater degradation rate on crater size. *Planetary and Space Science,162,* 31–40. https://doi.org/10.1016/j.pss.2017.06.001

Cintala, M. J., Wood, C.A., & Head, J. W. (1977). The effects of target characteristics on fresh crater morphology: Preliminary results for the Moon and Mercury. *Proceedings of the Eighth Lunar Science Conference,* 3409-3425.

Crider, D. H., & Vondrak, R. R. (2002). Hydrogen migration to the lunar poles by solar wind bombardment of the moon. *Advances in Space Research, 30(8),* 1869–1874. https://doi.org/10.1016/S0273-1177(02)00493-3

Crider, D. H., & Vondrak, R. R. (2000). The solar wind as a possible source of lunar polar hydrogen deposits. *Journal of Geophysical Research: Planets, 105(E11),* 26773–26782. https://doi.org/10.1029/2000JE001277

Deutsch, A. N., Head, J. W., & Neumann, G. A. (2020). Analyzing the ages of south polar craters on the Moon: Implications for the sources and evolution of surface water ice. *Icarus, 336,* 113455. https://doi.org/10.1016/j.icarus.2019.113455

Dyar, M. D., Hibbitts, C. A., & Orlando, T. M. (2010). Mechanisms for incorporation of hydrogen in and on terrestrial planetary surfaces. *Icarus, 208(1),* 425–437. https://doi.org/10.1016/j.icarus.2010.02.014

Fa, W., & Eke, V. R. (2018). Unravelling the mystery of lunar anomalous craters using radar and infrared observations. *Journal of Geophysical Research: Planets*, *123*(8), 2119–2137. https://doi.org/10.1029/2018JE005668

Farrell, W. M., Hurley, D. M., Poston, M. J., Hayne, P. O., Szalay, J. R., & McLain, J. L. (2019). The young age of the LAMP-observed frost in lunar polar cold traps. *Geophysical Research Letters, 46(15),* 8680–8688. https://doi.org/10.1029/2019GL083158

Fassett, C. I., King, I. R., Nypaver, C. A., & Thomson, B. J. (2018). Temporal evolution of S-band circular polarization ratios of kilometer-scale craters on the lunar maria.

Journal of Geophysical Research: Planets, *123*(12), 3133–3143. https://doi.org/10.1029/2018JE005741

Fassett, C. I., & Thomson, B. J. (2014). Crater degradation on the lunar maria: Topographic diffusion and the rate of erosion on the Moon. *Journal of Geophysical Research: Planets, 119(10),* 2255–2271. https://doi.org/10.1002/2014JE004698

Fisher, E. A., Lucey, P. G., Lemelin, M., Greenhagen, B. T., Siegler, M. A., Mazarico, E., et al. (2017). Evidence for surface water ice in the lunar polar regions using reflectance measurements from the Lunar Orbiter Laser Altimeter and temperature measurements from the Diviner Lunar Radiometer Experiment. *Icarus, 292,* 74–85. https://doi.org/10.1016/j.icarus.2017.03.023

Ghent, R. R., Hayne, P. O., Bandfield, J. L., Campbell, B. A., Allen, C. C., Carter, L. M., & Paige, D. A. (2014). Constraints on the recent rate of lunar ejecta breakdown and implications for crater ages. *Geology, 42(12),* 1059–1062. https://doi.org/10.1130/G35926.1

Hayne, P. O., Aharonson, O., Schorghofer, N., Rubanenko, L., & Paige, D. A. (2018). Cometary volatiles in micro cold traps on the Moon. *DPS, 50,* Abstract 116.05.

Hayne, Paul O., Hendrix, A., Sefton-Nash, E., Siegler, M. A., Lucey, P. G., Retherford, K. D., et al. (2015). Evidence for exposed water ice in the Moon's south polar regions from Lunar Reconnaissance Orbiter ultraviolet albedo and temperature measurements. *Icarus, 255,* 58–69. https://doi.org/10.1016/j.icarus.2015.03.032

Head, J. W. (1975). Processes of lunar crater degradation: Changes in style with geologic time. *The Moon, 12(3),* 299–329. https://doi.org/10.1007/BF02629699

Head, J. W. & Wilson, L. (2017). Generation, ascent and eruption of magma on the Moon: New insights into source depths, magma supply, intrusions and effusive/explosive eruptions (part 2: observations). *Icarus, 283,* 176-223, https://doi.org/10.1016/j.icarus.2016.05.031

Hiesinger, H., Head, J. W., Wolf, U., Jaumann, R., & Neukum, G. (2011). Ages and stratigraphy of lunar mare basalts: A synthesis. *Geological Society of America Special Papers, 477,* 1–51. https://doi.org/10.1130/2011.2477(01)

Hurley, D. M., Lawrence, D. J., Bussey, D. B. J., Vondrak, R. R., Elphic, R. C., & Gladstone, G. R. (2012). Two-dimensional distribution of volatiles in the lunar regolith from space weathering simulations. *Geophysical Research Letters, 39(9),* L09203. https://doi.org/10.1029/2012GL051105

Jones, B. M., Aleksandrov, A., Hibbitts, K., Dyar, M. D., & Orlando, T. M. (2018). Solar wind-induced water cycle on the Moon. *Geophysical Research Letters, 45(20),* 10959-10967. https://doi.org/10.1029/2018GL080008

Kreslavsky, M. A., & Head, J. W. (2000). Kilometer-scale roughness of Mars: Results from MOLA data analysis. *Journal of Geophysical Research: Planets, 105(E11),* 26695–26711. https://doi.org/10.1029/2000JE001259

Kreslavsky, M. A., Head, J. W., Neumann, G. A., Rosenburg, M. A., Aharonson, O., Smith, D. E., & Zuber, M. T. (2013). Lunar topographic roughness maps from Lunar Orbiter Laser Altimeter (LOLA) data: Scale dependence and correlation with geologic features and units. *Icarus, 226(1),* 52–66. https://doi.org/10.1016/j.icarus.2013.04.027

Lawrence, D. J. (2017). A tale of two poles: Toward understanding the presence, distribution, and origin of volatiles at the polar regions of the Moon and Mercury. *Journal of Geophysical Research: Planets*, *122*(1), 2016JE005167. https://doi.org/10.1002/2016JE005167

Li, Y., Basilevsky, A. T., Xie, M., & Ip, W.-H. (2018). Correlations between ejecta boulder spatial density of small lunar craters and the crater age. *Planetary and Space Science*, *162*, 52–61. https://doi.org/10.1016/j.pss.2017.08.007

Li, S., Lucey, P. G., Milliken, R. E., Hayne, P. O., Fisher, E., Williams, J.-P., et al. (2018). Direct evidence of surface exposed water ice in the lunar polar regions. *Proceedings of the National Academy of Sciences, 115,* 8907–8912. https://doi.org/10.1073/pnas.1802345115

Losiak, A., Wilhelms, D. E., Byrne, C. J., Thaisen, K. G., Weider, S. Z., Kohout, T., et al. (2009). A new lunar impact crater database. *Lunar Planet. Sci., 40,* Abstract 1532.

Mahanti, P., Robinson, M. S., Thompson, T. J., & Henriksen, M. R. (2018). Small lunar craters at the Apollo 16 and 17 landing sites - morphology and degradation. *Icarus, 299,* 475–501. https://doi.org/10.1016/j.icarus.2017.08.018

Mandt, K. E., Greathouse, T. K., Retherford, K. D., Randall Gladstone, G., Jordan, A. P., Lemelin, M., et al. (2016). LRO-LAMP detection of geologically young craters within lunar permanently shaded regions. *Icarus, 273,* 114–120. https://doi.org/10.1016/j.icarus.2015.07.031

Mazarico, E., Neumann, G. A., Smith, D. E., Zuber, M. T., & Torrence, M. H. (2011). Illumination conditions of the lunar polar regions using LOLA topography. *Icarus, 211(2),* 1066–1081. https://doi.org/10.1016/j.icarus.2010.10.030

Mazrouei, S., Ghent, R. R., Bottke, W. F., Parker, A. H., & Gernon, T. M. (2019). Earth and Moon impact flux increased at the end of the Paleozoic. *Science, 363(6424),* 253–257. https://doi.org/10.1126/science.aar4058

Moon, S., Paige, D. A., Siegler, M., & Russell, P. (2019). Quantifying the connections between topographic characteristics and lunar regolith properties in the permanently shadowed regions. *AGU Fall Meeting, 100,* Abstract P51D-3402.

Needham, D. H., & Kring, D. A. (2017). Lunar volcanism produced a transient atmosphere around the ancient Moon. *Earth and Planetary Science Letters, 478,* 175–178. https://doi.org/10.1016/j.epsl.2017.09.002

Nesvorný, D., Roig, F., & Bottke, W. F. (2017). Modeling the historical flux of planetary impactors. *The Astronomical Journal, 153(3),* 103. https://doi.org/10.3847/1538-3881/153/3/103

Neumann, G. A., Glaeser, P. A., Hiesinger, H., Zuber, M. T., & Smith, D. E. (2015). Copernican-age craters and LOLA decameter-scale roughness. *Lunar Planet. Sci., 46,* Abstract 2218.

Offield, T. W., & Pohn, H. A. (1970). Lunar crater morphology and relative age determination of lunar geologic units—Part 1. Applications. U.S. Geol. Surv. Prof. Paper, 700-C, C163-C169.

Ong, L., Asphaug, E. I., Korycansky, D., & Coker, R. F. (2010). Volatile retention from cometary impacts on the Moon. *Icarus, 207(2),* 578–589. https://doi.org/10.1016/j.icarus.2009.12.012

Pike, R. J. (1977). Apparent depth/apparent diameter relation for lunar craters. *Lunar Science Conf. 8th Proceedings, 3,* 3427–3436.

Pohn, H. A., & Offield, T. W. (1970). Lunar crater morphology and relative age determination of lunar geologic units—Part 1. Classification. U.S. Geol. Surv. Prof. Pap., 700-C, C153–C162.

Pokorný, P., Janches, D., Sarantos, M., Szalay, J. R., Horányi, M., Nesvorný, D., & Kuchner, M. J. (2019). Meteoroids at the Moon: Orbital properties, surface vaporization, and impact ejecta production. *Journal of Geophysical Research: Planets, 124(3),* 752–778. https://doi.org/10.1029/2018JE005912

Putzig, N. E., Phillips, R. J., Campbell, B. A., Mellon, M. T., Holt, J. W., & Brothers, T. C. (2014). SHARAD soundings and surface roughness at past, present, and proposed landing sites on Mars: Reflections at Phoenix may be attributable to deep ground ice. *Journal of Geophysical Research: Planets, 119(8),* 1936–1949. https://doi.org/10.1002/2014JE004646

Rosenburg, M. A., Aharonson, O., Head, J. W., Kreslavsky, M. A., Mazarico, E., Neumann, G. A., et al. (2011). Global surface slopes and roughness of the Moon from the Lunar Orbiter Laser Altimeter. *Journal of Geophysical Research: Planets, 116(E2).* https://doi.org/10.1029/2010JE003716

Rubanenko, L., Mazarico, E., Neumann, G. A., & Paige, D. A. (2018). Ice in micro cold traps on Mercury: Implications for age and origin. *Journal of Geophysical Research: Planets, 123(8),* 2178–2191. https://doi.org/10.1029/2018JE005644

Rubanenko, L., & Aharonson, O. (2017). Stability of ice on the Moon with rough topography. *Icarus, 296,* 99–109. https://doi.org/10.1016/j.icarus.2017.05.028

Rubanenko, L., Venkatraman, J., & Paige, D. A. (2019). Thick ice deposits in shallow simple craters on the Moon and Mercury. *Nature Geoscience, 12(8),* 597. https://doi.org/10.1038/s41561-019-0405-8

Schorghofer, N., & Aharonson, O. (2014). The lunar thermal ice pump. *The Astrophysical Journal, 788(169),* 1–7. https://doi.org/10.1088/0004-637X/788/2/169Siegler, M. A., Miller, R. S., Keane, J. T., Laneuville, M., Paige, D. A., Matsuyama, I., et al. (2016). Lunar true polar wander inferred from polar hydrogen. *Nature*, *531*(7595), 480–484. https://doi.org/10.1038/nature17166

Smith, D. E., Zuber, M. T., Jackson, G. B., Cavanaugh, J. F., Neumann, G. A., Riris, H., et al. (2010). The Lunar Orbiter Laser Altimeter Investigation on the Lunar Reconnaissance Orbiter Mission. *Space Science Reviews, 150,* 209–241. https://doi.org/10.1007/s11214-009-9512-y

Smith, D. E., Zuber, M. T., Neumann, G. A., Mazarico, E., Lemoine, F. G., Head III, J. W., et al. (2017). Summary of the results from the Lunar Orbiter Laser Altimeter after seven years in lunar orbit. *Icarus, 283,* 70–91. https://doi.org/10.1016/j.icarus.2016.06.006

Szalay, J. R., Pokorný, P., Sternovsky, Z., Kupihar, Z., Poppe, A. R., & Horányi, M. (2019). Impact ejecta and gardening in the lunar polar regions. *Journal of Geophysical Research: Planets, 124(1),* 143–154. https://doi.org/10.1029/2018JE005756

Vasavada, A. R., Paige, D. A., & Wood, S. E. (1999). Near-surface temperatures on Mercury and the Moon and the stability of polar ice deposits. *Icarus, 141(2),* 179–193. https://doi.org/10.1006/icar.1999.6175

Wang, J. T., Kreslavsky, M. A., Liu, J. Z., Head, J. W., & Kolenkina, M. M. (2019). Quantitative characterization of impact crater materials on the Moon: Implications for degradation processes and stratigraphic age. *Lunar Planet. Sci., 50,* abstract #1262, https://www.hou.usra.edu/meetings/lpsc2019/pdf/1262.pdf

Williams, J.-P., Paige, D. A., Greenhagen, B. T., & Sefton-Nash, E. (2017). The global surface temperatures of the Moon as measured by the Diviner Lunar Radiometer Experiment. *Icarus, 283,* 300–325. https://doi.org/10.1016/j.icarus.2016.08.012

Zuber, M. T., Head, J. W., Smith, D. E., Neumann, G. A., Mazarico, E., Torrence, M. H., et al. (2012). Constraints on the volatile distribution within Shackleton crater at the lunar south pole. *Nature, 486(7403),* 378–381. https://doi.org/10.1038/nature11216

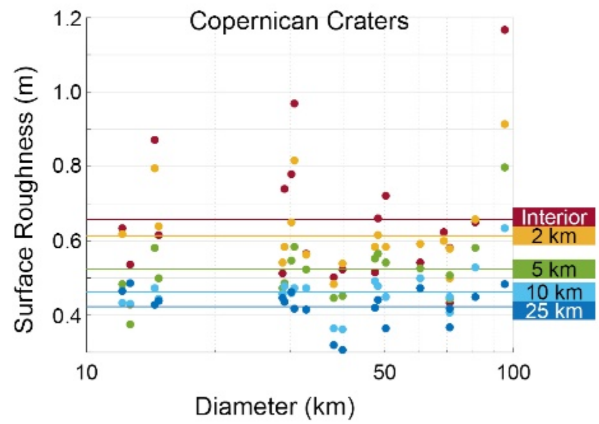

Figure 1. The roughness properties within Copernican craters (blue), and for 2-km-thick rings that are centered at various distances from the crater rim crest. Horizontal lines show the mean roughness values.

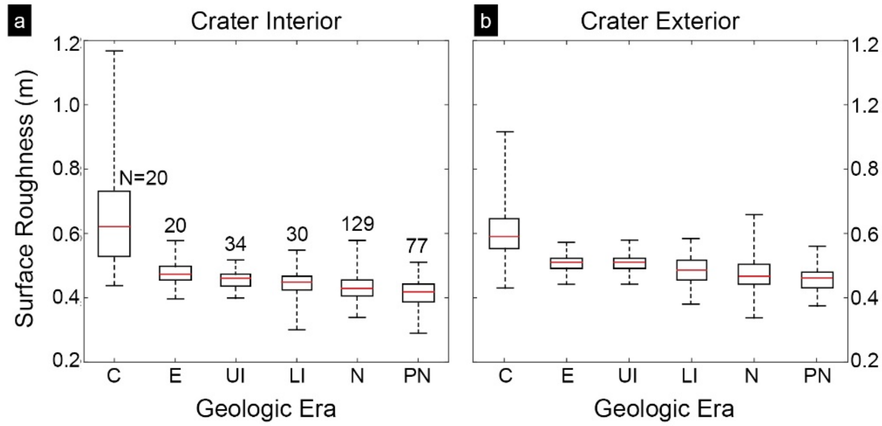

Figure 2. The mean roughness **(a)** within and **(b)** surrounding impact craters (Table S1) of different geologic eras. The box plots show the spread of data for each geologic era, increasing in age to the right: Copernican (C), Eratosthenian (E), Upper Imbrian (UI), Lower Imbrian (LI), Nectarian (N), and Pre-Nectarian (PN). For each era, the box denotes the innermost 50% of the analyzed crater population, the red line within each box denotes the median, and the dashed lines extending from the box denote the entire data range, from minimum to maximum.

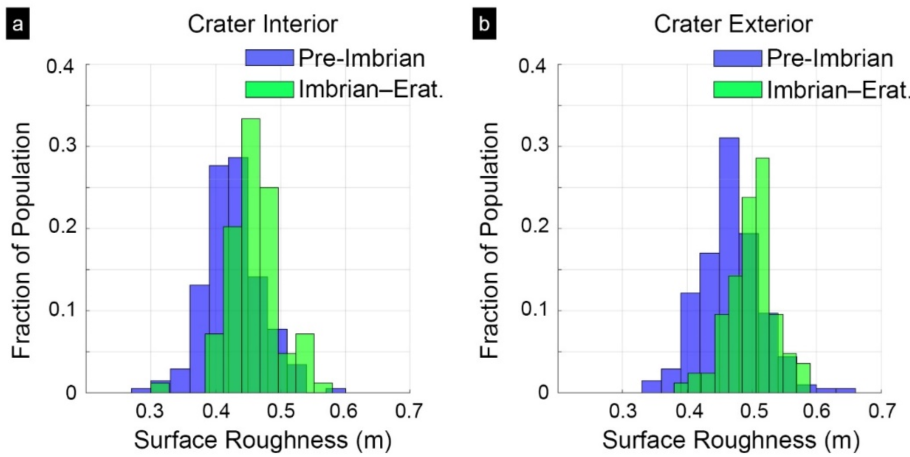

Figure 3. Histograms of the mean **(a)** interior and **(b)** exterior roughness values of Pre-Imbrian (Pre-Nectarian and Nectarian) craters in blue and of Imbrian–Eratosthenian craters in green.

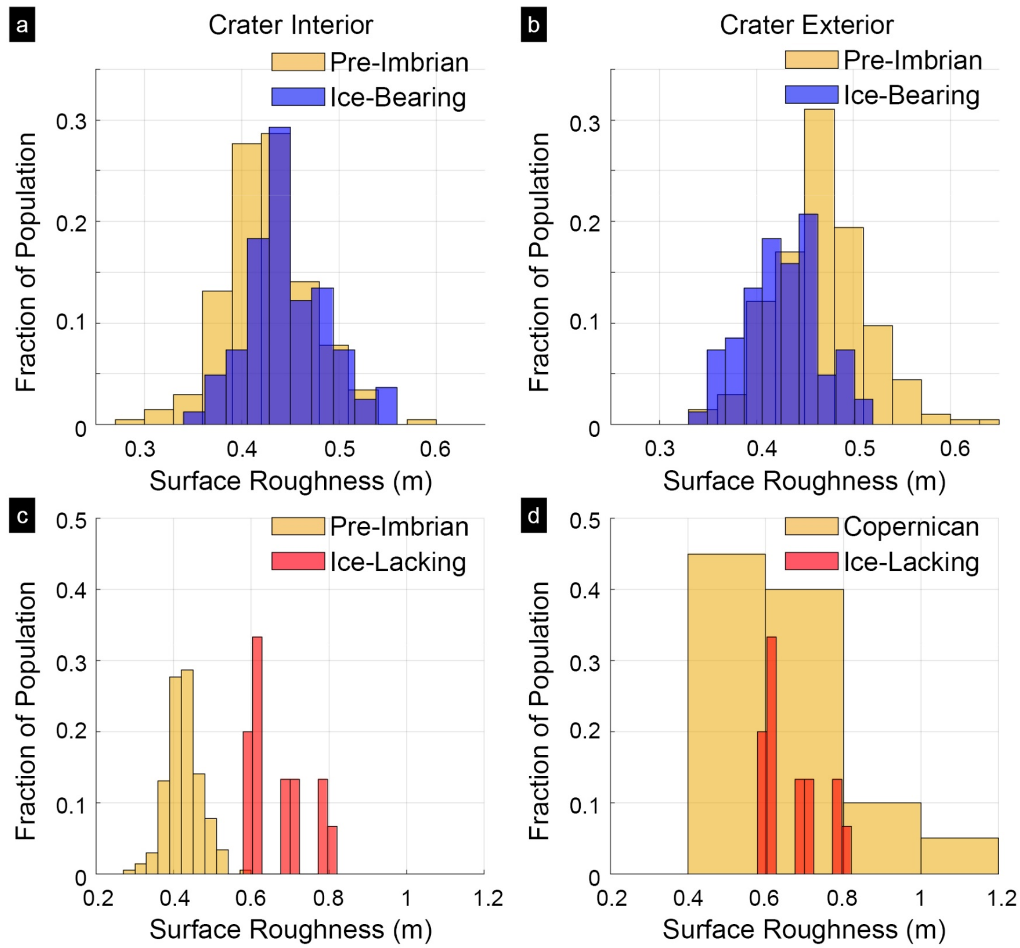

Figure 4. Histograms of the mean **(a)** interior and **(b)** exterior roughness values of 82 small ice-bearing craters (Li et al., 2018) in both polar regions and 206 craters of Nectarian and Pre-Nectarian age. Histograms of the mean interior roughness values of 15 craters lacking positive water-ice detections (Li et al., 2018) and **(c)** 206 Pre-Imbrian craters and **(d)** 20 Copernican craters.

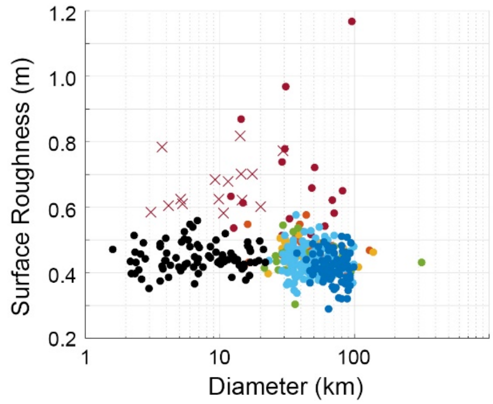

Figure 5. The mean interior roughness of craters analyzed. Ice-bearing craters (Li et al., 2018) are shown in black, and craters of different geologic eras are colored with respect to age: Copernican (red), Eratosthenian (orange), Upper Imbrian (yellow), Lower Imbrian (green), Nectarian (light blue), and Pre-Nectarian (blue). Craters that lack positive water-ice detections (Li et al., 2018) and lie distinctly within the Copernican-only domain of roughness space are denoted by red X's.

Supporting material

Introduction

In the following sections, we discuss in detail how the LPI crater database is used to determine the ages of lunar craters and potential limitations with the database. We then discuss how crater roughness does not depend on crater diameter in a statistically significant manner.

Determining the ages of lunar craters

In order to determine the surface roughness properties for craters formed in different geologic eras, we utilize the LPI lunar crater database, which was originally developed in 2008 by various LPI summer interns and has since been updated and revised in various years, through 2015. Details regarding the construction of this database are discussed in the Losiak et al. (2009) LPSC abstract (https://www.lpi.usra.edu/meetings/lpsc2009/pdf/1532.pdf), and the "Lunar Impact Crater Database (2015)" that we utilize is publically available for download at https://www.lpi.usra.edu/scientific-databases/.

The comprehensive database provides a wealth of information on lunar impact craters, most fundamentally the names, diameters, and locations of the craters. The database also includes various measured or calculated physical and morphological characteristics (e.g., crater dimensions, and transient cavity, ejecta, melt, and central peak properties). For some craters, the database also includes crater age classifications (Pre-Nectarian, Nectarian, Lower Imbrian, Upper Imbrian, Eratosthenian, or Copernican). All ages included in the database are compiled from previous works, including Wilhelms

(1987), Wilhelms (personal communication, 2008), and Wilhelms and Byrne (2009). These original studies use various geologic principles of stratigraphy for relative dating (Wilhelms, 1987; Wilhelms and Byrne, 2009). These studies do not utilize surface roughness as a tool for estimating the formation period of the craters, although sometimes use crater morphologies (sharp vs. degraded) or slope measurements (steep vs. gentle) in absence of good stratigraphic control (Wilhelms, 1987; Wilhelms and Byrne, 2009).

In our analysis, we utilize impact craters from the LPI crater database that are <100 km in diameter, thereby avoiding larger peak-ring or multi-ring basins (Baker et al., 2012, 2017). All of the craters that we analyze (Table S1) are between 40°N–90°N or 40°S–90°S, covering the entire extent of the Lunar Orbiter Laser Altimeter (LOLA) Digital Roughness Maps that we use (LDRM_40S_1000M; LDRM_40N_1000M; http://imbrium.mit.edu/DATA/LOLA_GDR /). We do not include any impact craters that have more than one age classification reported for its age (e.g., Upper Imbrian and Lower Imbrian) and we do not include craters that are reported in the database to have qualifiers (e.g., "Possibly Nectarian" or "Probably Upper Imbrian").

Variation in crater roughness with crater size

We analyze the roughness properties of lunar craters (~10–100 km) with respect to their size, and find that crater roughness does not depend on crater diameter in a statistically significant manner (Fig. S1). Therefore, we find it appropriate to directly compare the roughness properties of 10–100 km-diameter craters from the LPI database (Losiak et al., 2009) that have been classified into geologic eras to the roughness properties of smaller (<~15 km in diameter) craters that are not included in the LPI database.

References

Baker, D. M. H., Head, J. W., Neumann, G., Smith, D. E., & Zuber, M. T, (2012). The transition from complex craters to multi-ring basins on the Moon: Quantitative geometric properties from Lunar Reconnaissance Orbiter Lunar Orbiter Laser Altimeter (LOLA). *Journal of Geophysical Research: Planets, 117,* E00H16. https://doi.org/10.1029/2011JE004021

Baker, D. M. H., Head, J. W., Phillips, R. J., Neumann, G. A., Bierson, C. J., Smith, D. E., & Zuber, M. T., (2017). GRAIL gravity observations of the transition from complex crater to peak-ring basin on the Moon: Implications for crustal structure and impact basin formation. *Icarus, 292,* 54–73. https://doi.org/10.1016/j.icarus.2017.03.024

Losiak, A., Wilhelms, D. E., Byrne, C. J., Thaisen, K. G., Weider, S. Z., Kohout, T., et al. (2009). A new lunar impact crater database. *Lunar and Planetary Science Conference, 40*, Abstract 1532.

Wilhelms D. E., (1987). The geologic history of the Moon: U.S. Geological Survey Professional Paper, 1348, p. 302.

Wilhelms, D. E., & Byrne, C. J., (2009). Stratigraphy of lunar craters, Image again online: http://www.imageagain.com/Strata/StratigraphyCraters.2.0.htm.

Table S1. The location, size, and formation era of impact craters analyzed in this study.

Crater name	Latitude (°N)	Longitude (°E)	Diameter (km)	Age
Schomberger A	-78.61	23.52	29.44	Copernican
Zucchius	-61.38	-50.65	63.18	Copernican
Rutherfurd	-61.15	-12.25	49.98	Copernican
Fechner T	-58.74	122.82	14.33	Copernican
Reimarus H	-49.26	62.23	11.17	Copernican
Guthnick	-47.76	-94.04	37.03	Copernican
Janssen K	-46.19	42.31	15	Copernican
Tycho	-43.3	-11.22	85.29	Copernican
Anaxagoras	73.48	-10.17	51.9	Copernican
Philolaus	72.22	-32.88	71.44	Copernican
Carpenter	69.52	-51.23	59.06	Copernican
Hayn	64.56	83.87	86.21	Copernican
Bel'kovich K	63.63	93.61	47.03	Copernican
Thales	61.74	50.27	30.75	Copernican
Birkhoff Z	60.98	-145.88	28.63	Copernican
Harpalus	52.73	-43.49	39.77	Copernican
Burg	45.07	28.21	41.04	Copernican
Eudoxus	44.27	16.23	70.16	Copernican
Wiener F	41.19	149.97	44.92	Copernican
Wiechert J	-85.2	-177.64	34.89	Eratosthenian
Moretus	-70.63	-5.95	114.45	Eratosthenian
Helmholtz D	-66.38	54.09	44.59	Eratosthenian
Grotrian	-66.15	128.28	36.78	Eratosthenian
Hommel B	-55.34	36.94	33.02	Eratosthenian
Biela C	-54.28	53.5	26.89	Eratosthenian
Rydberg	-46.43	-96.43	48.03	Eratosthenian
Rozhdestvenskiy K	82.19	-147.01	42.87	Eratosthenian
Scoresby	77.73	14.13	54.93	Eratosthenian
Ricco	74.92	177.05	65.83	Eratosthenian
Kirkwood	68.34	-156.66	68.12	Eratosthenian
Hayn E	67.02	66.1	41.64	Eratosthenian
Pythagoras	63.68	-62.98	144.55	Eratosthenian
Archytas	58.87	4.99	31.95	Eratosthenian
Tsinger Y	57.68	175.25	32.36	Eratosthenian

Rowland J	52.72	-155.84	49.85	Eratosthenian
Aristoteles	50.24	17.32	87.57	Eratosthenian
Sharp A	47.62	-42.67	17.26	Eratosthenian
Petrie	45.14	108.47	32.86	Eratosthenian
Cepheus	40.68	45.78	39.43	Eratosthenian
Schomberger	-76.64	24.69	85.8	Upper Imbrian
Le Gentil A	-74.63	-52.63	37	Upper Imbrian
Hale	-74.13	91.71	84.42	Upper Imbrian
Neumayer M	-71.73	80.36	35.44	Upper Imbrian
Doerfel S	-69.77	-120.48	29.12	Upper Imbrian
Antoniadi	-69.3	-173.06	137.92	Upper Imbrian
Lyman	-64.96	162.47	83.25	Upper Imbrian
Pontecoulant J	-61.74	64.26	39.54	Upper Imbrian
Hagecius K	-61.26	52.08	31.36	Upper Imbrian
Pikel'ner	-48.37	124.25	40.96	Upper Imbrian
Faraday G	-45.92	10.06	29.62	Upper Imbrian
Carver L	-45.78	128.8	24.61	Upper Imbrian
Lovelace	82.08	-109.51	57.06	Upper Imbrian
Plaskett	81.63	176.71	114.34	Upper Imbrian
Schjellerup	69.04	158.24	62.82	Upper Imbrian
Gamow U	66.39	136.6	32	Upper Imbrian
C. Mayer	63.26	17.31	37.54	Upper Imbrian
Timaeus	62.91	-0.55	32.81	Upper Imbrian
Democritus	62.31	34.99	37.78	Upper Imbrian
van't Hoff F	61.18	-126.78	45.16	Upper Imbrian
Xenophanes A	60.07	-84.83	43.18	Upper Imbrian
Endymion C	58.37	60.55	32.74	Upper Imbrian
Stormer	57.14	146.65	68.62	Upper Imbrian
d'Alembert Z	55.25	165.77	41.7	Upper Imbrian
Endymion A	54.61	62.56	29.75	Upper Imbrian
Markov	53.43	-62.84	39.92	Upper Imbrian
Keldysh	51.23	43.65	32.75	Upper Imbrian
Bianchini	48.78	-34.37	37.59	Upper Imbrian
McLaughlin U	47.06	-96.99	31.63	Upper Imbrian
Rayet	44.65	114.5	27.76	Upper Imbrian
Perrine T	41.94	-130.33	33.71	Upper Imbrian
Mairan	41.6	-43.5	39.49	Upper Imbrian
Lacchini	41.29	-107.83	57.95	Upper Imbrian
Von Neumann	40.28	153.25	74.83	Upper Imbrian

Boguslawsky F	-75.42	52.97	31.05	Lower Imbrian
Schrodinger	-74.73	132.93	316.39	Lower Imbrian
Zeeman Y	-72.47	-137.7	32.21	Lower Imbrian
Wexler	-68.88	90.71	52.44	Lower Imbrian
Dawson	-66.99	-135.05	44.32	Lower Imbrian
Watson G	-63.2	-120.26	31.17	Lower Imbrian
Scheiner B	-59.7	-33.57	29.1	Lower Imbrian
Hommel Q	-56.18	38.31	28.18	Lower Imbrian
Vlacq G	-55	38.01	27.11	Lower Imbrian
Mendel J	-51.51	-107.2	57.59	Lower Imbrian
Grissom M	-49	-148.42	38.73	Lower Imbrian
Alder	-48.63	-177.88	82.12	Lower Imbrian
Crocco G	-47.43	152.52	40.18	Lower Imbrian
Brianchon T	75.28	-99.31	29.25	Lower Imbrian
Karpinskiy	72.61	166.8	91.4	Lower Imbrian
Desargues M	68.42	-74.42	27.47	Lower Imbrian
Fontenelle	63.42	-18.96	37.68	Lower Imbrian
Babbage A	59.14	-55.65	32.28	Lower Imbrian
van't Hoff N	57.62	-132.88	46.96	Lower Imbrian
Protagoras	56.02	7.34	21.05	Lower Imbrian
Kramers U	53.9	-133.03	38.58	Lower Imbrian
van Rhijn T	52.13	140.11	32.96	Lower Imbrian
Slipher	49.28	160.27	74.65	Lower Imbrian
Egede	48.72	10.64	34.18	Lower Imbrian
Campbell Z	48.58	153	23.78	Lower Imbrian
Millikan R	45.75	117.84	48.99	Lower Imbrian
Montgolfier P	45.71	-161.29	36.24	Lower Imbrian
Gullstrand	44.95	-129.67	45.05	Lower Imbrian
Fowler C	44.78	-142.1	35.05	Lower Imbrian
Bragg H	41.47	-101.35	36.61	Lower Imbrian
Wiechert P	-85.13	151.76	38.62	Nectarian
De Forest N	-79.17	-165.76	40.09	Nectarian
Boussingault A	-69.96	53.87	75.4	Nectarian
Curtius	-67.08	4.4	99.29	Nectarian
Cysatus	-66.21	-6.34	47.77	Nectarian
Pentland C	-65.06	16.43	32.13	Nectarian
Curtius B	-63.76	4.63	40.26	Nectarian
Lyman V	-62.74	152.88	37.19	Nectarian
Lemaitre S	-61.8	-156.81	34.51	Nectarian

Lemaitre F	-61.51	-148.53	33.94	Nectarian
Lemaitre	-61.36	-149.98	93.7	Nectarian
Moulton H	-61.16	100.64	50.65	Nectarian
Zach	-60.92	5.25	68.54	Nectarian
Jacobi C	-59.85	10.49	33.91	Nectarian
Priestley K	-58.96	110.41	33.74	Nectarian
Chamberlin	-58.83	96.04	60.41	Nectarian
Fechner	-58.25	125.03	59.32	Nectarian
Haret C	-57.6	-173.7	28.47	Nectarian
Rosenberger D	-57.6	43.04	46.58	Nectarian
Hommel C	-54.91	29.82	51.41	Nectarian
Poincare Z	-53.9	164.31	34.88	Nectarian
Longomontanus C	-53.49	-19.11	31.54	Nectarian
Boyle	-53.29	177.89	57.13	Nectarian
Baco A	-52.99	20.21	38.71	Nectarian
Karrer	-52.06	-142.28	55.56	Nectarian
Bayer	-51.62	-35.14	48.51	Nectarian
Pikel'ner K	-51.01	125.48	33.25	Nectarian
Hopmann	-51.01	159.23	87.84	Nectarian
Tseraskiy P	-50.96	139.33	38.34	Nectarian
Pitiscus	-50.61	30.57	79.85	Nectarian
Lebedev K	-50.02	109.36	20.99	Nectarian
Cassegrain B	-49.57	114.64	26.97	Nectarian
Garavito Q	-49.37	153.93	45.93	Nectarian
Hagen J	-49.23	137.91	42.79	Nectarian
Lyot A	-48.99	79.94	38.39	Nectarian
Noggerath	-48.82	-45.84	32.12	Nectarian
Vlacq D	-48.73	36.17	31.93	Nectarian
Tseraskiy	-48.66	142.64	65.59	Nectarian
Mallet B	-46.71	52.17	32.04	Nectarian
Spallanzani	-46.38	24.73	30.86	Nectarian
Lockyer	-46.27	36.59	35.08	Nectarian
Licetus F	-46.07	0.94	28.89	Nectarian
Nansen A	82.83	65	44.92	Nectarian
Sylvester	82.65	-81.22	59.28	Nectarian
De Sitter M	81.11	37.57	75.52	Nectarian
De Sitter	79.81	38.57	63.79	Nectarian
Poncelet A	79.58	-75.58	30.96	Nectarian

Milankovic E	77.57	-177.49	49.3	Nectarian
Petermann D	77.15	66.52	33.57	Nectarian
Milankovic	76.53	171.35	94.21	Nectarian
Shi Shen	75.78	104.13	46.52	Nectarian
Merrill	74.83	-117.45	56.99	Nectarian
Petermann	74.35	67.89	76.95	Nectarian
Shi Shen Q	73.99	96.18	33.85	Nectarian
Cusanus	71.82	69.4	60.87	Nectarian
Hippocrates	70.26	-146.54	59.24	Nectarian
Schwarzschild L	69.08	121.83	45.38	Nectarian
Schjellerup R	68.61	151.5	49.75	Nectarian
Roberts N	68.39	-175.91	49.15	Nectarian
Hayn F	68.01	85.75	62.54	Nectarian
Epigenes	67.5	-4.62	54.51	Nectarian
Schwarzschild K	67.35	124.81	40.97	Nectarian
Nother	66.35	-114.18	64.8	Nectarian
Gamow V	66.13	139.26	44.96	Nectarian
Nother T	65.95	-121.86	44.9	Nectarian
Dugan	64.12	103.11	49.65	Nectarian
Emden U	64.1	178.24	39.07	Nectarian
Emden D	63.87	-171.25	44.85	Nectarian
Dyson B	63.33	-118.27	49.64	Nectarian
Hayn A	63.01	71.11	52.28	Nectarian
Paneth	62.6	-94.63	60.92	Nectarian
Oberth	62.49	154.84	49.52	Nectarian
Zsigmondy A	62.48	-102.42	61.2	Nectarian
Strabo	61.94	54.42	54.72	Nectarian
Yablochkov U	61.88	120.28	30.73	Nectarian
Cleostratus F	61.53	-80.58	49.22	Nectarian
Dyson	60.87	-121.71	63.14	Nectarian
Cleostratus	60.32	-77.4	63.23	Nectarian
Smoluchowski	60.22	-96.91	84.26	Nectarian
C. Mayer B	60.19	15.44	32.7	Nectarian
Endymion B	59.86	67.75	59	Nectarian
Zsigmondy	59.52	-105.3	66.88	Nectarian
Olivier	58.72	138.44	78.45	Nectarian
Bel'kovich A	58.65	87.41	57.26	Nectarian
Dyson M	58.17	-121.53	31.5	Nectarian
Birkhoff K	57.4	-144.81	58.23	Nectarian

Coulomb C	57.17	-111.38	34.17	Nectarian
Tsinger	56.54	175.71	44.21	Nectarian
van't Hoff M	56.41	-132.51	39.95	Nectarian
Birkhoff L	56.34	-145.34	35.15	Nectarian
Coulomb	54.46	-115	89.72	Nectarian
Regnault	54.04	-87.88	51.31	Nectarian
Paraskevopoulos Y	52.95	-150.88	48.09	Nectarian
Ellison P	52.62	-110.08	31.91	Nectarian
Compton R	52.52	91.06	34.37	Nectarian
van Rhijn	52.47	146.37	46.16	Nectarian
Mercurius M	50.85	74.12	41.52	Nectarian
Boss L	50.85	82.48	40.95	Nectarian
Repsold G	50.55	-80.65	43.98	Nectarian
Coulomb P	50.26	-117.74	35.7	Nectarian
Debye E	50.11	-170.83	40.97	Nectarian
Weber	50.06	-123.79	43.95	Nectarian
De Moraes	49.38	143	54.41	Nectarian
Sarton	49.12	-121.14	71.33	Nectarian
De Moraes S	48.75	140.48	43.19	Nectarian
Duner A	47.12	179.78	37	Nectarian
Perkin	47.02	-175.73	62.48	Nectarian
Chernyshev	47.01	174.41	59.31	Nectarian
Millikan	46.76	121.52	93.97	Nectarian
Mercurius	46.66	66.07	64.3	Nectarian
Wegener	45.21	-113.81	95.78	Nectarian
Zeno	45.15	72.98	66.78	Nectarian
Schlesinger M	45	-138.71	44.15	Nectarian
Pawsey	44.24	145.29	59.98	Nectarian
Langevin	44.17	162.69	57.8	Nectarian
Millikan Q	43.74	118.67	32.4	Nectarian
Bridgman	43.39	136.98	81.89	Nectarian
Chandler G	43.23	175.71	32.12	Nectarian
Wegener K	43.18	-112.26	31.16	Nectarian
Quetelet	42.66	-135.3	54.77	Nectarian
Quetelet T	42.52	-137.99	46.98	Nectarian
Becquerel X	42.02	128.21	34.24	Nectarian
Perrine S	41.97	-128.87	61.6	Nectarian
Chandler P	41.54	170.15	65.59	Nectarian

Schneller	41.34	-163.73	56.87	Nectarian
Hooke	41.14	54.86	34.35	Nectarian
Becquerel E	40.95	131.45	30.45	Nectarian
Ehrlich	40.82	-172.27	33.58	Nectarian
Kurchatov W	40.14	140.31	31.85	Nectarian
Newton G	-78.08	-18.96	62.47	pre-Nectarian
Alekhin	-67.94	-131.85	74.82	pre-Nectarian
Curtius D	-64.7	8.35	57.19	pre-Nectarian
Gill	-63.77	75.95	63.9	pre-Nectarian
Nearch	-58.58	39.01	72.79	pre-Nectarian
Jeans N	-58.52	90.62	66.69	pre-Nectarian
Hagecius A	-58.26	47.1	54.33	pre-Nectarian
Asclepi	-55.19	25.52	40.56	pre-Nectarian
Hess	-54.47	174.19	90.44	pre-Nectarian
Vlacq	-53.39	38.69	89.21	pre-Nectarian
Brisbane Z	-52.89	72.82	64.73	pre-Nectarian
Rosenberger C	-52.28	42.2	46.67	pre-Nectarian
Rosenberger B	-52.06	46.21	33.76	pre-Nectarian
Lyot H	-51.5	78	63.59	pre-Nectarian
Cuvier	-50.29	9.69	77.3	pre-Nectarian
Brisbane E	-50.26	71.41	57.35	pre-Nectarian
Brisbane	-49.2	68.76	44.32	pre-Nectarian
Peirescius D	-48.17	72.11	42.8	pre-Nectarian
Reimarus	-47.69	60.42	47.62	pre-Nectarian
Licetus	-47.19	6.54	75.42	pre-Nectarian
Peirescius	-46.4	67.8	61.53	pre-Nectarian
Peary	88.63	24.4	78.75	pre-Nectarian
Rozhdestvenskiy W	85.89	114.64	74.96	pre-Nectarian
Byrd	85.43	10.07	97.49	pre-Nectarian
Nansen F	84.95	62.44	61.62	pre-Nectarian
Poinsot	78.9	-146.21	65.11	pre-Nectarian
De Sitter L	78.86	34.52	69.4	pre-Nectarian
Mouchez	78.38	-26.82	82.78	pre-Nectarian
Poncelet C	77.56	-74.5	67.95	pre-Nectarian
Euctemon	76.26	30.57	62.7	pre-Nectarian
Poncelet	75.91	-54.57	67.57	pre-Nectarian
Thiessen	74.86	-169.5	66.39	pre-Nectarian
Baillaud	74.61	37.35	89.44	pre-Nectarian

Philolaus D	74.37	-27.66	91.35	pre-Nectarian
Seares	73.74	147.23	99.5	pre-Nectarian
Anaximenes	72.49	-44.98	81.12	pre-Nectarian
Meton D	72.16	24.46	78.77	pre-Nectarian
Mezentsev	71.77	-129.64	84.51	pre-Nectarian
Philolaus C	71.23	-32.82	98.14	pre-Nectarian
Roberts	70.66	-174.25	89.37	pre-Nectarian
Meton C	70.45	18.87	86.12	pre-Nectarian
Desargues	70.25	-73.42	84.85	pre-Nectarian
Mezentsev M	68.29	-127.59	84.62	pre-Nectarian
Anaximander B	68.08	-61.21	79.1	pre-Nectarian
Arnold	66.98	35.83	93.13	pre-Nectarian
Anaximander	66.97	-51.44	68.71	pre-Nectarian
Anaximander D	65.78	-50.68	96.63	pre-Nectarian
Boole	63.79	-87.29	61.34	pre-Nectarian
Boole H	61.73	-88.83	82.4	pre-Nectarian
Tikhov	61.66	172.29	83.97	pre-Nectarian
Birkhoff X	61.62	-150.42	76.58	pre-Nectarian
Zsigmondy S	59.36	-107.28	66.76	pre-Nectarian
Dyson Q	59.19	-126.13	93.24	pre-Nectarian
Babbage D	58.65	-61.17	70.96	pre-Nectarian
Omar Khayyam	58.21	-102.22	68.64	pre-Nectarian
Yamamoto	58.16	161.87	77.46	pre-Nectarian
Oenopides	57.13	-64.2	73.47	pre-Nectarian
Olivier N	56.63	137.08	60.77	pre-Nectarian
Chappell	54.53	-176.77	73.92	pre-Nectarian
Endymion J	53.51	50.71	66.05	pre-Nectarian
Kramers	53.28	-127.98	61.59	pre-Nectarian
von Bekesy	51.92	126.73	96.25	pre-Nectarian
Paraskevopoulos	50.09	-150.34	98.87	pre-Nectarian
Chapman	50.09	-100.47	76.83	pre-Nectarian
Paraskevopoulos S	48.57	-155.26	71.45	pre-Nectarian
McLaughlin C	48.17	-91.79	57.55	pre-Nectarian
Esnault-Pelterie	47.41	-141.83	76.79	pre-Nectarian
Schlesinger	47.12	-138.98	97.28	pre-Nectarian
Montgolfier	47.06	-160.08	83.71	pre-Nectarian
McLaughlin	47.01	-92.83	75.29	pre-Nectarian
Rynin	46.78	-103.73	77.88	pre-Nectarian

Duner	44.68	179.46	65.07	pre-Nectarian
Schumacher	42.42	60.81	61.31	pre-Nectarian
Bragg	42.33	-103.44	77.21	pre-Nectarian
Von Zeipel	42.19	-141.93	83.41	pre-Nectarian
Becquerel	40.79	129.5	62.86	pre-Nectarian
Alexander	40.25	13.69	94.8	pre-Nectarian

Table S2. The location and size of small craters analyzed in this study that do have surface water-ice detections (Li et al., 2018).

Crater name	Latitude (°N)	Longitude (°E)	Diameter (km)
Kuhn	-84.48	207.52	16.6
-	-84.89	-153.89	12.67
-	-84.55	-150.63	6.3
-	-85.31	-150.05	6.99
-	-85.51	-119.86	1.59
-	-85.61	-119.56	2.51
-	-86.73	-127.67	2.96
-	-86.79	-127.02	2.6
-	-86.57	-15.98	4.98
Ibn Bajja	-86.3	284.96	11.98
-	-84.27	-13.05	10.48
-	-85.8	-15.34	5.65
-	-86.57	-18.05	5.76
-	-87.53	-24.8	5.55
-	-87.56	-26.51	5.76
-	-87.5	-12.34	6.14
-	-89.51	-80.28	15.06
-	-89.23	-18.5	3.98
-	-88.7	-13.11	14.3
-	-87.6	-47.2	13.35
-	-87.87	-132.74	4.87
-	-79.93	-171.56	2.35
-	-84.08	176.98	4.97
-	-87.99	166.52	3.69
-	-88.27	156.15	6.04
-	-88.05	89.15	2.72
-	-88.58	85.59	2.39
-	-89.3	19.9	3.99
-	-89.39	16.77	3.92
-	-88.46	57.9	5.73
-	-87.84	40.32	2.79
-	-88.28	39.13	2.33
-	-87.98	55.76	3.6
-	-88.04	50.78	7.56
-	-88.73	165.15	14.88

-	-87.63	28.35	4.11
-	-87.13	40.97	8.11
-	-86.98	32.53	4.76
-	-87.11	26.79	2.29
-	-87.03	15.03	4.17
-	-86.39	31.46	13.59
-	-84.61	30.42	4.3
-	-86.79	53.38	6.93
-	-83.81	60.88	6.35
-	-86.79	77.67	2.21
Malinkin	-87.22	75.94	8.28
-	-84.27	55.96	15.97
-	-82.34	60.71	2.58
-	81.52	-146.28	9.41
-	82.36	-162.63	16.9
-	81.38	121.17	6.32
-	82.84	141.19	10.87
-	84.44	-91.08	12.34
-	88.26	-170.78	5.46
Aepinus	87.96	250.31	16.74
-	87.79	125.52	12.2
Bosch	86.81	133.54	19.58
-	87.41	110.01	6
-	87.57	113.9	2.15
-	84.39	97.79	15.99
-	81.26	107.78	8.51
-	83.77	85.69	10.15
Nansen E	83.36	72.7	15.12
-	84.13	76.75	14.57
Nansen D	83.88	65.81	21.66
-	88.22	45.03	3.59
-	88.26	25.29	7.01
Erlanger	86.99	28.62	10.93
-	86.34	53.48	10.49
-	88.11	-8.19	4.72
-	87.12	-33.46	6.81
-	87.01	-36.93	5.37
-	87.4	-29.25	3.79
-	87.18	-61.15	5.83

Hermite A	87.94	308.98	19.86
-	87.13	-86.35	8.49
Grignard	84.54	284.17	12.95
Gore	86.18	297.69	9.41
Poncelet Q	79.93	299.42	14
Fibiger	86.14	37.13	21.1
-	82.26	64.22	18.23
-	79.21	41.24	6.52

Table S3. The location and size of small impact craters analyzed in this study that do not have surface water-ice detections (Li et al., 2018) and have enhanced roughness properties suggestive of Copernican ages.

Crater name	Latitude (°N)	Longitude (°E)	Diameter (km)
Wapowski	-83.08	53.79	11.45
Simpelius J	-75.86	8.11	17.54
-	-77.07	96.47	5.11
-	-77.42	120.46	10.56
-	-81.93	135.44	9.15
-	-82	156.94	5.28
-	-76	115.27	4.17
Schomberger A	-78.61	23.52	29.44
-	-83.13	24.22	3.06
Sylvester N	82.41	291.32	19.98
Whipple	89.14	120.02	14.53
Main L	81.44	22.73	14.32
-	84.85	35.72	9.77
-	75.44	140.93	14.21
-	79.97	-81.2	3.7

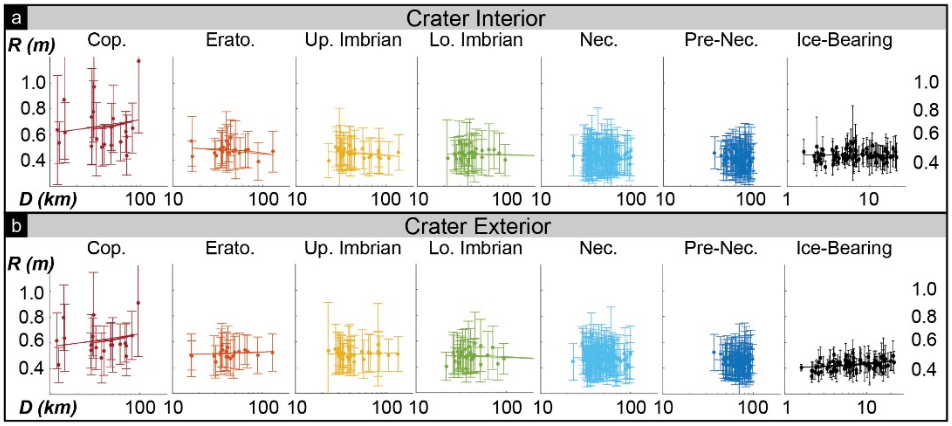

Figure S1. The mean roughness for the (a) interior and (b) exterior of different-sized impact craters from different geologic eras (Table S1), as well as craters identified as ice-bearing (Table S2; Li et al., 2018). Error bars associated with each surface roughness measurement are plotted, representing the standard deviation from the mean. Also shown are formal linear regression lines, however correlation between roughness and diameter is not statistically significant for any data subset. Note that crater diameter is shown on a log-scale.

Chapter 4

The flux of volcanic eruptions on Mercury:

Potential contributions to transient atmospheres and buried polar deposits

Ariel N. Deutsch[a], James W. Head III[a], Stephen, W. Parman[a], Lionel Wilson[a,b],

Gregory A. Neumann[b], Finnian Lowden[a]

[a]Department of Earth, Environmental and Planetary Sciences, Brown University, Providence, RI 02912, USA

[b]Lancaster Environment Centre, Lancaster University, Lancaster LA1 4YQ, UK

[c]NASA Goddard Space Flight Center, Greenbelt, MD 20771, USA

In review in *Earth and Planetary Science Letters* (MS EPSL-D-20-00151)

Deutsch, A. N., Head, J. W., Parman, S. W., Wilson, L. Neumann, G. A., Lowden, F., *In review*. The flux of volcanic eruptions on Mercury: Potential contributions to transient atmospheres and buried polar deposits. *Earth and Planetary Science Letters.*

Abstract

The surface of Mercury is dominated by extensive, widespread lava plains that primarily formed early in its history. The emplacement of these lavas was accompanied by the release of magmatic volatiles, the bulk of which were lost to space via thermal escape or photodissociation. Here we consider whether these erupted volatiles left any trace by quantifying the volumes of erupted volcanic plains and the associated volumes of erupted volatiles. The actual volatile species present within Mercury's magmas remain unknown, but we use a variety of experimental petrology studies to predict the dominant species and their abundances. We provide estimates for both low-gas and high-gas scenarios for oxygen fugacity (fO_2) values between iron-wüstite-3 and -7. The volumes of erupted volatiles are greater under lower fO_2 conditions. We calculate that the average duration of a transient volcanic atmosphere would be between ~500 and ~40,000 years, depending on the volume, degassed volatile content, and eruption rate of an individual eruption, as well as the fO_2 conditions. If a transient dense atmosphere was surface-bound long enough for the released volatiles to be transported to and cold-trapped at Mercury's polar regions, the volatiles are predicted to exist as a diffuse layer beneath at least 16 m of regolith. These volatiles would have a composition and age distinctly different from the H_2O-ice deposits observed at the poles of Mercury today.

1 Introduction

Discovering that Mercury is volatile rich is one of the most exciting findings of the MErcury Surface, Space ENvironment, GEochemistry, and Ranging (MESSENGER) mission given its heliocentric distance. Mercury has abundant and widely distributed pyroclastic deposits indicative of volatile-rich eruptions (e.g., Head et al., 2009; Kerber et al., 2009). The size of these deposits suggests that they formed from an eruptive process that was even more volatile-rich than the process that formed lunar pyroclastic deposits (Kerber et al., 2009). Mercury also has intriguing hollows, which are bright, irregularly-shaped depressions suggestive of sublimation, implying that abundant volatiles are present beneath the surface (Blewett et al., 2011). Additionally, MESSENGER X-Ray Spectrometer (XRS) and Gamma-Ray Spectrometer (GRS) measurements revealed elevated abundances of the volatiles K, C, S, Na, and Cl, indicating that the planet is volatile-rich (e.g., Nittler et al. 2011; Peplowski et al. 2012, 2014; Evans et al. 2015).

Mercury has been extensively resurfaced by large expanses of lava plains (Fig. 1) (Head et al., 2009, 2011; Denevi et al., 2013; Byrne et al., 2016, 2018) and magmatism is a primary mechanism by which volatiles are transferred from the interiors of planets to the surface (e.g., Moore, 1970; Greeley, 1987). For example, laboratory analyses of Apollo samples revealed the presence of volatiles (H_2O as well as CO_2, F, S, and Cl) trapped in primitive magmas (e.g., Saal et al., 2008), suggesting that lunar volcanism has effectively transferred indigenous volatiles to the surface of the Moon. Understanding the overall flux of volatiles delivered to the lunar surface has important implications for the geochemical, thermal, and atmospheric evolution of the Moon.

Needham and Kring (2017) recently estimated that ~10^{16} kg of CO and S and ~10^{14} kg of H_2O were released during the formation of lunar lava plains (the maria), with the bulk of volatiles being released during peak mare emplacement ~3.5 Ga. The mare-erupted volatiles may have even been present in sufficient volumes to produce a transient atmosphere (Needham and Kring, 2017), although the duration of and intervals between mare-forming eruptions have an important control on the density and lifetime of any volcanically-derived atmosphere (Wilson et al., 2019). Interestingly, the production of a substantially dense atmosphere would aid in the transport of volatiles to cold-trapping regions, and volcanically-derived volatiles are predicted to be cold-trapped at the lunar poles today (e.g., Arnold, 1979; Crotts and Hummels, 2009; Needham and Kring, 2017).

If volcanism released substantial volatiles on the Moon during the production of the maria (Needham and Kring, 2017), it is possible that substantial volatiles were also released on Mercury during the production of volcanic plains, albeit with different chemical species and abundances (Nittler et al., 2011; Zolotov et al., 2013). Here we seek to understand the flux, timing, and potential fate of the erupted volatiles. We analyze the flux of volcanism that produced the widespread plains on Mercury, and estimate the flux of released gases associated with these eruptions, specifically for volatiles predicted to be indigenous to the planet. We discuss the potential fate of erupted volatiles and their relationship to volatiles observed in high-latitude cold traps on Mercury (e.g., Lawrence et al., 2013).

2 Methods

2.1 Flux of volcanism on Mercury

Similar to the approach used by Needham and Kring (2017) to estimate the flux of lunar mare volcanism, we estimate the production of basalt released through time during the emplacement of volcanic plains on Mercury. Establishing this production function requires knowledge of the volume (Section 2.1.1) and timing (Section 2.1.2) of plains-forming eruptions.

2.1.1 Volume of erupted basalts

Figure 1 shows the distribution of volcanic plains on Mercury. Smooth plains (SPs) are widely distributed across the planet and were originally suggested to be volcanic due to their tendency to embay other features and pond in topographic lows (e.g., Murray et al., 1974; Strom et al., 1975). Observations of these plains with MESSENGER later revealed a variety of volcanic landforms and morphologies, such as ridge-like structures and smooth textures (Head et al., 2009, 2011; Byrne et al., 2016; Denevi et al., 2013). The combination of embayment relationships, compositional properties (Denevi and Robinson, 2008), and morphologic properties indicate that the SPs are volcanic, interpreted to be from effusive, flood-mode eruptions (Head et al., 2009, 2011; Byrne et al., 2016, 2018).

Figure 1 also delineates intercrater plains (ICPs), the most spatially dominant unit on Mercury. The ICPs are more heavily cratered than the SPs, suggesting they are relatively older (Whitten et al., 2014), and are also rougher than the SPs with a hummocky texture (Fa et al., 2016). The ICPs were originally suggested to be volcanic because they occupy large volumes and because there is no obvious impact basin from which they may have been sourced as ejecta (e.g., Murray et al., 1974; Strom et al., 1975). It has been suggested that ICP regions were once more reminiscent of SPs and have since been modified by impact cratering (Denevi et al., 2013; Whitten et al., 2014; Byrne et al., 2018) because the color properties of ICPs and SPs are similar (Murchie et al., 2015), and many of the contacts between ICPs and SPs exist as gradational boundaries (Whitten et al., 2014). Overall, it is likely that much of the ICP unit is volcanic, emplaced in multiple, large-volume effusive flows (similar to the SPs) and has since been modified by impacts. However, the origin of the ICPs is still unclear and so we treat two different scenarios for estimating the total flux of effused basalts: first considering only the SPs and then also including the ICPs.

For these two scenarios, we estimate the volume of basaltic material forming the plains shown in Fig. 1 by multiplying the surface area of each plains deposit by its estimated thickness (Byrne et al., 2018 and references therein). Previous analyses indicate that the majority of volcanic plains on Mercury are between 0.5 km and 4 km thick (Byrne et al., 2018 and references therein). For plains that do not have previously resolved thicknesses, we estimate their thicknesses for three cases: (1) low volume (assuming a plains thickness, T, of 0.1 km), (2) high volume (T=4 km), and (3) intermediate volume (T=1.1 km).

2.1.2 Timing of erupted basalts

The ages of each volcanic unit are informed from previous analyses of unit ages when possible (Byrne et al., 2018 and references therein). Crater density statistics indicate that the majority of large SPs have surface ages between 3.7 and 3.9 Gyr (Byrne et al., 2018 and references therein) and that plains-forming eruptions largely ceased by ~3.5 Gyr (Byrne et al., 2016). Here, we determine the ages of five of the largest SP deposits that were previously undated: Otaared Planitia, Utaridi Planitia, and plains located south of Nathair Facula, north of Lange crater, and around Holbein crater (Fig. 1).

Dating these five deposits removes some uncertainty in the timing of the eruptions of the remaining SPs on Mercury, as they represent an additional ~4% of SP surface area (shaded blue in Fig. 1).

In each of the five volcanic deposits dated here, we identify impact craters ≥ 10 km in diameter and derive crater size-frequency distributions (Fig. 2). Models of the crater-derived retention ages are fit to the chronology and production curves for Mercury (Le Feuvre and Wieczorek, 2011) to estimate absolute model ages (AMAs) for each plains deposit.

Four of the five previously undated plains deposits have AMAs between ~3.5 and ~3.7 Gyr (Fig. 2), aligning well with previously estimated ages of SP deposits (Byrne et al., 2018 and references therein). The fifth unit that we dated has a lower crater density and a slightly younger AMA of $3.08\ \mathrm{Ga}\ ^{+0.37\ \mathrm{Ga}}_{-0.47\ \mathrm{Ga}}$ (Fig. 2). From all of the dated terrains (including those dated in previous studies and those dated here), we establish a production function of SP-forming eruptions on Mercury. We estimate the volumes of the remaining undated SPs following the methods in 2.1.1, and then distribute these volumes following the production function as a best estimate for when they formed. For the scenario in which we include ICPs in our analysis (interpreting them to be of volcanic origin), we model the flux of ICP-forming eruptions as a constant flux, although it is possible the flux was increasing over time until peak SP-forming activity ~3.8 Ga (Whitten et al., 2014).

Note that the surface age of any plains unit does not accurately describe the age of the entire volcanic deposit, given that each unit is likely to include older volcanic deposits that formed earlier (Head et al., 2009; 2011; Whitten et al., 2014; Byrne et al., 2016). Without sequence stratigraphy of the volcanic deposits, it is not possible to accurately describe the volume of basalt released at different times. However, using the surface age to describe the age of the entire deposit provides a maximum estimate of the volume of basalt effused at any single time.

2.2 Mercury's magmatic volatile content

In contrast to the Moon, we do not currently have any samples of Mercury's volcanic deposits which would allow for the determination of its degassed volatile content. By exploring a wide parameter space of degassed contents and oxygen fugacities, we aim to provide reasonable estimates for the flux of gas released on Mercury. XRS and GRS measurements of Mercury's surface and near-surface can provide some insight into Mercury's volatile content. These measurements - indicating elevated abundances of K (Peplowski et al., 2012), C (Murchie et al., 2015), S (Nittler et al., 2011), Na (Peplowski et al., 2014), and Cl (Evans et al., 2015) - have been used widely in experiments and petrologic modeling to infer the melting conditions and mantle source compositions for surface lavas (e.g., Namur et al., 2016). The measurements of elevated S abundances (up to 4 wt. % at the surface; Nittler et al., 2011) also allow for the calculation of the planet's oxygen fugacity (fO_2), which is estimated to be between IW-3 and IW-7 (where IW-3 is 3 log units below the iron-wüstite oxygen buffer), indicating that Mercury is the most reduced terrestrial planet (Zolotov et al., 2013; Namuer et al., 2016; McCubbin et al., 2017).

At such reducing conditions, S is an important element that affects volatile partitioning and speciation of melts (Zolotov et al., 2013; Armstrong et al., 2015; Anzures et al., 2017), and it is the first species we consider as a potential component of a mercurian melt. Sulfide stability at highly reducing conditions promotes high S solubility, and has been measured in a variety of experimental petrology studies (McCoy et al., 1999; Namur et al., 2016; Anzures et al., 2017). Ion probe analyses indicate that S solubility in a sulfide-saturated experimental mercurian mantle melt increases from ~1 wt. % to ~7 wt. % as fO_2 decreases from IW-3 to IW-7 (Anzures et al., 2017). At present, how much of this S will degas from the magma (versus precipitating as sulfide) is not known. In this study, we consider two cases: Model A, a low-gas scenario in which only 1% of the S content degasses, and Model B, a high-gas scenario in which 10% of the S content degasses. The S contents in the melts are assumed to be the experimentally-measured sulfur concentrations at sulfide saturation (SCSS) for a given fO_2 (Table 1).

For Mercury's interior, a major consideration is how elevated S abundances influence the melt, given that S saturation affects the bonding environment of other species, particularly in a low-O system. Measurements of sulfide-saturated experimental melts indicate that there is an increase in Cl solubility with decreasing fO_2 (Anzures et al., 2017). From these experiments, we estimate that Cl may be present in mercurian melts at abundances between 1,300 ppm and 1,700 ppm for fO_2 values between IW-3 and IW-7, respectively. Again, it is not yet understood how much of any specific volatile species is released during eruptions on Mercury, so we estimate degassed contents for Cl of 10% and 100% for our low-gas (Model A) and high-gas (Model B) models.

Armstrong et al. (2015) studied the solubility and speciation of dissolved volatiles in mafic glasses quenched from high pressure, specifically for C-O-H-N species. Their experiments were conducted over a range of fO_2 conditions down to IW-3.65, which is similar to the higher values predicted for Mercury's interior conditions (Zolotov et al., 2013; Namuer et al., 2016). Notably, the experiments of Armstrong et al. (2015) included the presence of H_2O, which is not predicted to be stable in Mercury's interior (Nittler et al., 2011; Zolotov et al., 2013). However, these experiments still provide valuable insight into what C-O-H-N species may be stable in mercurian melts: CH_4 (methane) and N–H.

To estimate CH_4 melt content, we use the C content measured in experimental melts. As with S and Cl, C content increases with decreasing fO_2 in a sulfide-saturated system (Anzures et al., 2017). We estimate a CH_4 abundance of 200 ppm for IW-3 and 2,000 ppm for IW-7 and use degassing contents of 10% and 100% for Models A and B, respectively.

The other major volatile group that Armstrong et al. (2015) predicted to be stable at high pressure and reducing conditions is N–H complexes, consistent with previous studies. Here we model N–H from the predicted N content under reducing conditions. Libourel et al. (2003) measured N solubility in sulfur-free basaltic melts at a range of fO_2 values between IW-1.3 and IW-8.3. We estimate N content for IW-3 and IW-7 from these experiments and use N–H magma concentrations of 10 and 100 ppm (Table 1). We again estimate a degassing content of 10% and 100% for Models A and B, respectively.

We estimate the total mass of volatiles delivered to the surface during plains eruptions on Mercury. We use the terms "delivered to the surface" and "released" to describe all of the volatiles that reach the surface, including both the volatiles that were outgassed to the atmosphere during initial pyroclastic activity and those that remain locked in the solidified magma (e.g., vesicles, etc.) and diffuse out over much longer time scales (e.g., Wilson and Head, 2017). With our best estimates of species released during mercurian eruptions (Table 1), we calculate the total mass of released volatiles, G, for each volcanic plains deposit from

$$G = V \times \rho_m \times n \qquad \text{(Eq. 1)},$$

where V is the erupted volume, ρ_m is the bulk density of volcanic deposits on Mercury (~3014 kg m^{-3}), and n is the estimated mass of volatiles delivered to the surface (Table 1).

We stress that Table 1 represents our best estimates of the possible volatiles that were released during plains eruptions on Mercury, but the actual volatile species and their degassed content remain unknown. We examine a wide parameter space of degassed contents and oxygen fugacities in order to derive reasonable estimates for the flux of gas released on Mercury during plains eruptions. As discussed in Section 5, future in-situ analyses are essential for more accurately describing the volatile speciation and content of mercurian lavas.

3 Results

3.1 Volume of erupted basalts through time

The total volume of erupted basalts estimated for Mercury's SPs ranges between ~1.7 x 10^7 and 7.1 x 10^7 km^3 depending on the estimated thicknesses of the plains (Fig. 3). If we consider the ICPs to also be large volcanic flows (Murray et al., 1974; Strom et al., 1975; Denevi et al., 2013; Whitten et al., 2014; Byrne et al., 2018), then the estimated volume of erupted basalts increases by up to two orders of magnitude; the total erupted SP and ICP volume is estimated to be ~3.6×10^7–6.5×10^9 km^3 (Fig. 3). The total volume of erupted basalts on Mercury is at least an order of magnitude higher than that predicted for the Moon (8.9×10^6 km^3; Needham and Kring, 2017), and up to 3 orders of magnitude if the ICPs on Mercury are indeed volcanic plains. In a manner similar to mare volcanism on the Moon (Needham and Kring, 2017), the volume of SP volcanism on Mercury peaks at ~3.8 Ga (Fig. 3).

Uncertainties in the erupted volume stem from uncertainties associated with the estimates of volcanic plains thicknesses. While the thicknesses of some individual plains units have been resolved from stratigraphy (Byrne et al., 2018 and references therein), the thicknesses of the majority of plains units have not been analyzed in detail. Individual plains units are not predicted to be uniform in thickness; they vary in thickness as a function of eruption conditions, magmatic flux, viscosity, and geologic setting (Wilson and Head, 2008, 2017; Head et al., 2009, 2011; Denevi et al., 2013). To account for these uncertainties, as discussed in Section 2.1.1, here we have computed the volume for three different volume scenarios. Additionally, as discussed in Section 2.1.2, the production function of these eruptions relies on the estimates of plains ages, and many plains deposits are not yet dated (Fig. 1). The time-resolved flux in Figure 3 represents a general trend in the production function of erupted basalts on Mercury.

3.2 Mass of erupted volatiles through time

We calculate the time-resolved mass of effused volatiles on Mercury (Fig. 4) using estimates of total erupted basaltic material for the low-volume, high-volume, and intermediate cases (Fig. 3). First, we consider only the volatiles released during SP-forming eruptions. Assuming an upper fO_2 of IW-3 in the intermediate case, we estimate that ~1 x 10^{16} kg of S and Cl, ~2 x 10^{15} kg of CH_4, and ~1 x 10^{14} kg of N–H were released during the formation of SPs in a low-gas scenario (Model A). When assuming a lower fO_2 of IW-7 for Model A, these estimates increase to ~7 x 10^{16} kg for S, ~2 x 10^{16} kg for Cl and CH_4, and ~1 x 10^{15} kg for N–H.

In Model B, we consider higher degassing rates (Table 1). For both fO_2 scenarios, the estimated masses of volatiles released during SP-forming eruptions increase by an order of magnitude in this high-gas scenario (Fig. 4).

If the ICPs are indeed volcanic (Murray et al., 1974; Strom et al., 1975; Denevi et al., 2013; Whitten et al., 2014; Byrne et al., 2018), then the estimated masses of released volatiles would be even greater. For example, for the intermediate case and an fO_2 of IW-3, we estimate that ~6 x 10^{17} kg of S, ~8 x 10^{17} kg of Cl, ~1 x 10^{17} kg of CH_4, and ~6 x 10^{15} kg of N–H were released in Model A when including the contributions from both SP-forming and ICP-forming eruptions. When assuming a lower fO_2 of IW-7 for Model A, these estimates increase to ~4 x 10^{18} kg for S, ~1 x 10^{18} kg for Cl and CH_4, and ~6 x 10^{16} kg for N–H. Again, for both fO_2 scenarios, these estimated masses increase by an order of magnitude in Model B.

For our intermediate-volume case, the most abundant volatile species predicted for Mercury (S, Cl, and CH_4) released during SP eruptions are up to 3 orders of magnitude more abundant than what is predicted for the most abundant volatiles released during lunar mare eruptions (CO, S, and H_2O; Needham and Kring, 2017). When considering the ICP eruptions as well, the released volatiles predicted for Mercury are 1 to 5 orders of magnitude more abundant.

The difference in the abundance of released volatiles between Mercury and the Moon is largely a function of the total volume of erupted basalts, which is substantially greater on Mercury (Section 3.1). As discussed in detail in Section 2.2, volatile speciation and degassing content are still unknown quantities for Mercury, and here we provide a range of estimates informed by experimental petrology studies (Libourel et al., 2003; Armstrong et al., 2015; Anzures et al., 2017). Overall, the large volumes of erupted basalts on the surface imply that the plains-forming eruptions released at least ~10^{16} kg of volatiles over time.

4 The potential for volcanically-derived, transient atmospheres

Although abundant volatiles are predicted to have been released during the formation of lava plains on Mercury (Fig. 4) and the Moon (Needham and Kring, 2017), the fate of these volatiles is an important open question. It has been proposed that large volumes of released volatiles on the Moon could produce a transient atmosphere that would aid in the transport of volatiles to cold-trapping regions (Needham and Kring, 2017). Critically, the possibility of such an atmosphere is dependent not only on volatile abundances, but also on eruption lifetimes, atmospheric gas dynamics, and atmospheric loss rates.

The Moon, for example, was very volcanically active between ~4 and 3.5 Ga on geologic timescales, but individual eruptions occurred on relatively short (~100 day) timescales (Wilson and Head, 2017, 2018), implying that there were significant periods of inactivity between eruptions. We estimated this repose time for lunar eruptions, assuming that three times as much magma was erupted between 3 and 4 Ga than was erupted between 2 and 3 Ga (Wilson et al., 2019). With ~30,000 to 100,000 eruptions occurring over this whole 2-Gyr period, there would be an average of 13,000 to 40,000 years between eruptions (Wilson et al., 2019).

Here, we perform similar calculations for Mercury to solve for the average time interval between eruptions, τ_i, from

$$\tau_i = \frac{\tau_T}{V_T/V_e} \qquad \text{(Eq. 2)},$$

where τ_T is the timespan of volcanic activity (estimated to be ~2 Gyr; Byrne et al., 2018), V_T is the total erupted volume of basaltic plains (estimated to be ~10^7 km^3 for SPs and ~10^9 km^3 for SPs and ICPs in Section 3.1), and V_e is the average volume of a single eruption (estimated to be ~200–400 km^3; Wilson and Head, 2008). If we assume that volcanic activity was relatively constant over τ_T, the average time interval between eruptions is estimated to be between ~40,000 and 80,000 years for SP-forming eruptions, but between ~400 and 800 years when also considering ICP-forming eruptions. As with the Moon, it is likely that the frequency of eruptions was higher at the start of τ_T and then decreased through time, given the thermal and crustal evolution of the planet (e.g., Wilson and Head, 2008; 2017). Therefore, we again assume that three times more magma was released during the first billion-year period of activity than in the following billion-year period. Such a flux suggests that earlier SP-forming eruptions took place every ~27,000 to 53,000 years, and that as the flux of eruptions decreased with time, there were longer time intervals between the eruptions. When considering ICP-forming eruptions as well, τ_T may have been as short as ~270 to 530 years.

Released volatiles must remain in the atmosphere for sufficient durations in order to migrate and become cold-trapped before they are photochemically destroyed or lost to space (Section 5). In order to determine the duration of volcanically-derived transient atmospheres on Mercury, we first calculate the average eruption duration, τ_e, from

$$\tau_e = \frac{V}{F_l} \qquad \text{(Eq. 3)},$$

where V, as in Eq. 1, is the volume of erupted lava and F_l is the flux of erupted lava. For typical eruptions on Mercury, V is between 200 and 400 km^3 and F_l is between 10^3 and 10^7 m^3 s^{-1} (Wilson and Head, 2008); thus, τ_e is estimated to be between ~2,300 and 4,600 days for low-flux eruptions, and < 1 day for extremely high-flux eruptions (Table 2).

From τ_e, we calculate the flux of erupted gas, F_g, using

$$F_g = \frac{G}{\tau_e} \qquad \text{(Eq. 4)},$$

where G is the mass of gas released for an average eruption. While we estimate that the total estimated mass of erupted volatiles on Mercury ranges between ~10^{14} and 10^{19} kg (Section 3.2), it will inevitably be less for individual eruptions. Wilson and Head (2008) estimate that the average volume of a single eruption is between ~200 and 400 km^3, which implies that the total gas released, G, for average mercurian eruptions is ~1.5 x 10^{11}–3.0 x 10^{12} kg assuming an fO_2 of IW-3 and ~6.5 x 10^{11}–1.3 x 10^{13} kg assuming an

fO_2 of IW-7 (Table 2). With these values, F_g is estimated to be ~750–7.5 x 10^7 kg s^{-1} for IW-3, and ~3,300–3.3 x 10^8 kg s^{-1} for IW-7 (Table 2).

We next estimate the scale height, H, of a volcanically-derived atmosphere to be 31 km from

$$H = \frac{Q \times T}{m \times g} \qquad \text{(Eq. 5)},$$

where Q is the universal gas constant (8.314 kJ mol^{-1} K^{-1}), T is Mercury's mean surface temperature (~440 K), m is the mean molecular mass of erupted volatiles (~32 kg $kmol^{-1}$ assuming a S atmosphere), and g is the gravitational acceleration at Mercury's surface (3.7 m s^{-2}). Note that because of Mercury's greater surface gravity, H is less than the estimated H for a lunar volcanically-derived atmosphere (48 km; Wilson et al., 2019).

We use H to solve for the surface density of a volcanically-derived atmosphere, ρ_s, using

$$\rho_s = \frac{G}{4\,\pi\,R^2 \times H} \qquad \text{(Eq. 6)},$$

where R is the planet's radius (2440 km). For IW-3, ρ_s is estimated to be ~6.5 x 10^{-8}–1.3 x 10^{-6} kg m^{-3} and for IW-7, ρ_s is estimated to be ~2.8 x 10^{-7}–5.6 x 10^{-6} kg m^{-3} (Table 2).

The pressure of this atmosphere, P_s, is calculated using

$$P_s = \rho_s \times \mathrm{g} \times H \qquad \text{(Eq. 7)}.$$

We estimate P_s to be ~7.5 x 10^{-3}–0.15 Pa for IW-3 and ~3.2 x 10^{-2}–0.64 Pa for IW-7 (Table 2).

Finally, the flux of gas released during individual eruptions can be compared with the loss rate of gases into the atmosphere. We estimate the total duration of a volcanically-derived atmosphere, τ_d, from

$$\tau_d = \frac{G}{F_{esc}} \qquad \text{(Eq. 8)},$$

where the rate of atmospheric escape, F_{esc}, is estimated to be 10 kg s^{-1} from Vondrak (1974). Solving for τ_d implies that a typical volcanically-derived atmosphere would decay within ~500 to ~40,000 years (Table 2). Above we estimated the average time between eruptions on Mercury, τ_T, to be between ~27,000 and 53,000 years, although possibly as short as ~270–530 years if the ICPs are volcanic. Comparisons between τ_d and τ_T indicate the following:

1. If SPs are the only volcanic plains on Mercury, then a transient, volcanic atmosphere would likely have dissipated prior to a subsequent eruption for a low-volume, low fO_2 scenario. It is possible that transient, volcanic atmospheres co-existed in low fO_2 (IW-7) and high-gas (Model B) conditions given that the predicted lifetime of volcanically-derived atmospheres would have been longer.
2. In the more likely case that ICPs, like the SPs, are volcanic (Denevi et al., 2013; Whitten et al., 2014; Byrne et al., 2018 and references therein), then we predict that the duration of almost any transient, volcanic atmosphere would have exceeded the duration between individual eruptions, suggesting that the frequency of eruptions may have resulted in the combination of denser, longer-lived atmospheres. Only for a low-volume, low-gas, and high fO_2 scenario would this not be the case.

Determining the ultimate fate of volatiles in transiently dense atmospheres on nominally airless bodies requires detailed modeling that depends on eruption dynamics, atmospheric loss rates, and gas dynamics in an atmosphere that is evolving on geologically rapid timescales (e.g., Prem et al., 2015). This modeling is an important next step in assessing how volcanic eruptions altered Mercury's atmospheric density and composition, and how the collisional dynamics of transiently dense atmospheres affected volatile transport and retention on Mercury.

5 Buried volatiles at the poles of Mercury?

Needham and Kring (2017) point out that only a fraction of the predicted water released from mare formation (~10^{14} kg) is needed to account for all of the remotely sensed water at the lunar poles (~10^{11} kg). If mare volcanism did deliver ice to the lunar poles, it is likely to be buried in the subsurface (e.g., Needham and Kring, 2017). Interestingly, we find that Mercury released even greater volumes of volcanic material over time than the Moon (Fig. 3), and therefore greater volumes of volatiles were likely released (Fig. 4). Is it possible that some fraction of erupted volatiles was deposited in polar cold traps on Mercury?

It is well-understood that ices are cold-trapped at the poles of Mercury today. These ices have highly reflective radar properties indicative of a nearly pure H_2O composition, with <5% silicates by volume (Butler et al., 1993). The detection of enhanced neutron suppression at Mercury's north polar region are also consistent with a nearly pure H_2O composition (Lawrence et al., 2013). The ice deposits have not been covered by regolith gardening processes (Butler et al., 1993; Crider and Killen, 2005) and have distinct reflectance properties (Chabot et al., 2016), sharp geologic contacts (Chabot et al., 2016), and crater densities (Deutsch et al., 2019) suggestive of geologically young ages between 10's and 100's of Myr (Crider and Killen, 2005; Lawrence et al., 2013; Deutsch et al., 2019).

Importantly, the composition and age of these surface ice deposits indicate that they are not derived from volcanism. At mantle pressures and Mercury's extremely reducing conditions, H_2O is not predicted to be present in the magma (e.g., Nittler et al., 2011; Zolotov et al., 2013) and the very young surface age of the ice (Crider and Killen, 2005; Deutsch et al., 2019) is inconsistent with the timing of Mercury's volcanic activity. The H_2O-ices observed at the surface of the poles are more likely to have been delivered by an external, cometary impactor (e.g., Butler et al., 1993; Paige et al., 2013; Chabot et al., 2016; Ernst et al., 2018; Deutsch et al., 2019).

However, given our analysis here, we find it important to consider the possibility that volatiles other than H_2O were released from Mercury's interior and contributed some fraction of materials to polar cold-traps. These volatiles would be distinctly different from the polar deposits observed today, raising the question: Where would they be and how could they be identified?

Any volatiles that are deposited on the surface of Mercury (whether indigenous in origin or externally delivered) must face the space weathering environment, including strong irradiation and thermal stresses (e.g., McCord and Clark, 1979; Domingue et al., 2014) and high micrometeorite fluxes with high-velocity impactors (e.g., Borin et al., 2009; Domingue et al., 2014). Interestingly, these harsh environmental factors may aid in the efficiency of volatile-trapping in the regolith. The regolith is predicted to have relatively abundant lattice defects due to the high radiation stresses imparted on the surface (e.g., Bennet et al., 2013; Domingue et al., 2014) and is predicted to be composed of fine grain sizes due to the high impact velocities and bombardment flux (e.g., Borin et al., 2009). Lattice defects and larger surface-to-volume ratios are more efficient sinks for volatiles (Krähenbühl et al. 1977; Domingue et al., 2014), and the elevated elemental abundances of volatiles on Mercury (Nittler et al., 2011; Peplowski et al., 2011, 2012; Evans et al., 2012) suggest that perhaps the regolith is indeed effective at trapping volatiles.

The high impact rates on Mercury also aid in the preservation of surface materials by burying them through regolith overturn. Regolith gardening rates describe the timescales of surface modification and can be used to estimate how quickly surficial material is buried to a given depth. Crider and Killen (2005) estimated that the present-day regolith burial rate on Mercury is ~0.43 cm Myr^{-1}. We use this regolith gardening rate to predict the depth of potential volcanically-derived volatiles.

If we assume that a layer of volcanically-derived volatiles was cold-trapped at Mercury's poles at 3.8 Gyr (during the peak of volcanism), then the regolith gardening rate derived by Crider and Killen (2005) suggests that the peak concentration of remnant volatiles would be concentrated ~16 m in the subsurface today. We consider this depth to be a lower estimate, given that the regolith gardening rate derived by Crider and Killen (2005) is for the recent past (<100 Ma) and the volcanism we analyze here was most active before ~3.5 Ga, when impact rates were much higher (e.g., Le Feuvre and

Wieczorek, 2011). The volatiles would have a highly heterogeneous spatial distribution due to the stochastic impact gardening process (e.g., Crider and Killen, 2005). A diffuse layer of indigenous volatiles buried at least 16 m within the subsurface would not have been detectable by MESSENGER, given that its spectrometers had sensing depths of less than ~1 m.

While measuring volatile deposits sequestered many meters in the subsurface was not feasible with MESSENGER, the detection of volcanically-derived volatiles would provide important new insight into Mercury's volcanic history, interior geochemical conditions, and exospheric/atmospheric evolution. Here we outline a variety of measurements that may be considered in future missions, such as BepiColombo (Benkhoff et al., 2010) and beyond (Ernst et al., 2020), for testing the hypothesis of cold-trapped volcanically-derived volatiles:

1. *Plains morphometry.* BepiColombo topographic measurements and stereo images (Benkhoff et al., 2010) of plains stratigraphy can improve estimates of the thicknesses, extent, and topographic variability of volcanic plains units in order to better constrain the volume of erupted basalts.
2. *Surface chemistry.* Additional elemental measurements (particularly of S) using BepiColombo's various spectrometers (Benkhoff et al., 2010) can help refine geochemical models used to estimate the oxygen fugacity of Mercury's interior (e.g., Nittler et al., 2011; Zolotov et al., 2013; McCubbin et al., 2017). We found that changing the fO_2 value from IW-3 to IW-7 could change the estimated degassed mass by an order of magnitude.

3. *In-situ petrology.* Sample analyses of Mercury's volcanic plains are essential to directly measure the speciation and degassed volatile content of volcanic basalts. Landed surface operations are essential to better understand the geochemistry and mineralogy of the surface (e.g., Ernst et al., 2020).
4. *In-situ geochronology.* Analyses of the geochemical and isotopic properties of major surface units on Mercury would help refine our understanding of the ages of the various surface units, including SP units, as well as ICPs, which represent some of the oldest terrains on Mercury and whose timing is not well-resolved. Such analyses are again supportive of landed science investigations (e.g., Ernst et al., 2020).

6 Conclusion

On the Moon, volcanism may represent a substantial pathway for the transport of volatiles to the lunar surface (e.g., Saal et al., 2008). It has been predicted that volatiles released during the formation of the lunar maria may have been present in sufficient volumes to produce a transient atmosphere capable of aiding in the transport of H_2O to cold-trapping regions (Needham and Kring, 2017). At mantle pressures and with Mercury's extremely reducing conditions, H_2O is not predicted to be present in mercurian magmas (Nittler et al., 2011; Zolotov et al., 2013); however, volatiles other than H_2O are predicted to be stable (Libourel et al., 2003; Zolotov et al., 2013; Armstrong et al., 2015; Anzures et al., 2017), though without sample analyses of mercurian lavas, the precise speciation and degassed content of erupted basalts remain important open questions.

Here we provide the first comprehensive estimates of the flux of predicted volatiles (S, Cl, CH_4, and N–H) released on Mercury via volcanic plains-forming eruptions using a variety of fO_2 conditions, degassing scenarios, and basaltic volume estimates. We find that an order of magnitude more basalts were erupted to form smooth plains on Mercury than erupted to form the lunar maria. Importantly though, a critical open question is the origin of Mercury's intercrater plains, which are the most spatially dominant geologic unit on the planet (Whitten et al., 2014). If these are also volcanic, as previously suggested (Murray et al., 1974; Strom et al., 1975; Denevi et al., 2013; Whitten et al., 2014; Byrne et al., 2018), then potentially up to 3 orders of magnitude more basalts were erupted to form volcanic plains on Mercury than erupted to form the lunar maria. The large volumes of erupted basalts on Mercury imply that large volumes of volatiles were released during the eruptions, which may have resulted in the transient production of enhanced atmospheric pressures with lifetimes between ~500 and ~40,000 years.

It is possible that these atmospheric lifetimes were greater than the time of repose between average mercurian eruptions (~270–53,000 years), therefore aiding the conditions necessary for volatiles to migrate across the planet and increasing the probability of the volatiles being cold-trapped. For volatiles that did become cold-trapped at Mercury's poles, we estimate that they would exist as a diffuse, weathered layer that is buried at least ~16 m below the subsurface. Such sequestered volatiles would be distinctly different from the polar H_2O-ice deposits observed on Mercury's surface today, both in composition (Butler et al., 1993; Lawrence et al., 2013) and in age (Crider and Killen, 2005; Lawrence et al., 2013; Deutsch et al., 2019).

Acknowledgements

We thank Bill McKinnon for his editorial handling of this manuscript and two anonymous reviewers for their helpful reviews of this work. This work is supported by NASA (Grant Number 80NSSC19K1289) issued through the Harriett G. Jenkins Graduate Fellowship to A. N. D., by the Solar System Exploration Research Virtual Institute (Grant number NNA14AB01A) to J. W. H., by the Leverhulme Trust through an Emeritus Fellowship to L. W., and by NASA's Planetary Science Division Research Program to G. A. N.

References

Anzures, B.A., Parman, S.W., Boesenberg, J.S., Milliken, R.E., 2019. Using volatile (S, C, H, F, Cl) contents on enstatite in reduced meteorites to estimate oxygen fugacity and equilibrium melt compositions. Lunar Planet. Sci. Conf. 50, Abstract #2179.

Armstrong, L.S., Hirschmann, M.M., Stanley, B.D., Falksen, E.G., Jacobsen, S.D., 2015. Speciation and solubility of reduced C–O–H–N volatiles in mafic melt: Implications for volcanism, atmospheric evolution, and deep volatile cycles in the terrestrial planets. Geochimica et Cosmochimica Acta 171, 283–302. https://doi.org/10.1016/j.gca.2015.07.007

Arnold, J.R., 1979. Ice in the lunar polar regions. J. Geophys. Res. 84, 5659–5668. https://doi.org/10.1029/JB084iB10p05659

Benkhoff, J., van Casteren, J., Hayakawa, H., Fujimoto, M., Laakso, H., Novara, M., Ferri, P., Middleton, H.R., Ziethe, R., 2010. BepiColombo—Comprehensive exploration of Mercury: Mission overview and science goals. Planetary and Space Science, Comprehensive Science Investigations of Mercury: The scientific goals of the joint ESA/JAXA mission BepiColombo 58, 2–20. https://doi.org/10.1016/j.pss.2009.09.020

Bennett, C.J., Pirim, C., Orlando, T.M., 2013. Space-Weathering of Solar System Bodies: A Laboratory Perspective. Chem. Rev. 113, 9086–9150. https://doi.org/10.1021/cr400153k

Blewett, D.T., Chabot, N.L., Denevi, B.W., Ernst, C.M., Head, J.W., Izenberg, N.R., Murchie, S.L., Solomon, S.C., Nittler, L.R., McCoy, T.J., Xiao, Z., Baker, D.M.H., Fassett, C.I., Braden, S.E., Oberst, J., Scholten, F., Preusker, F., Hurwitz, D.M., 2011. Hollows on Mercury: MESSENGER Evidence for Geologically Recent Volatile-Related Activity. Science 333, 1856–1859. https://doi.org/10.1126/science.1211681

Borin, P., Cremonese, G., Marzari, F., Bruno, M., Marchi, S., 2009. Statistical analysis of micrometeoroids flux on Mercury. Astronomy and Astrophysics 503, 259–264. https://doi.org/10.1051/0004-6361/200912080

Butler, B.J., 1997. The migration of volatiles on the surfaces of Mercury and the Moon. J. Geophys. Res. 102, 19283–19291. https://doi.org/10.1029/97JE01347

Byrne, P. K., Whitten, J. L., Klimczak, C., McCubbin, F. M., Ostrach, L. R., 2018a. The volcanic character of Mercury. Mercury: The view after MESSENGER. Edited by

Solomon S. C., Nittler, L. R., Anderson, B. J. Cambridge Univ. Press, pp. 287–323.

Byrne, P.K., Ostrach, L.R., Fassett, C.I., Chapman, C.R., Denevi, B.W., Evans, A.J., Klimczak, C., Banks, M.E., Head, J.W., Solomon, S.C., 2016. Widespread effusive volcanism on Mercury likely ended by about 3.5 Ga. Geophys. Res. Lett. 43, 2016GL069412. https://doi.org/10.1002/2016GL069412

Chabot, N.L., Ernst, C.M., Paige, D.A., Nair, H., Denevi, B.W., Blewett, D.T., Murchie, S.L., Deutsch, A.N., Head, J.W., Solomon, S.C., 2016. Imaging Mercury's polar deposits during MESSENGER's low-altitude campaign. Geophys. Res. Lett. 43, 9461–9468. https://doi.org/10.1002/2016GL070403

Cintala, M.J., 1992. Impact-induced thermal effects in the lunar and Mercurian regoliths. J. Geophys. Res. 97, 947–973. https://doi.org/10.1029/91JE02207

Crider, D., Killen, R.M., 2005. Burial rate of Mercury's polar volatile deposits. Geophys. Res. Lett. 32, L12201. https://doi.org/10.1029/2005GL022689

Crotts, A.P.S., Hummels, C., 2009. Lunar Outgassing, Transient Phenomena, and the Return to the Moon. II. Predictions and Tests for Outgassing/Regolith Interactions. ApJ 707, 1506. https://doi.org/10.1088/0004-637X/707/2/1506

Denevi, B.W., Ernst, C.M., Meyer, H.M., Robinson, M.S., Murchie, S.L., Whitten, J.L., Head, J.W., Watters, T.R., Solomon, S.C., Ostrach, L.R., Chapman, C.R., Byrne, P.K., Klimczak, C., Peplowski, P.N., 2013. The distribution and origin of smooth plains on Mercury. J. Geophys. Res. Planets 118, 891–907. https://doi.org/10.1002/jgre.20075

Denevi, B.W., Robinson, M.S., 2008. Mercury's albedo from Mariner 10: Implications for the presence of ferrous iron. Icarus 197, 239–246. https://doi.org/10.1016/j.icarus.2008.04.021

Deutsch, A.N., Head, J.W., Neumann, G.A., 2019. Age constraints of Mercury's polar deposits suggest recent delivery of ice. Earth and Planetary Science Letters 520, 26–33. https://doi.org/10.1016/j.epsl.2019.05.027

Domingue, D.L., Chapman, C.R., Killen, R.M., Zurbuchen, T.H., Gilbert, J.A., Sarantos, M., Benna, M., Slavin, J.A., Schriver, D., Trávníček, P.M., Orlando, T.M., Sprague, A.L., Blewett, D.T., Gillis-Davis, J.J., Feldman, W.C., Lawrence, D.J., Ho, G.C., Ebel, D.S., Nittler, L.R., Vilas, F., Pieters, C.M., Solomon, S.C., Johnson, C.L., Winslow, R.M., Helbert, J., Peplowski, P.N., Weider, S.Z., Mouawad, N., Izenberg, N.R., McClintock, W.E., 2014. Mercury's Weather-Beaten Surface: Understanding Mercury in the Context of Lunar and Asteroidal Space Weathering Studies. Space Sci Rev 181, 121–214. https://doi.org/10.1007/s11214-014-0039-5

Ernst, C. M., et al., 2020. Mercury Lander. Planetary Mission Concept Studies, ROSES 2018 NRA.

Ernst, C.M., Chabot, N.L., Barnouin, O.S., 2018. Examining the Potential Contribution of the Hokusai Impact to Water Ice on Mercury. Journal of Geophysical Research: Planets 123, 2628–2646. https://doi.org/10.1029/2018JE005552

Evans, L.G., Peplowski, P.N., McCubbin, F.M., McCoy, T.J., Nittler, L.R., Zolotov, M.Yu., Ebel, D.S., Lawrence, D.J., Starr, R.D., Weider, S.Z., Solomon, S.C.,

2015. Chlorine on the surface of Mercury: MESSENGER gamma-ray measurements and implications for the planet's formation and evolution. Icarus 257, 417–427. https://doi.org/10.1016/j.icarus.2015.04.039

Fa, W., Cai, Y., Xiao, Z., Tian, W., 2016. Topographic roughness of the northern high latitudes of Mercury from MESSENGER Laser Altimeter data. Geophysical Research Letters 43, 3078–3087. https://doi.org/10.1002/2016GL068120

Greeley, R., 1987. Release of Juvenile Water on Mars: Estimated Amounts and Timing Associated with Volcanism. Science 236, 1653–1654. https://doi.org/10.1126/science.236.4809.1653

Head, J.W., Chapman, C.R., Strom, R.G., Fassett, C.I., Denevi, B.W., Blewett, D.T., Ernst, C.M., Watters, T.R., Solomon, S.C., Murchie, S.L., Prockter, L.M., Chabot, N.L., Gillis-Davis, J.J., Whitten, J.L., Goudge, T.A., Baker, D.M.H., Hurwitz, D.M., Ostrach, L.R., Xiao, Z., Merline, W.J., Kerber, L., Dickson, J.L., Oberst, J., Byrne, P.K., Klimczak, C., Nittler, L.R., 2011. Flood Volcanism in the Northern High Latitudes of Mercury Revealed by MESSENGER. Science 333, 1853–1856. https://doi.org/10.1126/science.1211997

Head, J.W., Murchie, S.L., Prockter, L.M., Solomon, S.C., Chapman, C.R., Strom, R.G., Watters, T.R., Blewett, D.T., Gillis-Davis, J.J., Fassett, C.I., Dickson, J.L., Morgan, G.A., Kerber, L., 2009. Volcanism on Mercury: Evidence from the first MESSENGER flyby for extrusive and explosive activity and the volcanic origin of plains. Earth and Planetary Science Letters, MESSENGER's First Flyby of Mercury 285, 227–242. https://doi.org/10.1016/j.epsl.2009.03.007

Kerber, L., Head, J.W., Solomon, S.C., Murchie, S.L., Blewett, D.T., Wilson, L., 2009. Explosive volcanic eruptions on Mercury: Eruption conditions, magma volatile content, and implications for interior volatile abundances. Earth and Planetary Science Letters, MESSENGER's First Flyby of Mercury 285, 263–271. https://doi.org/10.1016/j.epsl.2009.04.037

Krähenbühl, U., Grütter, A., von Gunten, H. R., Meyer, G., Wegmüller, F., & Wyttenbach, A., 1977. Volatile and non-volatile elements in grain-size fractions of Apollo 17 soils 75081, 72461, and 72501. Lunar Sci. Conf. 3, 3901-3916.

Lawrence, D.J., Feldman, W.C., Goldsten, J.O., Maurice, S., Peplowski, P.N., Anderson, B.J., Bazell, D., McNutt, R.L., Nittler, L.R., Prettyman, T.H., Rodgers, D.J., Solomon, S.C., Weider, S.Z., 2013. Evidence for Water Ice Near Mercury's North Pole from MESSENGER Neutron Spectrometer Measurements. Science 339, 292–296. https://doi.org/10.1126/science.1229953

Le Feuvre, M., Wieczorek, M.A., 2011. Nonuniform cratering of the Moon and a revised crater chronology of the inner Solar System. Icarus 214, 1–20. https://doi.org/10.1016/j.icarus.2011.03.010

Libourel, G., Marty, B., Humbert, F., 2003. Nitrogen solubility in basaltic melt. Part I. Effect of oxygen fugacity. Geochimica et Cosmochimica Acta 67, 4123–4135. https://doi.org/10.1016/S0016-7037(03)00259-X

McCord, T.B., Clark, R.N., 1979. The Mercury soil: Presence of Fe2+. Journal of Geophysical Research: Solid Earth 84, 7664–7668. https://doi.org/10.1029/JB084iB13p07664

McCoy, T.J., Dickinson, T.L., Lofgren, G.E., 1999. Partial melting of the Indarch (EH4) meteorite: A textural, chemical, and phase relations view of melting and melt migration. Meteoritics & Planetary Science 34, 735–746. https://doi.org/10.1111/j.1945-5100.1999.tb01386.x

McCubbin, F.M., Vander Kaaden, K.E., Peplowski, P.N., Bell, A.S., Nittler, L.R., Boyce, J.W., Evans, L.G., Keller, L.P., Elardo, S.M., McCoy, T.J., 2017. A Low O/Si Ratio on the Surface of Mercury: Evidence for Silicon Smelting? Journal of Geophysical Research: Planets 122, 2053–2076. https://doi.org/10.1002/2017JE005367

Moore, J.G., 1970. Water Content of Basalt Erupted on the ocean floor. Contr. Mineral. and Petrol. 28, 272–279. https://doi.org/10.1007/BF00388949

Murchie, S.L., Klima, R.L., Denevi, B.W., Ernst, C.M., Keller, M.R., Domingue, D.L., Blewett, D.T., Chabot, N.L., Hash, C.D., Malaret, E., Izenberg, N.R., Vilas, F., Nittler, L.R., Gillis-Davis, J.J., Head, J.W., Solomon, S.C., 2015. Orbital multispectral mapping of Mercury with the MESSENGER Mercury Dual Imaging System: Evidence for the origins of plains units and low-reflectance material. Icarus 254, 287–305. https://doi.org/10.1016/j.icarus.2015.03.027

Murray, B.C., Belton, M.J.S., Danielson, G.E., Davies, M.E., Gault, D.E., Hapke, B., O'Leary, B., Strom, R.G., Suomi, V., Trask, N., 1974. Mercury's Surface: Preliminary Description and Interpretation from Mariner 10 Pictures. Science 185, 169–179. https://doi.org/10.1126/science.185.4146.169

Namur, O., Charlier, B., Holtz, F., Cartier, C., McCammon, C., 2016. Sulfur solubility in reduced mafic silicate melts: Implications for the speciation and distribution of sulfur on Mercury. Earth and Planetary Science Letters 448, 102–114. https://doi.org/10.1016/j.epsl.2016.05.024

Needham, D.H., Kring, D.A., 2017. Lunar volcanism produced a transient atmosphere around the ancient Moon. Earth and Planetary Science Letters 478, 175–178. https://doi.org/10.1016/j.epsl.2017.09.002

Nittler, L.R., Starr, R.D., Weider, S.Z., McCoy, T.J., Boynton, W.V., Ebel, D.S., Ernst, C.M., Evans, L.G., Goldsten, J.O., Hamara, D.K., Lawrence, D.J., McNutt, R.L., Schlemm, C.E., Solomon, S.C., Sprague, A.L., 2011. The Major-Element Composition of Mercury's Surface from MESSENGER X-ray Spectrometry. Science 333, 1847–1850. https://doi.org/10.1126/science.1211567

Peplowski, P.N., Evans, L.G., Stockstill-Cahill, K.R., Lawrence, D.J., Goldsten, J.O., McCoy, T.J., Nittler, L.R., Solomon, S.C., Sprague, A.L., Starr, R.D., Weider, S.Z., 2014. Enhanced sodium abundance in Mercury's north polar region revealed by the MESSENGER Gamma-Ray Spectrometer. Icarus 228, 86–95. https://doi.org/10.1016/j.icarus.2013.09.007

Peplowski, P.N., Lawrence, D.J., Rhodes, E.A., Sprague, A.L., McCoy, T.J., Denevi, B.W., Evans, L.G., Head, J.W., Nittler, L.R., Solomon, S.C., Stockstill-Cahill, K.R., Weider, S.Z., 2012. Variations in the abundances of potassium and thorium on the surface of Mercury: Results from the MESSENGER Gamma-Ray

Spectrometer. Journal of Geophysical Research: Planets 117. https://doi.org/10.1029/2012JE004141

Prem, P., Artemieva, N.A., Goldstein, D.B., Varghese, P.L., Trafton, L.M., 2015. Transport of water in a transient impact-generated lunar atmosphere. Icarus, Lunar Volatiles 255, 148–158. https://doi.org/10.1016/j.icarus.2014.10.017

Saal, A.E., Hauri, E.H., Cascio, M.L., Orman, J.A.V., Rutherford, M.C., Cooper, R.F., 2008. Volatile content of lunar volcanic glasses and the presence of water in the Moon's interior. Nature 454, 192–195. https://doi.org/10.1038/nature07047

Strom, R.G., Trask, N.J., Guest, J.E., 1975. Tectonism and volcanism on Mercury. Journal of Geophysical Research: Solid Earth 2478–2507. https://doi.org/10.1029/JB080i017p02478@10.1002/(ISSN)2169-9356.MERC1

Vondrak, R.R., 1974. Creation of an artificial lunar atmosphere. Nature 248, 657–659. https://doi.org/10.1038/248657a0

Whitten, J.L., Head, J.W., Denevi, B.W., Solomon, S.C., 2014. Intercrater plains on Mercury: Insights into unit definition, characterization, and origin from MESSENGER datasets. Icarus 241, 97–113. https://doi.org/10.1016/j.icarus.2014.06.013

Wilson, L., Head, J. W., Deutsch, A. N., 2019. Volcanically-induced transient atmospheres on the Moon: Assessment of duration and significance. Lunar Planet. Sci. Conf. 50, Abstract 1343.

Wilson, L., Head, J.W., 2008. Volcanism on Mercury: A new model for the history of magma ascent and eruption. Geophysical Research Letters 35. https://doi.org/10.1029/2008GL035620

Wilson, L., Head, J.W., 2017. Generation, ascent and eruption of magma on the Moon: New insights into source depths, magma supply, intrusions and effusive/explosive eruptions (Part 1: Theory). Icarus, Lunar Reconnaissance Orbiter - Part II 283, 146–175. https://doi.org/10.1016/j.icarus.2015.12.039

Zolotov, M.Yu., Sprague, A.L., Hauck, S.A., Nittler, L.R., Solomon, S.C., Weider, S.Z., 2013. The redox state, FeO content, and origin of sulfur-rich magmas on Mercury. J. Geophys. Res. Planets 118, 138–146. https://doi.org/10.1029/2012JE004274

Table 1. Predicted volatile species for mercurian magmas. S abundances are estimated to be 1% of the estimated sulfur concentration at sulfide saturation (SCSS) for Model A and 10% of the estimated SCSS for Model B. CH_4, Cl, and N–H abundances for Models A and B are estimated from degassing amounts of 10% and 100%, respectively.

	Estimated Mass of Volatiles Delivered to the Surface, n (ppm)			
	IW-3		IW-7	
Species	Model A	Model B	Model A	Model B
S	100	1,000	700	7,000
CH_4	20	200	200	2,000
Cl	130	1,300	170	1,700
N–H	1	10	10	100

Table 2. Predicted values to describe mercurian eruptions and resulting volcanically-derived atmospheres, including average volume of a single eruption (V_e), oxygen fugacity (fO_2), mass of total erupted gas (G), eruption rate (F_l), eruption duration (τ_e), gas release rate (F_g), transient atmospheric surface density (ρ_s), transient atmospheric surface pressure (P_s), and transient atmosphere duration (τ_d).

	V_e (km^3)	fO_2	Degassing Model	G (kg)	F_l (m^3 s^{-1})	τ_e (days)	F_g (kg s^{-1})	ρ_s (kg m^{-3})	P_s (Pa)	τ_d (years)
Low-Flux Scenario										
Low-volume scenario	200	IW-3	A	1.5×10^{11}	10^3	2,300	750	6.5×10^{-8}	7.5×10^{-3}	480
			B	1.5×10^{12}			7,500	6.5×10^{-7}	7.5×10^{-2}	4,800
		IW-7	A	6.5×10^{11}			3,300	2.8×10^{-7}	3.2×10^{-2}	2,100
			B	6.5×10^{12}			33,000	2.8×10^{-6}	0.32	21,000
High-volume scenario	400	IW-3	A	3.0×10^{11}		4,600	750	1.3×10^{-7}	1.5×10^{-2}	950
			B	3.0×10^{12}			7,500	1.3×10^{-6}	0.15	9,500
		IW-7	A	1.3×10^{12}			3,300	5.6×10^{-7}	6.4×10^{-2}	4,100
			B	1.3×10^{13}			33,000	5.6×10^{-6}	0.64	41,000
High-Flux Scenario										
Low-volume scenario	200	IW-3	A	1.5×10^{11}	10^7	0.23	7.5×10^6	6.5×10^{-8}	7.5×10^{-3}	480
			B	1.5×10^{12}			7.5×10^7	6.5×10^{-7}	7.5×10^{-2}	4,800
		IW-7	A	6.5×10^{11}			3.3×10^7	2.8×10^{-7}	3.2×10^{-2}	2,100
			B	6.5×10^{12}			3.3×10^8	2.8×10^{-6}	0.32	21,000
High-volume scenario	400	IW-3	A	3.0×10^{11}		0.46	7.5×10^6	1.3×10^{-7}	1.5×10^{-2}	950
			B	3.0×10^{12}			7.5×10^7	1.3×10^{-6}	0.15	9,500
		IW-7	A	1.3×10^{12}			3.3×10^7	5.6×10^{-7}	6.4×10^{-2}	4,100
			B	1.3×10^{13}			3.3×10^8	5.6×10^{-6}	0.64	41,000

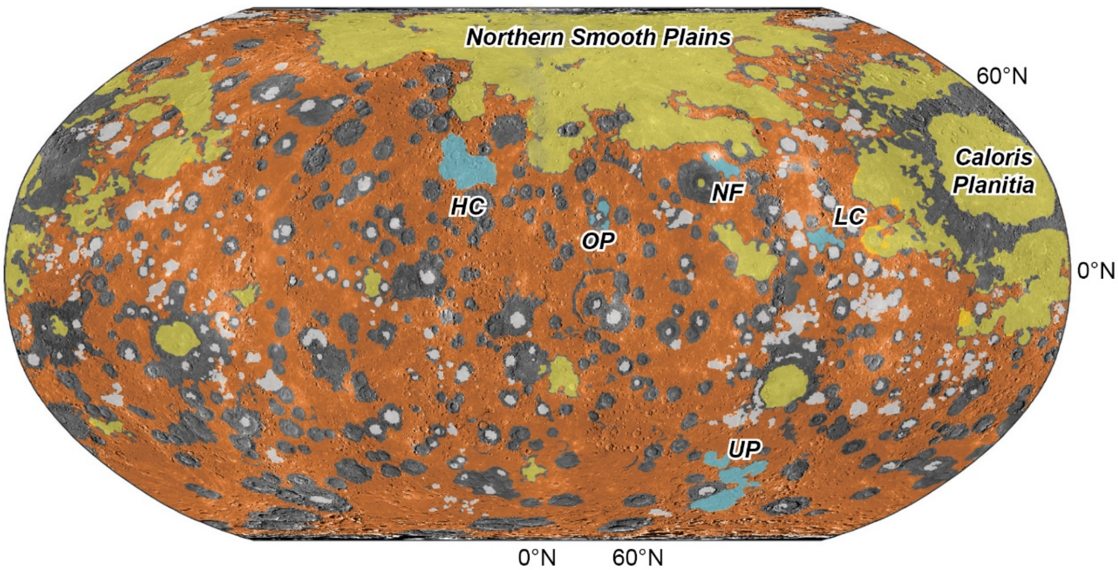

Figure 1. The global distribution of intercrater plains (ICPs) and smooth plains (SPs) on Mercury (modified from Byrne et al., 2018). ICPs are shaded in orange, mapped by Prockter et al. (2016). SPs that were dated in this analysis are shaded in blue: Otaared Planitia (OP), Utaridi Planitia (UP), south of Nathair Facula (NF), north of Lange crater (LC), and surrounding Holbein crater (HC). SPs that were dated in previous analyses (Fassett et al., 2009; Denevi et al., 2013; Whitten et al., 2014; Ostrach et al., 2015) are shaded in yellow and those that remain to be dated are in light gray.

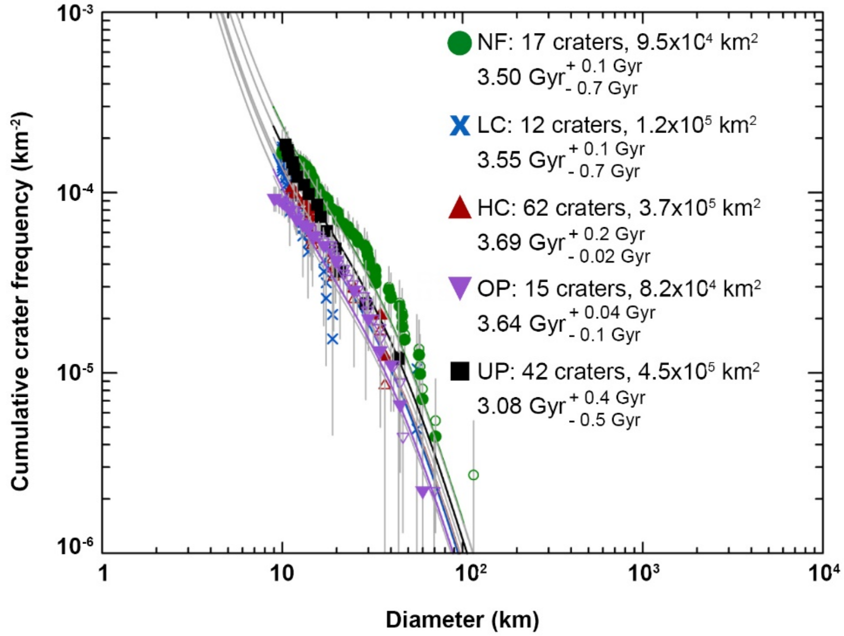

Figure 2. The estimated absolute model ages for five previously undated SP deposits: Otaared Planitia (OP), Utaridi Planitia (UP), south of Nathair Facula (NF), north of Lange crater (LC), and surrounding Holbein crater (HC). The ages are derived from fitting crater size-frequency distributions of the SP surfaces ($N > 10$) to the chronology and production curves for Mercury (Le Feuvre and Wieczorek, 2011).

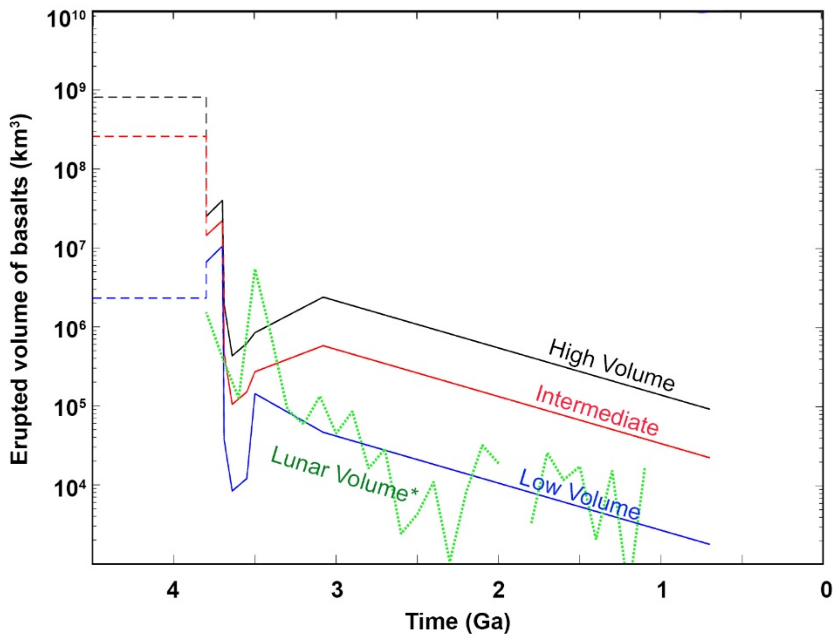

Figure 3. Estimates of the volume of erupted basalts on Mercury at specific times, as inferred from the surface ages of the SPs (solid) and ICPs (dashed), interpolated over time from 4.5 Ga to 0.7 Ga. Volume estimates are calculated for low-volume (blue), high-volume (black), and intermediate-volume (red) cases. The predicted volume of erupted basalts on the Moon is shown in green using the data from Needham and Kring (2017). Note that the volume is shown on a log scale.

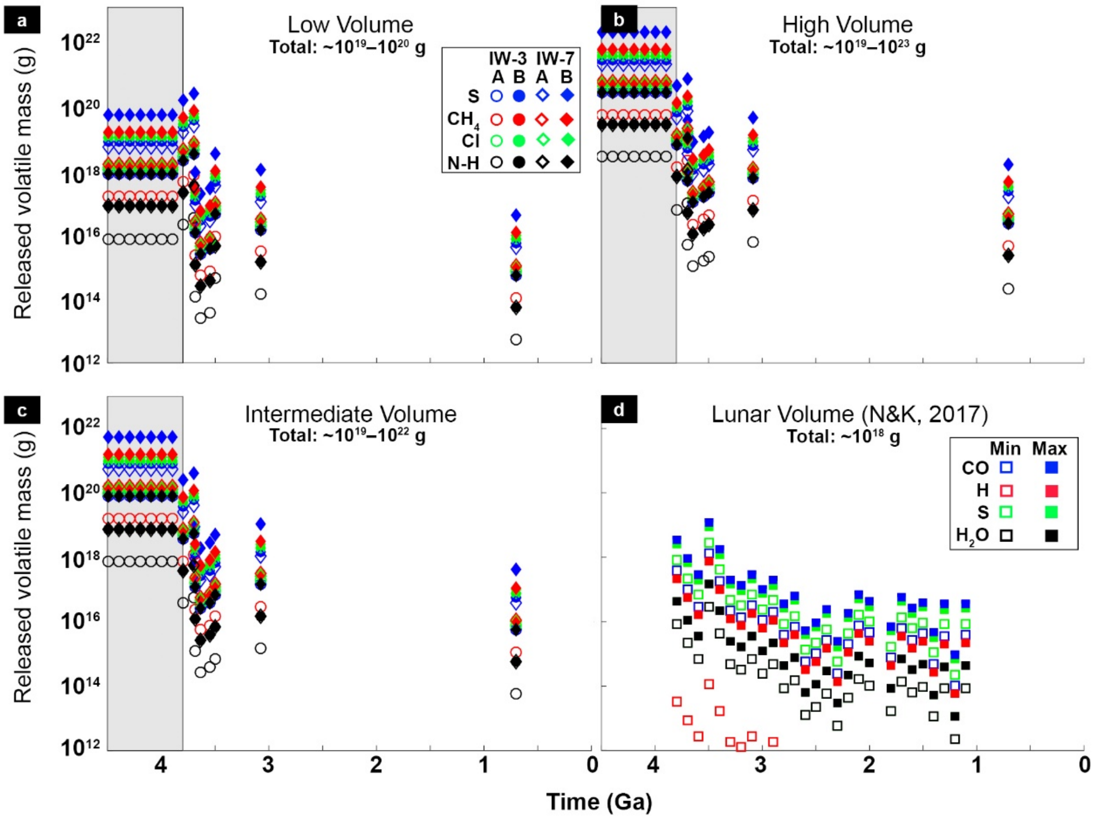

Figure 4. Estimates of the mass of S (blue), CH_4 (red), Cl (green), and N–H (black) released on Mercury at specific times, as inferred from the surface ages of the volcanic plains units. For fO_2 values of IW-3 and IW-7, estimates are computed for low-gas (Model A) and high-gas (Model B) scenarios. Estimates are calculated for three different plains-volume scenarios by exploring a range in estimated plains thicknesses: (a) low volume, (b) intermediate volume, and (c) high volume. Estimates are derived for volatiles released both during SP-forming eruptions, and also ICP-forming eruptions (shaded in grey in each panel). These estimates can be compared to (d) the predicted mass of volatiles released during the formation of the maria by Needham and Kring (2017).

Chapter 5

Temperature-dependent changes

in the normal albedo of the lunar surface at 1064 nm

Ariel N. Deutsch[a], James W. Head III[a], Gregory A. Neumann[b], Paul G. Lucey[c]

[a]Department of Earth, Environmental and Planetary Sciences, Brown University, Providence, RI 02912, USA

[b]NASA Goddard Space Flight Center, Greenbelt, MD 20771, USA

[c]Hawaii Institute of Geophysics and Planetology, University of Hawaii at Manoa, Honolulu, HI, 96822

Accepted for publication in *Journal of Geophysical Research: Planets*

Deutsch, A. N., Head, J. W., Neumann, G. A., Lucey, P. G., *Accepted*. Temperature-dependent changes in the normal albedo of the lunar surface at 1064 nm. *Journal of Geophysical Research: Planets.*

Abstract

Over the extreme temperature variations experienced in a single lunar day ($\Delta T \approx 300$ K), particular minerals common to the lunar surface show spectral changes at discrete near-infrared wavelengths in laboratory settings (Singer and Roush, 1985; Roush and Singer, 1986, 1987). Variations in temperature can cause variations in the size and shape of crystallographic sites, which control the position, shape, and depth of crystal field absorptions. At an observation wavelength of 1064 nm, the Lunar Orbiter Laser Altimeter (LOLA) should be highly sensitive to temperature-dependent changes of orthopyroxene. Here we analyze temperature-dependent spectral changes of the lunar surface as measured from orbit by LOLA. We couple LOLA measurements of normal albedo with measurements of surface temperature from the Diviner Lunar Radiometer Experiment, analyzing the maria and highlands between ±50°. We provide the first evidence of temperature-dependent spectral changes on the lunar surface from orbital observations, finding that the majority of the surface between ±50° demonstrates a small, yet measurable, negative change in 1064-nm-albedo with temperature ($-\Delta R/\Delta T$). The measurable effect is on the order of a few percent change in reflectance per ~80 K, indicating temperature changes do not have a large effect on measurements of albedo at the sensitivity of the LOLA instrument. Stronger $-\Delta R/\Delta T$ values tend to be associated with regions with elevated orthopyroxene, and the maria typically have higher levels of orthopyroxene and stronger $-\Delta R/\Delta T$ values than the highlands. Our results suggest that single-wavelength lasers may be powerful tools for understanding the distribution of particular minerals on the lunar surface.

Plain language summary

In a single day, the surface temperature of the Moon varies over 300 K (540°F). This massive swing in temperature can affect the ways in which we measure light that is scattered from the lunar surface. The properties of scattered light are important tools for understanding the color and mineralogy of the Moon's surface; therefore, understanding the influence of temperature on these properties is particularly important in interpreting the presence of different rock-forming minerals or ices on the Moon. Here we measure the effect that temperature has on measurements of surface reflectance specifically for the Lunar Orbiter Laser Altimeter, which is an instrument onboard the Lunar Reconnaissance Orbiter and currently orbiting the Moon. We find that there is a small, yet measurable effect where surfaces tend to appear brighter when the surface is colder. This change is consistent with previous laboratory studies of lunar minerals and soils that detected a temperature-dependent change in reflectance properties.

1. Introduction

The thermal environment of the lunar surface is extreme due to the lack of any appreciable atmosphere, the Moon's slow rotation, and the highly insulating nature of the surface (Vasavada et al., 2012). As a result, equatorial surface temperatures drop ~300 K between local noon and night (Williams et al., 2017). Interestingly, over this great temperature range, mafic rock-forming minerals common to the lunar surface (pyroxene and olivine) show spectral changes in the near-infrared (IR) wavelengths (e.g., Singer and Roush, 1985; Roush and Singer, 1986, 1987; Hinrichs and Lucey, 2002). Variations in temperature cause variations in the size and shape of crystallographic sites, which control the position, shape, and depth of crystal field absorptions (Singer and Roush, 1985).

Multiple laboratory studies have demonstrated the near-IR spectral changes that pyroxene and olivine show with respect to temperature (Singer and Roush, 1985; Roush and Singer, 1986, 1987; Hinrichs and Lucey, 2002). For a constant mineralogy, higher temperatures (red colors in Fig. 1) produce a broader absorption band at near-IR wavelengths. In contrast, lower temperatures (blue colors in Fig. 1) result in site contraction, producing a narrower absorption band, an increase in the crystal field splitting energy, and an increase in reflectance (Singer and Roush, 1985; Roush and Singer, 1986, 1987; Hinrichs et al., 1999). The spectral dependence on temperature with wavelength is referred to as the thermo-reflectance spectrum, and can be quantified as the change in reflectance with temperature as a function of wavelength, $\Delta R/\Delta T$, in units of K^{-1} (Hinrichs and Lucey, 2002). Hinrichs and Lucey (2002) demonstrated that the thermo-reflectance spectra of pyroxene and olivine are distinct, and the wavelengths that are most sensitive to the $\Delta R/\Delta T$ of each mineral are unique.

The unique thermo-reflectance spectra of pyroxene and olivine have been used previously to characterize the mineralogy of small airless bodies. For example, the spectral properties of Eros as measured by the NEAR-Shoemaker spacecraft were observed to vary with temperature in the near-IR (Lucey et al., 2002). These variations were used to assess the abundance of olivine, and to suggest that Eros has a surface composition similar to that of an LL chondrite (Lucey et al., 2002). Temperature-dependent spectral effects have also been used to explain the differences between the spectra of olivine-rich A-asteroids (observed at low temperatures in space) and the laboratory spectra of olivines (measured in ambient conditions); the spectra of A-asteroids were most similar to laboratory measurements of low-Fe olivines acquired at low temperatures reasonable for the heliocentric distance of the main asteroid belt (Lucey et al., 1998).

Temperature-dependent spectral effects of different rock-forming minerals are dependent on wavelength and one of the largest changes for pyroxene overlaps with the 1064-nm observation wavelength of the Lunar Orbiter Laser Altimeter (LOLA; Smith et al., 2010; 2017) (Fig. 1). Fig. 2 demonstrates how temperature has a drastic effect on the measured reflectance of pyroxene specifically at LOLA's observing wavelength. Over the range of temperatures experienced by the lunar surface during the course of a single day ($\Delta T \approx 300$ K), low-calcium pyroxene varies in spectral reflectance at 1064 nm by a factor greater than 1.5. Fig. 2 illustrates that at its observation wavelength of 1064 nm, LOLA should be highly sensitive to temperature-dependent changes of orthopyroxene, although not to olivine.

LOLA is also expected to not be sensitive to temperature-dependent changes of most high-Ca pyroxenes, although temperature-dependent spectra have not been collected for such samples. Using Gaussian fits to pure pyroxenes from Denevi et al. (2007), we produce Figure 3 that shows the predicted wavelengths for the maximum temperature effect as a function of pyroxene composition. These wavelengths are calculated assuming that the principal temperature activity of any pyroxene occurs on the long wavelength side of the 1-µm absorption, at the position of the full width-half maximum of the absorption band, as is true for orthopyroxene. LOLA should be sensitive to pyroxenes with maximum temperature-dependent changes between 1.014 and 1.114 μm, given that such changes are within a factor of 2 (50 nm) of the laser's wavelength (1064 nm). This includes essentially all orthopyroxenes as well as the most-magnesian, least-calcic clinopyroxenes (magnesian pigeonite) (Fig. 3). The sensitivity of LOLA to temperature-dependent changes in all other clinopyroxenes is low.

On the lunar surface, which is a complex mixture of many components, there is naturally a more complicated relationship between temperature and reflectance at this wavelength. The abundance of minerals other than pyroxene and also space weathering effects dilute the strong temperature-dependent spectral effects of the pyroxene content. Hinrichs and Lucey (2002) analyzed 11 Apollo soils and found a measureable temperature-dependent spectral effect for the lunar soils (Fig. 2). The change in relative reflectance with temperature was on the order of 1% or less per 100 K, which is substantially less than the 5–10% per 100 K for ordinary chondrites and HEDs or the ~35% per 100 K for pure minerals (Hinrichs and Lucey, 2002). The relative weakness of the $\Delta R/\Delta T$ measured in these specific Apollo samples is likely to be related to (1) the masking effect of submicroscopic iron present in the highly mature soils, (2) the overall low levels of iron in the analyzed samples, and (3) the low sensitivity of the measurements relative to the low-reflectance of the soils analyzed (Hinrichs and Lucey, 2002).

Overall, the few percent variation in reflectance at 1064 nm measured in the Apollo soils over the 100–400 K temperature range is close to the noise level of a single

LOLA observation (Section 2.1). However, LOLA has been acquiring measurements of the Moon's surface reflectance for nearly a decade (e.g., Smith et al., 2010; Smith et al., 2017), and the tens of millions of LOLA observations enable statistically significant analyses of temperature-dependent changes (Table S1).

Understanding how the reflectance of the lunar surface varies in response to the Moon's drastic thermal environment is important in our interpretations of remotely sensed data, as well as our understanding of the mineralogy of the surface. Specifically, understanding the thermal response of the lunar surface to solar forcing is important in the characterization of regolith structure and thermophysical properties (e.g., Vasavada et al., 1999, 2012; Hayne et al., 2017; Williams et al., 2017), surface roughness (e.g., Lawrence et al., 2013; Bandfield et al., 2015), and surface rock abundance (Bandfield et al., 2011, 2014; Ghent et al., 2014) and the photometric behavior of the lunar surface (e.g., Barker et al., 2016; Domingue et al., 2018), and the optical properties of lunar soils are highly relevant to studies of other airless bodies (e.g., Pieters et al., 2000). Understanding the temperature-dependent spectral behavior of the lunar surface can also help constrain the distribution of specific minerals important in the crustal evolution of the Moon (e.g., Klima et al., 2008, 2011; Lemelin et al., 2019). Furthermore, as additional payloads (with higher resolution and precision) are being prepared to support lunar science and exploration, future remote sensing measurements of the lunar surface should account for temperature changes experienced during observations. This is of particular interest to the volatiles community, given that enhanced reflectance is often used as observational support for the presence of frost and water on airless bodies (e.g., Zuber et al., 2012; Neumann et al., 2013; Deutsch et al., 2017; Ermakov et al., 2017; Fisher et al., 2017).

Thus, here we are interested in how the surface reflectance of the Moon, as measured from orbit by LOLA, changes over the course of a lunar day during the extreme temperature fluctuations. We couple LOLA measurements of lunar surface reflectance with Diviner measurements of lunar surface temperature in order to analyze temperature-dependent changes in highlands and maria reflectance. We discuss implications for using single-wavelength remote sensing instruments as mineralogical sensors, and the importance of accounting for temperature-dependent spectral effects in future exploration of the Moon.

2. Methods and data

2.1. Diurnal changes in the lunar surface reflectance at 1064 nm

LOLA measures the Moon's surface reflectance via the strength of the returned altimetric laser pulse (Smith et al., 2010). Measurements are acquired from nadir at a wavelength of 1064 nm, which is coincident with a diagnostic absorption feature of pyroxene (centered near 1 μm) due to the presence of Fe^{2+} in the M2 site of the crystal (Adams, 1974). The M2 site refers to one of two octahedral sites in the crystallographic structure (the "M" nomenclature is used to designate a "metal" or cation site without specifying the cation that occupies the site) (Morimoto, 1988). At LOLA's wavelength, this iron absorption feature has been observed in laboratory studies to reveal strong temperature-dependent spectral changes (Fig. 1) (e.g., Roush and Singer, 1987; Hinrichs et al., 1999).

We analyze the normal albedo of the lunar surface using LOLA data acquired by Detector 3 on Laser 1 during the Nominal Mission Phase (LRO_NO_01 through LRO_NO_13) and the Science Mission Phase (LRO_SM_02 through LRO_SM_17). The normal albedo is defined as the ratio of brightness of a surface observed at zero phase angle (where the angle between the illumination source, surface, and detector is zero) from an arbitrary direction to the brightness of a perfectly diffuse surface located at the same position, but illuminated and observed perpendicularly (Hapke, 2012). The normal albedo is measured independent of illumination conditions, and is not influenced by the local surface topography (Hapke, 1993; Smith et al., 2010; Lucey et al., 2014).

Previously, Lemelin et al. (2016a) produced calibrated LOLA data that were acquired during the first 10 months of the Nominal Mission Phase. These data were corrected for the sensitivity drift of the lasers with time (i.e., the natural degradation of the lasers) and for anomalous data, which were primarily acquired when the received energy was < 0.14 fJ, when the spacecraft was pointing off-nadir, or when the range was > 70 km (Lemelin et al., 2016a). The data were scaled to the normal albedo presented by Lucey et al. (2014), who calibrated LOLA reflectance measurements to Kaguya Multiband Imager observations acquired at zero phase angle at 1050 nm.

In order to increase the spatial and temporal data coverage for this analysis, we supplement Nominal Mission Phase (NO) data with Science Mission Phase (SM) data. Including these additional data more than doubles the coverage in local time (Table S1), allowing for a more robust statistical analysis. All of the data we use are calibrated to agree with the Lemelin et al. (2016a) data, by accounting for the long-term drift of

Detector 3 during NO and SM via a cubic polynomial, with a step function offset between the nominal and science mission phases (Fig. S1).

In this calibration, we utilize all daytime data (solar incidence <89°) and discard observations that were acquired >3° off nadir or during the few days during NO_01 when the laser gains were not fixed (GAINS=FSW). We correct each observation for drift in each mission month and hour of local time (between 07:00 and 16:00) by the polynomial function, and bin the data in 1°x1° spatial bins in order to minimize intrinsic reflectance variations and to suppress anomalies associated with the laser thermal blanket. The data in each local hour for each mission month are regressed between ±25° latitude against the Gridded Data Record Albedo Map LDAM_4 (https://ode.rsl.wustl.edu/mars/pagehelp/quickstartguide/index.html?lola_gdrdam.htm) to obtain the best linear fit to the normal albedo map. The regression coefficients are mapped to the fraction of the LOLA mission month (NO or SM) that they represent, and we fit a cubic polynomial to the slope and a linear polynomial to the intercept to remove the long-term drift in a manner similar to Lemelin et al. (2016a), as shown in the Supplemental Material. We use our calibration on both the nominal and science mission phases data to produce our final dataset of lunar normal albedo (Fig. S1).

During the nine years of still ongoing operations, LOLA has nominally collected data throughout the lunar day, although returns are minimal when the LRO spacecraft crosses the terminator due to an artifact introduced from instrument cooling and contraction (Smith et al., 2010); thus, the bulk of calibrated LOLA reflectance data have been acquired between the local hours of 07:00 and 16:00. Our data analysis is limited to local hours of 08:00 and 15:00 to avoid times where the laser blanket anomalies are strongest. Here we analyze the LOLA data for differences in mean normal albedo during the cycle of the lunar day (between the local hours of 08:00 and 15:00) at 1-hr bins by sorting the data based on the local hour at which the data were acquired. Each local hour represents the beginning time of each hourly bin.

The mean normal albedo at each grid cell (1°x1°) is computed from several thousand individual observations, and our analysis utilizes more than 53 million LOLA observations to enable statistically significant albedo variations (Table S1). We quantify the systematic error by estimating the standard error of the linear comparison of the gridded data with the Terrain Camera(TC)-calibrated data (Lucey et al., 2014) and estimate that the error for our LOLA normal albedo is <3% error. Lemelin et al. (2016a) found that the greatest absolute errors in normal albedo (3–4 %) stem from off-nadir geometries and so here we exclude off-nadir observations from our analysis.

Our analysis covers the lunar surface between 50°N and 50°S, latitudes between which temperature fluctuations are greatest (Williams et al., 2017). We find that beyond these latitudes, the laser thermal blanket anomalies strongly interfere with the laser's measurements of normal albedo. The data are binned in 1°x1° spatial bins, representing surface areas that are ~30x30 km^2. Latitude-dependent reflectance variations associated with space weathering have been observed with LOLA (Lucey et al., 2014; Hemingway et al., 2015; Lemelin et al., 2016a; Smith et al., 2017), and thus we limit the extent of each analyzed spatial cell. We also analyze how diurnal changes differ between the highlands and maria, given that these terrains have intrinsically different reflectance properties (e.g., Pieters, 1978; 1986; McEwen and Robinson, 1995; Lucey et al., 2014). We use the lunar maria boundaries as mapped by Nelson et al. (2014) from a 643-nm monochromatic Lunar Reconnaissance Orbiter Camera (LROC) Wide-Angle Camera (WAC) image mosaic generated from the ratio of band 1 (321 nm) and band 3 (415 nm), and a Clementine color ratio product.

Note that for simplicity, we use the term "reflectance" to mean the normal albedo of the lunar surface, describing the bidirectional reflectance of the surface at zero phase angle; thus, these measurements are independent of illumination conditions.

2.2. Diurnal changes in the lunar surface temperature

The Diviner Lunar Radiometer Experiment characterizes the Moon's thermal environment by mapping the thermal emission from the lunar surface over complete spatial (latitude, longitude) and temporal (diurnal, seasonal) ranges (e.g., Paige et al., 2010; Williams et al., 2017). With the Diviner instrument, we estimate the surface temperature at 1-hr bins between the local hours of 08:00 and 15:00 in order to complement the local time-of-day reflectance measurements from LOLA. We use bolometric temperature data from the Diviner global cumulative product, which provides data at a spatial resolution of 0.5° and a temporal resolution of 0.25 h local time (http://pds-geosciences.wustl.edu/lro/lro-l-dlre-4-rdr-v1/lrodlr_1001/data/gcp/). The bolometric temperature is derived from the brightness temperatures of the individual Diviner spectral channels that measure the Moon's radiance, and is thus a measure of the spectrally integrated flux of IR radiation emerging from the lunar surface (Paige et al., 2010; Williams et al., 2017).

The surface temperature at each grid cell (1°x1°) is calculated from a dataset composed of more than 10 million Diviner observations to enable statistically significant temperature variations. The greatest standard deviations of the Diviner temperature measurements are associated with higher latitude observations, but here our analysis targets only the latitudes between 50°N and 50°S, where associated errors are smallest (Williams et al., 2017). The one-sigma standard deviation of the mean indicates an error of <1.5%.

3. Results

3.1. Temperature-dependent changes in the lunar surface reflectance

Measurements of lunar surface reflectance and temperature for local hours between 08:00 and 15:00 are shown in Fig. 4. During this time window, the surface experiences a maximum temperature change of ~80 K, with peak temperatures around local noon. There is an asymmetry around these peaks due to the thermal inertia of the lunar regolith, such that the surface is slightly warmer in the afternoon (Williams et al., 2017).

Between the hours of 08:00 and 15:00, there are subtle yet recognizable changes in the measured surface reflectance as measured by LOLA at 1064 nm (Fig. 4). Specifically, the surface appears to have a relatively lower reflectance when it is warmest at 12:00, and appears to have a relatively higher reflectance when the surface is coldest, around 08:00 or 15:00. The most distinctive changes are easily identifiable in the maria and in the regions immediately adjacent to the maria (Fig. 4).

3.2. The strength of temperature-dependent reflectance changes

We quantify the mean thermo-reflectance value at each individual degree of latitude between ±50°, separately for the highlands and maria, in order to (1) minimize latitude-dependent reflectance variations associated with space weathering (Lucey et al., 2014; Hemingway et al., 2015; Lemelin et al., 2016a; Smith et al., 2017) and (2) disentangle intrinsic reflectance differences between the two major geologic terrains (e.g., Lucey et al., 2014). The mean thermo-reflectance value at each degree of latitude is calculated from a few hundred thousand LOLA observations (thousands of individual observations at each local hour between 08:00 and 15:00) (Table S1). The temperature-dependent change in surface reflectance at 1064 nm is, on average, stronger in the maria ($\Delta R/\Delta T*1000 = -0.36$) than in the highlands ($\Delta R/\Delta T*1000 = -0.20$) (Table S2).

In Fig. 5, we show examples of thermo-reflectance spectra for the highlands and maria. For example, the first row in Fig. 5 shows the temperature-dependent changes in surface reflectance at 1064 nm specifically for the latitudinal region between 10°N and 11°S, for both the highland and mare surfaces. The least-squares fit to the slop is plotted in grey, representing the mean thermo-reflectance value ($\Delta R/\Delta T*1000$). In the subsequent rows of Fig. 5, we show the same data, but for groups of latitudinal bins. For each degree of latitude between 50°N and 50°S within the highlands and maria, we plot the *mean surface reflectance at 1064 nm* for each local hour between 08:00 and 15:00 with respect to the *mean surface temperature* for each local hour between 08:00 and 15:00. Again, for each degree of latitude, we solve for a least-squares fit to the hourly points (grey lines in Fig. 5). The data are displayed in subplots based on latitudinal groups in order to view the $\Delta R/\Delta T$ with more clarity.

The average thermo-reflectance value ($\Delta R/\Delta T*1000$) reported in each subplot is calculated from the temperature-reflectance relationship of a single degree of latitude, for both the maria and the highlands. As discussed in Section 2, the systematic error of these data is estimated to be <2%. From the associated error of the LOLA and Diviner measurements, we estimate that the uncertainties of our derived thermo-reflectance values to be on the order of 2.5%.

We find that the majority of the lunar surface between 50°N and 50°S demonstrates a small, yet measurable, negative change in the surface reflectance at 1064 nm with temperature, consistent with the presence of pyroxene. For 9 of the 10 subplots, the mean $\Delta R/\Delta T$ has a negative slope, indicating a general darkening in the surface reflectance with a warming of the surface. The outlier to this trend is the highlands group between 30°N and 50°N. The maria consistently show stronger $\Delta R/\Delta T$ values than the highlands, meaning that they show a more drastic temperature-dependent change in the measured surface reflectance at 1064 nm (Table S2). For the maria, the mean $\Delta R/\Delta T*1000$ values are on the order of ~-0.2 to -0.5 K^{-1}. The lunar highlands also tend to show a negative $\Delta R/\Delta T$ trend, although the $\Delta R/\Delta T*1000$ values of the highlands are relatively lower (~0 to -0.4 K^{-1}) than those of the maria. However, for some latitudinal bands, these highland values are nearly equivalent in strength to the $\Delta R/\Delta T$ of the lunar maria (Fig. 5). Pure orthopyroxene has a $\Delta R/\Delta T*1000$ of ~-0.9 K^{-1} at 1064 nm for the temperature range that is experienced by the lunar surface between the local hours of 08:00 and 15:00 (Fig. 2).

In Table S2, we document the maximum thermo-reflectance values for the highlands and maria, analyzed at a spatial resolution of 1 latitudinal degree (see Supporting Information). We find that, overall, the maria have a stronger (more negative) $\Delta R/\Delta T*1000$ value (-0.36) in comparison to the highlands (-0.20). Overall, the highlands show the strongest temperature-dependent changes in the equatorial region (15°N – 15°S) and southern mid-latitudes (15°S–30°S). The maria also show the strongest temperature-dependent changes within these regions, although similarly strong changes were detected for the maria between 30°N and 50°N as well. A coarse spatial correlation between the terrane type (Fig. 6b) and the strength of temperature-dependent reflectance changes in reflectance (Fig. 6a) can be observed in Fig. 6.

This negative relationship between surface reflectance and temperature changes is depicted in Fig. 6(a), where the mean $\Delta R/\Delta T*1000$ values are shown for 1°x1° spatial bins. These values typically range from ~0 to -1 K^{-1}. There are also some anomalous regions on the surface area (shown in white) that experience either a positive or no change in surface reflectance with temperature changes. These regions are typically found along the latitudinal fringes of the study area, where laser thermal blanket anomalies are most prevalent in the data (Fig. 4).

4. Discussion

4.1. Temperature-dependent spectral changes in the highlands and maria

The results presented here provide the first evidence for temperature-dependent spectral changes of the lunar surface. These results are consistent with laboratory studies that observe a temperature-dependent spectral change for common lunar minerals (Singer and Roush, 1985; Roush and Singer, 1986) and Apollo samples (Hinrichs and Lucey, 2002). Measurements of returned lunar soils revealed a change in relative reflectance with temperature of ~1% or less per 100 K at near-IR wavelengths (Hinrichs and Lucey, 2002). This is similar to the ΔR/ΔT that we measure (Fig. 5). We find that this change may be indicative of the mineralogy of the surface (Section 4.2), which suggests important opportunities for understanding surface mineralogy remotely at a single wavelength.

We find that the majority of the lunar surface between 50°N and 50°S demonstrates a small, yet measurable, negative change in the surface reflectance at 1064 nm with temperature; however, our entire study region does not reveal this measurable ΔR/ΔT relationship. One factor complicating this analysis is the sensitivity of the LOLA instrument in detecting these extremely small changes in surface reflectance, which are on the order of a few percent change. This change is detected by co-adding the LOLA data that features single shot uncertainty of 12% (Smith et al., 2010), but importantly results from analyzing statistical datasets that include >17 million individual laser shots for each of the local hour groups (Table S1). Thus, we find that our analysis is statistically robust and note that the extremely small changes measured here are comparable to the change in relative reflectance with temperature measured for Apollo soils, which was on the order of 1% or less per 100 K (Hinrichs and Lucey, 2002).

It is also possible that LOLA does not observe a uniformly strong temperature-dependent reflectance change across all the maria or all the highlands due to differences in optical maturity (Hinrichs and Lucey, 2002). Mature soils show less contrast due to the attenuating effect of submicroscopic iron that has accumulated through time from space weathering processes (e.g., Pieters et al., 2000; Hapke, 2001; Pieters and Noble, 2016). The cumulative amount of submicroscopic iron affects the optical properties of measured and modeled soils, resulting in spectral darkening and reddening and subdued absorption bands in the near-IR (e.g., Pieters et al., 2000). Additionally, surfaces that are low in pyroxene will show a weaker temperature-dependent spectral change at LOLA's wavelength (Hinrichs and Lucey, 2002). Changes in absorption band symmetry at 1064 nm occur as Fe^{2+} crystal field absorptions become narrower with decreasing temperature, and these changes are due to the intrinsic absorbance properties of the minerals (Singer and Roush, 1985; Roush and Singer, 1986, 1987; Schade and Wasch, 1999; Moroz et al., 2000; Hinrichs et al., 1999). Finally, the surface reflectance measured by LOLA may also be affected by grain size effects given that varying grain size can cause variations in absolute reflectance at near-IR wavelengths (Adams and Filice, 1967; Pieters, 1983; Clark and Roush, 1984; Pieters et al., 1993; Hapke, 1993, 2012; Mustard and Hays, 1997; Milliken and Mustard, 2007). However, grain size is effectively normalized by the process of regolith formation (Fischer and Pieters, 1994) and Lucey (2006) demonstrated that empirical methods for the derivation of elemental abundances that depend on spectral-elemental correlations (e.g., Lawrence et al., 2002) require a narrow grain size to function, and would be ineffective if grain sizes varied significantly at the 100-m scale. Overall, variations in maturity and grain size may affect measurements of surface reflectance at 1064 nm, but are not expected to substantially influence our analysis of the lunar surface between ±50°. Importantly, variations in maturity and grain size are not expected to produce temperature-dependent effects. Absorbing species other than orthopyroxene, however, can limit or even prohibit temperature-dependent changes in the 1064-nm surface reflectance at the sensitivity of the LOLA data.

4.2. LOLA as a mineralogical sensor

As discussed in Section 1, different minerals have unique thermo-reflectance spectra that are wavelength-dependent, which have been used in the past to characterize the mineralogy of asteroids (Lucey et al., 1998, 2002). The observation wavelength of LOLA is particularly sensitive to temperature-dependent spectral changes of low-calcium pyroxene (Fig. 2). While it is not commonly considered to be a mineralogical sensor, our results suggest that future laser altimeters as well as LOLA could be used to map the relative abundance of particular minerals (here, pyroxene) from detections of temperature-dependent reflectance changes. Pyroxenes are the most prevalent mafic mineral on the Moon, and are commonly used as a tool for understanding the magmatic source, composition, and cooling history of remotely sensed surfaces (e.g., Adams, 1974; Cloutis and Gaffey, 1991; Sunshine and Pieters, 1993; Greenhagen et al., 2010; Klima et al., 2008, 2011; Yamashita et al., 2012). Understanding the distribution of pyroxene mineralogies is important to our understanding of the crustal evolution on the Moon.

There is substantial heterogeneity in the distribution and absolute abundance of orthopyroxene at the lunar surface (Fig. 6c). Analyses of Kaguya Multiband Imager data indicate that low-calcium pyroxene is abundant (up to ~50 wt.%) in the Procellarum KREEP Terrane and in Mare Tranquilitatis, and is the dominant mafic mineral in the South Pole-Aitken basin (Fig. 6c; Lemelin et al., 2016b; 2019). We find that the parts of the surface that do have higher levels of orthopyroxene, indeed show a negative ΔR/ΔT relationship (Fig. 6), consistent with laboratory studies (Singer and Roush, 1985; Roush and Singer, 1986; Hinrichs and Lucey, 2002). However, we observe temperature-dependent reflectance changes even on parts of the surface that are orthopyroxene-poor.

In Figure 7, we show the correlation between the amount of orthopyroxene (wt. %) and the thermo-reflectance spectra (K^{-1}) for the highlands (red) and maria (blue). In general, the maria have higher abundances of orthopyroxene exposed at the surface than do the highlands (Lemelin et al., 2016b, 2019). We find that, on average, the maria also have stronger negative ΔR/ΔT values, as indicated by the spread of data shifted to the left in the box plot below Fig. 7. This trend suggests that the mare surfaces show a slightly larger change in the surface reflectance at 1064 nm between the local hours or 08:00 and 15:00 than do the highlands.

We also note that there is considerable overlap between the ΔR/ΔT values calculated for the maria and highlands. Thus, there are likely to be other factors that are influencing how different regions of the surface experience the changes of surface reflectance as measured by LOLA during these different times of day. Figure 6 shows that the greatest temperature-dependent changes in reflectance are concentrated near the boundaries of the maria. There are likely to be some mixing effects between the boundaries of the maria and highlands, given that these contacts are diffuse due to mixing processes through time (Fischer and Pieters, 1995; Li and Mustard, 2000, 2003, 2005). Spectral mixture analyses indicate that large impact craters have resulted in highland contamination of the spectral properties of mare surfaces (Li and Mustard, 2003), as lateral transport is more efficient than vertical transport during mixing along these boundaries (Li and Mustard, 2000).

As discussed in Section 4.1., other factors that complicate thermo-reflectance spectra may include differences in iron levels, grain size, or optical maturity. For example, the absorption features of mature surfaces are relatively subdued as a result of space weathering processes (e.g., Pieters et al., 1993; 2000; Lucey et al., 2000; Noble et al., 2001). The optical maturity index derived by Lucey et al. (2000) indicates that lunar surface maturity is partly dependent on geologic setting, given that crater interiors tend to mature more slowly compared to their ejecta and that larger ejecta features tend to mature more slowly than smaller features. Generally, Copernican surfaces are relatively more immature compared to older surfaces (Lucey et al., 2000), and are associated with lower surface porosities (Mandt et al., 2016), higher rock abundances (Ghent et al., 2014; Mazrouei et al., 2019) and rougher surfaces (Neumann et al., 2015). The most immature surface on the lunar surface today include surfaces near Tycho, Stevinus, Giordano Bruno, and some northern highlands, between De La Rue, Hayn, and Bel'kovich craters. These regions tend to show stronger $\Delta R/\Delta T$ values (Fig. 6), consistent with the understanding that more immature surfaces exhibit stronger contrast in absorption features.

Importantly, variations in maturity and grain size are not expected to result in temperature-dependent variations in surface reflectance. Therefore, while variations in these factors may help explain why particular surfaces exhibit more subdued temperature-dependent spectral changes, variations in these factors are not expected to contribute to the presence of temperature-dependent spectral changes.

We also observe heterogeneity in the strength of $\Delta R/\Delta T$ values within the mare deposits (Fig. 6a), which vary in orthopyroxene abundances (Fig. 6c; Lemelin et al., 2016b; 2019) as well as in age (e.g., Hiesinger et al. 2003; 2010; 2011). The mineralogy of mare basalts shows both temporal and spatial heterogeneity. For example, young Oceanus Procellarum basalts are rich in olivine and show a stratigraphic gradation with underlying units of lower olivine abundance, while young Orientale basalts are olivine-poor and rich in high-Ca pyroxene (Varatharajan et al., 2014). This heterogeneity suggests variability in FeO content in younger basalts across the Moon (Varatharajan et al., 2014), and such heterogeneity may affect the strength of the temperature-dependent signal detected here.

5. Conclusions

We have documented the first evidence of temperature-dependent spectral changes on the lunar surface from orbital observations. Our statistical analysis, incorporating more than 53 million individual LOLA shots, indicate that temperature variations do have a measurable effect on the reflectance of the surface at 1064 nm wavelength. Specifically, measurements of higher reflectance were acquired by LOLA when the surface temperatures of the Moon were lower. The measurable effect discussed here is on the order of a few percent change in reflectance per ~80 K, indicating that temperature changes do not have a large effect on measurements of the lunar surface at the sensitivity of the LOLA instrument.

An ability to understand how the lunar surface varies with temperature will provide important constraints for future remote sensing observations of the Moon. Such observations can help assess the relative abundance of particular rock-forming minerals (here, pyroxene) that exhibit a change in spectral reflectance with temperature, using a single-wavelength laser.

Temperature-dependent spectral changes have important implications for future remotely sensed observations of the Moon, as additional spectrometers and single-wavelength lasers with higher resolution and precisions are designed and operated. These results suggest that additional laser wavelengths targeted at olivine can provide independent data for the distribution of that mineral. For example, a laser with an observation wavelength at 1460 nm should be sensitive to temperature-dependent spectral changes of olivine, although not pyroxene. However, as discussed in detail in Sections 1 and 4, there are various factors that can potentially complicate orbital measurements of temperature-dependent spectral changes, such as iron levels, grain size, or surface maturity. Of particular interest is understanding these effects on interpretations of the presence of surface volatiles. Both the science and exploration communities have strong interests in the presence of surface ice on the Moon (and beyond). Enhanced surface reflectance has been used to characterize the presence of surface ice not only on the Moon (e.g., Zuber et al., 2012; Fisher et al., 2017; Qiao et al., 2019), but also on Mercury (Neumann et al., 2013; Chabot et al., 2014; Deutsch et al., 2017), smaller airless bodies (e.g., Platz et al., 2016; Ermakov et al., 2017), Mars (e.g., Smith et al., 1998; Bell et al., 1999), and beyond. Thus, understanding how temperature affects observations of surface reflectance has widespread importance in the planetary community.

Acknowledgements

We thank Deanne Rogers for her editorial handling of the manuscript, as well as Wenzhe Fa and two anonymous reviewers for providing helpful feedback. This work is supported by NASA issued through the Harriett G. Jenkins Graduate Fellowship to A.N.D. (Grant Number NNX16AT19H), by the NASA Discovery Program to G.A.N, by NASA-Goddard to J.W.H. for participation in the Lunar Reconnaissance Orbiter (LRO) Lunar Orbiter Laser Altimeter (LOLA) Experiment Team (NNX11AK29G, NNX13AO77G and 80NSSC19K0605), and also by the LRO LOLA Experiment to P.G.L. The time-ordered, globally calibrated normal albedo data used in this study can be accessed from the LOLA PDS Data Node at http://imbrium.mit.edu/DATA/LOLA_RADR/laser1/. The Diviner temperature data can be accessed at http://pds-geosciences.wustl.edu/lro/lro-l-dlre-4-rdr-v1/lrodlr_1001/data/gcp/. The Kaguya Lunar Multiband Imager data of surface orthopyroxene content can be accessed at https://astrogeology.usgs.gov/search/map/Moon/Kaguya/MI/MineralMaps/Lunar_Kaguya_MIMap_MineralDeconv_OrthopyroxenePercent_50N50S. Temperature-dependent reflectance changes of the lunar surface at 1064 nm and supplementary Tables S1 and S2

have been archived at the Brown Digital Repository and can be accessed at https://doi.org/10.26300/y5ep-4j46.

References

Adams, J. B. (1974). Visible and near-infrared diffuse reflectance spectra of pyroxenes as applied to remote sensing of solid objects in the solar system. *Journal of Geophysical Research*, *79*(32), 4829–4836. https://doi.org/10.1029/JB079i032p04829.

Adams, J. B., & Filice, A. L. (1967). Spectral reflectance 0.4 to 2.0 microns of silicate rock powders. *Journal of Geophysical Research (1896-1977)*, *72*(22), 5705–5715. https://doi.org/10.1029/JZ072i022p05705.

Bandfield, J. L., Ghent, R. R., Vasavada, A. R., Paige, D. A., Lawrence, S. J., & Robinson, M. S. (2011). Lunar surface rock abundance and regolith fines temperatures derived from LRO Diviner Radiometer data. *Journal of Geophysical Research: Planets*, *116*(E12). https://doi.org/10.1029/2011JE003866.

Bandfield, J. L., Hayne, P. O., Williams, J.-P., Greenhagen, B. T., & Paige, D. A. (2015). Lunar surface roughness derived from LRO Diviner Radiometer observations. *Icarus*, *248*, 357–372. https://doi.org/10.1016/j.icarus.2014.11.009.

Bandfield, J. L., Song, E., Hayne, P. O., Brand, B. D., Ghent, R. R., Vasavada, A. R., & Paige, D. A. (2014). Lunar cold spots: Granular flow features and extensive insulating materials surrounding young craters. *Icarus*, *231*, 221–231. https://doi.org/10.1016/j.icarus.2013.12.017.

Barker, M.K., Sun, X., Mazarico, E., Neumann, G.A., Zuber, M.T., & Smith, D.E. (2016). Lunar phase function at 1064 nm from Lunar Orbiter Laser Altimeter passive and active radiometry. *Icarus, 273*, 96–113. https://doi.org/10.1016/j.icarus.2016.02.008.

Bell, J. F., Wolff, M. J., Daley, T. C., Crisp, D., James, P. B., Lee, S. W., et al. (1999). Near-Infrared Imaging of Mars from HST: Surface Reflectance, Photometric Properties, and Implications for MOLA Data. *Icarus, 138*, 25–35. https://doi.org/10.1006/icar.1998.6057.

Chabot, N. L., Ernst, C. M., Denevi, B. W., Nair, H., Deutsch, A. N., Blewett, D. T., et al. (2014). Images of surface volatiles in Mercury's polar craters acquired by the MESSENGER spacecraft. *Geology, 42*, 1051–1054. https://doi.org/10.1130/G35916.1.

Clark, R. N., & Roush, T. L. (1984). Reflectance spectroscopy: Quantitative analysis techniques for remote sensing applications. *Journal of Geophysical Research: Solid Earth*, *89*(B7), 6329–6340. https://doi.org/10.1029/JB089iB07p06329.

Cloutis, E. A., & Gaffey, M. J. (1991). Pyroxene spectroscopy revisited: Spectral-compositional correlations and relationship to geothermometry. *Journal of Geophysical Research: Planets*, *96*(E5), 22809–22826. https://doi.org/10.1029/91JE02512.

Denevi, B. W., Lucey, P. G., Hochberg, E. J., & Steutel, D. (2007). Near-infrared optical constants of pyroxene as a function of iron and calcium content. *Journal of Geophysical Research: Planets, 112*(E5). https://doi.org/10.1029/2006JE002802

Deutsch, A. N., Neumann, G. A., & Head, J. W. (2017). New evidence for surface water ice in small-scale cold traps and in three large craters at the north polar region of Mercury from the Mercury Laser Altimeter. *Geophysical Research Letters*, *44*, 9233–9241. https://doi.org/10.1002/2017GL074723.

Domingue, D., Palmer, E., Gaskell, R., & Staid, M. (2018). Characterization of lunar surface within Tsiolkovsky crater: Photometric properties. *Icarus, 312*, 61–99. https://doi.org/10.1016/j.icarus.2018.02.034.

Ermakov, A. I., Mazarico, E., Schröder, S. E., Carsenty, U., Schorghofer, N., Preusker, F., et al. (2017). Ceres's obliquity history and its implications for the permanently shadowed regions. *Geophysical Research Letters*, *44*(6), 2652–2661. https://doi.org/10.1002/2016GL072250.

Fischer, E. M., & Pieters, C. M. (1994). Remote determination of exposure degree and iron concentration of lunar soils using VIS-NIR spectroscopic methods. *Icarus, 111*(2), 475–488. https://doi.org/10.1006/icar.1994.1158

Fischer, E. M., & Pieters, C. M. (1995). Lunar surface aluminum and iron concentration from Galileo solid state imaging data, and the mixing of mare and highland materials. *Journal of Geophysical Research: Planets, 100*(E11), 23279–23290. https://doi.org/10.1029/95JE02359.

Fisher, E. A., Lucey, P. G., Lemelin, M., Greenhagen, B. T., Siegler, M. A., Mazarico, E., et al. (2017). Evidence for surface water ice in the lunar polar regions using reflectance measurements from the Lunar Orbiter Laser Altimeter and temperature measurements from the Diviner Lunar Radiometer Experiment. *Icarus*, *292*, 74–85. https://doi.org/10.1016/j.icarus.2017.03.023.

Ghent, R. R., Hayne, P. O., Bandfield, J. L., Campbell, B. A., Allen, C. C., Carter, L. M., & Paige, D. A. (2014). Constraints on the recent rate of lunar ejecta breakdown and implications for crater ages. *Geology*, *42*(12), 1059–1062. https://doi.org/10.1130/G35926.1.

Greenhagen, B. T., Lucey, P. G., Wyatt, M. B., Glotch, T. D., Allen, C. C., Arnold, J. A., et al. (2010). Global Silicate Mineralogy of the Moon from the Diviner Lunar Radiometer. *Science, 329*(5998), 1507–1509. https://doi.org/10.1126/science.1192196.

Hapke, B. (1993). Theory of Reflectance and Emittance Spectroscopy by Bruce Hapke. https://doi.org/10.1017/CBO9780511524998.

Hapke, B. (2001). Space weathering from Mercury to the asteroid belt. *Journal of Geophysical Research: Planets*, *106*(E5), 10039–10073. https://doi.org/10.1029/2000JE001338.

Hapke, B. (2012). Theory of Reflectance and Emittance Spectroscopy by Bruce Hapke. https://doi.org/10.1017/CBO9781139025683.

Hayne, P. O., Bandfield, J. L., Siegler, M. A., Vasavada, A. R., Ghent, R. R., Williams, J.-P., et al. (2017). Global regolith thermophysical properties of the Moon from the Diviner Lunar Radiometer Experiment. *Journal of Geophysical Research: Planets*, *122*(12), 2017JE005387. https://doi.org/10.1002/2017JE005387.

Hemingway, D. J., Garrick-Bethell, I., & Kreslavsky, M. A. (2015). Latitudinal variation in spectral properties of the lunar maria and implications for space weathering. *Icarus, 261,* 66–79. https://doi.org/10.1016/j.icarus.2015.08.004

Hiesinger H., Head J. W., Wolf U., Jaumann R., & Neukum G. (2003). Ages and stratigraphy of mare basalts in Oceanus Procellarum, Mare Nubium, Mare Cognitum, and Mare Insularum. *Journal of Geophysical Research: Planets, 108*(E7), 5065. https://doi.org/10.1029/2002JE001985.

Hiesinger, H., Head, J.W., Wolf, U., Jaumann, R., & Neukum, G. (2011). Ages and stratigraphy of lunar mare basalts: A synthesis. *Geological Society of America Special Papers, 477*, 1–51. https://doi.org/10.1130/2011.2477(01).

Hiesinger, H., Head, J.W., Wolf, U., Jaumann, R., Neukum, G., 2010. Ages and stratigraphy of lunar mare basalts in Mare Frigoris and other nearside maria based on crater size-frequency distribution measurements. *Journal of Geophysical Research: Planets, 115*, E03003. https://doi.org/10.1029/2009JE003380.

Hinrichs, J. L., & Lucey, P. G. (2002). Temperature-dependent near-infrared spectral properties of minerals, meteorites, and lunar soil. *Icarus*, *155*(1), 169–180. https://doi.org/10.1006/icar.2001.6754.

Hinrichs, J. L., Lucey, P. G., Robinson, M. S., Meibom, A., & Krot, A. N. (1999). Implications of temperature-dependent near-IR spectral properties of common minerals and meteorites for remote sensing of asteroids. *Geophysical Research Letters*, *26*(12), 1661–1664. https://doi.org/10.1029/1999GL900334.

Klima, R. L., Pieters, C. M., & Dyar, M. D. (2008). Characterization of the 1.2 μm M1 pyroxene band: Extracting cooling history from near-IR spectra of pyroxenes and pyroxene-dominated rocks. *Meteoritics & Planetary Science*, *43*(10), 1591–1604. https://doi.org/10.1111/j.1945-5100.2008.tb00631.x.

Klima, R. L., Pieters, C. M., Boardman, J. W., Green, R. O., Head, J. W., Isaacson, P. J., et al. (2011). New insights into lunar petrology: Distribution and composition of prominent low-Ca pyroxene exposures as observed by the Moon Mineralogy Mapper (M3). *Journal of Geophysical Research: Planets*, *116*(E6). https://doi.org/10.1029/2010JE003719.

Lawrence, D. J., Feldman, W. C., Elphic, R. C., Little, R. C., Prettyman, T. H., Maurice, S., Lucey, P. G., & Binder, A. B. (2002). Iron abundances on the lunar surface as measured by the Lunar Prospector gamma-ray and neutron spectrometers. *Journal of Geophysical Research: Planets, 107*(E12), 13-1–13-26. https://doi.org/10.1029/2001JE001530

Lawrence, S. J., Stopar, J. D., Hawke, B. R., Greenhagen, B. T., Cahill, J. T. S., Bandfield, J. L., et al. (2013). LRO observations of morphology and surface roughness of volcanic cones and lobate lava flows in the Marius Hills. *Journal of Geophysical Research: Planets*, *118*(4), 615–634. https://doi.org/10.1002/jgre.20060.

Lemelin, M., Lucey, P. G., Gaddis, L. R., Hare, T., & Ohtake, M. (2016b). Global map products from the Kaguya Multiband Imager at 512 ppd: Minerals, FeO and OMAT. 47th LPSC, 2994.

Lemelin, M., Lucey, P. G., Miljković, K., Gaddis, L. R., Hare, T., & Ohtake, M. (2019). The compositions of the lunar crust and upper mantle: Spectral analysis of the inner rings of lunar impact basins. *Planetary and Space Science*, *165*, 230–243. https://doi.org/10.1016/j.pss.2018.10.003.

Lemelin, M., Lucey, P. G., Neumann, G. A., Mazarico, E. M., Barker, M. K., Kakazu, A., et al. (2016a). Improved calibration of reflectance data from the LRO Lunar Orbiter Laser Altimeter (LOLA) and implications for space weathering. *Icarus*, *273*, 315–328. https://doi.org/10.1016/j.icarus.2016.02.006.

Li, L., & Mustard, J. F. (2000). Compositional gradients across mare-highland contacts: Importance and geological implication of lateral transport. *Journal of Geophysical Research: Planets, 105*(E8), 20431–20450. https://doi.org/10.1029/1999JE001168.

Li, L., & Mustard, J. F. (2003). Highland contamination in lunar mare soils: Improved mapping with multiple end-member spectral mixture analysis (MESMA). *Journal of Geophysical Research: Planets, 108*(E6). https://doi.org/10.1029/2002JE001917.

Li, L., & Mustard, J. F. (2005). On lateral mixing efficiency of lunar regolith. *Journal of Geophysical Research: Planets, 110*(E11). https://doi.org/10.1029/2004JE002295.

Lucey, P. G. (2006). Radiative transfer modeling of the effect of mineralogy on some empirical methods for estimating iron concentration from multispectral imaging of the Moon. *Journal of Geophysical Research, 111*(E8), E08003. https://doi.org/10.1029/2005JE002661

Lucey, P. G., Hinrichs, J., Kelly, M., Wellnitz, D., Izenberg, N., Murchie, S., et al. (2002). Detection of temperature-dependent spectral variation on the asteroid Eros and new evidence for the presence of an olivine-rich silicate assemblage. *Icarus*, *155*(1), 181–188. https://doi.org/10.1006/icar.2001.6747.

Lucey, P. G., Keil, K., & Whitely, R. (1998). The influence of temperature on the spectra of the A-asteroids and implications for their silicate chemistry. *Journal of Geophysical Research: Planets*, *103*(E3), 5865–5871. https://doi.org/10.1029/97JE03691.

Lucey, P. G., Neumann, G. A., Riner, M. A., Mazarico, E., Smith, D. E., Zuber, M. T., et al. (2014). The global albedo of the Moon at 1064 nm from LOLA. *Journal of Geophysical Research: Planets, 119*(7), 2013JE004592. https://doi.org/10.1002/2013JE004592.

Lucey, P.G., Blewett, D.T., Taylor, G.J., & Hawke, B.R. (2000). Imaging of lunar surface maturity. *Journal of Geophysical Research: Planets, 105*, 20377–20386. https://doi.org/10.1029/1999JE001110.

Mandt, K. E., Greathouse, T. K., Retherford, K. D., Randall Gladstone, G., Jordan, A. P., Lemelin, M., et al. (2016). LRO-LAMP detection of geologically young craters within lunar permanently shaded regions. *Icarus, 273,* 114–120. https://doi.org/10.1016/j.icarus.2015.07.031

Mazrouei, S., Ghent, R. R., Bottke, W. F., Parker, A. H., & Gernon, T. M. (2019). Earth and Moon impact flux increased at the end of the Paleozoic. *Science*, *363*(6424), 253–257. https://doi.org/10.1126/science.aar4058

McEwen, A. S., & Robinson, M. S. (1995). Global albedo variations on the Moon: Clementine 750-nm observations. Abstracts of the Lunar and Planetary Science Conference, 26, 931.

Milliken, R. E., & Mustard, J. F. (2007). Estimating the water content of hydrated minerals using reflectance spectroscopy: II. Effects of particle size. *Icarus, 189(2),* 574–588. https://doi.org/10.1016/j.icarus.2006.12.028

Morimoto, N. (1988). Nomenclature of pyroxenes. *Mineralogy and Petrology, 39(1)*, 55–76. https://doi.org/10.1007/BF01226262

Moroz, L., Schade, U., & Wäsch, R. (2000). Reflectance Spectra of Olivine–Orthopyroxene-Bearing Assemblages at Decreased Temperatures: Implications for Remote Sensing of Asteroids. *Icarus*, *147*(1), 79–93. https://doi.org/10.1006/icar.2000.6430.

Mustard, J. F., & Hays, J. E. (1997). Effects of hyperfine particles on reflectance spectra from 0.3 to 25 µm. *Icarus*, *125*(1), 145–163. https://doi.org/10.1006/icar.1996.5583.

Nelson, D. M., Koeber, S. D., Daud, K., Robinson, M. S., Watters, T. R., Banks, M. E., & Williams, N. R. (2014, March). Mapping lunar maria extents and lobate scarps using LROC image products. In Lunar and Planetary Science Conference (Vol. 45, p. 2861).

Neumann, G. A., Cavanaugh, J. F., Sun, X., Mazarico, E. M., Smith, D. E., Zuber, M. T., et al. (2013). Bright and dark polar deposits on Mercury: Evidence for surface volatiles. *Science*, *339*(6117), 296–300. https://doi.org/10.1126/science.1229764.

Neumann, G. A., Glaeser, P. A., Hiesinger, H., Zuber, M. T., & Smith, D. E. (2015). Copernican-age craters and LOLA decameter-scale roughness. *Lunar Planet. Sci. 46*, Abstract 2218.

Noble, S.K., Pieters, C.M., Taylor, L.A., Morris, R.V., Allen, C.C., McKAY, D.S., & Keller, L.P. (2001). The optical properties of the finest fraction of lunar soil: Implications for space weathering. *Meteoritics & Planetary Science, 36*, 31–42. https://doi.org/10.1111/j.1945-5100.2001.tb01808.x.

Pieters, C. M. (1978). Mare basalt types on the front side of the Moon: A summary of spectral reflectance data. Lunar and Planetary Science Conference, 9th, Houston, Tex., 3, 2825–2849.

Pieters, C. M. (1983). Strength of mineral absorption features in the transmitted component of near-infrared reflected light: First results from RELAB. *Journal of Geophysical Research: Solid Earth*, *88*(B11), 9534–9544. https://doi.org/10.1029/JB088iB11p09534.

Pieters, C. M. (1986). Composition of the lunar highland crust from near-infrared spectroscopy. *Reviews of Geophysics, 24*(3), 557–578. https://doi.org/10.1029/RG024i003p00557.

Pieters, C. M., & Noble, S. K. (2016). Space weathering on airless bodies. *Journal of Geophysical Research: Planets*, *121*(10), 2016JE005128. https://doi.org/10.1002/2016JE005128.

Pieters, C. M., Fischer, E. M., Rode, O., & Basu, A. (1993). Optical effects of space weathering: The role of the finest fraction. *Journal of Geophysical Research*, *98*(E11), 20817. https://doi.org/10.1029/93JE02467.

Pieters, C. M., Taylor, L. A., Noble, S. K., Keller, L. P., Hapke, B., Morris, R. V., et al. (2000). Space weathering on airless bodies: Resolving a mystery with lunar samples. *Meteoritics & Planetary Science*, *35*(5), 1101–1107. https://doi.org/10.1111/j.1945-5100.2000.tb01496.x.

Platz, T., Nathues, A., Schorghofer, N., Preusker, F., Mazarico, E., Schröder, S. E., et al. (2016). Surface water-ice deposits in the northern shadowed regions of Ceres. *Nature Astronomy, 1*(1), 1–6. https://doi.org/10.1038/s41550-016-0007.

Qiao, L., Ling, Z., Head, J.W., Ivanov, M.A., & Liu, B. (2019). Analyses of Lunar Orbiter Laser Altimeter 1,064-nm albedo in permanently shadowed regions of polar crater flat floors: Implications for surface water ice occurrence and future in situ exploration. *Earth and Space Science, 6,* 467–488. https://doi.org/10.1029/2019EA000567

Roush, T. L., & Singer, R. B. (1986). Gaussian analysis of temperature effects on the reflectance spectra of mafic minerals in the 1-µm region. *Journal of Geophysical Research: Solid Earth*, *91*(B10), 10301–10308. https://doi.org/10.1029/JB091iB10p10301.

Roush, T. L., & Singer, R. B. (1987). Possible temperature variation effects on the interpretation of spatially resolved reflectance observations of asteroid surfaces. *Icarus*, *69*(3), 571–574. https://doi.org/10.1016/0019-1035(87)90026-1.

Schade, U., & Wäsch, R. (1999). NIR reflectance spectroscopy of mafic minerals in the temperature range between 80 and 473 K. *Advances in Space Research*, *23*(7), 1253–1256. https://doi.org/10.1016/S0273-1177(99)00193-3.

Singer, R. B., & Roush, T. L. (1985). Effects of temperature on remotely sensed mineral absorption features. *Journal of Geophysical Research: Solid Earth*, *90*(B14), 12434–12444. https://doi.org/10.1029/JB090iB14p12434.

Smith, D. E., Zuber, M. T., Frey, H. V., Garvin, J. B., Head, J. W., Muhleman, D. O., et al. (1998). Topography of the Northern Hemisphere of Mars from the Mars Orbiter Laser Altimeter. *Science, 279*(5357), 1686–1692. https://doi.org/10.1126/science.279.5357.1686.

Smith, D. E., Zuber, M. T., Jackson, G. B., Cavanaugh, J. F., Neumann, G. A., Riris, H., et al. (2010). The Lunar Orbiter Laser Altimeter investigation on the Lunar Reconnaissance Orbiter mission. *Space Science Reviews*, *150*(1–4), 209–241. https://doi.org/10.1007/s11214-009-9512-y.

Smith, D. E., Zuber, M. T., Neumann, G. A., Mazarico, E., Lemoine, F. G., Head III, J. W., et al. (2017). Summary of the results from the Lunar Orbiter Laser Altimeter after seven years in lunar orbit. *Icarus*, *283*, 70–91. https://doi.org/10.1016/j.icarus.2016.06.006.

Varatharajan, I., Srivastava, N., & Murty, S.V.S. (2014). Mineralogy of young lunar mare basalts: Assessment of temporal and spatial heterogeneity using M3 data from Chandrayaan-1. *Icarus, 236*, 56–71. https://doi.org/10.1016/j.icarus.2014.03.045.

Vasavada, A. R., Bandfield, J. L., Greenhagen, B. T., Hayne, P. O., Siegler, M. A., Williams, J.-P., & Paige, D. A. (2012). Lunar equatorial surface temperatures and regolith properties from the Diviner Lunar Radiometer Experiment. *Journal of Geophysical Research: Planets*, *117*(E12). https://doi.org/10.1029/2011JE003987.

Vasavada, A. R., Paige, D. A., & Wood, S. E. (1999). Near-surface temperatures on Mercury and the Moon and the stability of polar ice deposits. *Icarus*, *141*(2), 179–193. https://doi.org/10.1006/icar.1999.6175.

Williams, J.-P., Paige, D. A., Greenhagen, B. T., & Sefton-Nash, E. (2017). The global surface temperatures of the Moon as measured by the Diviner Lunar Radiometer Experiment. *Icarus*, *283*, 300–325. https://doi.org/10.1016/j.icarus.2016.08.012.

Yamashita, N., Gasnault, O., Forni, O., d'Uston, C., Reedy, R. C., Karouji, Y., et al. (2012). The global distribution of calcium on the Moon: Implications for high-Ca pyroxene in the eastern mare region. *Earth and Planetary Science Letters, 353–354*, 93–98. https://doi.org/10.1016/j.epsl.2012.08.010.

Zuber, M. T., Head, J. W., Smith, D. E., Neumann, G. A., Mazarico, E., Torrence, M. H., et al. (2012). Constraints on the volatile distribution within Shackleton crater at the lunar south pole. *Nature*, *486*(7403), 378–381. https://doi.org/10.1038/nature11216.

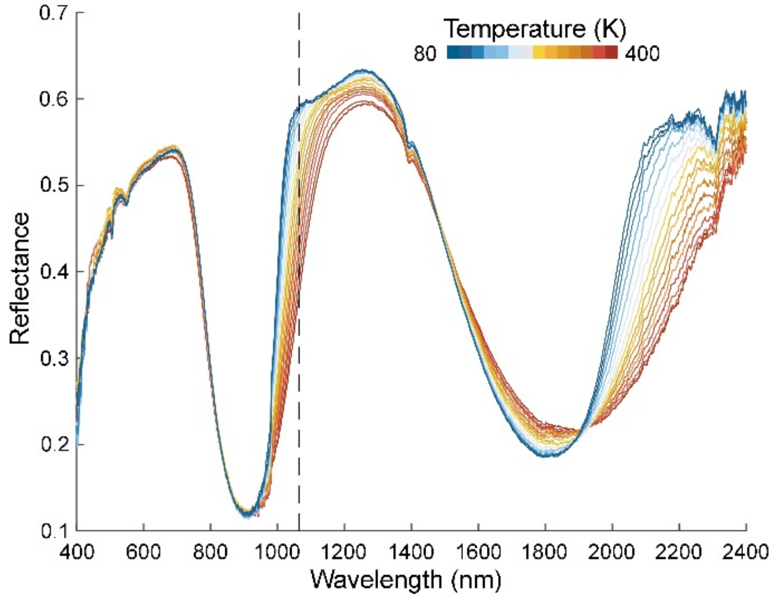

Figure 1. The reflectances of orthopyroxene (En88) samples that were wet-sieved to 45–90 μm and measured at temperatures between 80 and 400 K by Hinrichs et al. (1999) in the near-IR wavelengths (0.4–2.4 μm). The observation wavelength of LOLA (1064 nm) is marked by the dashed vertical line. At LOLA's wavelength, higher reflectances are measured for orthopyroxenes at lower temperatures than orthopyroxenes at higher temperatures.

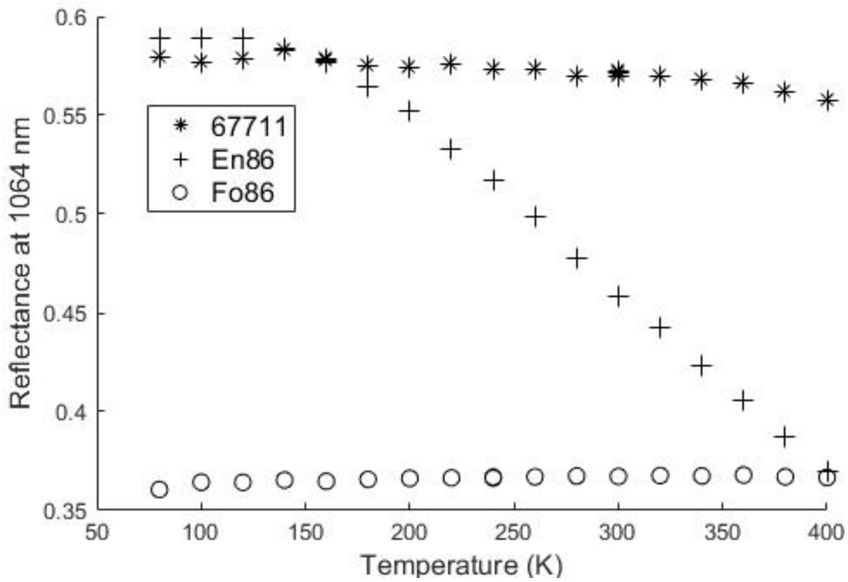

Figure 2. The thermo-reflectance spectra of lunar minerals and soils at 1064 nm, which is the observation wavelength of LOLA. The reflectances of orthopyroxene (En86) and olivine (Fo86) were measured by Hinrichs et al. (1999) and the reflectances of Apollo sample 67711 were measured by Hinrichs and Lucey (2002) for a range of temperatures between 80 K and 400 K. LOLA's observation wavelength is strongly sensitive to temperature-dependent spectral changes in orthopyroxene, although not to olivine.

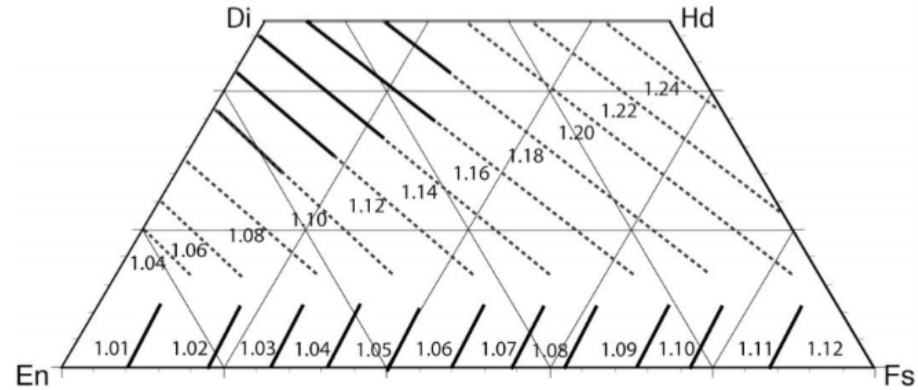

Figure 3. The wavelengths of maximum temperature-dependent reflectance changes are shown with respect to pyroxene composition (Di = diopside; Hd = hedenburgite; Fs = ferrosilite; En = enstatite) on a pyroxene quadrilateral diagram.

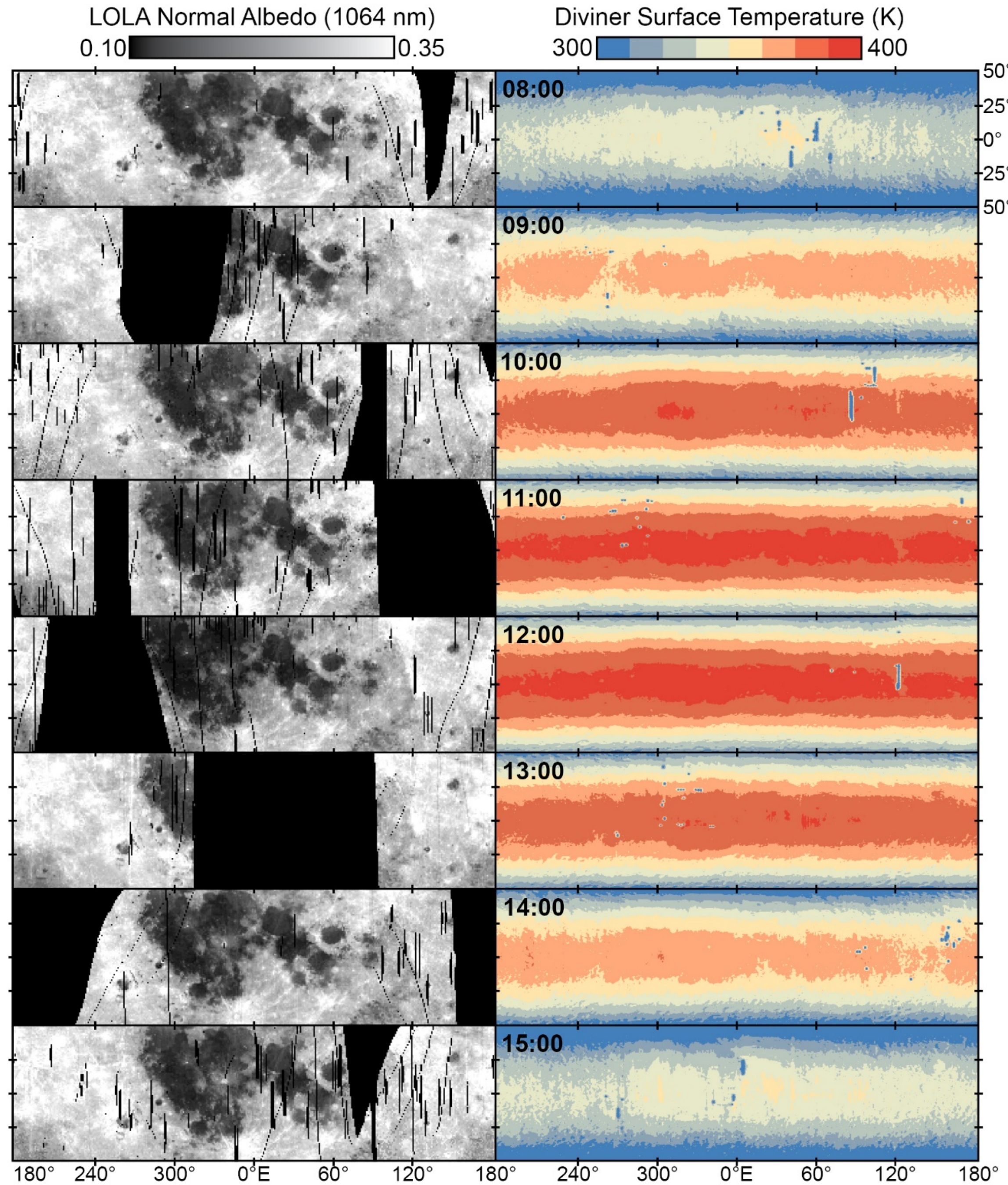

Figure 4. The LOLA-derived normal albedo (referred to in the text as "surface reflectance") at 1064 nm (left) and Diviner-derived temperatures (right) of the lunar surface vary throughout the lunar day. Each row displays the data acquired at a specific hour of local time, between 08:00 and 15:00, and black grids depict regions for which no LOLA data exist. The cylindrically projected maps are centered at 0°E and include latitudes between 50°S and 50°N.

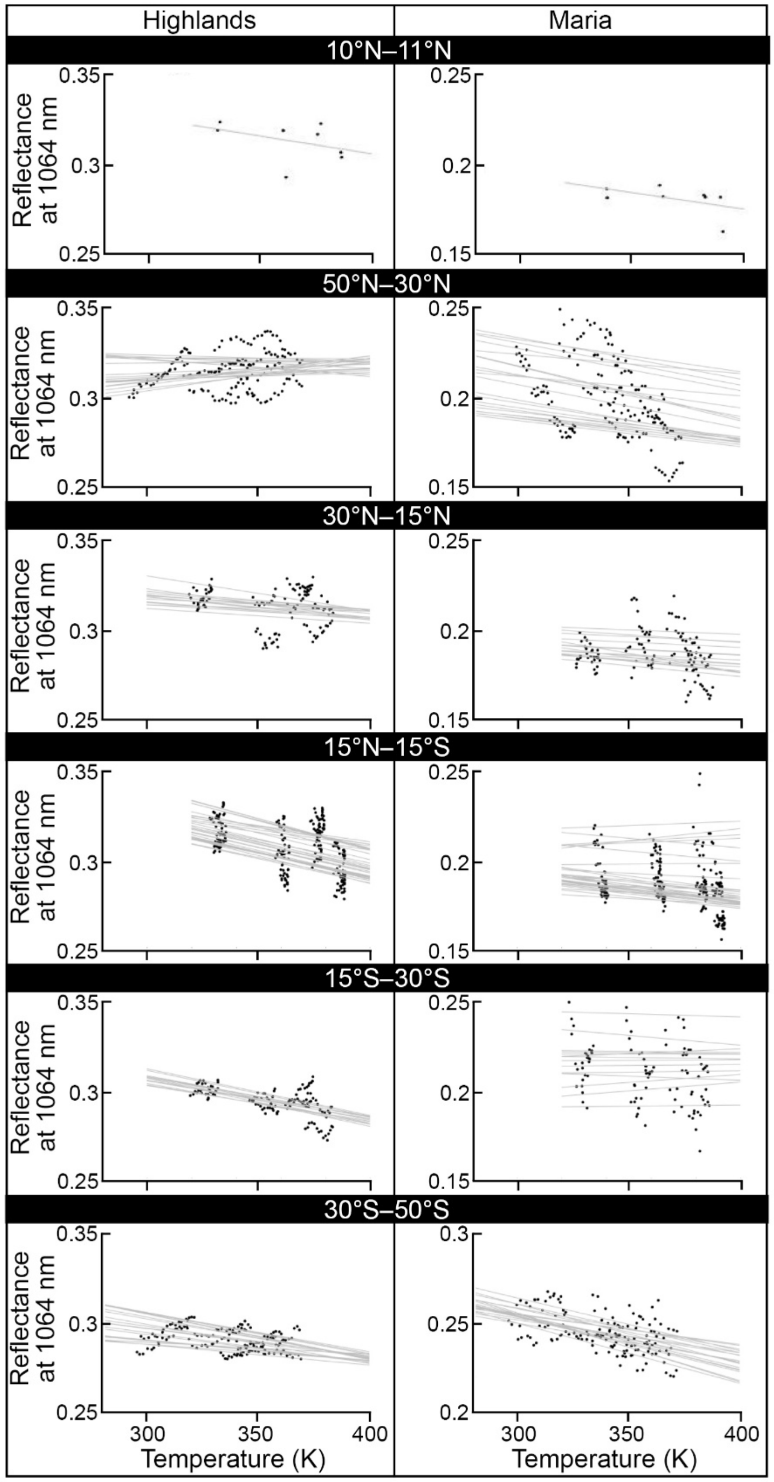

Figure 5. The 1064-nm surface reflectance of the lunar highlands (left) and maria (right) are shown with respect to the surface temperature during the time of data acquisition. The

individual data are plotted as circles and lines of best fit (each derived from a few hundred thousand observations (Table S1)) are shown for each degree of latitude between 50°N and 50°S, representing a single thermo-reflectance value ($\Delta R/\Delta T$). Different latitude ranges are displayed in subplots for clarity. The annual mean surface temperatures for each terrain type for each degree of latitude are correlated by time-of-day to the LOLA data.

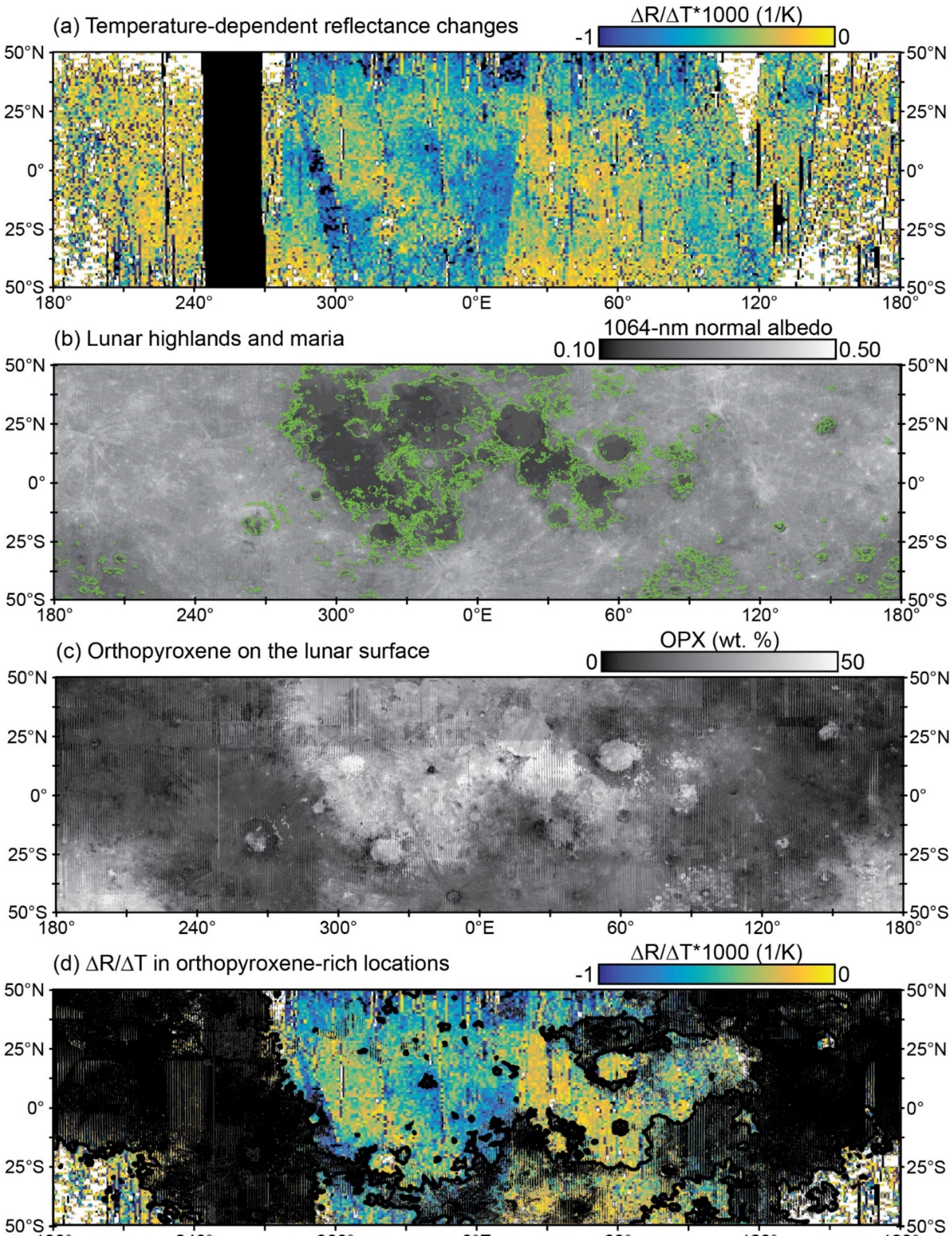
(a) Temperature-dependent reflectance changes
ΔR/ΔT*1000 (1/K)
-1
0
(b) Lunar highlands and maria
1064-nm normal albedo
0.10
0.50
(c) Orthopyroxene on the lunar surface
OPX (wt. %)
0
50
(d) ΔR/ΔT in orthopyroxene-rich locations
ΔR/ΔT*1000 (1/K)
-1
0
50°N
25°N
0°
25°S
50°S
180°
240°
300°
0°E
60°
120°
180°

Figure 6. The temperature-dependent changes in lunar reflectance in panel (a) are compared to the distributions of lunar highlands and maria in panel (b) and of low-calcium pyroxene in panel (c). Specifically, panel (a) expresses the magnitude of temperature-dependent reflectance changes ($\Delta R/\Delta T*1000$). All colored pixels (1° x 1° in spatial extent) have higher reflectances at lower temperatures and white pixels either show no change or have lower reflectances at lower temperatures. Black pixels indicate regions with insufficient temporal LOLA coverage for the analysis, and lineations are an artefact from the data coverage. Panel (b) displays the normal albedo of the lunar surface calibrated by Lemelin et al. (2016a). Boundaries of the maria are outlined in green, as mapped by Nelson et al. (2014). Panel (c) displays the absolute orthopyroxene abundance on the lunar surface, expressed as weight percent (wt. %), as derived from the Kaguya Lunar MI (Lemelin et al., 2016b, 2019). Panel (d) shows the temperature-dependent reflectance changes specifically within regions with elevated orthopyroxene abundances. All four maps are in a cylindrical projection centered at 0°E and include latitudes between 50°S and 50°N.

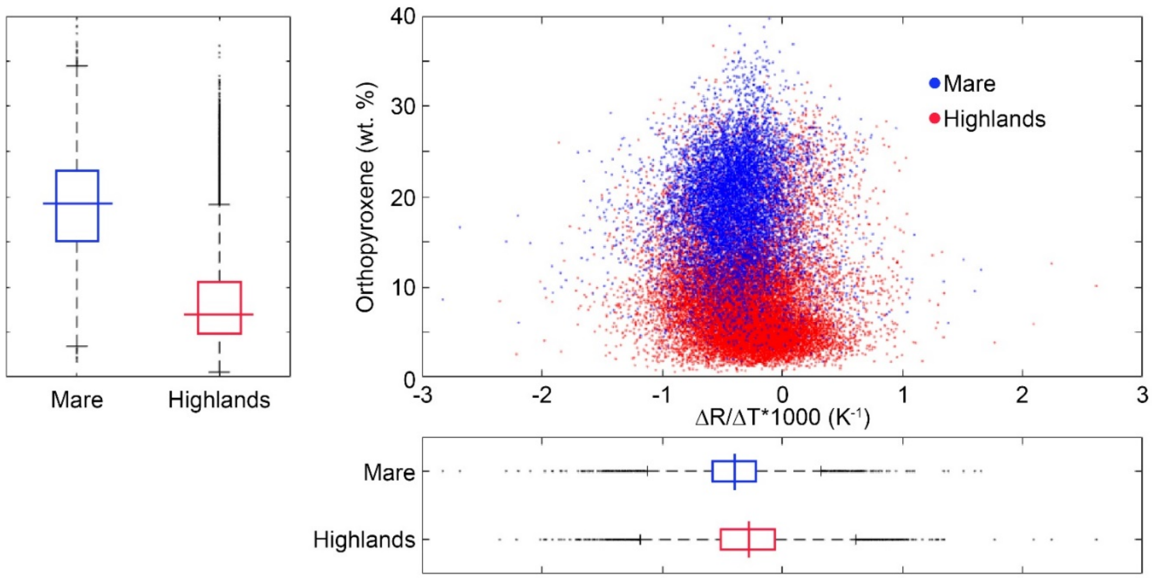

Figure 7. The correlation between temperature-dependent reflectance changes (ΔR/ΔT*1000) and orthopyroxene abundance (wt. %) within the lunar highlands (red) and maria (blue). The box plots show the spread of orthopyroxene values (left) and ΔR/ΔT*1000 values (bottom) for the highlands (red) and maria (blue). For each box plot, the box denotes the innermost 50% of the data and the line within each box denotes the statistical median of the data. The dashed whisker lines extending from each box denote the outermost 25% of the data, on either side of the median. The small, black dots beyond the dashed lines represent statistical outliers of the dataset, which are determined as values that are less than $[q_1 - w \times (q_3 - q_1)]$ or greater than $[q_3 + w \times (q_3 - q_1)]$, where q_1 and q_3 are the 25th and 75th percentiles of the data, respectively, and w is the maximum whisker length.

Supporting material

Introduction

The supplemental materials provide additional information on the calibration of the reflectance data from the Lunar Orbiter Laser Altimeter (LOLA) instrument (Fig. S1) and details on the spread of LOLA data utilized in this statistical analysis (Table S1). The supplementary data also include a list of the maximum temperature-dependent 1064-nm reflectance changes found for the highlands and maria for each degree of latitude between ±50°. Finally, we provide examples that illustrate LOLA time-of-day patterns both for surfaces with strong temperature-dependent changes and also for surfaces with weak/no temperature-dependent changes (Fig. S2).

Description of methods: Calibration of LOLA 1064-nm reflectance data

The LOLA data used in this and the previous referenced studies were obtained from the LOLA RDR collection, calibrated for post-launch changes in the instrument as incorporated into the software programs (http://imbrium.mit.edu/SOFTWARE/). The normal albedo was obtained for each profile in each mission phase that operated on laser 1, using the option "B", for "bidirectional reflectance" and "3" for Detector 3. The software can be configured to select for nominal incidence angle conditions and instrument settings.

As output by the software programs, we analyze the normal albedo of the lunar surface using LOLA data acquired by Detector 3 on Laser 1 during the Nominal Mission Phase (LRO_NO_01 through LRO_NO_13) and the Science Mission Phase (LRO_SM_02 through LRO_SM_17). LOLA observations are corrected for drift in each

LOLA mission month (Nominal Mission Phase (NO) or Science Mission Phase (SM)) by a cubic polynomial function with a step function offset between the NO and SM phases (Fig. S1). The linear fit to the regression intercept (in mission months) is polynomial:

$$Y_0 = -0.0407031024479\ +\ 0.00150450253316 * \mathrm{m} \qquad \text{(Eq. S1).}$$

For the nominal mission phases, the cubic fit to the regression slopes is:

$$Y_{phase} = 1.33324536294 + 0.00306123514405 * m - 0.0047453967058 * m^2\ + 0.000101223404893 * m^3 \quad \text{(Eq. S2).}$$

For the science mission phases, the cubic fit to the regression slopes is:

$$Y_{phase} = 1.13324536294 + 0.00306123514405 * \mathrm{m} - 0.0047453967058 * \mathrm{m}^2 + 0.000101223404893 * \mathrm{m}^3 \quad \text{(Eq. S3).}$$

The coefficients Y_0 and Y_{phase} are evaluated for each mission month subset and used to rescale the apparent reflectance to match the Lucey et al. (2016) map in the PDS via the formula:

$$[albedo] = \frac{[LOLA\_D3] - Y_0}{Y_{phase} - step} \qquad \text{(Eq. S4).}$$

where step=0 during Nominal Mission months and step = 0.2 during Science Mission months.

In order to analyze the LOLA 1064-nm reflectance data, we use both Nominal Mission Phase (NOMGRD) and Science Mission Phase (SCIGRD) data. These data provide strong spatial and temporal coverage of the lunar surface due to the hundreds of thousands of individual observations (Table S1).

Results: The strength of temperature-dependent reflectance changes

Table S2 documents maximum thermo-reflectance values ($\Delta R/\Delta T*1000$) for the highlands and maria, analyzed at a spatial resolution of 1 latitudinal degree, between the latitudes of ±50°. These maximum values are determined by first finding the hours between which the greatest difference in surface temperature exists (individually for each 1°bin), as measured by Diviner. We then determine the corresponding change in 1064-nm surface reflectance. The ratio of these two values (multiplied by 1000) allows us to find the maximum $\Delta R/\Delta T*1000$ for each spatial bin.

Additionally, in Figure S2 we provide examples to illustrate LOLA time-of-day patterns, contrasting surfaces with strong temperature-dependent changes (more negative values) and surfaces with weak/no temperature-dependent changes.

Table S1. The number of individual LOLA observations utilized for this statistical analysis, divided by phase of data acquisition and local time of day. Table available at the Brown Digital Repository and can be accessed at https://doi.org/10.26300/y5ep-4j46.

Local Time	Mission Phase	Mission Month	Number of LOLA ots
08:00	NOMGRD	03	8858508
		09	12117607
	SCIGRD	03	10311044
		09	7809286
		10	3233635
		16	10967911
09:00	NOMGRD	09	8923350
	SCIGRD	02	9108857
		03	1999123
		09	11175819
		15	3099038
		16	6393027
10:00	NOMGRD	01	5055197
	SCIGRD	02	11197387
		09	1223020
		15	8141911
11:00	NOMGRD	01	5599733
		07	6174418
	SCIGRD	02	401127
		07	782747
		15	4925580
12:00	NOMGRD	01	68169
		07	11838993
		13	1239757
	SCIGRD	07	10682889
13:00	NOMGRD	01	691065
		07	4162239
		13	12625063
	SCIGRD	06	1617555
		07	8791281
		13	9019401
14:00	NOMGRD	13	8156525
	SCIGRD	06	11134889
		12	363418
		13	12392194
15:00	NOMGRD	05	8775505
	SCIGRD	05	4374966

		06	6293350
		12	8546987
		13	405022

Table S2. The maximum thermo-reflectance values (ΔR/ΔT*1000) for the highlands and maria (±50°N), analyzed at a spatial resolution of 1 latitudinal degree. Table available at the Brown Digital Repository and can be accessed at https://doi.org/10.26300/y5ep-4j46.

	Maximum dR/dT*1000 (K^{-1})	
Central Latitude (°)	**Highlands**	**Maria**
50.5	0.11	-0.76
49.5	0.09	-0.04
48.5	-0.09	-0.04
47.5	-0.09	0.10
46.5	-0.09	0.12
45.5	-0.15	-0.54
44.5	0.05	-0.43
43.5	-0.22	-0.52
42.5	-0.25	-0.59
41.5	0.13	-0.58
40.5	0.08	-0.55
39.5	0.09	-0.56
38.5	0.09	-0.56
37.5	0.08	-0.56
36.5	0.06	-0.52
35.5	0.06	-0.51
34.5	0.05	-0.46
33.5	0.05	-0.43
32.5	0.03	-0.38
31.5	0.03	-0.37
30.5	0.04	-0.35
29.5	0.03	-0.39
28.5	0.09	-0.40
27.5	0.15	-0.40
26.5	0.03	-0.37
25.5	0.00	-0.27
24.5	0.01	-0.23
23.5	-0.02	-0.25
22.5	0.04	-0.29
21.5	-0.05	-0.33
20.5	-0.03	-0.30
19.5	0.05	-0.23
18.5	-0.03	-0.22

17.5	-0.07	-0.28
16.5	-0.22	-0.32
15.5	-0.28	-0.40
14.5	-0.27	-0.41
13.5	-0.24	-0.41
12.5	-0.27	-0.38
11.5	-0.25	-0.39
10.5	-0.27	-0.45
9.5	-0.36	-0.46
8.5	-0.37	-0.41
7.5	-0.35	-0.25
6.5	-0.34	-0.31
5.5	-0.31	-0.30
4.5	-0.36	-0.30
3.5	-0.40	-0.33
2.5	-0.40	-0.39
1.5	-0.36	-0.35
0.5	-0.37	-0.34
-0.5	-0.33	-0.33
-1.5	-0.36	-0.39
-2.5	-0.35	-0.38
-3.5	-0.35	-0.41
-4.5	-0.35	-0.35
-5.5	-0.37	-0.31
-6.5	-0.45	-0.34
-7.5	-0.35	-0.32
-8.5	-0.45	-0.44
-9.5	-0.41	-0.55
-10.5	-0.40	-0.71
-11.5	-0.48	-0.53
-12.5	-0.42	-0.51
-13.5	-0.44	-0.49
-14.5	-0.47	-0.45
-15.5	-0.44	-0.44
-16.5	-0.41	-0.56
-17.5	-0.41	-0.54
-18.5	-0.40	-0.35
-19.5	-0.40	-0.46
-20.5	-0.44	-0.45

-21.5	-0.39	-0.46
-22.5	-0.41	-0.55
-23.5	-0.40	-0.52
-24.5	-0.41	-0.67
-25.5	-0.40	-0.30
-26.5	-0.36	-0.34
-27.5	-0.32	-0.57
-28.5	-0.34	-0.40
-29.5	-0.36	-0.55
-30.5	-0.36	-0.36
-31.5	-0.33	0.04
-32.5	-0.32	-0.45
-33.5	-0.30	-0.10
-34.5	-0.32	-0.42
-35.5	-0.31	-0.11
-36.5	-0.30	-0.25
-37.5	-0.25	-0.29
-38.5	-0.21	-0.30
-39.5	-0.15	-0.25
-40.5	-0.16	-0.16
-41.5	-0.18	-0.01
-42.5	-0.14	-0.11
-43.5	-0.10	-0.14
-44.5	-0.05	-0.16
-45.5	-0.02	-0.20
-46.5	-0.02	-0.13
-47.5	0.00	-0.14
-48.5	-0.01	-0.21
-49.5	0.04	-0.12
-50.5	0.05	-0.57

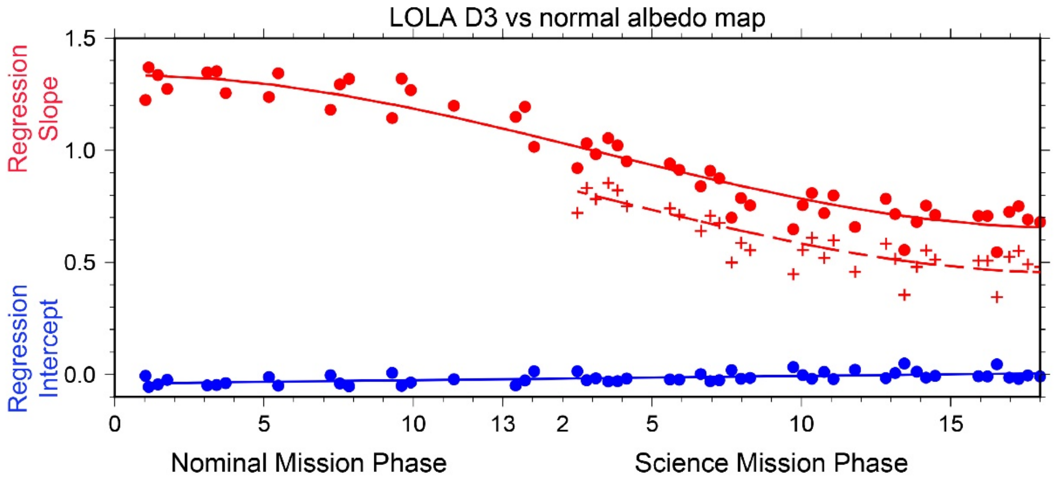

Figure S1. The blue symbols show the regression intercept and the red symbols show the regression slope. The regression coefficients are mapped to the fraction of the LOLA mission month that they represent. The plus symbols are the slope data before shifting upwards by a step-function to achieve a reasonable cubic fit.

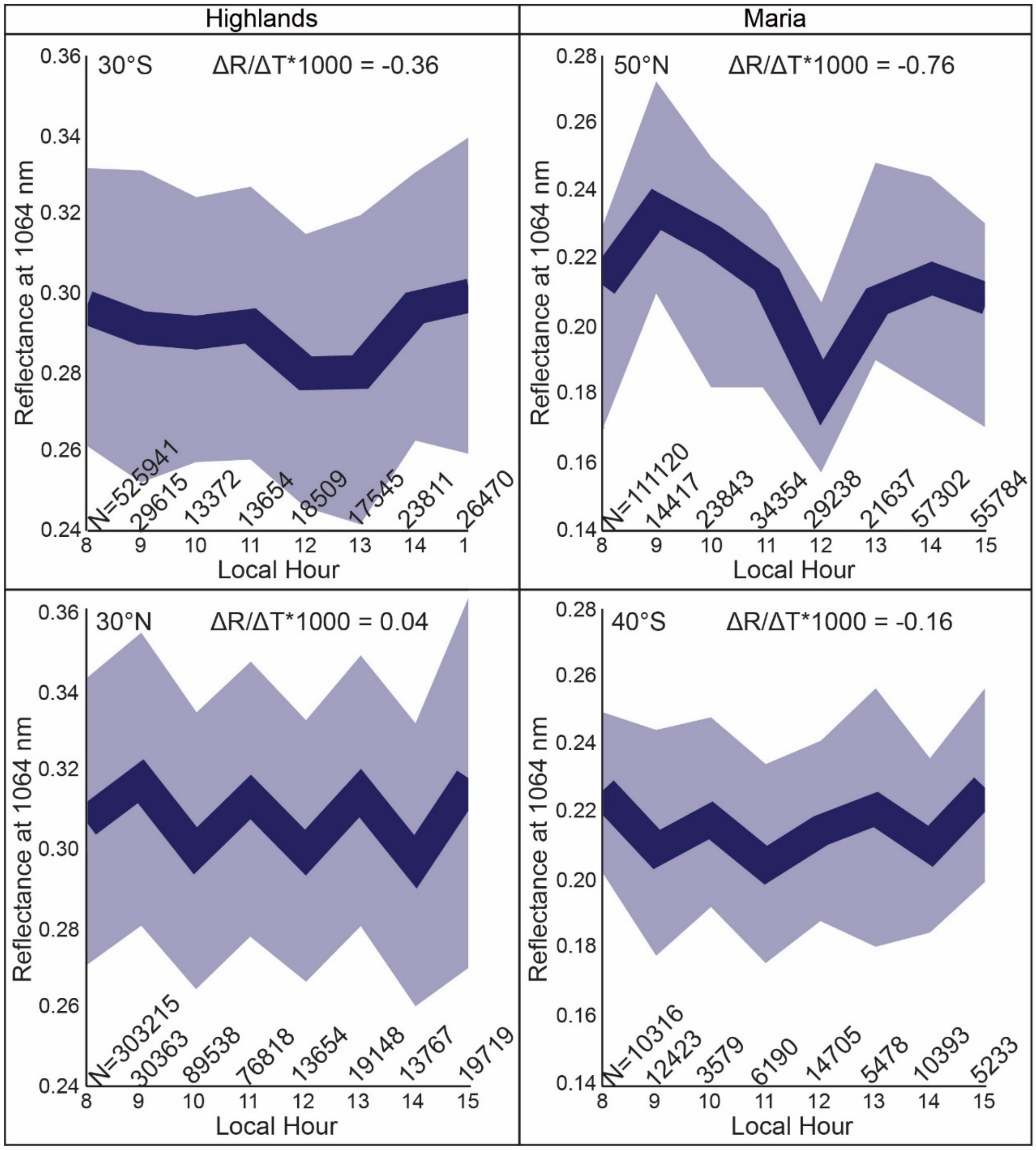

Figure S2. LOLA surface reflectance at 1064 nm is shown for highland (left) and mare (surfaces). For each subplot, the data are for a single degree of latitude, centered at the latitude identified in the upper left corner. The dark purple lines show the mean surface reflectance at each local hour and the shaded region shows all data between quartiles 1 and 3. The top row shows examples of surfaces that revealed a strong temperature-dependent change in surface reflectance at 1064 nm., as quantified by the thermo-reflectance value ($\Delta R/\Delta T$*1000). The bottom row shows examples of surfaces that did not show a strong temperature-dependent change in surface reflectance at 1064 nm.

Chapter 6

Synthesis and forward thinking: Open questions regarding polar volatiles on Mercury and the Moon and opportunities with future exploration

Ariel N. Deutsch

Department of Earth, Environmental and Planetary Sciences, Brown University, Providence, RI 02912, USA

1. Introduction

In the last decade, our understanding of the Moon as a dry rocky body has been transformed by discoveries of water (H_2O and OH) in the lunar interior, trapped in primitive magmas and lunar rocks (e.g., Saal et al., 2008; Boyce et al., 2010; McCubbin et al., 2010; Greenwood et al., 2011; Hauri et al., 2011, 2015; Chen et al., 2015; Milliken & Li, 2017), and cold-trapped in polar shadows (e.g., Colaprete et al., 2010; Li et al., 2018). Similarly, the MErcury Surface, Space ENvironment, GEochemistry, and Ranging (MESSENGER) spacecraft has revolutionized our understanding of the innermost planet to be volatile rich, with abundant and widely distributed pyroclastic deposits (e.g., Head et al., 2008; Kerber et al., 2009, 2011; Goudge et al., 2014; Weider et al., 2016; Jozwiak et al., 2018), intriguing hollows suggestive of recent sublimation (Blewett et al., 2011; 2013; Thomas et al., 2014), elevated abundances of the volatiles K, C, S, Na, and Cl in the surface/near-surface (Nittler et al., 2011; Evans et al., 2015; Peplowski et al. 2012, 2014, 2015, 2016), chaotic terrains potentially indicative of devolatilization (Rodriguez et al., 2020), and thick (e.g., Deutsch et al., 2018) hydrogen-rich deposits (Lawrence et al., 2013) cold-trapped in polar regions of permanent shadow (Deutsch et al., 2016; Chabot et al., 2018).

The water inventory cold-trapped at the poles of Mercury and the Moon are particularly fascinating because they may represent multi-billion-year records of the supply of water to the inner Solar System. A detailed understanding of the distribution of polar water is essential in understating the nature of water cycles on Mercury and the Moon, and the processes that govern the supply, retention, modification, and loss of volatiles. The poles of each body may harbor volatiles from comets and asteroids (e.g., Ong et al., 2010; Stewart et al., 2011; Prem et al., 2015), which would provide important constraints on the chemistry of outer Solar System materials, and volatiles from early volcanic outgassing (e.g., Crotts and Hummels, 2009; Needham and Kring, 2017; Deutsch et al., *in review*). Chemical measurements of ancient ices could help provide insight into water delivered to early Earth (Chyba, 1987; Morbidelli et al., 2000; Owen and Bar-Nun, 2001; Drake, 2005; Hartogh et al., 2011; McCubbin and Barnes, 2019). Additionally, the poles of Mercury and the Moon may contain volatiles delivered by ongoing micrometeorite bombardment (e.g., Szalay and Horányi, 2016; Pokorný et al., 2019) or derived from in-situ interactions between the regolith and the solar wind (e.g., Crider and Vondrak, 2000; McCord et al., 2011; Tucker et al., 2018; Jones et al., 2020). The age and chemical composition of polar volatiles on Mercury and the Moon will provide critical information regarding the timing and sources of volatile delivery, and in-situ chemical analyses (e.g., Byrne et al. 2018; Vander Kaaden et al., 2019; Colaprete et al., 2020; Ernst et al., 2020) and sample return (e.g., Mitchell et al., 2020) should be priorities in future exploration.

The work explored in this dissertation directly links the scientific and exploration interests of NASA through a detailed scientific analysis of polar volatile resources on Mercury and the Moon. The work presented in the preceding chapters helps to address larger cross-cutting themes related to NASA's planetary science objectives, including (1) building new worlds (What governed the accretion, supply of water, and chemistry of the inner planets and the evolution of their atmospheres?), (2) planetary habitats (What were the primordial sources of organic matter?), and (3) workings of Solar Systems (How have the myriad chemical and physical processes that shaped the Solar System operated, interacted, and evolved over time?) (National Academies, 2011). This dissertation also helps address strategic knowledge gaps outlined by the Human Exploration and Operations Mission Directorate (HEOMD) to understand lunar resource potential and how to work on the lunar surface (LEAG, 2012) and is directly related to Space Policy Directive-1 (National Academies, 2019). Furthermore, the work in the preceding chapters and the proposed future investigations outlined in this chapter are aligned with several cornerstone reports developed by the scientific community (National Academies., 2007; LEAG, 2014, 2017, 2018; Byrne et al., 2018), helping address critical steps in furthering the scientific understanding of inner Solar System volatiles, and in developing a sustainable program of exploration of the Moon and beyond.

In this chapter, I highlight some of the major findings of Chapters 1–5 in order to frame the importance of this dissertation toward understanding the nature and evolution of polar volatiles on Mercury and the Moon. I also discuss major outstanding questions in this field and suggest paths for future investigation to better understand water cycles on Mercury and the Moon (Sections 2–6), especially in the context of the upcoming BepiColombo mission to Mercury and the Volatiles Investigating Polar Exploration Rover (VIPER) mission to the Moon (Section 7).

2. Chapter 1: Age constraints of Mercury's polar deposits suggest recent delivery of ice

In Chapter 1, we provided the first quantitative estimates of the ages of polar deposits on Mercury from direct observations of the ice surfaces (Deutsch et al., 2019). This work is particularly exciting because prior to our analysis, quantitative age estimates relied on the analysis of Earth-based radar data (Crider and Killen, 2005) or indirect estimates of ice thickness from neutron spectrometry (Lawrence et al., 2013). We found that individual ice surfaces on Mercury are all conservatively <330 Ma, and possibly as young as only a few Ma (Deutsch et al., 2019). With these quantitative constraints on the age of ice surfaces, our work provides critical insight into the possible delivery mechanism(s) for the ice. This is an important framework for assessing the contributions of recent impact events or a single impact. It has previously been suggested that the Hokusai impactor may account for all of the water ice observed at the surface of Mercury today (Ernst et al., 2018). Intriguingly, Hokusai is Kuiperian in age and thus aligns with our estimates of ice surface ages derived in Chapter 1.

2.1. Outstanding questions and opportunities for future investigation

One of the major outstanding questions regarding the derived ice surface ages is how representative our ages are of all ice deposits on Mercury. In our analysis, we were only able to derive ages for six specific north polar craters due to limitations of MESSENGER image coverage. Therefore, it is important to determine what the ages of the remaining ice deposits are, and how they compare to the age estimates presented in Chapter 1 (Deutsch et al., 2019).

If the error statistics from our crater counting are precise, then the surface ages of all of the individual ice deposits do not overlap, suggesting that the analyzed ice surfaces may have been replenished in multiple discrete, recent episodes. However, the derived errors are from counting statistics alone (i.e., do not take into account errors associated with the chronology and production functions), and we found that our derived ages overlap between at least 2/3 of the craters in all cases. Therefore, the possibility that the surface ice was delivered by a single impact event (e.g., Chabot et al., 2016; Rubanenko et al., 2018; Ernst et al., 2018) cannot be ruled out.

One of the strongest arguments for the delivery of a single impactor on Mercury relies on the assertion that the ice deposits are astonishingly pure; modeling of Earth-based radar observations suggests that the radar-bright ice deposits have <5% volume fraction of silicates (Butler et al., 1993). It is difficult to maintain such high degree of purity through time if the ice has accumulated over multiple discrete events. With the advent of more recent observations of the radar-bright polar deposits on Mercury (Harmon et al., 2011; Chabot et al., 2018; Rivera-Valentín et al., 2020), further modeling of these ice observations is warranted in order to derive additional constraints on ice purity. If higher fractions of silicates are predicted to be mixed within the ice, perhaps the ice has been delivered and resupplied in multiple discrete events (as suggested by individual ages), which would suggest ice replenishment on Mercury has been relatively active in the last few 100 Myrs.

As BepiColombo (Benkhoff et al., 2009) prepares to enter its orbit around Mercury, our results (Deutsch et al., 2019) will serve as an important test for understanding the age of ice deposits on Mercury, as the first high-resolution images of the south polar permanently shadowed regions (PSRs) are acquired. By imaging permanently shadowed surfaces with the Spectrometers and Images for MPO BepiColombo Integrated Observatory System (SIMBIO-SYS) (Flamini et al., 2010), BepiColombo can help determine crater populations within southern PSRs, allowing us to compare absolute surface ages between northern (Deutsch et al., 2019) and southern ice deposits.

Beyond BepiColombo, there are several important investigations regarding the age and origin of ice on Mercury that can likely only be resolved with in-situ (landed) exploration. These include:

- How does the surface age of an ice deposit compare to the age of the deposit as a whole?
- What is the chemical stratigraphy of ice deposits on Mercury?
- What is the chemistry of the low-reflectance materials that insulate lower-latitude ice deposits?
- How do the chemistries of the ice and low-reflectance materials compare to the chemistries of outer Solar System objects, including carbonaceous chondrites and Jupiter-family comets?
- As ice deposits are exposed to the space weathering environment at Mercury, how do the chemistry and abundance of ices evolve with time?

3. Chapter 2: Analyzing the ages of south polar craters on the Moon: Implications for the sources and evolution of surface water ice

In Chapter 2, we provided quantitative estimates of the ages of south polar impact craters on the Moon (Deutsch et al., 2020) that both do host and do not host water-ice detections (Li et al., 2018). This analysis provided an important framework for understanding the timing of ice delivery on the Moon. Notably, we found that (1) ice is predominantly contained in ancient craters, which provide an upper estimate for the age of the contained surface ice. We also found that (2) ice is not found within particular permanently shadowed ancient craters that would not have been stable for the cold-trapping of ice prior to the true polar wander (TPW) predicted by Siegler et al. (2016), suggesting that ice may not have been delivered in sufficient quantities to these craters post-TPW, or that such ice has since been destroyed. Additionally, we found that (3) there are water-ice detections (Li et al., 2018) within Nobile and Shackleton craters, which are present-day cold traps, but not predicted to have been paleo cold traps on the basis of TPW simulations by Siegler et al. (2016). Therefore, ice in these craters can help provide constraints on post-TPW hydrogen emplacement. Finally, we found that (4) there are some individual craters that host ice that are younger than the predicted peak of lunar volcanic activity that occurred at 3.5 Gyr, suggesting that mare-vented water cannot explain all of the surface ice observed at the lunar south pole, as suggested by Needham and Kring (2017). All of these results help us to construct an important framework in understanding the timing and sources of water-ice delivery to the Moon.

3.1. Outstanding questions and opportunities for future investigation

A natural follow-on to our work presented in Chapter 2 (Deutsch et al., 2020) is to analyze the ages of north polar craters. A comprehensive understanding of the ages of circumpolar craters is essential in reconstructions of the evolution of polar topography and cold-trapping areas on the Moon, and this work is currently underway (Cannon, Deutsch, et al., 2020). The goal of this ongoing work is to understand how the time-history of impact formation influences the delivery, removal, and burial of ice. Specifically, we are working to (1) extend the age dating of large polar craters from the south pole (Deutsch et al., 2020) to the north pole, (2) assess the burial effects of ejecta from large craters (>20 km) on the stratigraphy of polar ice deposits, (3) estimate the combined deposition of water ice derived from impactors, volcanic sources, and solar wind-regolith interactions over time, and (4) model realistic stratigraphies of ice and ejecta, assessing the variations between different cold traps and within individual cold traps. In carrying out these goals, we can derive estimates for the total amount of water ice delivered to the poles, and the fraction of this ice that may be accessible for near-surface exploration in the future (Cannon, Deutsch, et al., 2020). Preliminary work indicates that Haworth crater (87.5°S, 354.8°E; 51.4-km diameter) is a promising exploration target due to the sequestration of near-surface ice reservoirs.

The work in Chapter 2 (Deutsch et al., 2020) also highlights multiple candidate targets for future exploration that can help better constrain the timing and sources of water-ice delivery to the Moon. Excitingly, extensive in-situ exploration of the Moon is being planned with various landed missions expected to explore the polar regions this decade (e.g., Colaprete et al., 2020), as well as human missions supported by NASA's Artemis program, which will allow for the analysis of polar samples returned to Earth (e.g., Mitchell et al., 2020). Important samples for future in-situ and/or returned analysis include:

- *Samples delivered post-TPW.* Nobile (85.3°S, 53.3°E; 79.3-km diameter) and Shackleton (89.7°S, 129.8°E; 20.9-km diameter) craters are not predicted to have been stable for surface ice before the onset of TPW (Siegler et al., 2016), yet surface-ice detections (Li et al., 2018) are present within both craters. Therefore, the age of ice observed within these craters can place an upper constraint on the age of post-TPW hydrogen emplacement.
- *Samples delivered post-peak volcanic activity.* Unnamed 3 (83.9°S, 338.3°E; 22.3-km diameter), Wiechert J (85.2°S, 182.4°E; 34.9-km diameter), and Shackleton (89.7°S, 129.8°E; 20.9-km diameter) craters all have estimated formation ages younger than 3.5 Gyr, which is the time when the Moon is expected to have been experiencing a peak in volcanic activity. Needham and Kring (2017) previously suggested that the water vented during mare volcanism may be sufficient to explain all of the hydrogen observed at the lunar poles. Sampling ice in craters that formed after this volcanic peak would help us to determine what mechanisms delivered ice to the surface of the Moon more recently.
- *Samples from the oldest thermal environments.* It is possible that lunar ice detections (Li et al., 2018) represent a heterogeneous mixture of cold-trapped volatiles derived from various sources. Exploration of some of the oldest lunar cold traps may provide the opportunity to sample volatiles of different origins, as they have been bearing witness to the volatile flux for billions of years. Some of the oldest cold traps we identified that were stable to the cold-trapping of ice

before the onset of predicted TPW (Siegler et al., 2016) and through today include Haworth (87.5°S, 354.8°E; 51.4-km diameter), Shoemaker (88.1°S, 45.9°E, 51.8-km diameter), and Faustini (87.2°S, 84.3°E, 42.5-km diameter).

4. Chapter 3: Assessing the roughness properties of circumpolar lunar craters: Implications for the timing of water-ice delivery to the Moon

In Chapter 3 (Deutsch et al., *accpeted-a*), we analyzed the roughness characteristics within and surrounding small (<~15 km in diameter) polar craters. We found that the distribution of craters that host water-ice detections (Li et al., 2018) is slightly skewed toward roughness values that are higher than those of pre-Imbrian craters, with a statistically significant difference between the two populations (p-value = 0.002). This skew suggests that some ice-bearing craters (and thus the ice they contain) may be younger than Nectarian in age, especially because their surface textures are likely to be subdued by the presence of surface ice (Kreslavsky and Head, 2000; Putzig et al., 2014; Moon et al., 2019). Interestingly, we did not identify any ice-bearing craters that are within the Copernican-only domain in roughness space. All of the 15 rough polar craters (between ±75° and ±90°) that are found within the Copernican-only roughness domain lack water-ice detections (Li et al., 2018). If surface ice is stable in these permanently shadowed craters, then the lack of surface ice in rough craters interpreted to be of Copernican age suggests that either ice has not been delivered to these young craters since their formation, or that it has since been destroyed. If these craters, however, are not thermally stable environments for surface ice, then the youngest ice-bearing craters on the Moon appear to be Imbrian–Eratosthenian in age, on the basis of surface roughness (Deutsch et al., *accepted-a*) and crater-density statistics (Deutsch et al., 2020).

4.1. Outstanding questions and opportunities for future investigation

To help address some of the uncertainties in this work, higher-resolution roughness data could greatly improve the statistics analyzed here. The roughness data that we analyzed (Deutsch et al., *accepted-a*) have a pixel resolution of 1000 m (Neumann et al., 2015; Smith et al., 2017); therefore, the mean surface roughness values calculated for the exterior portions of the small impact craters rely on only a few individual roughness values. Higher-spatial-resolution roughness products would allow us to better probe the roughness properties within and surrounding small craters. Additional work integrating measurements of rock abundance and thermal inertia from the Diviner Lunar Radiometer Experiment and circular polarization ratios from the Miniature Radio Frequency (Mini-RF) instrument could help probe surface characteristics of small circumpolar craters on the Moon.

Overall, the results of Chapter 3 (Deutsch et al., *accepted-a*) have produced some interesting questions regarding the distribution of surface ice on the Moon. For example, we found that no Copernican craters host surface water ice. Are these Copernican craters capable of hosting surface ice? If these craters are thermally stable environments for the survival of water ice, then the absence of ice within them would place a very important constraint on the age of surface ice – specifically, the first *lower* bound on the age of water-ice detections by Li et al. (2018). Alternatively, if Copernican craters are not thermally stable environments for water ice, then where are the youngest cold traps on the Moon, and are they occupied by ice? Future investigation is needed to determine how the lifetimes of polar cold traps compare to the timescales of volatile supply, modification, and destruction processes.

5. Chapter 4: The flux of volcanic eruptions on Mercury: Potential contributions to transient atmospheres and buried polar deposits

In Chapter 4 (Deutsch et al., *in review*), we provided the first comprehensive estimates of the total erupted magma on Mercury through time, and the estimated associated production of lunar volatiles by exploring a wide parameter space of oxygen fugacities and degassed content informed from experimental petrology studies (Libourel et al., 2003; Armstrong et al., 2015; Anzures et al., 2017). We find that if the intercrater plains (ICPs) on Mercury are volcanic in origin (e.g., Murray et al., 1974; Strom et al., 1975; Spudis and Guest, 1988; Denevi et al., 2009; Whitten et al., 2014), then it is possible that the duration of volcanically-derived, transient atmospheres exceeded the time of repose between average mercurian eruptions. With buildup of sufficient densities, transient atmospheres may have aided the migration and delivery of volatiles to polar cold traps. We estimate that if any volcanically-derived volatiles were ever cold-trapped at the poles of Mercury, then they would exist as a diffuse, weathered layer buried at least ~16 m in the subsurface. Such sequestered volatiles would be distinctly different from the polar H_2O-ice deposits observed on Mercury's surface today, both in composition (Butler et al., 1993; Lawrence et al., 2013; Paige et al., 2013) and in age (Crider and Killen, 2005; Lawrence et al., 2013; Deutsch et al., 2019).

5.1. Outstanding questions and opportunities for future investigation

The study presented in Chapter 4 (Deutsch et al., *in review*) explores an extremely wide parameter space of oxygen fugacities and degassed volatile contents given that these values remain relatively unconstrained for Mercury and the actual volatile species degassed during mercurian eruptions remain unknown. In order to refine the history of densities, flux, and timescales of any volcanically-derived atmospheres on Mercury, future in-situ analyses (e.g., Ernst et al., 2020) are critical for more accurately describing the volatile speciation and content of mercurian lavas. With better estimates of atmospheric characteristics, future work can evaluate the ultimate fate of volatiles in transiently dense atmospheres on nominally airless bodies. Such work requires detailed modeling that incorporates eruption dynamics, atmospheric loss rates, and gas dynamics in an atmosphere that is evolving on geologically rapid timescales (Stewart et al., 2011; Prem et al., 2015, 2018, 2019) and is an important next step in assessing how volcanic eruptions altered Mercury's atmospheric density and composition, and how the collisional dynamics of transiently dense atmospheres affect volatile transport and retention on Mercury.

In Chapter 4 (Deutsch et al., *in review*), we outlined various measurements that could assist in testing the hypothesis of cold-trapped, volcanically-derived volatiles, including:

- *Measurements of volcanic plains morphometry.* Topographic measurements acquired by the BepiColombo Laser Altimeter (BELA; Thomas et al., 2007) and stereo images acquired by the SIMBIO-SYS instrument (Flamini et al., 2009) of plains stratigraphy can help improve our estimates of the thicknesses, extent, and topographic variability of volcanic plains units in order to better constrain the total volume of erupted basalts on Mercury.

- *Measurements of surface chemistry.* Elemental measurements (particularly of S) can help refine geochemical models used to estimate the oxygen fugacity of Mercury's interior (e.g., Nittler et al., 2011; Zolotov et al., 2013; McCubbin et al., 2017). We found that changing the fO_2 value from IW-3 to IW-7 could change the estimated degassed mass by an order of magnitude. BepiColombo is equipped with various spectrometers that can help in these measurements, including the MErcury Radiometer and Thermal Infrared Spectrometer (MERTIS; Hiesinger et al., 2009), the Mercury Gamma-Ray and Neutron Spectrometer (MGNS; Mitrofanov et al., 2010), and the Mercury Imaging X-ray Spectrometer (MIXS; Fraser et al., 2009).
- *In-situ petrologic measurements.* Sample analyses of Mercury's volcanic plains are essential to directly measure the speciation and degassed volatile content of volcanic basalts. Landed surface operations are essential to better understand the geochemistry and mineralogy of the surface (Byrne et al., 2018; Vander Kaaden et al., 2019; Ernst et al., 2020).
- *In-situ measurements of geochronology.* Analyses of the geochemical and isotopic properties of major surface units on Mercury would help refine our understanding of the ages of different surface units, and thus the eruption histories and time-evolution of Mercury's surface. This is important for both major SP units, as well as ICPs, which represent some of the oldest terrains on Mercury and whose timing

is not well-resolved. Such analyses are again supportive of landed science investigations (e.g., Byrne et al., 2018; Vander Kaaden et al., 2019; Ernst et al., 2020).

Chapter 4 (Deutsch et al., *in review*) highlights the critical importance that understanding the potential contributions of outgassed species to polar cold traps requires much more than an understanding of the total volume of volatiles released through time. Assessing the potential contributions requires a fundamental understanding of individual eruption characteristics (flow volume, timing, flux, and volatile content) and the repose periods between individual eruptions. Building upon these acknowledgements, we have utilized forward-modeling of individual lunar basaltic eruptions with the observed geologic record to predict the magma volumes, eruption frequency, and rates of volcanic volatile release on the Moon to determine whether lunar conditions were ever favorable for the formation of volcanically-induced, transient atmospheres on the Moon (Head, Wilson, Deutsch, et al., *in prep.*). We found that only under exceptional circumstances, such as with the largest known lunar eruption (Schröter's Valley), would sufficient volatiles have been released in a single eruption to form a tenuous atmosphere that lasted more than a few thousand years. These new results suggest that volcanically-derived, transient atmospheres on the Moon were not sufficient in the production, transportation, and delivery of volatiles to lunar polar cold traps. As with Mercury, multiple measurements can help refine our estimates of erupted magma volumes and rates and the associated release of volatiles. These include additional detailed measurements of lava flow thicknesses, areal extents, volumes, ages, and volatile contents as well as the identification and analyses of discrete flow units.

Finally, one of the more interesting observations from the Gamma-Ray Spectrometer (GRS) onboard MESSENGER is that there is an enhancement of sodium (a moderately volatile element) concentrated at the north polar region of Mercury (Peplowski et al., 2014). There has been considerable debate in the scientific community regarding the nature of this concentration, and it has been proposed to be due to a unique elemental composition of the northern volcanic smooth plains (SPs) (e.g., Peplowski et al., 2014). Interestingly though, this sodium enhancement is also consistent with temperature-induced mobilization of sodium (Peplowski et al., 2014), which does not require compositional variability between the northern SPs and other volcanic SPs on Mercury. If the sodium has migrated to the north polar region due to sublimation-desublimation processes, then the sodium anomaly is an example of a volatile migrating to the poles, as we propose could have happened with outgassed species early on in mercurian history. A critical test of the competing origin hypotheses for the northern sodium anomaly will be BepiColombo measuring the abundance of sodium at the south polar region of Mercury, where there is no large volcanic plains unit, but there is a thermal environment similar to that of the north pole that would allow for the cold-trapping of volatiles.

6. Chapter 5: Temperature-dependent changes in the normal albedo of the lunar surface at 1064 nm

In Chapter 5 (Deutsch et al., *accepted-b*), we emphasize the important of temperature-dependent reflectance changes in future measurements of surface reflectance of airless bodies. We provided the first evidence of temperature-dependent spectral changes on the lunar surface from 1064-nm orbital observations, finding a small, yet measurable, negative change in normal albedo at 1064 nm with temperature ($-\Delta R/\Delta T$). The measurable effect is on the order of a few percent change in reflectance per ~80 K, indicating that surface temperature variations do not have a large effect on measurements of surface reflectance at the sensitivity of the Lunar Orbiter Laser Altimeter (LOLA) instrument. However, as future instruments of higher resolution and precision are flown, temperature-dependent changes will be essential to take into account in reflectance measurements and calibrations. Our results also suggest that single-wavelength lasers may be helpful tools in assessing the relative abundance of particular rock-forming minerals (here, pyroxene) that exhibit a change in spectral reflectance with temperature. For example, a laser with an observation wavelength at 1460 nm should be sensitive to temperature-dependent spectral changes of olivine, although not pyroxene.

6.1. Outstanding questions and opportunities for future investigation

The results presented in Chapter 5 (Deutsch et al., *accepted-b*) are particularly interesting to the volatile community because surface reflectance is an important tool for characterizing the presence and nature of surface ice, and has been employed to study surface ice both on the Moon (e.g., Zuber et al., 2012; Fisher et al., 2017; Qiao et al., 2018) and Mercury (Neumann et al., 2013; Deutsch et al., 2017), as well as on smaller airless bodies (e.g., Platz et al., 2016; Ermakov et al., 2017), Mars (e.g., Smith et al., 1998; Bell et al., 1999), and beyond. Thus, understanding how temperature affects observations of surface reflectance has widespread importance in the planetary community. While laboratory analyses have been successful in deriving temperature-reflectance relationships down to ~80 K (Hinrichs et al., 1999; Hinrichs and Lucey, 2002), the permanently shadowed environments where ice is cold-trapped are characterized by freezing temperatures that can approach ~20 K (Vasavada et al., 1999; Paige et al., 2010, 2013; Williams et al., 2017, 2019). Therefore, characterizing the temperature-dependent spectral changes for common minerals at discrete wavelengths specifically at these extremely low temperatures remains an outstanding priority.

7. Future exploration

Two of the most exciting opportunities for continuing the study of polar volatiles on Mercury and the Moon in the near future include the BepiColombo mission to Mercury (Benkhoff et al., 2010), a joint ESA-JAXA mission expected to insert orbit around Mercury in 2025, and the Volatiles Investigating Polar Exploration Rover (VIPER) mission to the Moon (Colaprete et al., 2020), a prospecting mission developed through NASA's Lunar Discovery and Exploration Program expected to land in 2023. In the final section of this dissertation, I would like to highlight a few of the major outstanding questions regarding volatiles on Mercury and the Moon and discuss how these two upcoming missions can help address them.

7.1. Future exploration of Mercury with BepiColombo

BepiColombo consists of two spacecrafts: the ESA-led Mercury Planetary Orbiter (MPO) to study the surface and composition of Mercury and the JAXA-led Mercury

Magnetospheric Orbiter (MMO) to study Mercury's magnetosphere. Launched in 2018, the spacecrafts are predicted to arrive in Mercury orbit in late 2025, at which time both spacecrafts will enter polar orbits that are particularly favorable to the continued study of mercurian polar volatiles. In fact, one of the primary mission objectives of BepiColombo is to investigate the composition and origin of polar deposits on Mercury, and thus the MPO is equipped with a highly capable payload that can address some of the greatest open questions regarding polar ice on Mercury (Benkhoff et al., 2010). Previously, I outlined some specific measurements that can help constrain the ages of mercurian polar deposits (Section 2.1) and potential contributions of volcanically-derived volatiles to polar cold traps (Section 5.1), and here I will highlight some additional investigations that can help address the composition, nature, and extent of polar ice on Mercury with BepiColombo.

7.1.1. Composition of polar deposits on Mercury

Understanding the composition of Mercury's ice is important to determine the processes that originally delivered ice to Mercury's poles and processes that have since modified the ice. The payload of BepiColombo includes various spectrometers that will assist in determining the composition of polar volatiles, including MERTIS (Hiesinger and Helbert, 2010) and SIMBIO-SYS (Flamini et al., 2010).

While the most poleward ice deposits on Mercury are exposed at the surface and have high-reflectance properties (Neumann et al., 2013; Deutsch et al., 2017), the majority of ice deposits are insulated by a ~10–30 cm-thick layer of low-reflectance materials (Lawrence et al., 2013). Images revealed brightness variations within these low-reflectance deposits that sometimes correlate with variations in surface temperature, suggesting that the low-reflectance deposits may contain multiple volatile compounds (Chabot et al., 2016). The reflectance properties and the thermal environments of these materials suggest that they are composed of a volatile other than water, such as macromolecular carbonaceous material or simple organic compounds (e.g., Ar, SO_2, H_2O, $C_5H_9NO_2$, S, $C_{24}H_{12}$) (Zhang and Paige, 2009; Paige et al., 2013; Delitsky et al., 2017). SIMBIO-SYS and MERTIS will provide the first compositional measurements of these curious low-reflectance surfaces, and understanding their composition is paramount to understanding the origin of the ice.

Additionally, MERTIS will enable studies of surface temperature variations and thermal inertia (Hiesinger and Helbert, 2010), which will help us determine the thermal controls on the presence and composition of ice so that processes that act to retain and modify the ice can be better understood. Measurements of surface temperatures within north and south polar PSRs will also help to determine the extent to which thermal environments vary between and within PSRs at each pole.

7.1.2. Nature of polar deposits on Mercury

In addition to resolving the chemical composition of Mercury's polar deposits, BepiColombo can help us better understand the physical nature of the ice, including its surface age, stratigraphy, and roughness. Investigating the physical nature of the ice is essential both in determining the age and origin of the ice and also in determining processes that have acted to modify or deplete the ice since its original delivery.

For example, imaging the permanently shadowed surfaces at the north and south polar regions with SYMBIO-SYS will help (a) determine the stratigraphy within Mercury's PSRs, including that of ice, impact craters, regolith, ejecta, and mass wasting materials so that relative ages can be derived for the ice and so that the modification of ice surfaces by impact cratering and regolith gardening can be observed, (b) determine the crater populations within Mercury's PSRs so that absolute surface ages can be derived for Mercury's ice, (c) determine the extent to which surface characteristics vary between north and south polar ice deposits so that a global understanding of the nature of Mercury's ice can be provided, and (d) determine the geologic characteristics of the albedo boundaries of Mercury's ice so that the modification of ice contacts can be studied.

Additionally, the BepiColombo Laser Altimeter (BELA; Thomas et al., 2007) will be useful in measuring the topography of polar environments and cold-trapped ice deposits. These measurements can be used to help determine the thickness of the ice (especially in the south polar region) so that we can refine estimates of ice volume – important constraints for determining ice delivery mechanisms (Harmon, 2007; Black et al., 2010; Eke et al., 2017; Deutsch et al., 2018a; Rubanenko et al., 2019; Susorney et al., 2019). Furthermore, topographic measurements may allow for the characterization of surface roughness properties, which can provide insight into surface modification processes and the physical weathering history of the volatile deposits (Kreslavsky and Head, 2000; Putzig et al., 2014; Moon et al., 2019).

7.1.3. Extent of polar deposits on Mercury

Finally, understanding the extent of ice on Mercury is important to determine the distribution and total quantity of ice, which has distinct implications for delivery mechanisms (Deutsch et al., 2016; Chabot et al., 2018). With the first low-altitude observations of Mercury's south polar region, BepiColombo can help (1) map the presence of anomalously high- and low-reflectance surfaces within south polar PSRs using BELA and SYMBIO-SYS, (2) measure the thickness of ice deposits within southern PSRs using BELA, (3) measure elemental composition of the shallow subsurface within the south polar region using MGNS, and (4) measure the surface temperatures within north and south polar PSRs using MERTIS. All four of these objectives will help provide a detailed global view of Mercury's polar environments and a comprehensive understanding of the planet's total ice inventory.

7.2. Future exploration of the Moon with VIPER

VIPER is a volatiles prospecting mission that will land on and rove one of the lunar poles, likely arriving in late 2023. The primary mission goal is to evaluate the potential for in-situ resource utilization (ISRU) in order to inform future NASA and commercial spaceflight architectures (Colaprete et al., 2020). By targeting polar regions with particularly short lunar nights, the nominal mission duration is 90 Earth days, during which the rover is expected to traverse > 20 km in distance. An exciting aspect of this mission will be the combined power of both pre-flight planning and real-time decision making, enabled by real-time Earth-rover communications, that will facilitate informed and efficient exploration of the lunar pole. Although VIPER is a prospecting mission and not a science-directorate mission, it will provide critical information on the distribution, abundance, and form of volatiles at the lunar poles. Thus, in line with the goals of this dissertation, VIPER will contribute significant scientific knowledge to our understanding of the sources, evolution, and current state of polar volatiles.

7.2.1. Distribution of polar ice on the Moon

Along with a sampling drill, there are three prospecting instruments onboard VIPER that will continuously function during rover driving operations. (1) The Neutron Spectrometer System (NSS) will provide insight into the estimated subsurface hydrogen abundance through measurements of epithermal neutron fluxes, as well as the bulk regolith chemistry through measurements of thermal and epithermal neutron fluxes (Elphic et al., 2015, 2017; Ennico-Smith et al., 2020). (2) The Near InfraRed Volatiles Spectrometer System (NIRVSS) is a compound instrument that will help characterize the lunar surface composition, thermophysical properties, and morphology with near-infrared spectrometry and thermal radiometry (Roush et al., 2015). In addition to its roving observations, the NIRVSS will directly observe VIPER drill cuttings as they are deposited on the surface (Colaprete et al., 2019; Ennico-Smith et al., 2020). (3) Finally, the Mass Spectrometer observing lunar operations (MSolo) instrument will provide critical insight into the speciation, relative abundance, and isotopic ratios of polar volatiles by differentiation of low molecular-weight volatiles between atomic mass units of 1 and 100 (Ennico-Smith et al., 2020). MSolo will also be able to detect volatiles that sublimate from VIPER drill cuttings. Overall, the continuous ground operations of these three prospecting instruments will provide important ground truthing of various orbital observations of the lunar poles (e.g., Feldman et al., 1998; 2000; 2001; Eke et al., 2009;

Colaprete et al., 2010; Paige et al., 2010; Miller et al., 2012; Fisher et al., 2017; Li et al., 2018) and detailed measurements of the lateral and vertical distribution of polar volatiles at unprecedented spatial scales.

The lateral and vertical distribution of lunar ice is critically tied to understanding the source and evolution of the ice (e.g., Siegler et al., 2016; Deutsch et al., 2020), and provides key information regarding processes that control the emplacement, retention, modification, and loss of polar volatiles. Additionally, the distribution of lunar ice provides insight into the overall resource potential and resource inventory of the Moon (e.g., Anand et al., 2012), which will inform future landing site decisions, rover transects, and drilling sites.

7.2.2. Composition of polar ice on the Moon

Excitingly, VIPER is also equipped with The Regolith and Ice Drill for Exploration of New Terrains (TRIDENT), which is a 1-m drill that captures subsurface samples in ~10-cm intervals (Zacny et al., 2013, 2019). The delivery of drill cuttings to the surface will allow the NIRVSS and MSolo instruments to directly observe subsurface polar samples, providing in-situ chemical measurements of lunar subsurface volatiles. The composition and relative abundance of cold-trapped volatiles provide critical information regarding the sources of volatile delivery to the Moon. Chemical measurements of these ices could help provide insight into the nature of water delivered to early Earth (Chyba, 1987; Morbidelli et al., 2000; Owen and Bar-Nun, 2001; Drake, 2005; Hartogh et al., 2011; McCubbin and Barnes, 2019).

7.2.3. Cold-trapping environments on the Moon

In addition to enabling detailed measurements of the form of lunar volatiles, TRIDENT will measure the vertical distribution of subsurface temperature. Temperature is a primary control on the distribution of volatiles (Vasavada et al., 1999; Paige et al., 2010; Hayne et al., 2015, 2019; Siegler et al., 2016) and modulates the rates of volatile diffusion and sublimation (Hibbitts et al., 2011; Schorghofer and Aharonson, 2014). Therefore, in-situ measurements of polar temperature profiles will provide key information regarding volatile sinks, as well as retention and modification processes.

Finally, TRIDENT will provide key insight into the strength of the polar lunar regolith, and how regolith strength varies with depth. These measurements will provide essential insight into the form of cold-trapped volatiles, such as whether the volatiles are distributed as ice particles mixed within the regolith or whether the subsurface is an ice-cemented ground (Ennico-Smith et al., 2020; Sargeant et al., 2020).

References

Anand, M., Crawford, I. A., Balat-Pichelin, M., Abanades, S., van Westrenen, W., Péraudeau, G., et al. (2012). A brief review of chemical and mineralogical resources on the Moon and likely initial in situ resource utilization (ISRU) applications. *Planetary and Space Science*, *74*(1), 42–48. https://doi.org/10.1016/j.pss.2012.08.012

Anzures, B.A., Parman, S.W., Boesenberg, J.S., & Milliken, R.E. (2019). Using volatile (S, C, H, F, Cl) contents on enstatite in reduced meteorites to estimate oxygen fugacity and equilibrium melt compositions. *Lunar and Planetary Science*

Conference, 50, Abstract #2179.
https://www.hou.usra.edu/meetings/lpsc2019/pdf/2179.pdf

Armstrong, L. S., Hirschmann, M. M., Stanley, B. D., Falksen, E. G., & Jacobsen, S. D. (2015). Speciation and solubility of reduced C–O–H–N volatiles in mafic melt: Implications for volcanism, atmospheric evolution, and deep volatile cycles in the terrestrial planets. *Geochimica et Cosmochimica Acta*, *171*, 283–302. https://doi.org/10.1016/j.gca.2015.07.007

Bell, J. F., Wolff, M. J., Daley, T. C., Crisp, D., James, P. B., Lee, S. W., et al. (1999). Near-infrared imaging of Mars from HST: Surface reflectance, photometric properties, and implications for MOLA data. *Icarus*, *138*(1), 25–35. https://doi.org/10.1006/icar.1998.6057

Benkhoff, J., van Casteren, J., Hayakawa, H., Fujimoto, M., Laakso, H., Novara, M., et al. (2010). BepiColombo—Comprehensive exploration of Mercury: Mission overview and science goals. *Planetary and Space Science*, *58*(1), 2–20. https://doi.org/10.1016/j.pss.2009.09.020

Black, G. J., Campbell, D. B., & Harmon, J. K. (2010). Radar measurements of Mercury's north pole at 70cm wavelength. *Icarus*, *209*(1), 224–229. https://doi.org/10.1016/j.icarus.2009.10.009

Blewett, D. T., Chabot, N. L., Denevi, B. W., Ernst, C. M., Head, J. W., Izenberg, N. R., et al. (2011). Hollows on Mercury: MESSENGER evidence for geologically recent volatile-related activity. *Science*, *333*(6051), 1856–1859. https://doi.org/10.1126/science.1211681

Blewett, D. T., Vaughan, W. M., Xiao, Z., Chabot, N. L., Denevi, B. W., Ernst, C. M., et al. (2013). Mercury's hollows: Constraints on formation and composition from analysis of geological setting and spectral reflectance. *Journal of Geophysical Research: Planets*, *118*(5), 1013–1032. https://doi.org/10.1029/2012JE004174

Boyce, J. W., Liu, Y., Rossman, G. R., Guan, Y., Eiler, J. M., Stolper, E. M., & Taylor, L. A. (2010). Lunar apatite with terrestrial volatile abundances. *Nature*, *466*(7305), 466–469. https://doi.org/10.1038/nature09274

Butler, B. J., Muhleman, D. O., & Slade, M. A. (1993). Mercury: Full-disk radar images and the detection and stability of ice at the north pole. *Journal of Geophysical Research: Planets*, *98*(E8), 15003–15023. https://doi.org/10.1029/93JE01581

Byrne, P.K., et al. (2018). Landed Mercury Exploration and the Timely Need for a Mission Concept Study. https://bit.ly/2GqsmC2.

Cannon, K. M., Deutsch, A. N., & Head, J. W. (2020). Stratigraphy of ice and ejecta deposits at the lunar poles. *Lunar and Planetary Science Conference, 51,* Abstract #1488. https://www.hou.usra.edu/meetings/lpsc2020/pdf/1488.pdf

Chabot, N. L., Ernst, C. M., Paige, D. A., Nair, H., Denevi, B. W., Blewett, D. T., et al. (2016). Imaging Mercury's polar deposits during MESSENGER's low-altitude campaign. *Geophysical Research Letters*, *43*(18), 9461–9468. https://doi.org/10.1002/2016GL070403

Chabot, N. L., Shread, E. E., & Harmon, J. K. (2018). Investigating Mercury's south polar deposits: Arecibo radar observations and high-resolution determination of illumination conditions. *Journal of Geophysical Research: Planets*, *123*(2), 666–681. https://doi.org/10.1002/2017JE005500

Chen, Y., Zhang, Y., Liu, Y., Guan, Y., Eiler, J., & Stolper, E. M. (2015). Water, fluorine, and sulfur concentrations in the lunar mantle. *Earth and Planetary Science Letters*, *427*, 37–46. https://doi.org/10.1016/j.epsl.2015.06.046

Chyba, C. F. (1987). The cometary contribution to the oceans of primitive Earth. *Nature*, *330*(6149), 632–635. https://doi.org/10.1038/330632a0

Colaprete, A., Benton, J., Bielawski, R., Cook, A., Forgione, J., Jin, F., McMurry, W., Middour C., Roush, T., & White, B. (2019). The Near InfraRed Volatiles Spectrometer System (NIRVSS). *Lunar Exploration Analysis Group Meeting., 51*, Abstract #5057. https://www.hou.usra.edu/meetings/leag2019/pdf/leag2019_program.htm

Colaprete, A., Elphic, R. C., Shirley, M., Ennico-Smith, K., Heldmann, J., Lim, D. S. S., Falcone, L., Siegler, M., & Coyan, J. (2020). The Volatiles Investigating Polar Exploration Rover (VIPER) Mission: Measurement goals and traverse planning. *Lunar and Planetary Science Conference, 51*, Abstract #2241. https://www.hou.usra.edu/meetings/lpsc2020/pdf/2241.pdf

Colaprete, A., Schultz, P., Heldmann, J., Wooden, D., Shirley, M., Ennico, K., et al. (2010). Detection of water in the LCROSS ejecta plume. *Science*, *330*(6003), 463–468. https://doi.org/10.1126/science.1186986

Crider, D. H., & Vondrak, R. R. (2000). The solar wind as a possible source of lunar polar hydrogen deposits. *Journal of Geophysical Research: Planets*, *105*(E11), 26773–26782. https://doi.org/10.1029/2000JE001277

Crider, D., & Killen, R. M. (2005). Burial rate of Mercury's polar volatile deposits. *Geophysical Research Letters*, *32*(12), L12201. https://doi.org/10.1029/2005GL022689

Crotts, A. P. S., & Hummels, C. (2009). Lunar outgassing, transient phenomena, and the return to the Moon. II. Predictions and tests for outgassing/regolith interactions. *The Astrophysical Journal*, *707*(2), 1506. https://doi.org/10.1088/0004-637X/707/2/1506

Delitsky, M. L., Paige, D. A., Siegler, M. A., Harju, E. R., Schriver, D., Johnson, R. E., & Travnicek, P. (2017). Ices on Mercury: Chemistry of volatiles in permanently cold areas of Mercury's north polar region. *Icarus*, *281*, 19–31. https://doi.org/10.1016/j.icarus.2016.08.006

Denevi, B. W., Robinson, M. S., Solomon, S. C., Murchie, S. L., Blewett, D. T., Domingue, D. L., et al. (2009). The evolution of Mercury's crust: A global perspective from MESSENGER. *Science*, *324*(5927), 613–618. https://doi.org/10.1126/science.1172226

Deutsch, A. N., Head, J. W., Neumann, G. A., Kreslavsky, M. A., & Barker, M. K. (Accepted-a). Assessing the roughness properties of circumpolar lunar craters: Implications for the timing of water ice delivery to the Moon. *Geophysical Research Letters.*

Deutsch, A. N., Head, J. W., Parman, S. W., Neumann, G. A., & Lowden, F. (In review). The flux of volcanic eruptions on Mercury: Potential contributions to transient atmospheres and buried polar deposits.

Deutsch, A. N., Neumann, G. A., Head, J. W., & Lucey, P. G. (Accepted-b). Temperature-dependent changes in the normal albedo of the lunar surface at 1064 nm. *Journal of Geophysical Research: Planets*.

Deutsch, A. N., Head, J. W., & Neumann, G. A. (2020). Analyzing the ages of south polar craters on the Moon: Implications for the sources and evolution of surface water ice. *Icarus*, *336*, 113455. https://doi.org/10.1016/j.icarus.2019.113455

Deutsch, Ariel N., Chabot, N. L., Mazarico, E., Ernst, C. M., Head, J. W., Neumann, G. A., & Solomon, S. C. (2016). Comparison of areas in shadow from imaging and altimetry in the north polar region of Mercury and implications for polar ice deposits. *Icarus*, *280*, 158–171. https://doi.org/10.1016/j.icarus.2016.06.015

Deutsch, Ariel N., Head, J. W., & Neumann, G. A. (2019). Age constraints of Mercury's polar deposits suggest recent delivery of ice. *Earth and Planetary Science Letters*, *520*, 26–33. https://doi.org/10.1016/j.epsl.2019.05.027

Deutsch, Ariel N., Head, J. W., Chabot, N. L., & Neumann, G. A. (2018). Constraining the thickness of polar ice deposits on Mercury using the Mercury Laser Altimeter and small craters in permanently shadowed regions. *Icarus*, *305*, 139–148. https://doi.org/10.1016/j.icarus.2018.01.013

Deutsch, Ariel N., Neumann, G. A., & Head, J. W. (2017). New evidence for surface water ice in small-scale cold traps and in three large craters at the north polar region of Mercury from the Mercury Laser Altimeter. *Geophysical Research Letters*, *44*, 9233–9241. https://doi.org/10.1002/2017GL074723

Drake, M. J. (2005). Origin of water in the terrestrial planets. *Meteoritics & Planetary Science*, *40*(4), 519–527. https://doi.org/10.1111/j.1945-5100.2005.tb00960.x

Eke, V. R., Teodoro, L. F. A., & Elphic, R. C. (2009). The spatial distribution of polar hydrogen deposits on the Moon. *Icarus*, *200*(1), 12–18. https://doi.org/10.1016/j.icarus.2008.10.013

Eke, Vincent R., Lawrence, D. J., & Teodoro, L. F. A. (2017). How thick are Mercury's polar water ice deposits? *Icarus*, *284*, 407–415. https://doi.org/10.1016/j.icarus.2016.12.001

Elphic, R. C., Fritzler, E. L., Mobilia, J., & Kou, A. (2017). The Resource Prospector Neutron Spectrometer System: RP's bloodhound. *NASA Exploration Science Forum*, *4*, Abstract #NESF2017-126. https://nesf2017.arc.nasa.gov/abstract/nesf2017-126

Elphic, Richard C., Heldmann, J. L., Marinova, M. M., Colaprete, A., Fritzler, E. L., McMurray, R. E., et al. (2015). Simulated real-time lunar volatiles prospecting with a rover-borne neutron spectrometer. *Advances in Space Research*, *55*(10), 2438–2450. https://doi.org/10.1016/j.asr.2015.01.035

Ennico-Smith, K., Colaprete, A., Elphic, R., Captain, J., Quinn, J., & Zachny, K. (2020). The Volatiles Investigating Polar Exploration Rover payload*. Lunar and Planetary Science Conference, 51*, Abstract #2898. https://www.hou.usra.edu/meetings/lpsc2020/pdf/2898.pdf

Ermakov, A. I., Mazarico, E., Schröder, S. E., Carsenty, U., Schorghofer, N., Preusker, F., et al. (2017). Ceres's obliquity history and its implications for the permanently shadowed regions. *Geophysical Research Letters*, *44*(6), 2652–2661. https://doi.org/10.1002/2016GL072250

Ernst, C. M., Chabot, N. L., & Barnouin, O. S. (2018). Examining the potential contribution of the Hokusai impact to water ice on Mercury. *Journal of Geophysical Research: Planets*, *123*(10), 2628–2646. https://doi.org/10.1029/2018JE005552

Ernst, C. M., et al. (2020). Mercury Lander. Planetary Mission Concept Studies, ROSES 2018 NRA. http://lib.jhuapl.edu/papers/mercury-lander/

Evans, L. G., Peplowski, P. N., McCubbin, F. M., McCoy, T. J., Nittler, L. R., Zolotov, M. Yu., et al. (2015). Chlorine on the surface of Mercury: MESSENGER gamma-ray measurements and implications for the planet's formation and evolution. *Icarus*, *257*, 417–427. https://doi.org/10.1016/j.icarus.2015.04.039

Feldman, W. C., Lawrence, D. J., Elphic, R. C., Barraclough, B. L., Maurice, S., Genetay, I., & Binder, A. B. (2000). Polar hydrogen deposits on the Moon. *Journal of Geophysical Research: Planets*, *105*(E2), 4175–4195. https://doi.org/10.1029/1999JE001129

Feldman, W. C., Maurice, S., Binder, A. B., Barraclough, B. L., Elphic, R. C., & Lawrence, D. J. (1998). Fluxes of fast and epithermal neutrons from Lunar Prospector: Evidence for water ice at the lunar poles. *Science*, *281*(5382), 1496–1500. https://doi.org/10.1126/science.281.5382.1496

Feldman, W. C., Maurice, S., Lawrence, D. J., Little, R. C., Lawson, S. L., Gasnault, O., et al. (2001). Evidence for water ice near the lunar poles. *Journal of Geophysical Research: Planets*, *106*(E10), 23231–23251. https://doi.org/10.1029/2000JE001444

Fisher, E. A., Lucey, P. G., Lemelin, M., Greenhagen, B. T., Siegler, M. A., Mazarico, E., et al. (2017). Evidence for surface water ice in the lunar polar regions using reflectance measurements from the Lunar Orbiter Laser Altimeter and temperature measurements from the Diviner Lunar Radiometer Experiment. *Icarus*, *292*, 74–85. https://doi.org/10.1016/j.icarus.2017.03.023

Flamini, E., Capaccioni, F., Colangeli, L., Cremonese, G., Doressoundiram, A., Josset, J. L., et al. (2010). SIMBIO-SYS: The spectrometer and imagers integrated observatory system for the BepiColombo planetary orbiter. *Planetary and Space Science*, *58*(1), 125–143. https://doi.org/10.1016/j.pss.2009.06.017

Fraser, G. W., Carpenter, J. D., Rothery, D. A., Pearson, J. F., Martindale, A., Huovelin, J., et al. (2010). The Mercury Imaging X-ray Spectrometer (MIXS) on BepiColombo. *Planetary and Space Science*, *58*(1), 79–95. https://doi.org/10.1016/j.pss.2009.05.004

Goudge, T. A., Head, J. W., Kerber, L., Blewett, D. T., Denevi, B. W., Domingue, D. L., et al. (2014). Global inventory and characterization of pyroclastic deposits on Mercury: New insights into pyroclastic activity from MESSENGER orbital data. *Journal of Geophysical Research: Planets*, *119*(3), 635–658. https://doi.org/10.1002/2013JE004480

Greenwood, J. P., Itoh, S., Sakamoto, N., Warren, P., Taylor, L., & Yurimoto, H. (2011). Hydrogen isotope ratios in lunar rocks indicate delivery of cometary water to the Moon. *Nature Geoscience*, *4*(2), 79–82. https://doi.org/10.1038/ngeo1050

Harmon, J. K. (2007). Radar imaging of Mercury. *Space Science Reviews*, *132*(2–4), 307–349. https://doi.org/10.1007/s11214-007-9234-y

Harmon, J. K., Slade, M. A., & Rice, M. S. (2011). Radar imagery of Mercury's putative polar ice: 1999–2005 Arecibo results. *Icarus*, *211*(1), 37–50. https://doi.org/10.1016/j.icarus.2010.08.007

Hartogh, P., Lis, D. C., Bockelée-Morvan, D., de Val-Borro, M., Biver, N., Küppers, M., et al. (2011). Ocean-like water in the Jupiter-family comet 103P/Hartley 2. *Nature*, *478*(7368), 218–220. https://doi.org/10.1038/nature10519

Hauri, E. H., Saal, A. E., Rutherford, M. J., & Van Orman, J. A. (2015). Water in the Moon's interior: Truth and consequences. *Earth and Planetary Science Letters*, *409*, 252–264. https://doi.org/10.1016/j.epsl.2014.10.053

Hauri, E. H., Weinreich, T., Saal, A. E., Rutherford, M. C., & Orman, J. A. V. (2011). High pre-eruptive water contents preserved in lunar melt inclusions. *Science*, *333*(6039), 213–215. https://doi.org/10.1126/science.1204626

Hayne, P. O., Siegler, M. A., Paige, D. A., Lucey, P. G., & Fisher, E. A. (2019). Carbon dioxide frost at the poles of the Moon: Thermal stability and observational evidence from the Lunar Reconnaissance Orbiter. *Lunar and Planetary Science Conference, 50*, 2628.

Hayne, Paul O., Hendrix, A., Sefton-Nash, E., Siegler, M. A., Lucey, P. G., Retherford, K. D., et al. (2015). Evidence for exposed water ice in the Moon's south polar regions from Lunar Reconnaissance Orbiter ultraviolet albedo and temperature measurements. *Icarus*, *255*(Supplement C), 58–69. https://doi.org/10.1016/j.icarus.2015.03.032

Head, J. W., Murchie, S. L., Prockter, L. M., Robinson, M. S., Solomon, S. C., Strom, R. G., et al. (2008). Volcanism on Mercury: Evidence from the first MESSENGER flyby. *Science*, *321*(5885), 69–72. https://doi.org/10.1126/science.1159256

Head, J. W., Wilson, L., Deutsch, A. N., Rutherford, M. J., & Saal, A. E. (*In prep.*) Volcanically-induced transient atmospheres on the Moon: Assessment of duration, significance, and contributions to polar volatile traps.

Hibbitts, C. A., Grieves, G. A., Poston, M. J., Dyar, M. D., Alexandrov, A. B., Johnson, M. A., & Orlando, T. M. (2011). Thermal stability of water and hydroxyl on the surface of the Moon from temperature-programmed desorption measurements of lunar analog materials. *Icarus*, *213*(1), 64–72. https://doi.org/10.1016/j.icarus.2011.02.015

Hiesinger, H., & Helbert, J. (2010). The Mercury Radiometer and Thermal Infrared Spectrometer (MERTIS) for the BepiColombo mission. *Planetary and Space Science*, *58*(1), 144–165. https://doi.org/10.1016/j.pss.2008.09.019

Hinrichs, J. L., Lucey, P. G., Robinson, M. S., Meibom, A., & Krot, A. N. (1999). Implications of temperature-dependent near-IR spectral properties of common minerals and meteorites for remote sensing of asteroids. *Geophysical Research Letters*, *26*(12), 1661–1664. https://doi.org/10.1029/1999GL900334

Hinrichs, John L., & Lucey, P. G. (2002). Temperature-dependent near-infrared spectral properties of minerals, meteorites, and lunar soil. *Icarus*, *155*(1), 169–180. https://doi.org/10.1006/icar.2001.6754

National Academies (2019). Review of the planetary science aspects of NASA SMD's Lunar Science and Exploration Initiative. National Academies of Sciences. https://doi.org/10.17226/25373

LEAG (2017). LEAG Volatiles Specific Action Team 2 (VSAT2) Final Report. https://www.lpi.usra.edu/leag/reports/V-SAT-2-Final-Report.pdf

Jones, B. M., Sarantos, M., & Orlando, T. M. (2020). A new in situ quasi-continuous solar-wind source of molecular water on Mercury. *The Astrophysical Journal*, *891*(2), L43. https://doi.org/10.3847/2041-8213/ab6bda

Jozwiak, L. M., Head, J. W., & Wilson, L. (2018). Explosive volcanism on Mercury: Analysis of vent and deposit morphology and modes of eruption. *Icarus*, *302*, 191–212. https://doi.org/10.1016/j.icarus.2017.11.011

Kerber, L., Head, J. W., Blewett, D. T., Solomon, S. C., Wilson, L., Murchie, S. L., et al. (2011). The global distribution of pyroclastic deposits on Mercury: The view from MESSENGER flybys 1–3. *Planetary and Space Science*, *59*(15), 1895–1909. https://doi.org/10.1016/j.pss.2011.03.020

Kerber, L., Head, J. W., Solomon, S. C., Murchie, S. L., Blewett, D. T., & Wilson, L. (2009). Explosive volcanic eruptions on Mercury: Eruption conditions, magma volatile content, and implications for interior volatile abundances. *Earth and Planetary Science Letters*, *285*(3), 263–271. https://doi.org/10.1016/j.epsl.2009.04.037

Kreslavsky, M. A., & Head, J. W. (2000). Kilometer-scale roughness of Mars: Results from MOLA data analysis. *Journal of Geophysical Research: Planets*, *105*(E11), 26695–26711. https://doi.org/10.1029/2000JE001259

Lawrence, D. J., Feldman, W. C., Goldsten, J. O., Maurice, S., Peplowski, P. N., Anderson, B. J., et al. (2013). Evidence for water ice near Mercury's north pole from MESSENGER Neutron Spectrometer measurements. *Science*, *339*(6117), 292–296. https://doi.org/10.1126/science.1229953

LEAG (2018). Lunar Exploration Analysis Group Advancing Science of the Moon: Report of the Specific Action Team. https://www.lpi.usra.edu/leag/reports/ASM-SAT-Report-final.pdf

Li, S., Lucey, P. G., Milliken, R. E., Hayne, P. O., Fisher, E., Williams, J.-P., et al. (2018). Direct evidence of surface exposed water ice in the lunar polar regions. *Proceedings of the National Academy of Sciences*, *115*, 8907–8912. https://doi.org/10.1073/pnas.1802345115

Libourel, G., Marty, B., & Humbert, F. (2003). Nitrogen solubility in basaltic melt. Part I. Effect of oxygen fugacity. *Geochimica et Cosmochimica Acta*, *67*(21), 4123–4135. https://doi.org/10.1016/S0016-7037(03)00259-X

LEAG (2014). LEAG Volatiles Specific Action Team (VSAT) Final Report. https://www.lpi.usra.edu/leag/reports/vsat_report_123114x.pdf

McCord, T. B., Taylor, L. A., Combe, J.-P., Kramer, G., Pieters, C. M., Sunshine, J. M., & Clark, R. N. (2011). Sources and physical processes responsible for OH/H2O in the lunar soil as revealed by the Moon Mineralogy Mapper (M3). *Journal of Geophysical Research: Planets*. https://doi.org/10.1029/2010JE003711@10.1002/(ISSN)2169-9100.MOONMMI1

McCubbin, F. M., & Barnes, J. J. (2019). Origin and abundances of H2O in the terrestrial planets, Moon, and asteroids. *Earth and Planetary Science Letters*, *526*, 115771. https://doi.org/10.1016/j.epsl.2019.115771

McCubbin, F. M., Steele, A., Hauri, E. H., Nekvasil, H., Yamashita, S., & Hemley, R. J. (2010). Nominally hydrous magmatism on the Moon. *Proceedings of the National Academy of Sciences*, *107*(25), 11223–11228. https://doi.org/10.1073/pnas.1006677107

McCubbin, F. M., Vander Kaaden, K. E., Peplowski, P. N., Bell, A. S., Nittler, L. R., Boyce, J. W., et al. (2017). A low O/Si ratio on the surface of Mercury: Evidence for silicon smelting? *Journal of Geophysical Research: Planets*, *122*(10), 2053–2076. https://doi.org/10.1002/2017JE005367

Milliken, R. E., & Li, S. (2017). Remote detection of widespread indigenous water in lunar pyroclastic deposits. *Nature Geoscience*, *10*(8), 561–565. https://doi.org/10.1038/ngeo2993

Miller, R. S., Nerurkar, G., & Lawrence, D. J. (2012). Enhanced hydrogen at the lunar poles: New insights from the detection of epithermal and fast neutron signatures.

Journal of Geophysical Research: Planets, *117*(E11), E11007. https://doi.org/10.1029/2012JE004112

Mitchell, J. L., Zeigler, R. A., McCubbin, F. M., Needham, D. H., Amick, C. L., Lewis, E. K., Graff, T. G., John, K. K., Naids, A. J., & Lawrence, S. J. (2020). Artemis curation: Preparing for sample return from the lunar south pole. *Lunar and Planetary Science Conference, 51*, Abstract #2615. https://www.hou.usra.edu/meetings/lpsc2020/pdf/2615.pdf

Mitrofanov, I. G., Kozyrev, A. S., Konovalov, A., Litvak, M. L., Malakhov, A. A., Mokrousov, M. I., et al. (2010). The Mercury Gamma and Neutron Spectrometer (MGNS) on board the Planetary Orbiter of the BepiColombo mission. *Planetary and Space Science*, *58*(1), 116–124. https://doi.org/10.1016/j.pss.2009.01.005

Moon, S., Paige, D. A., Siegler, M., & Russell, P. (2019). Quantifying the connections between topographic characteristics and lunar regolith properties in the permanently shadowed regions. *AGU Fall Meeting, 100,* Abstract P51D-3402. https://agu.confex.com/agu/fm19/meetingapp.cgi/Paper/562771

Morbidelli, A., Chambers, J., Lunine, J. I., Petit, J. M., Robert, F., Valsecchi, G. B., & Cyr, K. E. (2000). Source regions and timescales for the delivery of water to the Earth. *Meteoritics & Planetary Science*, *35*(6), 1309–1320. https://doi.org/10.1111/j.1945-5100.2000.tb01518.x

Murchie, S. L., Klima, R. L., Denevi, B. W., Ernst, C. M., Keller, M. R., Domingue, D. L., et al. (2015). Orbital multispectral mapping of Mercury with the MESSENGER Mercury Dual Imaging System: Evidence for the origins of plains units and low-reflectance material. *Icarus*, *254*, 287–305. https://doi.org/10.1016/j.icarus.2015.03.027

Murray, B. C., Belton, M. J. S., Danielson, G. E., Davies, M. E., Gault, D. E., Hapke, B., et al. (1974). Mercury's surface: Preliminary description and interpretation from Mariner 10 pictures. *Science*, *185*(4146), 169–179. https://doi.org/10.1126/science.185.4146.169

Needham, D. H., & Kring, D. A. (2017). Lunar volcanism produced a transient atmosphere around the ancient Moon. *Earth and Planetary Science Letters*, *478*(Supplement C), 175–178. https://doi.org/10.1016/j.epsl.2017.09.002

Neumann, G.A., Glaeser, P. A., Hiesinger, H., Zuber, M. T., & Smith, D. E. (2015). Copernican-age craters and LOLA decameter-scale roughness. *Lunar and Planetary Science Conference, 46*, Abstract 2218.

Neumann, Gregory A., Cavanaugh, J. F., Sun, X., Mazarico, E. M., Smith, D. E., Zuber, M. T., et al. (2013). Bright and dark polar deposits on Mercury: Evidence for surface volatiles. *Science*, *339*(6117), 296–300. https://doi.org/10.1126/science.1229764

Nittler, L. R., Starr, R. D., Weider, S. Z., McCoy, T. J., Boynton, W. V., Ebel, D. S., et al. (2011). The major-element composition of Mercury's surface from MESSENGER X-ray spectrometry. *Science*, *333*(6051), 1847–1850. https://doi.org/10.1126/science.1211567

Ong, L., Asphaug, E. I., Korycansky, D., & Coker, R. F. (2010). Volatile retention from cometary impacts on the Moon. *Icarus*, *207*(2), 578–589. https://doi.org/10.1016/j.icarus.2009.12.012

Owen, T. C., & Bar-Nun, A. (2001). Contributions of icy planetesimals to the Earth's early atmosphere. *Origins of Life and Evolution of the Biosphere*, *31*(4), 435–458. https://doi.org/10.1023/A:1011809412925

Paige, D. A., Siegler, M. A., Harmon, J. K., Neumann, G. A., Mazarico, E. M., Smith, D. E., et al. (2013). Thermal stability of volatiles in the north polar region of Mercury. *Science*, *339*(6117), 300–303. https://doi.org/10.1126/science.1231106

Paige, D. A., Siegler, M. A., Zhang, J. A., Hayne, P. O., Foote, E. J., Bennett, K. A., et al. (2010). Diviner Lunar Radiometer observations of cold traps in the Moon's south polar region. *Science*, *330*(6003), 479–482. https://doi.org/10.1126/science.1187726

National Academies (2007). The Scientific Context for the Exploration of the Moon. Committee on the Scientific Context for Exploration of the Moon, National Research Council of the National Academies. http://lroc.sese.asu.edu/files/FactSheets/ExplorationofMoon.pdf

Peplowski, P. N., Evans, L. G., Stockstill-Cahill, K. R., Lawrence, D. J., Goldsten, J. O., McCoy, T. J., et al. (2014). Enhanced sodium abundance in Mercury's north polar region revealed by the MESSENGER Gamma-Ray Spectrometer. *Icarus*, *228*, 86–95. https://doi.org/10.1016/j.icarus.2013.09.007

Peplowski, P. N., Klima, R. L., Lawrence, D. J., Ernst, C. M., Denevi, B. W., Frank, E. A., et al. (2016). Remote sensing evidence for an ancient carbon-bearing crust on Mercury. *Nature Geoscience*, *9*(4), 273–276. https://doi.org/10.1038/ngeo2669

Peplowski, P. N., Lawrence, D. J., Evans, L. G., Klima, R. L., Blewett, D. T., Goldsten, J. O., et al. (2015). Constraints on the abundance of carbon in near-surface materials on Mercury: Results from the MESSENGER Gamma-Ray Spectrometer. *Planetary and Space Science*, *108*, 98–107. https://doi.org/10.1016/j.pss.2015.01.008

Peplowski, P. N., Lawrence, D. J., Rhodes, E. A., Sprague, A. L., McCoy, T. J., Denevi, B. W., et al. (2012). Variations in the abundances of potassium and thorium on the surface of Mercury: Results from the MESSENGER Gamma-Ray Spectrometer. *Journal of Geophysical Research: Planets*, *117*(E12). https://doi.org/10.1029/2012JE004141

Platz, T., Nathues, A., Schorghofer, N., Preusker, F., Mazarico, E., Schröder, S. E., et al. (2016). Surface water-ice deposits in the northern shadowed regions of Ceres. *Nature Astronomy*, *1*(1), 1–6. https://doi.org/10.1038/s41550-016-0007

Pokorný, P., Janches, D., Sarantos, M., Szalay, J. R., Horányi, M., Nesvorný, D., & Kuchner, M. J. (2019). Meteoroids at the Moon: Orbital properties, surface vaporization, and impact ejecta production. *Journal of Geophysical Research: Planets*, *124*(3), 752–778. https://doi.org/10.1029/2018JE005912

Prem, P., Artemieva, N. A., Goldstein, D. B., Varghese, P. L., & Trafton, L. M. (2015). Transport of water in a transient impact-generated lunar atmosphere. *Icarus*, *255*, 148–158. https://doi.org/10.1016/j.icarus.2014.10.017

Prem, P., Goldstein, D. B., Varghese, P. L., & Trafton, L. M. (2018). The influence of surface roughness on volatile transport on the Moon. *Icarus*, *299*, 31–45. https://doi.org/10.1016/j.icarus.2017.07.010

Prem, P., Goldstein, D. B., Varghese, P. L., & Trafton, L. M. (2019). Coupled DSMC-Monte Carlo radiative transfer modeling of gas dynamics in a transient impact-generated lunar atmosphere. *Icarus*, *326*, 88–104. https://doi.org/10.1016/j.icarus.2019.02.036

Putzig, N. E., Phillips, R. J., Campbell, B. A., Mellon, M. T., Holt, J. W., & Brothers, T. C. (2014). SHARAD soundings and surface roughness at past, present, and proposed landing sites on Mars: Reflections at Phoenix may be attributable to deep ground ice. *Journal of Geophysical Research: Planets*, *119*(8), 1936–1949. https://doi.org/10.1002/2014JE004646

Qiao, L., Ling, Z., Head, J. W., Ivanov, M. A., & Liu, B. (2019). Analyses of Lunar Orbiter Laser Altimeter 1,064-nm albedo in permanently shadowed regions of polar crater flat floors: Implications for surface water ice occurrence and future in situ exploration. *Earth and Space Science*, *6*(3), 467–488. https://doi.org/10.1029/2019EA000567

Rivera-Valentín, E. G., Bhiravarasu, S. S., Meyer, H. M., Taylor, P. A., Nolan, M. C., Chabot, N. L., & Virkki, A. K. (2020). High-resolution radar images of Mercury from the 2019 inferior conjunction. *Lunar and Planetary Science Conference, 51,* Abstract #1593. https://www.hou.usra.edu/meetings/lpsc2020/pdf/1593.pdf

Rodriguez, J. A. P., Leonard, G. J., Kargel, J. S., Domingue, D., Berman, D. C., Banks, M., et al. (2020). The chaotic terrains of Mercury reveal a history of planetary volatile retention and loss in the innermost solar system. *Scientific Reports*, *10*(1), 1–14. https://doi.org/10.1038/s41598-020-59885-5

Roush, T. L., Colaprete, A., Elphic, R., Ennico-Smith, K., Heldmann, J., Stoker, C., et al. (2015). In Situ Resource Utilization (ISRU) field expedition 2012: Near-Infrared Volatile Spectrometer System (NIRVSS) science measurements compared to site knowledge. *Advances in Space Research*, *55*(10), 2451–2456. https://doi.org/10.1016/j.asr.2014.08.033

Rubanenko, L., Mazarico, E., Neumann, G. A., & Paige, D. A. (2018). Ice in micro cold traps on Mercury: Implications for age and origin. *Journal of Geophysical Research: Planets*, *123*(8), 2178–2191. https://doi.org/10.1029/2018JE005644

Rubanenko, Lior, Venkatraman, J., & Paige, D. A. (2019). Thick ice deposits in shallow simple craters on the Moon and Mercury. *Nature Geoscience*, *12*(8), 597–601. https://doi.org/10.1038/s41561-019-0405-8

Saal, A. E., Hauri, E. H., Cascio, M. L., Orman, J. A. V., Rutherford, M. C., & Cooper, R. F. (2008). Volatile content of lunar volcanic glasses and the presence of water in the Moon's interior. *Nature*, *454*(7201), 192–195. https://doi.org/10.1038/nature07047

Sargeant, H. M., Bickel, V. T., Honniball, C. I., Martinez, S. N., Rogaski, A., Bell, S. K., et al. (2020). Using boulder tracks as a tool to understand the bearing capacity of permanently shadowed regions of the Moon. *Journal of Geophysical Research: Planets*, *125*(2), e2019JE006157. https://doi.org/10.1029/2019JE006157

Schorghofer, N., & Aharonson, O. (2014). The lunar thermal ice pump. *The Astrophysical Journal*, *788*(169), 1–7. https://doi.org/10.1088/0004-637X/788/2/169

LEAG (2012). Strategic knowledge gaps for the "Moon First" human exploration scenario. Analysis and findings of Lunar Exploration Analysis Group (LEAG) GAP-Specific Action Team (SAT). https://www.lpi.usra.edu/leag/GAP_SAT_03_09_12.pdf

Siegler, M. A., Miller, R. S., Keane, J. T., Laneuville, M., Paige, D. A., Matsuyama, I., et al. (2016). Lunar true polar wander inferred from polar hydrogen. *Nature*, *531*(7595), 480–484. https://doi.org/10.1038/nature17166

Smith, D. E., Zuber, M. T., Frey, H. V., Garvin, J. B., Head, J. W., Muhleman, D. O., et al. (1998). Topography of the northern hemisphere of Mars from the Mars Orbiter Laser Altimeter. *Science*, *279*(5357), 1686–1692. https://doi.org/10.1126/science.279.5357.1686

Smith, David E., Zuber, M. T., Neumann, G. A., Mazarico, E., Lemoine, F. G., Head III, J. W., et al. (2017). Summary of the results from the Lunar Orbiter Laser Altimeter after seven years in lunar orbit. *Icarus*, *283*, 70–91. https://doi.org/10.1016/j.icarus.2016.06.006

Spudis, P.D., & Guest, J.E. (1988). Stratigraphy and geologic history of Mercury. F. Vilas, C.R. Chapman, M.S. Matthews (Eds.), Mercury, University of Arizona Press, Tucson, pp. 118-164.

National Academies (2011). Vision and voyages for planetary science in the decade 2013-2022. Committee on the Planetary Science Decadal Survey, Space Studies Board. National Research of the National Academies. https://doi.org/10.17226/13117

Stewart, B. D., Pierazzo, E., Goldstein, D. B., Varghese, P. L., & Trafton, L. M. (2011). Simulations of a comet impact on the Moon and associated ice deposition in polar cold traps. *Icarus*, *215*(1), 1–16. https://doi.org/10.1016/j.icarus.2011.03.014

Strom, R. G., Trask, N. J., & Guest, J. E. (1975). Tectonism and volcanism on Mercury. *Journal of Geophysical Research: Solid Earth*, 2478–2507. https://doi.org/10.1029/JB080i017p02478@10.1002/(ISSN)2169-9356.MERC1

Susorney, H. C. M., James, P. B., Johnson, C. L., Chabot, N. L., Ernst, C. M., Mazarico, E. M., et al. (2019). The thickness of radar-bright deposits in Mercury's northern hemisphere from individual Mercury Laser Altimeter tracks. *Icarus*, *323*, 40–45. https://doi.org/10.1016/j.icarus.2019.01.016

Szalay, J. R., & Horányi, M. (2016). Lunar meteoritic gardening rate derived from in situ LADEE/LDEX measurements. *Geophysical Research Letters*, *43*(10), 4893–4898. https://doi.org/10.1002/2016GL069148

Thomas, N., Spohn, T., Barriot, J.-P., Benz, W., Beutler, G., Christensen, U., et al. (2007). The BepiColombo Laser Altimeter (BELA): Concept and baseline design.

Planetary and Space Science, *55*(10), 1398–1413. https://doi.org/10.1016/j.pss.2007.03.003

Thomas, R. J., Rothery, D. A., Conway, S. J., & Anand, M. (2014). Hollows on Mercury: Materials and mechanisms involved in their formation. *Icarus*, *229*, 221–235. https://doi.org/10.1016/j.icarus.2013.11.018

Tucker, O. J., Farrell, W. M., Killen, R. M., & Hurley, D. M. (2018). Solar wind implantation into the lunar regolith: Monte carlo simulations of H retention in a surface with defects and the H2 exosphere. *Journal of Geophysical Research: Planets*, *124*(2), 278–293. https://doi.org/10.1029/2018JE005805

Vander Kaaden, K. E., McCubbin, F. M., Byrne, P. K., Chabot, N. L., Ernst, C. M., Johnson, C. L., & Thompson, M. S. (2019). Revolutionizing our understanding of the solar system via sample return from Mercury. *Space Science Reviews*, *215*(8), 49. https://doi.org/10.1007/s11214-019-0614-x

Vasavada, A. R., Paige, D. A., & Wood, S. E. (1999). Near-surface temperatures on Mercury and the Moon and the stability of polar ice deposits. *Icarus*, *141*(2), 179–193. https://doi.org/10.1006/icar.1999.6175

Weider, S. Z., Nittler, L. R., Murchie, S. L., Peplowski, P. N., McCoy, T. J., Kerber, L., et al. (2016). Evidence from MESSENGER for sulfur- and carbon-driven explosive volcanism on Mercury. *Geophysical Research Letters*, *43*(8), 3653–3661. https://doi.org/10.1002/2016GL068325

Whitten, J. L., Head, J. W., Denevi, B. W., & Solomon, S. C. (2014). Intercrater plains on Mercury: Insights into unit definition, characterization, and origin from

MESSENGER datasets. *Icarus*, *241*(Supplement C), 97–113. https://doi.org/10.1016/j.icarus.2014.06.013

Williams, J.-P., Greenhagen, B. T., Paige, D. A., Schorghofer, N., Sefton-Nash, E., Hayne, P. O., et al. (2019). Seasonal polar temperatures on the Moon. *Journal of Geophysical Research: Planets*, *124*(10), 2505–2521. https://doi.org/10.1029/2019JE006028

Williams, J.-P., Paige, D. A., Greenhagen, B. T., & Sefton-Nash, E. (2017). The global surface temperatures of the Moon as measured by the Diviner Lunar Radiometer Experiment. *Icarus*, *283*(Supplement C), 300–325. https://doi.org/10.1016/j.icarus.2016.08.012

Zacny, K., Paulsen, G., McKay, C. p., Glass, B., Davé, A., Davila, A. f., et al. (2013). Reaching 1 m deep on Mars: The icebreaker drill. *Astrobiology*, *13*(12), 1166–1198. https://doi.org/10.1089/ast.2013.1038

Zacny, K., Quinn, J., Kleinhenz, J., Smith, J., Captain, J., Mank, Z., Vendiola, V., & Paulsen, G. (2019). TRIDENT and PVEx drilling systems for delivery of regolith and volatiles. *Lunar Exploration Analysis Group Meeting., 51*, Abstract #5033. https://www.hou.usra.edu/meetings/leag2019/pdf/leag2019_program.htm

Zhang, J. A., & Paige, D. A. (2009). Cold-trapped organic compounds at the poles of the Moon and Mercury: Implications for origins. *Geophysical Research Letters*, *36*(16), L16203. https://doi.org/10.1029/2009GL038614

Zolotov, M. Yu., Sprague, A. L., Hauck, S. A., Nittler, L. R., Solomon, S. C., & Weider, S. Z. (2013). The redox state, FeO content, and origin of sulfur-rich magmas on

Mercury. *Journal of Geophysical Research: Planets*, *118*(1), 138–146. https://doi.org/10.1029/2012JE004274

Zuber, M., Head, J., E Smith, D., A Neumann, G., Mazarico, E., H Torrence, M., et al. (2012). Constraints on the volatile distribution within Shackleton crater at the lunar south pole. *Nature*, *486*, 378–381. https://doi.org/10.1038/nature11216